European Optical Society

Coherence for Europe ®

6th EOS Topical Meeting on Visual and Physiological Optics (EMVPO 2012)

20 - 22 August 2012, University College Dublin (UCD), Dublin, Ireland

FINAL PROGRAMME

Sponsors:

In cooperation with:

European Optical Society

Annual Meeting

EOS Annual Meeting 2012

25 - 28 September

Aberdeen Exhibition and Conference Centre, Scotland (UK)

Post-deadline submission
20 - 26 August

SAVE MONEY
AS WELL AS NERVES!

BOOK YOUR ALL-INCLUSIVE SHELL SCHEME PACKAGE.

EOSAM 2012 Exhibition

25 - 27 September

TOPICAL FOCUS OF THE EXHIBITION:

- Photonics for offshore applications ("blue photonics"®)
- Biomedical photonics
- Organic optoelectronics
- Micro-optical components and systems

aberdeen@myeos.org | www.myeos.org/events/eosam2012

ABOUT EOS

History

The European Optical Society (EOS) was founded in 1991. The purpose of the society is to contribute to progress in optics and related sciences, and to promote their applications at the European and international levels, by bringing together individuals and legal entities involved in these disciplines and their applications. EOS is a not for profit organisation and serves as the joint forum for all individuals, companies, organisations, educational institutions, and learned and professional societies, who recognise the opportunity and challenge that a common European base provides for the development of optics in its broadest sense. EOS organises recognized topical meetings, conferences, workshops and other events, publishes journals and is an important player on the European level. 22 national optical societies and a great number of individuals and companies are currently members of EOS (www.myeos.org).

EOS membership - Join us and...

- Be a part of the umbrella organisation of the national optical societies in Europe
- Connect with colleagues from all over Europe and beyond
- Contribute to strengthening Europe's future in optics and photonics
- Stay up-to-date about European Research Funding
- Benefit from discounts on EOS events and publications in the EOS online journal JEOS:RP
- Receive the Annual EOS Member Directory - your guide to the European optics and photonics community

Activities

- Organisation of topical meetings, workshops and conferences, and endorsement of other scientific events
- Operation of a virtual platform for the European optics and photonics community at www.myeos.org
- Focus Groups and Student Clubs (as of 2011)
- Publication of JEOS:RP, the electronic Journal of the European Optical Society - Rapid Publications (www.jeos.org)
- Bi-monthly electronic member newsletter
- Representation of the optics and photonics community on the European level (Photonics21 Technology Platform)
- Annual award of the EOS Prize

Membership modes and fees

Individual membership

Annual fee: 50 €

Individual membership through an EOS Branch

Every member of an EOS Branch is automatically an individual member of the EOS, too, with all benefits.

Annual fee: included in the Branch membership fee

Student membership

Annual fee: 10 €

Associate membership through an EOS Affiliated Society

Every member of an EOS Affiliated Society is automatically an associate member of the EOS, too, but with limited benefits.

Annual fee: included in the Affiliated Society membership fee

Upgrade for associate members

Upgrade to an individual EOS membership with full benefits.
Annual fee: 12.50 €

Corporate membership through an EOS Branch or Affiliated Society

Annual fee: 200 €

Direct corporate membership

Annual fee: 300 €

How to join?

To join the EOS as an individual, student or corporate member, please see our website at www.myeos.org/members.

Questions?

Please contact the EOS office at info@myeos.org.

VENUE

The capital city of Ireland, Dublin, has transformed immensely during the Celtic Tiger Years welcoming the visitor to its sights, its welcoming people and culture, and its attractive modern waterfront area. Dublin has always been strongly linked to the sea where also the Vikings made their mark sailing up the river Liffey more than a thousand years ago.
For a night out Temple Bar near the old Viking settlement is where a pint of Dublin's famous dark Guinness (or a whiskey with an 'e') can be enjoyed to the sound of Irish music, a lively chat, and possibly the story of fishmonger Molly Malone.

Literature is key to the Irish and to Dublin, in particular, where a string of eminent writers including Oscar Wilde, William Butler Yeats, Samuel Beckett, George Bernard Shaw, John Millington Synge, Bram Stoker, and of course James Joyce the author of the "Dubliners" have all left lasting impressions in the Writers Museum and in locations and statues across the city. Also not to be missed is the 1200 years-old Book of Kells.

Science has equally made its mark in Dublin where prominent scientists include George Stokes, William Rowan Hamilton, John Tyndall, Francis Fitz Gerald, Thomas Preston, John L. Synge, and Edward H. Synge, while also Erwin Schrödinger worked in Dublin for a number of years. Their work and that of many others has given rise to a modern Ireland soundly based on science and innovation that is reflected in Dublin City of Science 2012.

EMVPO 2012 is taking place at:

Clinton Auditorium, University College Dublin (UCD)
Belfield, Dublin 4, Ireland

GETTING THERE

The University College Dublin is located 4 km south of the centre of Dublin city on the Belfield Campus (Campus map: www.ucd.ie/maps) and can easily be reached by public transport.

BY PLANE

Dublin International Airport is situated north of the city centre and is served by 63 airlines connecting the capital city of Ireland with 28 airports in the UK and about 100 European destinations (www.dublinairport.com/gns/flight-information/destinations-airlines.aspx).

From the airport to the venue/city centre by *Aircoach*:
The *Aircoach* service is operating 24 hours/day and serves most of the major hotels in Dublin City as well as the UCD Belfield campus. To get directly to the venue exit at *UCD Slip road*.

For more information (e.g. on fares), please see:
www.aircoach.ie

BY TRAIN

Travelling to Dublin by train you will arrive at *Connolly* or *Heuston* Station which are the main railway stations in Dublin.

From *Connelly Station* to the venue:

- take a bus from *O'Connell Street* which is located about 500 m away from *Connelly Station* (to *O'Connell Street*: go down *Talbot Street*, then straightforward onto *Earl Street* and you are directly walking towards *O'Connell Street*)
- from there take the bus lines 2 (Stop No. 279; towards *Sandymount Tower, St. John's Church*) or 46A (Stop No. 271; towards *Dun Laoghaire*) and exit at *UCD Belfield (Stop No. 766)*. You can take as well the bus line 11 (Stop No. 271 or 272; towards *Sandyford Industrial estate*) and exit at *Clonskeagh Road, Junction Wynnsward Drive (Stop No. 860)*

From *Heuston Station* (Bus Stop No: 4320) to the venue:

- take the bus line 145 (towards *Kilmacanogue*) and exit at *Stillorgan/Opposite Woodbine Road* (Stop No. 2007). The entrance of the Belfield Campus is 200 m away.

Useful links:

- Plan you individual journey at the operator's website: www.dublinbus.ie/Route-Planner
- Website of the Dublin Suburban Rail network *Iarnród Éireann:* www.irishrail.ie/home

TO THE VENUE BY PUBLIC TRANSPORT

The UCD Belfield Campus is served by the following bus routes: 2, 3, 11, 17, 39A (terminates within the Belfield campus), 46A, 84 and 145.
Please note that Dublin city buses only accept payment with coins and do not give cash-back so bring plenty of coins.

Useful link:

- Plan you individual journey at the *Dublin Bus* website: www.dublinbus.ie/Route-Planner

BY FERRY & CAR

There are ferry routes to and from Great Britain to Dublin Port and Dun Laoghaire Harbour.

Further information:

- www.dublintourist.com
- www.visitdublin.com/travel/getting_here/Ferries

If you wish to go to Dublin by car the *AA Route Planner* may help you planning your journey: www2.aaireland.ie/routes_beta. **Please note:** it is left-hand traffic in Ireland and there are a few toll roads (for more details please see the paragraph "Toll information" on the next page)

GETTING THERE (continued)

TOLL INFORMATION

The *National Roads Authority (NRA)* collects tolls for the use of certain roads, e.g. on the M50 motorway around Dublin.

Useful links:

- General information on the toll system: www.citizensinformation.ie/en/travel_and_recreation/roads_and_safety/national_toll_roads_in_ireland.html
- Listing of all toll roads at the website of the *National Roads Authority (NRA)*: www.nra.ie/GeneralTollingInformation/KnowTheToll
- Information on the Barrier-Free tolling on the motorway M50 around Dublin: www.nra.ie/GeneralTollingInformation/KnowTheToll/M50BarrierFreeTolling

GETTING AROUND IN DUBLIN

PUBLIC TRANSPORT NETWORK

Dublin offers a well organised public transport system which is mainly based on an intensive bus network *Dublin Bus* and a tram service called *LUAS*.

Further information:

- Dublin Bus: www.dublinbus.ie
- LUAS: www.luas.ie
- Public transport maps: www.visitdublin.com/travel/Maps

General information about Dublin is available at:

- www.visitdublin.com
- www.dublintourist.com
- Dublin maps: www.dublintourist.com/maps
- Official *Transport for Dublin* website: www.transportfordublin.ie

CARE HIRE

The *Official Online Tourist Office of Dublin* offers a search engine for Car Hiring, please see: www.visitdublin.com/travel/Car_Hire

DUBLIN CABS

In Dublin taxis are of course available at the airport and at several taxi ranks throughout the city. For booking a taxi (e.g. to ensure travelling punctually to the airport also in peak periods) we would recommend to ask at your hotel.

Useful links:

- General information: www.dublin.info/taxi
- Listing of operating companies depending on the city district: www.dublincabs.com/index.php

SIGHTSEEING PROPOSALS

"The Wicklow way"
South of Dublin city the Dublin and Wicklow mountains have an air of their own appreciated by hikers and history buffs alike. The village Enniskerry is home to the Powerscourt Estate and its classical garden, nearby Johnnie Fox's pub lays claim to being the "highest pub in Ireland" and offers Irish music and excellent food. Further south, Glendalough has a spectacular scenary and a rich medieval history from the early days of Christianity. All is connected by a marked hiking route: "The Wicklow way".

Further touristic attractions in Dublin:
If you are planning to extend your stay in Dublin you may wish to discover the touristic sides of Dublin:

- Touristic attractions in Dublin: www.dublin.info/attractions
- See & Do in Dublin: www.visitdublin.com/See_and_Do




CAMPUS MAP: UCD ACCESS POINTS

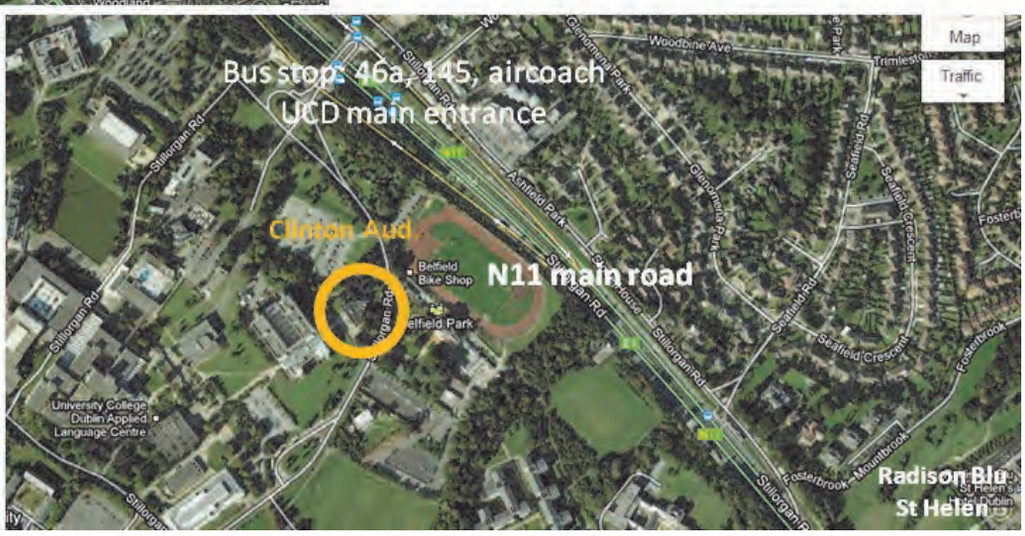

HOTEL LIST

Please note that the room rates as well as the information on internet facilities (internet plugs, Wi-fi etc.) are taken from the homepages of the listed hotels.
Rates may vary from the prices listed below (e.g. during fairs or depending on the season) according to room availability and reservation date. Please contact the hotel directly to make your reservation.

Rooms at a special rate have been blocked near the conference venue at UCD:

1) Stillorgan Park Hotel****

Address: Stillorgan Road,
Dublin 18, Ireland
Phone: +353 (0) 1 200 1814
Fax: +353 (0) 1 283 1610
Email: reservations@stillorganpark.com
Website: www.stillorganpark.com

Remarks:
- Free WiFi in rooms and common areas
- Free Car Parking available (300 car spaces)
- Complimentary Shuttle Bus Service from the hotel to UCD and back (Monday to Friday 7.30 - 11.15 and 14.30 - 18.30 CEST)
- Distance to UCD: 2.5 km (approx. 5 minutes by car)

Rates:
- 79.00 Euro/room - single room excl. breakfast
- 89.00 Euro/room - single room incl. breakfast
- 99.00 Euro/room - twin/ double room incl. breakfast

Booking details:
Please use the following registration form and refer directly to the hotel reservation via email, fax or phone:
www.myeos.org/download/EMVPO2012/Stillorgan Park Hotel Accommodation Booking Form EMVPO 2012.pdf

→ When making your reservation, please mention the booking code "98243".
This offer is **valid until 02 July 2012**. Following this date, all bookings will be subject to availability.

2) Radisson Blu St. Helens Hotel*****

Address: Stillorgan Road,
Dublin 4, Ireland
Phone: +353 (0) 1 218 6000
Fax: +353 (0) 1 218 6010
Reservations: +1 800 333 3333 US
+1 800 55 7474 Ireland
+353 (0) 1 706 0225 EU
Email info.dublin@radissonblu.com
Website www.radissonblu.ie/sthelenshotel-dublin

Remarks:
- Free Internet access and/or WiFi throughout the hotel
- Free Car Parking available (220 car spaces)
- Distance to UCD: 500 m (approx. 2 minutes walking)

Rates:
130.00 Euro/room - single room incl. breakfast
140.00 Euro/room - twin/double room incl. breakfast

Booking details:
Please refer directly to the hotel reservation when making your reservation.
This offer is **valid until 01 July 2012**. Following this date, all bookings will be subject to availability.

→ Booked period: 19 - 23 August 2012

3) UCD Campus Accomodation

Rates: 49.50 Euro/night/single ensuite room (breakfast incl.)
Address: Belfield,
Dublin 4, Ireland
URL: http://ucd.globalenginemedia.com/Conference?conf=EMVPO2012

Distance to the meeting venue: located on Belfield campus
Booking details:
Please refer directly to the registration website above to make your reservation.

→ Booked period: 19 - 25 August 2012

Address: Clonskeagh Road,
Dublin 14, Ireland
URL: www.irishbeds.com/bnb/dublin/216.html
Phone: +353 (0)1 269 8768
Internet: not specified
Distance to the meeting venue: about 2 km
To UCD: take the bus line 11 (towards *Sandyford Industrial Estate*) from 'Clonskeagh Road, Opposite Whitethorn Road' *(Bus Stop 859)*; change at 'Roebuck Road, Islamic Centre' *(Bus Stop 862)* into bus line 17 (towards *Blackrock Rail Station*) and exit at 'UCD Belfield Campus' *(Bus Stop 768)*



HOTELS LIST (continued)

ALTERNATIVE HOTELS

The Burlington Hotel****

Rates: 99-109 Euro/per night/single room (breakfast: not specified)
Address: Upper Leeson Street, Dublin 4, Ireland
URL: www.burlingtonhotel.ie
Phone: +353 (1) 6185600
Fax: +353 (1) 6185693
Email: info@burlingtonhotel.ie
Internet: Complimentary High Speed Internet Access
Distance to the meeting venue: about 6 km
To UCD: take bus lines 145 (towards *Kilmacanogue*), 46a (towards *Dun Laoghaire*), 7b (towards *Shankill*), 7d (towards *Dalkey*) from 'Leeson Street, Junction St. Stephen's Green East' *(Bus Stop 845)* and exit at 'UCD Belfield, Slip Road Stillorgan Dual Carriageway' *(Bus Stop 768)*

Hampton Hotel****

Rates: 84-169 Euro/night/person (breakfast: not specified)
Address: 19-29 Morehampton Road, Donnybrook, Dublin 4, Ireland
URL: www.hamptonhotel.ie
Phone: +353 (0)1 6680995
Email: info@hamptonhotel.ie
Internet: not specified
Distance to the meeting venue: about 4 km
To UCD: take the bus lines 145 (towards *Kilmacanogue*), 46a (towards *Dun Laoghaire*), 116 (towards *Whitechurch*), 7b (towards *Shankill*), 7d (towards *Dalkey*) from 'Morehampton Road, Junction Bloomfield Avenue' *(Bus Stop 777)* and exit at and exit at 'UCD Belfield, Opposite Woodbine Road' *(Bus Stop 2007)*

Tara Towers Hotel***

Rates: ~55-75 Euro/night/single room (breakfast: can be booked separately)
Address: Merrion Road, Dublin 4, Ireland
URL: www.taratowers.com
Phone: +353 (0)1 269 4666
Fax: +353 (0)1 269 1027
Email: info@taratowers.com
Internet: Free Wi-Fi access in the lobby, in rooms for an additional charge
Distance to the meeting venue: about 4 km (20 min walk from UCD)
To UCD: take the bus line 27x (towards *UCD Belfield*) from 'Merrion Road, Junction Merlyn Road' *(Bus Stop 420)* and exit at 'UCD Belfield, Slip Road Stillorgan Dual Carriageway' *(Bus Stop 4952)*

BED & BREAKFAST (B&B)

The Cottage B&B

Rates: from 50 Euro/night/person (breakfast: not specified)
Address: Clonskeagh Road, Dublin 14, Ireland
URL: www.irishbeds.com/bnb/dublin/216.html
Phone: +353 (0)1 269 8768
Internet: not specified
Distance to the meeting venue: about 2 km
To UCD: take the bus line 11 (towards *Sandyford Industrial Estate*) from 'Clonskeagh Road, Opposite Whitethorn Road' *(Bus Stop 859)*; change at 'Roebuck Road, Islamic Centre' *(Bus Stop 862)* into bus line 17 (towards *Blackrock Rail Station*) and exit at 'UCD Belfield Campus' *(Bus Stop 768)*

Morehampton Townhouse

Rates: from 54 Euro/night/person (breakfast: can be booked separately)
Address: 78 Morehampton Road, Donnybrook, Dublin 4, Reland
URL: www.morehamptontownhouse.com
Phone: +353 (0) 1 66 888 66
Fax: +353 (0) 1 66 879 73
Email: bookings@morehamptontownhouse.com
Internet: Free Wi-Fi (high speed) in rooms and public areas
Distance to the meeting venue: about 4 km
To UCD: take the bus line 39a (towards *UCD Belfield*) from 'Opposite Bloomfield Avenue' *(Bus Stop 756)* and exit at 'UCD Belfield Campus' *(Bus Stop 767)*

INFORMATION FOR AUTHORS AND ATTENDEES

ORAL PRESENTATIONS

Time slots: Presenting authors are allotted 15 minutes (12 minutes presentation plus 3 minutes for discussion). Please plan your presentation accordingly to meet the 15 minute maximum.

Presentation upload: Speakers are requested to upload their presentation to the computer in the meeting room well in advance to their talk.

Presentation format: Please bring your presentation on a USB mass storage, CD-ROM or DVD and include all video files. File formats: ppt, pptx and pdf. A Windows-based presentation computer will be provided.

For Mac users: To make sure your presentation is displayed correctly, please:
- bring your presentation as pdf-file with fonts embedded or
- restrict yourself to Arial/Times New Roman (not Times)/Courier New (not Courier)/Symbol/Wingdings when creating your ppt- or pptx-file.

Technical equipment: All technical equipment (presentation computer, video projector, sound system, laser pointer) will be available on-site. It is not possible to use your personal laptop.

POSTER PRESENTATIONS

Poster authors are requested to be present at their posters during the official poster session. Please **prepare and print** your poster in advance to the conference. Poster set-up and removal is in the responsibility of the authors. Any posters left on the boards at the close of the poster session will be discarded. Poster numbers will be displayed on the poster boards to show authors where to place their poster.

Required poster size: The posters should have a size of DIN A1 (594 x 841 mm) or DIN A0 (841 x 1189 mm) preferably in a portrait format (not landscape format). Double sided tape and similar pads will be provided by the organizer. The size of the poster boards is 90 cm (width) x 200 cm (height).

The official poster sessions will be held on
- Monday, 20 August, 14:00-15:30
- Wednesday, 22 August, 14:00-15:30
  in the Exhibition area.

EOS REGISTRATION DESK

Please collect your material on **Sunday afternoon or on Monday morning.**

On-site registration hours	
Sunday, 19 August	17:00-18:00
Monday, 20 August	08:00-18:15
Tuesday, 21 August	08:30-13:30
Wednesday, 22 August	08:30-18:00

Information / Receipts / Confirmation of attendance / Cash payment
Attendees requiring a payment receipt or confirmation of attendance may obtain these documents onsite at the EOS registration desk. Attendees paying by cash are requested to have the exact change ready in Euro.

REGISTRATION & FEES

At least one author of an accepted presentation is requested to register properly in advance to the conference.
The registration fee includes full-time admission to the meeting, coffee breaks and lunches on all three meeting days, the conference dinner on Tuesday, 21 August, one copy of the extended programme as well as an expense contribution of 24.00 EUR for the social programme on Tuesday, 21 August.

Registration category	**Early-bird fee** (until 19 July)		**Late/On-site fee** (after 19 July)	
	incl. 19 % VAT	**excl. VAT***	**incl. 19 % VAT**	**excl. VAT***
Registration for members	424.00 €	356.30 €	504.00 €	423.53 €
Registration for non-members	484.00 €	406.72 €	564.00 €	473.95 €
Registration for student members	224.00 €	188.24 €	274.00 €	230.25 €
Registration for student non-members	244.00 €	205.04 €	294.00 €	247.06 €

*** PLEASE NOTE:** Registrations from companies and non-university research institutes registered in EU countries (except Germany) are exempted from VAT, **if VAT no. is given.**

WELCOME RECEPTION

INFORMATION FOR AUTHORS AND ATTENDEES (continued)

All attendees of EMVPO 2012 are cordially invited to attend the welcome reception that will be taking place on **Sunday, 19 August, from 18:30 to 20:00** in the **Old Physics Theatre** (Newman House, 85/86 St. Stephens Green, Dublin 2).

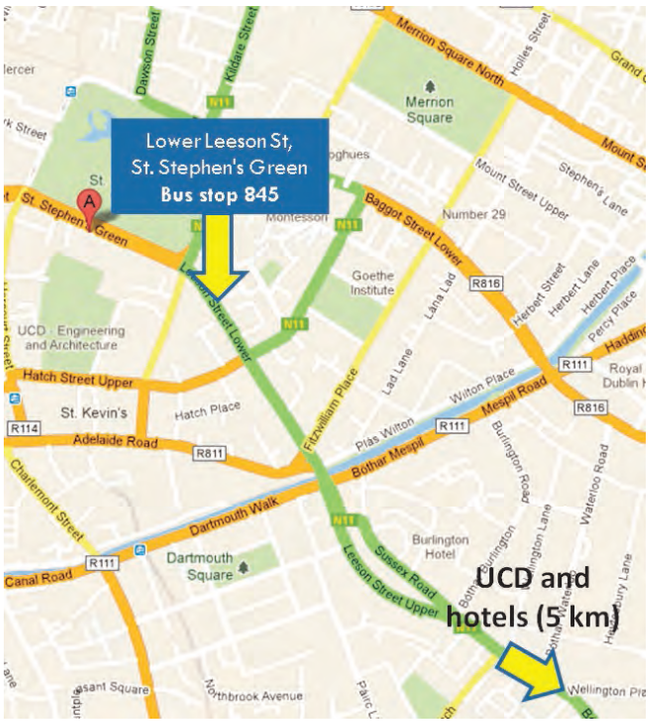

The Newman House is located in front of St Stephen's Green park in the city centre

Getting from UCD to Newman House by public transport
From *UCD, Stillorgan Road – Stop 768* take one of the follwoing bus lines:

- 46a, towards Phoenix Park (running every 5 min.)
- 145, towards Heuston Rail Station (running every 5 min.)
- 39a, towards Ongar
- 116, towards Burlington Hotel
- 118, towards D'Olier St.
- 46e, towards Mountjoy Sq.
- 7b, towards Mountjoy Sq.
- 7d, towards Mountjoy Sq.

Exit at *Lower Leeson St, St. Stephen's Green – Stop 845.*

From the bus stop the walking distance to Newman House is 500 m (~7 minutes). Go down the Lower Leeson Street towards Lower Hatch Street and then straight forward to St. Stephen's Green. The Newman House is situated on the left side.

SOCIAL PROGRAMME & CONFERENCE DINNER

When: Tuesday, 21 August 2012, 14:00 – 21:00

Join our guided Dublin Bay & Castle Tour followed by a conference dinner in the fishing village Howth just north of Dublin. The participation is included in your conference fee.

The Dublin Bay & Castle Tour will start with a scenic drive along Dublin's coastal drive with some spectacular view of the seaside and shores and end at the small fishing village Howth facing "Ireland's eye". You will have time to see the seals or wander through the picturesque village admiring its charming marina before stopping in one of the small restaurants for the conference dinner.

PAPER PUBLICATION IN OPHTHALMIC AND PHYSIOLOGICAL OPTICS (WILEY)

Following the conference, a special issue of Ophthalmic and Physiological Optics will be published including papers from EMVPO-6.
Submitted papers will undergo a rigorous reviewing process to ensure a high quality of all published work

BEST STUDENT PRESENTATION AWARD

Sponsored by Springer science+business media

The best student oral contribution and the best student poster presentation of EMVPO 2012 will be awarded a diploma, an EOS student membership for 2012 and a prize sponsored by Springer.
All student oral and poster contributions are eligible to the prize. The criteria for the award are relevance, originality, scientific merit and clarity.

WIFI ACCESS

Free WIFI access will be available at the conference location. Please ask at the registration desk for the password.

SYNOPSIS

The 6th EOS Topical Meeting on Visual and Physiological Optics (EMVPO 2012) will take place at the University College Dublin (UCD), Ireland, 20 - 22 August 2012. This is the sixth of a series of meetings that has previously taken place in Wroclaw, Poland (1999), Granada, Spain (2004), London, UK (2006), Heraklion, Greece (2008), and Stockholm, Sweden (2010).

The EMVPO meetings, attended by students and world-leading researchers in visual and physiological optics, are much appreciated due to their scientific quality and informal atmosphere encouraging discussions. Areas to be covered include basic and applied elements of vision research such as adaptive optics and eye dynamics, ocular aberrations and corrections, intraocular scattering, retinal image quality, cornea, lens, retina and photoreceptor optics.

EMVPO 2012 is organized by the Advanced Optical Imaging Group in UCD and the European Optical Society (EOS).

We look forward to welcoming you to Ireland and Dublin in 2012.

GENERAL CHAIR

Brian Vohnsen
Advanced Optical Imaging Group
School of Physics
University College Dublin (IE)

TOPICS

This conference will cover many aspects of visual and physiological optics, including clinical studies, basic research, and instrumentation, for example:

- Eye models and intraocular lenses
- Cornea and lens
- Anterior segment imaging
- Aberrations and retina image quality
- Ocular wavefront sensing
- Ocular biomechanics
- Peripheral wavefront sensing and vision
- Retina optics and photoreceptor function
- Vision and physiological optics
- Retinal imaging and analysis
- Novel instrumentation and techniques
- Numerical image processing
- Multiphoton techniques

PROGRAMME COMMITTEE

- **Pablo Artal,**
  Universidad de Murcia (ES)
- **David Atchison,**
  Queensland University of Technology (AU)
- **Ralf Blendowske,**
  Hochschule Darmstadt (DE)
- **Neil Charman,**
  University of Manchester (GB)
- **Christopher Dainty,**
  National University of Ireland (IE)
- **Luis Diaz-Santana,**
  The Technology Partnership plc (GB)
- **Harilaos Ginis,**
  University of Crete (GR)
- **José Ramón Jiménez Cuesta,**
  Universidad de Granada (ES)
- **Vasudevan Lakshminarayanan,**
  University of Waterloo (CA)
- **Linda Lundström,**
  KTH, Royal Institute of Technology (SE)
- **Susana Marcos,**
  CSIC (ES)
- **Barbara Pierscionek,**
  Kingston University (GB)
- **Larry N. Thibos,**
  Indiana University (US)
- **David R. Williams,**
  University of Rochester (US)
- **Brian Vohnsen,**
  University College Dublin (IE)
- **Henryk Kasprzak,**
  Wroclaw University of Technology (PL)

SUNDAY, 19 AUGUST	
17:00-18:00	Pre-Registration
18:30-20:30	Welcome Reception
MONDAY, 20 AUGUST | Room: Clinton Auditorium	
08:30-09:30	Registration
09:30-09:45	Welcome by the General Chair
09:45-10:30	**Keynote talk: An Eye for Optical Illusions** Michael Bach, Universitäts-Augenklinik Freiburg, Ophthalmology (DE)
10:30-11:00	Coffee break Sponsored by: imagine eyes
11:00-13:00	**Session I: Eye Models, Intraocular Lens Design and Analysis**
13:00-14:00	Lunch break
14:00-15:30	Poster Session I & Coffee break
15:30-18:30	**Session II: Retinal Imaging and Photoreceptor Analysis**
TUESDAY, 21 AUGUST | Room: Clinton Auditorium	
09:00-10:30	**Session III: Visual Acuity, Adaptation, and the Stiles-Crawford Effect**
10:30-11:00	Coffee break
11:00-13:00	**Session IV: Aberrations and Wavefront Sensing**
13:00-13:45	Lunch Break & Pick-up Lunch bags
14:00	Departure Social Programme
14:00-18:00	Social Programme
18:30-21:00	Conference Dinner
WEDNESDAY, 22 AUGUST | Room: Clinton Auditorium	
09:00-10:30	**Session V: Ocular Scattering Mechanisms and Analysis**
10:30-11:00	Coffee break
11:00-13:00	**Session VI: Accommodation, Presbyopia and Visual Impairment**
13:00-14:00	Lunch break
14:00-15:30	Poster Session II & Coffee break
15:30-17:00	**Session VII: Multiphoton Imaging and Analysis of the Eye**
17:00	EOS Student Awards & Farewell
17:15	End of EOS Topical Meeting

MONDAY, 20 AUGUST | Room: Clinton Auditorium

08:30-09:30 Registration

09:30-09:45 Welcome by the General Chair
B. Vohnsen, University College Dublin (IE)

09:45-10:30

Plenary Talk:
An Eye for Optical Illusions
M. Bach, Universitäts-Augenklinik Freiburg, Ophthalmology (DE)

10:30-11:00 Coffee break

Sponsored by: imagine eyes – Adaptive optics, adapted to eye care

11:00-13:00 **Session I: Eye Models, Intraocular Lens Design and Analysis**
Session Chair: P. Artal, Universidad de Murcia (ES)

11:00-11:30

Invited Talk: Optical Modelling of the Human Eye and IOL
A.V. Goncharov, Applied Optics Group, School of Physics, NUI Galway (IE)

11:30-11:45 STUDENT PRESENTATION
Gradient refractive index reconstruction in accommodating non-human primate crystalline lenses
A. de Castro[1], J. Birkenfeld[1], B. Maceo[2,3], F. Manns[2,3], J.M. Parel[2,3], S. Marcos[1]; [1]Instituto de Óptica "Daza de Valdés", CSIC (ES); [2]Ophthalmic Biophysics Center, Bascom Palmer Eye Institute, University of Miami, Miller School of Medicine (US); [3]Department of Biomedical Engineering, University of Miami College of Engineering (US)

11:45-12:00
Discontinuities in the index gradient of the eye lens
B. Pierscionek[1], M. Hoshino[2], N. Yagi[2], K. Uesugi[2], J. Regini[3]; [1]Faculty of Science, Engineering and Computing, Kingston University (GB); [2]Japan Synchrotron Radiation Research Institute (SPring8) (JP); [3]Optometry and Vision Sciences, Cardiff University (GB)

12:00-12:15
Statistical eye modelling and its applications
J.J. Rozema[1,2], D.A. Atchison[3], M.-J. Tassignon[1,2]; [1]Dept. of Ophthalmology, Antwerp University Hospital (BE), [2]Faculty of Medicine and Health Science, University of Antwerp (BE); [3]School of Optometry & Vision Science and Institute of Health & Biomedical Innovation, Queensland University of Technology (AU)

12:15-12:30
Dynamic Purkinje-meter system to evaluate lens stability
J. Tabernero, P. Artal; Laboratorio de Optica, Universidad de Murcia (ES)

12:30-12:45
Accommodating intraocular lens using a controllable liquid-liquid interface
V.V. Molebny, Institute of Biomedical Engineering (UA)

12:45-13:00
Extension of vision depth-of-field by corrective lenses with angular modulation of the optical power
K. Petelczyc[1], K. Kakarenko[1], I. Ducin[1], A. Czerwiński[1], Z. Jaroszewicz[2,3], A. Kołodziejczyk[1], M. Sypek[1]; [1]Faculty of Physics, Warsaw University of Technology (PL); [2]Institute of Applied Optics, Warsaw (PL); [3]National Institute of Telecommunications, Warsaw (PL)

13:00-14:00 Lunch break — UCD Main Restaurant

14:00-15:30 **Poster Session I & Coffee break** — Room: Exhibition area

15:30-18:30 **Session II: Retinal Imaging and Photoreceptor Analysis**
Session Chair: H. Ginis, University of Crete (GR)

15:30-16:00

Invited Talk: Adaptive Optics Imaging of the Retina
S.A. Burns, T.Y. Chui, D.A. VanNasdale, Z. Zhong, A.E. Elsner;
Indiana University, School of Optometry (US)

MONDAY, 20 AUGUST | Room: Clinton Auditorium

16:00-16:15 **Pupil apodization in scanning retinal imaging**
B. Vohnsen[1], B. Lochocki[1], D. Rativa[2], C. Vela[1]; [1]AOI Group, School of Physics, University College Dublin (IE); [2]Dep. Electronics and Systems, Universidade Federal de Pernambuco (BR)

16:15-16:30 **Positional sensitivity to microstimuli detected in the human retina**
W.M. Harmening[1], W.S. Tuten[1], A. Roorda[1], L.C. Sincic[2]; [1]Univ. of California, Berkeley, School of Optometry (US); [2]Univ. of Alabama at Birmingham, Dept. of Vision Sciences (US)

16:30-16:45 **Imaging Photoreceptor Structure in Retinitis Pigmentosa and Usher Syndrome: Results and Challenges**
J. Carroll[1,2], P. Godara[1], R.F. Cooper[2], V. Williams[1], P. Summerfelt[1], J.E. Kim[1], D.P. Han[1], D.V. Weinberg[1], K.E. Stepien[1], A. Dubra[1,2], T.B. Connor[1]; [1]Medical College of Wisconsin, Department of Ophthalmology (US); [2]Marquette University, Department of Biomedical Engineering (US)

16:45-17:00 **Cellular-resolution imaging of macaque retinas with an adaptive optics retinal camera designed for humans**
E. Odlund[1], K. Azartash[2], L. Vabre[1], B. Lamory-Bardet[1], N. Chateau[1]; [1]Imagine Eyes (FR), [2]Allergan, Inc., (US)

17:00-17:15 **Symmetry of inter-cone photoreceptor distance between fellow eyes**
M. Lombardo[1], G. Lombardo[2,3], D. Schiano Lomoriello[1], M. Rosati[1], P. Ducoli[1], S. Serrao[1]; [1]Fondazione G.B. Bietti IRCCS (IT); [2]CNR-IPCF Unit of Support Cosenza, LiCryL Laboratory, University of Calabria (IT); [3]Vision Engineering (IT)

17:15-17:30 **Simultaneous Multiple-depths en-Face Optical Coherence Tomography Imaging of the Retina**
J.A. Rogers, A.Gh. Podoleanu; Applied Optics Group, School of Physical Sciences, University of Kent, Canterbury (GB)

17:30-17:45 STUDENT PRESENTATION **Light focusing by photoreceptor cell nuclei**
Z. Blaszczak[1], M. Kreysing[1,2], J. Guck[1,3]; [1]Department of Physics, Cavendish Laboratory, University of Cambridge (GB); [2]Systems Biophysics, Ludwig-Maximilians-Universitaet Muenchen (DE); [3]Biotechnology Center, TU Dresden (DE)

17:45-18:00 STUDENT PRESENTATION **Estimation of the ocular point spread function by retina modeling**
N. Meitav, E.N. Ribak; Department of Physics, Technion – Israel Institute of Technology (IL)

18:00-18:30 **Discussion: Ideal adaptive optics for imaging and analysis of the eye**
Discussion leader: *S. Burns, Indiana University, School of Optometry (US)*

NOTES

TUESDAY, 21 AUGUST | Room: Clinton Auditorium

09:00-10:30 **Session III: Visual Acuity, Adaptation, and the Stiles-Crawford Effect**
Session Chair: R. Blendowske, Hochschule Darmstadt (DE)

09:00-09:30

Invited Talk:
Visual hyperacuity and optical superresolution
G. Westheimer, Division of Neurobiology, University of California (US)

09:30-09:45 STUDENT PRESENTATION
Analysis of the Stiles-Crawford effect of the first kind with tuneable interference gratings
S. Castillo, B. Vohnsen; Advanced Optical Imaging Group, School of Physics, University College Dublin (IE)

09:45-10:00
Impact of Spherical Aberration and Stiles Crawford Apodization on Refractive Error
R. Xu, A. Bradley, L.N. Thibos; Indiana University, School of Optometry (US)

10:00-10:15
Refractive error sensing in natural multifocal eyes
R. Navarro[1], V. Fernández-Sánchez[2], N. López-Gil[2]; [1]ICMA, Consejo Superior de Investigaciones Científicas & Universidad de Zaragoza (ES); [2]Grupo de Ciencias de la Visión. Universidad de Murcia (ES)

10:15-10:30 STUDENT PRESENTATION
Classification Method to Test Natural Adaptation to the High Order Aberrations of the Eye
L. Sawides[1], C. Dorronsoro[1], P. de Gracia[1], M. Vinas[1], A. Haun[2], E. Peli[2], S. Marcos[1]; [1]Instituto de Optica, CSIC (ES); [2]Schepens Eye Research Institute, Massachusetts Eye and Ear, Harvard Medical School (US)

10:30-11:00 Coffee break

11:00-13:00 **Session IV: Aberrations and Wavefront Sensing**
Session Chair: V. Nourrit, University of Manchester (GB)

11:00-11:15
Night myopia explanation in terms of different stimuli configuration between day and night
N. López-Gil[1], S.C. Peixoto-de-Matos[2], J.M. González-Méijome[2], L. Thibos[3]; [1]Grupo de Ciencias de la Visión, Universidad de Murcia (ES); [2]Clinical & Experimental Optometry Research Lab. Center of Physics (Optometry) - School of Sciences (PT); [3]School of Optometry, Indiana University (US)

11:15-11:30
Myopic eye analysis using Hartmann Shack sensor: Evaluating centroid detection methods for Poisson noise dominant spots
A. Vyas; Advanced Optical Imaging Group, University College Dublin (IE)

11:30-11:45
Optimized Microlens-Array Geometry for Hartmann-Shack Wavefront Sensor
O.G. Oliveira[1], D.W. de Lima Monteiro[2], R.F.O. Costa[2]; [1]Mediphacos Ltd., R&D Department (BR); [2]Universidade Federal de Minas Gerais, OptMAlab, DEE/UFMG (BR)

11:45-12:00
A signal-to-noise ratio for the study of the mean squared wavefront estimation error in eye aberrometry
E. Pailos[1,2], J. Arines[1], S. Bará[1]; [1]Universidade de Santiago de Compostela, Área de Óptica, Facultade de Óptica e Optometría (ES); [2]National University of Ireland Galway, Applied Optics Group, School of Physics (IE)

12:00-12:15
Fixation Quality with a Bessel Beacon in an Adaptive Optics System
E.M. Daly[1], A.J. Lambert[2], J.C. Dainty[1]; [1]Applied Optics, National University of Ireland Galway (IE); [2]School of Engineering and IT, UNSW@ADFA (AU)

12:15-12:30
Calibration of a commercial anterior segment OCT instrument foraccurate corneal topography
D. Siedlecki[1], S. Ortiz[2], S. Marcos[2]; [1]Wroclaw University of Technology, Institute of Physics (PL), [2]Consejo Superior de Investigaciones Cientificas, Instituto de Optica (ES)

12:30-12:45
Shape of the posterior cornea described by Zernike polynomials: influence of anterior corneal shape and central reference point
T. de Jong[1], M.T. Sheehan[2], S.A. Koopmans[1], N.M. Jansonius[1]; [1]Department of Ophthalmology, University Medical Center Groningen, University of Groningen (NL); [2]National University Ireland Galway (IE)

12:45-13:00 STUDENT PRESENTATION
Look-up table of quadrics applied to corneal topography
J. Espinosa[1,2], A.B. Roig[2], J. Pérez[1,2], D. Mas[1,2], C. Illueca[1,2]; [1]University of Alicante, IUFA CyT (ES) [2]University of Alicante, Dept. Optics, Pharmacology and Anatomy (ES)

13:00-13:45 Lunch break & Pick-up lunch bags

14:00 Departure Social Programme
14:00-18:00 Social Programme

18:30-21:00 Conference Dinner

WEDNESDAY, 22 AUGUST | Room: Clinton Auditorium

09:00-10:30 **Session V: Ocular Scattering Mechanisms and Analysis**
Session Chair: B. Pierscionek, Kingston University (GB)

09:00-09:30

Invited Talk
Intraocular scattering - measurement and analysis
G.M. Perez, Laboratorio de Óptica. Universidad de Murcia (ES)

09:30-09:45 **A new optical instrument for the optical measurement of intraocular scattering using modulated visible light**
H.S. Ginis[1], O. Sahin[1], G.M. Pérez[2], J.M. Bueno[2], P. Artal[2]; [1]Institute of Vision and Optics, University of Crete (GR); [2]Laboratorio de Optica, Universidad de Murcia (ES)

09:45-10:00 **Comparison of forward light scatter estimations using Hartmann-Shack spot patterns and C-Quant**
STUDENT PRESENTATION
P.B. Lopez, H. Radhakrishnan, V. Nourrit; University of Manchester, Faculty of Life Sciences (GB)

10:00-10:15 **Qantification of human corneal grafts transparency**
STUDENT PRESENTATION
O. Casadessus[1], L. Siozade Lamoine[1], G. Georges[1], C. Deumié[1], L. Hoffart[2]; [1]Institut Fresnel, UMR 7249, CNRS, Université d'Aix-Marseille, Ecole Centrale Marseille (FR); [2]Service d'ophtalmologie, Hôpital la Timone, APHM, Université d'Aix-Marseille (FR)

10:15-10:30 **Possible origin of black spots in interferometric measurements of tear film surface**
H.T. Kasprzak[1], D.T. Szczęsna-Iskander[1], D. Mas[2]; [1]Wrocław University of Technology, Institute of Physics (PL); [2]University of Alicante, Department of Optics (ES)

10:30-11:00 Coffee break

11:00-13:00 **Session VI: Accommodation, Presbyopia and Visual Impairment**
Session Chair: L. Lundström, KTH, Royal Institute of Technology (SE)

11:00-11:15 **Retinal Image Quality During Accommodation**
L. Thibos[1], J. Martin[1], T. Liu[1], A. Bradley[1], D. Diaz-Muñoz[2], N. López-Gil[2]; [1]School of Optometry, Indiana University (US); [2]Grupo de Ciencias de la Visión. Universidad de Murcia (ES)

11:15-11:30 **Measuring accommodative response with a double-pass system**
STUDENT PRESENTATION
M. Aldaba, M. Vilaseca, F. Díaz-Doutón, M. Arjona, J. Pujol, Universitat Politècnica de Catalunya (ES)

11:30-11:45 **Quantifying performance of accommodative intraocular lenses with 3-D anterior segment OCT**
S. Marcos[1], S. Ortiz[1], P. Pérez-Merino[1], J. Birkenfeld[1], S. Durán[1], I. Jiménez-Alfaro[2]; [1]Instituto de Optica, CSIC (ES); [2]Fundación Jiménez-Díaz (ES)

11:45-12:00 **Binocular Adaptive Optics Visual Analyzer to optimize optical solutions for presbyopia**
S. Manzanera, E.J. Fernández, C. Schwarz, J. Tabernero, P.M. Prieto, P. Artal; Laboratorio de Óptica, Instituto Universitario de investigación en Óptica y Nanofísica (IUiOyN), Universidad de Murcia (ES)

12:00-12:15 **Interocular Differences in Visual Latency Induced by Reduced-Aperture Contact Lenses or Corneal Inlays for Presbyopia**
S. Plainis[1], D. Petratou[1], T. Giannakopoulou[1], H. Radhakrishnan[2], I.G Pallikaris[1], W.N. Charman[2], [1]Institute of Vision and Optics, University of Crete (GR; [2]Faculty of Life Sciences, University of Manchester (GB)

12:15-12:30 **Driving with Monocular Bioptic Telescope: Strabismus Might Affect Hazard Detection with the Fellow Eye**
A. Doherty, A. Bowers, E. Peli; Schepens Eye Research Institute, Massachusetts Eye and Ear, Harvard Medical School (US)

12:30-12:45 **Peripheral Contrast Sensitivity Function with Adaptive Optics**
STUDENT PRESENTATION
R. Rosén, L. Lundström, S. Winter, A.P. Venkataraman, P. Unsbo, Royal Institute of Technology, Dept of Applied Physics (SE)

12:45-13:00 **Peripheral refraction out to 60 degrees from fixation using the Hartmann-Shack technique**
D.A. Atchison, A. Mathur; School of Optometry & Vision Science and Institute of Health & Biomedical Innovation, Queensland University of Technology (AU)

13:00-14:00 Lunch break — UCD Main Restaurant

14:00-15:30 **Poster Session II & Coffee Break** — Room: Exhibition area

WEDNESDAY, 22 AUGUST | Room: Clinton Auditorium

15:30-17:00 **Session VII: Multiphoton Imaging and Analysis of the Eye**
Session Chair: J. Carroll, Medical College of Wisconsin & Marquette University (US)

15:30-16:00

Invited Talk:
Two-photon imaging of the retina
J.J. Hunter[1A,B], R. Sharma[1B,C], B. Masella[1B,C], L. Yin[1B], W.H. Merigan[1A,B], G. Palczewska[2], K. Palczewski[2,3], D.R. Williams[1A,B,C]; [1]University of Rochester, [AF]Iaum Eye Institute, [B]Center for Visual Science, [C]The Institute of Optics, Rochester (US); [2]Polgenix, Inc., Cleveland (US); [3]Department of Pharmacology, Case Western Reserve University (US)

16:00-16:15 **Multimodal multiphoton imaging (THG-SHG-2PEF) of the human cornea**
N. Olivier[1], G. Latour[1], F. Aptel[2,3], A. Deniset-Besseau[1], J.-M. Legeais[3], K. Plamann[2], M.C. Schanne-Klein[1], E. Beaurepaire[1]; [1]Lab. for Optics and Biosciences, Ecole Polytechnique, CNRS (FR); [2]Laboratoire d'Optique Appliquée, ENSTA ParisTech (FR); [3]Lab. Biotechnologie et Œil, Univ. Paris V, Hôpital Hôtel Dieu (FR)

16:15-16:30 ***In vivo* polarization-resolved SHG imaging of the corneal microstructure**
G. Latour[1], I. Gusachenko[1], L. Kowalczuk[2], I. Lamarre[1], M.-C. Schanne-Klein[1]; [1]Ecole Polytechnique – CNRS – INSERM U696, Laboratory for Optics and Biosciences (FR); [2]ENSTA ParisTech - Ecole Polytechnique – CNRS, Laboratory for Applied Optics (FR).

16:30-17:00 **Discussion: Can we separate optical from neural effects?**
Discussion leader: *D. Atchison, Queensland University of Technology (AU)*

17:00 EOS Student Awards & Farewell

17:15 End of EOS Topical Meeting

POSTER SESSION I: Monday, 20 August | 14:00 - 15:30 CEST
Room: Exhibition area

EMVPO2012_5432_001	**Clinical measurements: entries of factor matrices of the dioptric power matrix** H. Abelman, S. Abelman; School of Computational and Applied Mathematics, University of the Witwatersrand (ZA)
EMVPO2012_5561_002 STUDENT PRESENTATION	**Spherocylindrical error for oblique gaze regarding the position of the center of rotation** S. Perchés, F. Palos, V. Collados, J. Ares; Universidad de Zaragoza, Departamento de Física Aplicada (ES)
EMVPO2012_5564_003	**Effects of contrast, cut-off spatial frequency and phase of the OTF on visual acuity and subjective image quality score** R. Legras[1], A.P. Sansot[1], G. Vandermeer[2], Y. Nochez[2], R. Navarro[3]; [1]Université Paris-Sud, Laboratoire Aimé Cotton (FR); [2]Université François Rabelais, Faculté de médecine (FR); [3]Consejo Superior de Investigaciones Científicas & Universidad de Zaragoza, ICMA ES)
EMVPO2012_5570_004	**The changes of shape of the human cornea with age** R. Navarro[1], J.J. Rozema[2], M.-José Tassignon[2]; [1]ICMA, Consejo Superior de Investigaciones Científicas & Universidad de Zaragoza (ES); [2]Department of Ophthalmology. Antwerp University Hospital (BE)
EMVPO2012_5669_005 STUDENT PRESENTATION	**Alternative Methodology for Intraocular Lenses Characterization** F.T. Amaral, D.W. de Lima Monteiro, Universidade Federal de Minas Gerais - UFMG, Department of Electrical Engineering (BR)
EMVPO2012_5672_006	**Theoretical evaluation of different corneal models for the correction of presbyopia by laser refractive surgery** R.G. Anera, A. Alarcon, J.R. Jimenez, M. Soler; Laboratory of Vision Sciences and Applications, Departamento de Óptica, Universidad de Granada (ES)
EMVPO2012_5679_007 STUDENT PRESENTATION	**Effect of the lens histology in optical aberrations** A. Gargallo[1], J. Arines[1,2], E. Acosta[1]; [1]Universidade de Santiago de Compostela, Departamento de Física Aplicada, Facultade de Física (ES); [2]Universidad de Zaragoza, Departamento de Física Aplicada, Facultad de Ciencias (ES)
EMVPO2012_5685_008	**Investigation of Hartmann Shack and curvature sensors in quantifying aberrations of the myopic eye** M.B. Roopashree[1], A. Vyas[2], S. J. Weddell[3], B. Raghavendra Prasad[1]; [1]Indian Institute of Astrophysics, II Block, Koramangala, Bangalore (IN); [2]Advanced Optical Imaging Group, University College Dublin (IE); [3]University of Canterbury (NZ)
EMVPO2012_5694_009 STUDENT PRESENTATION	**Non-rotational, aspherical models of the human optical system** S. Giovanzana[1], H.T. Kasprzak[2], Ş. Ţălu[3]; [1]University of Milan-Bicocca, Milano, 20125 (IT); [2]Wroclaw University of Technology, Visual Optics Group (PL); [3]Technical University of Cluj-Napoca, Discipline of Descriptive Geometry and Engineering Graphics (RO)
EMVPO2012_5698_010 STUDENT PRESENTATION	**Chromatic Null Screen corneal topographer with three LCD´s** M.I. Rodríguez-Rodríguez[1,2], A. Jaramillo Núñez[1], R. Díaz Uribe[2]; [1]Instituto Nacional de Astrofísica, Óptica y Electrónica (MX); [2]Universidad Nacional Autónoma de México, Centro de Ciencias Aplicadas y Desarrollo Tecnológico (MX)
EMVPO2012_5710_012 STUDENT PRESENTATION	**Expected Visual Acuity and Depth of Focus with spherical and aspheric Intraocular Lenses** F. Alba-Bueno[1], F. Vega[1], M.S. Millán[1], R. Navarro[2]; [1]Universitat Politècnica de Catalunya (UPC), Department of Optics and Optometry (ES); [2]ICMA, Consejo Superior de Investigaciones Científicas & Universidad de Zaragoza (ES)
EMVPO2012_5715_013 STUDENT PRESENTATION	**Zernike vs Bessel Circular Functions in Visual Optics** J.P. Trevino[1], J.E. Gomez-Correa[1], Robert Iskander[2], S. Chavez-Cerda[1]; [1]Instituto Nacional de Astrofísica, Optica y Electrónica. Depto. De Optica (MX); [2]Institute of Biomedical Engineering and Instrumentation, Wroclaw University of Technology (PL)

POSTER SESSION I: Monday, 20 August | 14:00 - 15:30 CEST
Room: Exhibition area

EMVPO2012_5728_014	**Corneal Topographer Based on Null-Screen Testing** A. Estrada-Molina[1], M. Campos-García[1], R. Díaz-Uribe[1], M. Ramírez-Ortiz[2]; [1]Universidad Nacional Autónoma de México, Centro de Ciencias Aplicadas y Desarrollo Tecnológico (MX); [2]Hospital Infantil de México Federico Gómez, Servicio de Oftalmología (MX)
EMVPO2012_5731_015 STUDENT PRESENTATION	**Imaging quality of multifocal intraocular lenses. Automated assessment setup.** L. Remón[1], A. Calatayud[1], J.A. Monsoriu[1], W.D. Furlan[2]; [1]Centro de Tecnologías Físicas, Universitat Politècnica de València (ES); [2]Departamento de Óptica, Universitat de València (ES)
EMVPO2012_5742_016 STUDENT PRESENTATION	**Automatic Selection and Registration of Adaptive Optics (AO) corrected Best Quality Retinal Images** G. Ramaswamy, N. Devaney; Applied Optics, School of Physics, National University of Ireland Galway (IE)
EMVPO2012_5746_017 STUDENT PRESENTATION	**Singular Optical fields used to calculate Wavefront aberrations** J.E. Gómez-Correa, J.P. Trevino, S.E. Balderas-Mata, S. Chávez-Cerda; Instituto Nacional de Astrofísica, Óptica y Electrónica, Departamento de Óptica (MX)
EMVPO2012_5751_018	**Improving retinal image via descattering for the detection of diabetic retinopathy** G. Russell[1], J. Oakley[2], N. McLoughlin[3], V. Nourrit[3]; [1]Health Intelligence Ltd, Saxon House (GB); [2]The University of Manchester, School of Electrical and Electronic Engineering Manchester (GB); [3]The University of Manchester , Faculty of Life Sciences (GB)
EMVPO2012_5752_019	**3D Modeling and reconstruction of human corneal surface using superellipsoids** Ș. Țălu[1], S. Giovanzana[2], M. Țălu[3], I.V. Petrescu-Mag[4]; [1]Technical University of Cluj-Napoca, Faculty of Mechanics, Discipline of Descriptive Geometry and Engineering Graphics (RO); [2]University of Milan (IT); [3]University of Craiova, Faculty of Mechanics, Department of Applied Mechanics (RO); [4]SC Bioflux SRL (RO)
EMVPO2012_5757_020 STUDENT PRESENTATION	**Defocus-corrected determination of the Stiles-Crawford effect of the first kind** B. Lochocki; B. Vohnsen, University College Dublin, School of Physics, AOI Group (IE)
EMVPO2012_5759_021 STUDENT PRESENTATION	**Health Risks of Artificial Stereopsis and a Natural Solution** E. Ansbro[1], C. Overhauser[2], Alova[2]; [1]Open University, PSSRI (GB); [2]RealView Innovations Ltd, Boyle (IE)
EMVPO2012_5760_022 STUDENT PRESENTATION	**Wavefront reconstruction for a thick fundus model using a Shack-Hartmann wavefront sensor** T. Liu, L.N. Thibos; Indiana University, School of Optometry (US)
EMVPO2012_5764_023	**Selection of a relevant human eye model to study visual performances of corneal inlays** J. Jarosz[1,3], F. Castignoles[3], T. Lépine[1,2], P. Tankam[1]; [1]Laboratoire Hubert Curien (UMR 5516 CNRS), Université de Lyon, Université Jean-Monnet (FR); [2]Institut d'Optique Rhône-Alpes (FR); [3]Presbeasy (FR)
EMVPO2012_5766_024 STUDENT PRESENTATION	**Individual biomechanical model of the human eyeball** E. Szul-Pietrzak, A. Hachoł; Wroclaw University of Technology, Group of Biomeasurements and Biomedical Signals Analysis (PL)
EMVPO2012_5771_026 STUDENT PRESENTATION	**Transposing the Stiles-Crawford Effect from Pupil to Retina in Eye Modelling** C. Vela, B. Lochocki, B, Vohnsen; AOI Group, University Dublin College, School of Physics (IE).
EMVPO2012_5778_027	**The minimum motion and heterochromatic techniques to differentiate lutein and zeaxanthin macular pigment optical density using CRT and different spectral emission LED light stimuli** M. Ozolinsh[1,2], P. Paulins[1]; [1]University of Latvia (LV); [2]Institute of Solid State Physics, University of Latvia (LV)

POSTER SESSION II: Wednesday, 22 August | 14:00 - 15:30 CEST
Room: Exhibition area

EMVPO2012_5337_028 STUDENT PRESENTATION	**Just-noticeable differences for ocular wavefront aberrations** H. Jungnickel[1], D. Weigel[2], H. Babovsky[2], A. Kiessling[2], R. Kowarschik[2], M. Gebhardt[1]; [1]University of Applied Sciences, SciTec Department (DE); [2]Friedrich Schiller University, Institute of Applied Optics (DE)
EMVPO2012_5563_029	**Application of multivariate analysis of variance (MANOVA) to distance refractive variability and mean distance refractive state** S. Abelman, H. Abelman; School of Computational and Applied Mathematics, University of the Witwatersrand (ZA)
EMVPO2012_5572_030	**Is the iris suitable as a biometric?** D. Rankin[1], B. Scotney[1], P. Morrow[1], B. Pierscionek[2]; [1]University of Ulster, School of Computing and Information Engineering, Cromore Road, Coleraine, BT52 1SA (GB); [2]Faculty of Science Engineering and Computing, Kingston University (GB)
EMVPO2012_5667_031	**Kinematics of eyelid movement and eye retraction in the blinking** J. Pérez[1,2], J. Espinosa[1,2], A.B. Roig[1], B. Domenech[1,2], D. Mas[1,2]; [1]University of Alicante, Dept. Optics, Pharmacology and Anatomy (ES); [2]University of Alicante, IUFACyT (ES)
EMVPO2012_5673_032	**Effects of various combinations of multifocal optics on binocular subjective image quality score** R. Legras[1], G. Vandermeer[2], Y. Nochez[2]; [1]Université Paris-Sud, Laboratoire Aimé Cotton (FR); [2]Université François Rabelais, Faculté de médecine (FR)
EMVPO2012_5681_033	**Variation with the orientation (horizontal - vertical) of a Ronchi achromatic grating in the vision of a color sequence located inside.** J. Montalvá Colomer, I. Tortajada Montañana, M. Aguilar Rico; Universidad Politécnica de Valencia, Escuela Técnica Superior de Ingeniería del Diseño (ES)
EMVPO2012_5697_034	**Correlative imaging of corneas from diabetic rats and human donors** G. Latour[1], L. Kowalczuk[2], M. Savoldelli[3], J.-L. Bourges[4], K. Plamann[2], F. Behar-Cohen[3], M.-C. Schanne-Klein[1]; [1]Ecole Polytechnique - CNRS - INSERM U696, Laboratory for Optics and Biosciences (FR); [2]ENSTA ParisTech – Ecole Polytechnique – CNRS, Laboratory for Applied Optics (FR); [3]Sorbonne Paris Cité, Paris Descartes University, Faculty of Medicine, Department of Ophthalmology (FR); [4]INSERM UMR872, Centre de Recherche des Cordeliers, Team 17 Physiopathology of ocular diseases (FR)
EMVPO2012_5701_035	**Monofractal and multifractal analysis in human retinal pathology** Ș. Țălu[1], S.D. Țălu[2], S. Giovanzana[3], M. Țălu[4], I.V. Petrescu-Mag[5]; [1]Technical University of Cluj-Napoca, Faculty of Mechanics, Discipline of Descriptive Geometry and Engineering Graphics (RO); [2]"Iuliu Hatieganu" University of Medicine and Pharmacy, Department of Surgical Specialties (RO); [3]University of Milan-Bicocca (IT); [4]University of Craiova, Department of Applied Mechanics (RO); [5]University of Agricultural Sciences and Veterinary Medicine Cluj-Napoca (RO)
EMVPO2012_5702_036 STUDENT PRESENTATION	**An estimate of the ocular media transmittance using an updated psychophysical method** P. Teikari[1,2], R.P. Najjar[1,2], K Knoblauch[1,2] , D. Dumortier[1,3], P.-L. Cornut[1,2,4], P. Denis[1,5], H.M. Cooper[1,2], C. Gronfier[1,2]; [1]INSERM, U846, Stem Cell and Brain Research Institute, Dept. of Chronobiology (FR); [2]University of Lyon, Lyon I, UMR-S 846 (FR); [3]ENTPE (FR); [4]Dept. of Ophthalmology, CHU de Lyon Hopital Edouard Herriot (FR); [5]Hôpital de la Croix Rousse (FR)
EMVPO2012_5711_037 STUDENT PRESENTATION	**Assessment of intraocular scattering. Comparative study using several techniques** J.A. Martínez-Roda[1], M. Vilaseca[2], J.C. Ondategui[1], L. Almudi[3], J. Pujol[2]; [1]University Vision Centre (CUV), Technical University of Catalunya (UPC) (ES); [2]Centre for Sensors, Instruments and Systems Development (CD6), Technical University of Catalunya (UPC) (ES); [3]Ophthalmology service, Hospital de Terrassa (ES)
EMVPO2012_5716_038	**Accommodative response to Chinese and Latin characters in myopes and emmetropes** L. LLorente[1,2], H. Radhakrishnan[3], A. Hartwig[4]; [1]Carl Zeiss Vision, R&D (AU); [2]Universiti Kebangsaan Malaysia, Faculty of Health Science, Optometry and Vision Science Programme (MY); [3]University of Manchester, Department of Optometry (GB); [4]Hartwig, Heikendorf (DE)

POSTER SESSION II: Wednesday, 22 August | 14:00 - 15:30 CEST
Room: Exhibition area

EMVPO2012_5717_039 STUDENT PRESENTATION	**Peripheral aberrations and changes in refractive error during one year** A. Hartwig, N.W. Charman, H. Radhakrishnan; University of Manchester, Faculty of Life Sciences (GB)
EMVPO2012_5730_040 STUDENT PRESENTATION	**Comparison of Accelerated Corneal Cross-Linking to Standard Cross-Linking using Second-Harmonic Optical Microscopy** R. McQuaid[1,2], J. Li[2], A. Cummings[1], M. Mrochen[3], B. Vohnsen[2]; [1]Wellington Eye Clinic (IE); [2]AOI-Group, School of Physics, University College Dublin (IE); [3]IROC (CH)
EMVPO2012_5743_041	**Demonstration of Digital Holographic Display, Optimized for Human Eye Perception** V. Venediktov[1,2], M. Lyakh[3], A. Sevryugin , M. Solov'ev[2], I. Pasechnik[1]; [1]St.-Petersburg State Electrotechnical University "LETI" (RU); [2]National Research University of Information Technologies, Mechanics and Optics (RU); [3]Intel Labs (RU)
EMVPO2012_5749_042 STUDENT PRESENTATION	**Waveform of the Pupil light reflex analysis taking into account intrinsically photosensitive retinal ganglion cells activity** W. Nowak[1], A. Hachoł[1], A. Sobaszek[1], M. Nakayama[2], H. Ishikawa[3]; [1]Wroclaw University of Technology, Group of Biomeasurements and Biomedical Signal Analysis (PL); [2]CRADLE, Tokyo Institute of Technology (JP); [3]School of Allied Health Sciences, Kitasato University (JP)
EMVPO2012_5753_043 STUDENT PRESENTATION	**Optical Quality and Intraocular Scattering in eyes treated of Amblyopia** J.C. Ondategui-Parra[1], J. Martínez-Roda[1], M. Vilaseca[2], A. Wert[3], J. Pujol[2]; [1]Technical University of Catalonia, University Vision Centre (ES); [2]Technical University of Catalonia, Centre for Sensors, Instruments and Systems Development (ES); [3]Instituto de Microcirugía Ocular (ES)
EMVPO2012_5762_044 STUDENT PRESENTATION	**A New Tool for Depth Perception Training for Autism and Other Conditions** E. Ansbro[1], C. Overhauser[2], Alova[2]; [1]Open University, PSSRI (GB); [2]RealView Innovations Ltd (IE)
EMVPO2012_5768_046 STUDENT PRESENTATION	**A Method to Evaluate Peripheral Visual Perception** I. Timrote, G. Krumina, T. Pladere, M. Skribe; University of Latvia, Department of Optometry and Vision Science (LV)
EMVPO2012_5770_047 STUDENT PRESENTATION	**Vortex beams in Visual Optics** J.P. Trevino, J.E. Gomez-Correa, S. Chavez-Cerda; Instituto Nacional de Astrofísica, Optica y Electrónica (MX)
EMVPO2012_5773_048 STUDENT PRESENTATION	**Second-harmonic cornea microscopy enhancement with annular aperture filters** J. Li, B. Vohnsen; AOI Group, University College Dublin, School of Physics (IE)
EMVPO2012_5774_049 STUDENT PRESENTATION	**Myopes visual acuity with positive and negative contrast stimuli** G. Ikaunieks, E. Caure, E. Kassaliete, Z. Meskovska; University of Latvia, Department of Optometry and Vision Science (LV)
EMVPO2012_5775_050 STUDENT PRESENTATION	**Measurement of accomodative response curve based on brightness of the retinal reflex** V. Karitans[1,2], M. Ozolinsh[1,2], E. Skutele[2]; [1]Institute of Solid State Physics, Department of Ferroelectrics (LV); [2]University of Latvia, Department of Optometry and Vision Science (LV)
EMVPO2012_5776_051 STUDENT PRESENTATION	**Printed test plates for color discrimination threshold determination** K. Luse[1], S. Fomins[2], M. Ozolinsh[1,2]; [1]University of Latvia, department of Optometry and Vision Science (LV); [2]University of Latvia, Institute of solid State Physics (LV)

09:30-09:45 Welcome by the General Chair

09:45-10:30 **KEYNOTE TALK**

An eye for optical illusions

M. Bach, Universitäts-Augenklinik Freiburg, Ophthalmology (DE).

As every delegate of this meeting will appreciate, the term "optical illusions", while standard, is a misnomer; With very few exceptions, optics do not play a role, so "visual illusions" would be more appropriate. And, again with very few exceptions, the underlying mechanisms are not located in the retina but rather in the visual cortex. Even the Herman grid illusion is insufficiently explained by lateral inhibition. Notwithstanding, visual illusions bring joy and fascination into life, not just for the visual scientist. I will cover the visual dimensions light, colour, gestalt and motion in interactive demonstrations – audience participation will be necessary. The phenomena will be interpreted in the Bayesian interpretation of perception: Simply stated, our visual system continuously "invents" an inner world as a basis for understanding and planning on incomplete information. Occasional missteps of our perceptual apparatus are called optical illusions and can reveal these inner mechanisms. [5676]

10:30-11:00 Coffee break Sponsored by: imagine eyes

11:00-13:00

EYE MODELS, INTRAOCULAR LENS DESIGN AND ANALYSIS

Session Chair: P. Artal, Universidad de Murcia (ES)

11:00-11:30 **INVITED TALK**

Optical Modelling of the Human Eye and IOL Design

A.V. Goncharov; Applied Optics Group, School of Physics, National University of Ireland, Galway (IE).

Email: alexander.goncharov@nuigalway.ie

Summary

The main focus of the paper is optical modelling of the eye as a basis for improving the outcomes of cataract surgery. The main challenges for the eye reconstruction in vivo for patient-specific eye models are considered. The intraocular lens (IOL) customization using personalized eye models and exact ray tracing is discussed. Promising approaches for customized IOL implantation in unusual eyes are outlined.

Introduction

A typical cataract surgery requires replacement of a partially opaque crystalline lens by a transparent ocular implant. This dramatically reduces internal light scattering and provides unobstructed image formation on the retina.[1] If the optical power of the IOL is chosen correctly, it can compensate for the major refractive error (defocus) of the cornea. IOL power calculations for patients undergoing cataract surgery are usually based on the measurement of the optical power of the cornea and the axial length of the eye.[2] Over the years, dozens of formulae have been proposed for IOL power calculation,[3] in all of them the anterior and posterior corneal surfaces are combined to one surface, and the IOL is approximated by a thin lens.[4]

The main difference between the formulae is the assumed position of the IOL. This so-called "effective" lens position (ELP) is not a true IOL position in the eye, but a fictitious position that gives the desired result. Currently there is no preoperative method to determine the true IOL position (TLP) after implantation. For each formula, the constants are adjusted by using regression analysis, so that on average the prediction of the ELP is satisfactory (the residual refractive error is less than 0.5 dioptres in 80% of cases).[5] However for unusual eyes, e.g. eyes that have undergone previous corneal refractive surgery, the current IOL power calculation is only successful in about 20% of cases, that is 4 out 5 people will need spectacles.

Discussion

To resolve this problem, one could apply an exact ray-tracing method[6] instead of regression formulae. Individual rays are traced through all refractive surfaces in the eye using Snell's law. The TLP prediction and IOL customization utilizes a personalized eye model describing all patient-specific parameters, such as corneal topography, the crystalline lens shape, inter-ocular distances and refractive indices. The main advantage of the ray-tracing approach is that one can take into account peculiar features of the patient's eye including optical irregularities of the cornea.

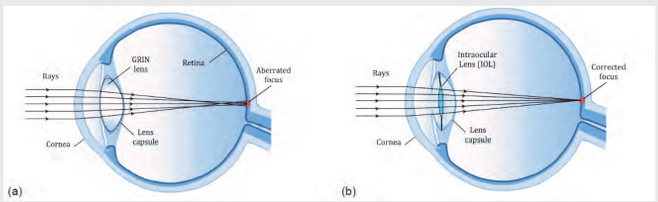

Fig. 1. Schematics of an aberrated pre-op eye (a) and corrected post-op eye (b).

The IOL power calculation is also based on ray tracing in the post-operative eye model in which the crystalline lens is replaced by an intraocular lens with a finite thickness and realistic anterior and posterior radius of curvature, asphericity and refractive index. In addition to finding the optimal optical power, the IOL shape can be fully customized to reduce the optical defects of irregular corneas such as spherical aberration, coma and astigmatism. These corneal aberrations show large subject variability and gradually increase with age; they are significantly larger for cataract patients with modified corneas (due to refractive surgery). For such patients if corneal aberrations are not corrected, their vision will suffer from a noticeable residual blur.

Conclusion

The ray-tracing method has much broader scope not only providing improved power calculations, but also enabling IOL customization based on the corneal topography and asphericity. An anatomically accurate eye model is necessary for this approach to work. Thus developing realistic models of aging crystalline lenses[7] and laser-modified corneas is vital for predicting the IOL position after implantation and finding the optimal IOL shape that corrects patient-specific corneal aberrations.

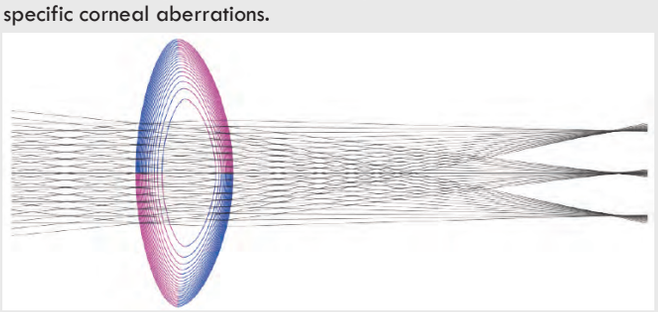

Fig. 2. Exact ray-tracing through a geometry-invariant gradient index (GRIN) lens.[7]

Acknowledgement

Funding support from Enterprise Ireland International Research Fund (IR-2008-0014) and Science Foundation of Ireland (07/IN.1/1906).

Reference

[1] B. Pierscionek, R. J. Green, and S. G. Dolgobrodov, "Retinal images seen through a cataractous lens modeled as a phase-aberrating screen," J. Opt. Soc. Am. A **19**, 1491- 1500 (2002).

[2] B. Seitz and, A. Langenbucher, "Intraocular lens power calculation in eyes after corneal refractive surgery," J. Refract. Surg. **16**:349-361 (2000).

[3] G. Savini, K. J. Hoffer, and M. Zanini, "IOL power calculation after LASIK and PRK", Cataract and Refract. Surg., 0407 (2007). http://www.crstodayeurope.com

[4] Hoffer KJ. The Hoffer-Q formula. "A comparison of theoretic and regression formulas", J. Cataract. Refract. Surg. **19**, 700-712 (1993).

[5] S. Norrby, "Sources of error in intraocular lens power calculation", J. Cataract Refract. Surg. **34**, 368–376 (2008).

[6] A.V. Goncharov, M. Nowakowski, M.T. Sheehan and J. C. Dainty, "Reconstruction of the optical system of the human eye with reverse ray-tracing," Opt. Express **16**, 1692- 1703 (2008).

[7] M. Bahrami and A. V. Goncharov, "Geometry-Invariant GRIN lens: analytical ray tracing", J. Biomed. Opt., in press.

[5782]

Room: Clinton Auditorium

11:30-11:45 STUDENT PRESENTATION

Gradient refractive index reconstruction in accommodating non-human primate crystalline lenses

A. de Castro[1], J. Birkenfeld[1], B. Maceo[2,3], F. Manns[2,3], J.M. Parel[2,3], S. Marcos[1]; [1]Instituto de Óptica "Daza de Valdés", CSIC, Madrid, 28006 (ES); [2]Ophthalmic Biophysics Center, Bascom Palmer Eye Institute, University of Miami Miller School of Medicine, Miami, FL 33136 (US); [3]Department of Biomedical Engineering, University of Miami College Of Engineering, Coral Gables, FL 33146 (US).
Email: a.decastro@csic.es

Summary
Crystalline monkey lenses were imaged in vitro with an Optical Coherence Tomography system under different states of accommodation. A search algorithm was used to find the gradient refractive index (GRIN) profile that fitted the measured optical path. The optics of the lens with the refractive index distribution was studied.

Introduction
Understanding the optical and structural changes of the crystalline lens upon accommodation is critical to understand the accommodative mechanism and its failure in presbyopia. The lens changes its external geometry with accommodation. However, both geometrical and GRIN changes should play a role in both the change in power, and spherical aberration. The contribution of the GRIN to the power of the lens is usually addressed in terms of the equivalent refractive index, defined as the refractive index of a homogeneous lens with the same external geometry and power as the GRIN lens. To our knowledge, the contribution of the GRIN to spherical aberration (SA) has not been experimentally investigated before.
In vivo studies using Purkinje imaging phakometry [1] and a simple gradient refractive index model, concluded little changes in the GRIN model as a function of accommodation. On the other hand, Scheimpflug densitometry images showed that the increase in thickness with accommodation was primarily driven by an increase in the thickness of the nucleus [2]. Recent in vivo studies using Magnetic Resonance Imaging [3] have found a decay in the refractive index that appears to be more gradual in accommodated than in the unaccommodated state in both meridional and axial directions. A constant equivalent refractive index with accommodation was also concluded by studies using a Scheiner system in vitro [4], and in vivo using Purkinje [1] and Scheimpflug imaging [5].
Three in vitro crystalline lenses from cynomolgus monkey (*Macaca fascicularis*) were studied in different states of simulated accommodation. The tissue was mounted in an optomechanical lens-stretching system, which simulates accommodation by simultaneous radial stretching of eight scleral segments (EVAS II) [4]. Two of the lenses were imaged in eleven different stretching states (the arms move 0.25 mm per step) and one was stretched to 6 different states. Cross-sectional images of the lens were collected using a custom-developed time-domain optical coherence tomography (OCT) system [6]. Two OCT images were obtained for each step of the stretcher, one with the anterior surface facing the OCT beam and the other with the lens flipped over, and the posterior surface facing the OCT beam. The correct shape of both lens surfaces was therefore obtained. Surfaces were segmented and fitted by conics in a 6 mm pupil diameter. The actual central thickness of the lens was estimated using the distortion produced in the cuvette holding the preservation media in which the crystalline lens is immersed, when this is imaged through the lens [6]. A search algorithm was used to calculate the best 3-variable GRIN that matched the optical path measured in the anterior-up and posterior-up image. The GRIN was
described by a power equation model. Data obtained at all the steps of the stretcher were analyzed simultaneously in a global optimization problem. The input variables of the model were the surface and nucleus refractive indices (the same for all the accommodation states) and the power coefficient (let free to change across steps). Custom ray tracing routines were used to estimate the focal length and crystalline lens wave aberrations (SA in particular), of the measured lens shape and refractive index (both the estimated GRIN and the corresponding equivalent index).

Results
The power coefficient did not change noticeably with accommodation. This implies that the same model variables would fit all the optical path difference data.
The equivalent index, estimated from the measured GRIN profile only showed a slight variation with accommodation. The relative contribution of the GRIN to the change in power remains, therefore, fairly constant across the accommodative range. The SA of the crystalline lens with the equivalent refractive index in a 6-mm pupil decreased with accommodation (Zernike coefficient between -2 and -5 μm), and the presence of GRIN shifted the spherical aberration towards more negative values (-10 μm). Accommodation produced a shift in the SA towards more negative values, and, the relatively larger (negative amount) SA in the presence of GRIN was highest in the accommodated state.

Discussion
We did not find a significant change in the power exponent describing the decay of the refractive index from the nucleus to the surface refractive index in the different accommodative states, in contrast with the (slight) changes in the GRIN profile with accommodation reported in a previous MRI study [3].

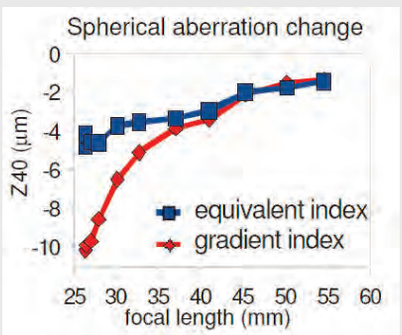

The influence of the GRIN distribution regarding the spherical aberration (6-mm pupil) increases with accommodation.

The estimation of the GRIN profile allowed direct computation of the equivalent index, indirectly inferred in previous studies [1,4,5]. Our results agree with previous findings of a constant equivalent refractive index with accommodation, which indicates a constant contribution of the GRIN to the change in power with accommodation. Measurement of the lens shape and GRIN profile allowed us to compute the SA of the lens, and their relative contribution.
While we found a consistent tendency for the SA to decrease with accommodation, we found larger SA magnitudes than those reported by Roorda and Glasser [7] in cynomolgus lenses in vitro (-1 to -3 μm). Unlike the focal length, where lens accommodative changes can be well described by changes in the external geometry, the gradient distribution appears to have a strong influence on the accommodative SA changes. To our knowledge this is the first experimental study that addresses experimentally the relative contribution of shape and GRIN to the spherical aberration of the crystalline lens.

References
[1] L.F. Garner and G. Smith, *Optom Vis Sci*, 74, 114, 1997.
[2] M. Dubbelman, R. van der Heijde, *Optom Vis Sci*, 78, 411, 2001.
[3] S. Kasthurirangan, E. L. Markwell, D. Atchison, J.M. Pope, *Invest Ophthalmol Vis Sci*, 49, 2531, 2008
[4] B. Maceo, F. Manns, D. Borja, D. Nankivil, S. Uhlhorn, E. Arrieta, A. Ho, R. Augusteyn,J.M. Parel, *J Vis*, 11, 2011
[5] E. Hermans, M. Dubbelman, R. van der Heijde, R. M. Heethaar, *Optom Vis Sci*, 85, 1179, 2008
[6] S. Uhlhorn, D. Borja, F. Manns, J.M. Parel, *Vision Res*, 48, 2732-2738, 2008.
[7] A. Roorda, A. Glasser, *J Vis*, 4, 250, 2004.

[5693]

NOTES

11:45-12:00

Discontinuities in the index gradient of the eye lens

B. Pierscionek[1], M. Hoshino[2], N. Yagi[2], K. Uesugi[2], J. Regini[3]; [1]Faculty of Science, Engineering and Computing, Kingston University, London SW15 3DW (GB); [2]Japan Synchrotron Radiation Research Institute (SPring8), Sayo, Hyogo (JP); [3]Optometry and Vision Sciences, Cardiff University, Cardiff CF24 4LU (GB).
Email: b.pierscionek@kingston.ac.uk

Summary
The refractive index gradient in the eye lens has been fitted with a number of mathematical functions ranging from parabolic to higher order polynomial depending to a large extent on the species. The general assumption has been that the index profile is smooth and gradually varying. Previous studies have suggested that there may be such kinks in the profiles of piscine lenses[1] and more recently, using a new technique, it has been found that there are discontinuities in the gradient index profiles of other animal lenses as well[2]. These may have functional significance and/or be representative of growth stages.

Introduction
Refractive index gradients in a selection of animal lenses: porcine, murine, piscine, newt, ranine were measured using X-ray Talbot grating interferometry constructed at the Spring8 synchrotron in Japan. The technique measures refractive index directly from phase shifts produced by ray passage through the lens and two transmission gratings: a phase and absorption grating. All lenses used were fresh and measurements were made in situ in equatorial and sagittal planes.

Discussion
Clear discontinuities were seen in the gradient index profiles and were particularly evident in porcine and murine lenses. These appear at similar distances on both sides of the optic axis suggesting that these are unlikely to be artefacts or areas of damage but real features. They may be indicative of changes in the growth mode or rate of growth of the lens that triggers a change in the complement of proteins laid down in the region of these irregularities. From a functional perspective, it is possible that these deviations are manifestations of the zones of discontinuity seen in the living human lens. These features do not affect refraction nor impair vision and their function is not known.

Conclusions
Discontinuities detected in the gradient index profiles of some animal lenses may be structural features and have some relevance to the zones of discontinuity in human lenses. They may additionally have some functional significance that requires further probing.

References
[1] Kröger, R.H.H., Campbell, M.C.W., .Fernald, R.D., 2001. The development of the crystalline lens is sensitive to visual input in the African cichlid fish, *Haplochromis burtoni*. Vision Res. 41, 549 -559.
[2] Hoshino, M., Uesugi, K., Yagi, N., Mohri, S., Regini, J. and Pierscionek, B., 2011. Optical properties of in situ eye lenses measured with X-ray Talbot interferometry: a novel measure of growth processes. PLoS ONE 6(9): e25140.doi:10.1371/journal.pone.0025140

[5689]

12:00-12:15

Statistical eye modelling and its applications

J.J. Rozema[1,2], D.A. Atchison[3], M.-J. Tassignon[1,2]; [1]Dept. of Ophthalmology, Antwerp University Hospital, Edegem, 2650 (BE); [2]Faculty of Medicine and Health Science, University of Antwerp, Wilrijk, 2600 (BE); [3]School of Optometry & Vision Science and Institute of Health & Biomedical Innovation, Queensland University of Technology, Brisbane, Q 4059 (AU).
Email: jos.rozema@uza.be

Summary
Statistical eye modelling enables generation of a large number of random, but plausible ocular biometry sets. This has potential applications such as performing calculations of the optical properties of the eye in a large population, in-depth comparison of epidemiological data, and the reconstruction of historical data.

Introduction
Mathematical eye models have been an important part of physiological optics since they were introduced in the 19th Century. Depending on the aspects of the eye that investigators wished to study, this led to the development of models that are either simplified or anatomically exact, describe the refraction along or away from the optical axis, describe the anatomical changes of the eye as a function of age, etc. While many useful literature contributions have been made with these models, their 'static' nature makes calculations based on them valid for only a small fraction of the eyes in the general population (e.g. about 0.67% for the Gullstrand eye model). This problem can be partially overcome by replacing model parameters with the measured biometry of a subject. However, this does not take the correlations between the various biometric parameters into account as some difficult-to-measure parameters are often replaced by the corresponding constant parameters of the original model. This problem can be solved by using statistical (or stochastic) modelling, first introduced by Thibos et al. [1]to generate random, but plausible wavefront aberrations based on average values and a covariance matrix derived from wavefront measurements. Recently, we extended this idea to generate random ocular biometry sets in which the original correlations between parameters were preserved [2].

Discussion
A statistical eye model can be set up using any set of minimally required ocular biometry data, provided its parameters follow a Gaussian distribution. These data should contain at least the ocular refraction, corneal curvature, crystalline lens power, anterior chamber depth, lens thickness and ocular axial length. With the exception of refraction, these parameters follow a Gaussian distribution (possibly after transformation), making them suitable for the model. Next, the average values and covariance matrix must be calculated for these Gaussian parameters, from which a multivariate Gaussian distribution can be defined that can be used to generate a large amount of data with the exact same distribution by means of a simple Matlab program. However the distribution of the calculated refraction obtained in this manner would be Gaussian as well, which is unrealistic. Hence the original refraction distribution must be used to 'filter out' any non-physiological data points. The final result is statistically indistinguishable from the original measured data [2] and can be used for many different purposes.
The main application is calculating optical properties for a large population, which may be useful for investigators in the fields of intraocular lenses or laser safety. The statistical model can also be used for data compression, e.g. reducing the data of 1000 eyes with the 6 minimal parameters from a [1000 x 6] matrix to a set of a [1 x 5], a [5 x 5] and a [1 x 21] matrix.
Provided the three model matrices are available, statistical eye modelling may also be used to reconstruct historical data that was lost over time. This was recently done for Stenström's 1946 data [3][4] (Figure 1). Given the high quality and completeness of Stenström's measurements, this reconstructed data could help in the study of how ocular biometry has changed in the past 70 years. Using the three model matrices, it is also possible to compare statistical models of two

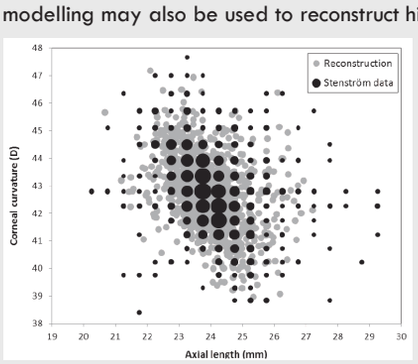

Fig. 1: Original and reconstructed data from Stenström's PhD thesis. Circle diameter is proportional to the number of subjects.

Room: Clinton Auditorium

separate populations by means of statistical methods commonly used in evolutionary biology [5]. These methods, such as t tests after a Fisher r-to-z transformation to compare correlation coefficients of different populations or a combination of the Flury hierarchy and random skewers to compare covariance matrices, can help to demonstrate hitherto unknown changes in correlations between biometric parameters. This will allow comparison of the biometry from subjects of various ethnic backgrounds to investigate whether, besides differences in average biometry, different ethnicities may also have differences in the correlations between the various biometric parameters. Thus, populations can be compared on three different levels: comparison of their average values, a comparison of their individual correlation coefficients and a comparison of their covariance matrices.

Conclusion
These examples show that statistical eye modelling offers many new possibilities in analysing biometric data that can lead to new insights.

References

[1] L. Thibos et al., *Ophthal. Physiol. Opt.* **22**:427-433, 2002.
[2] J.J. Rozema et al., *Invest. Ophthal. Vis. Sci.*, **52**, 4525-4533, 2011.
[3] S. Stenström, *Acta Ophthal.* Suppl. **26**, 1946.
[4] J.J. Rozema, M-J Tassignon, ARVO abstract 137, 2012
[5] J.J. Rozema et al. (*submitted*), 2012.

[5562]

12:15-12:30
Dynamic Purkinje-meter system to evaluate lens stability

J. Tabernero, P. Artal; Laboratorio de Optica, Universidad de Murcia, Campus de Espinardo (Edificio 34), 30100 Murcia (ES).
Email: juant@um.es

Summary
A new system based on recording the ocular reflections of a semicircular IR Led source during eye movements is presented. It can be used to track the subsequent lens or intraocular lens (IOL) wobbling effect and to quantify their dynamic stability.

Introduction
When the eye moves changing fixation, it acquires some kinect energy that is somehow released when it stops. As long as the internal components of the eye (fluids and the crystalline lens, or the IOL in case of pseudophakia) are not perfectly attached to the eye globe, part of this energy can be transferred to them and converted into periodic internal oscillations that generate the effect known as lens (or IOL) wobbling, i.e. the lens performs dumped oscillations after a saccadic eye movement [1,2]. From the dynamic analysis of the wobbling effect, it is possible to quantify the stability of the lens (or IOL) against eye movements.

Methods
The wobbling effect can be quantified recording the ocular reflections originated from a certain source of light (Purkinje images). With a previous version of our Purkinje-meter prototype [3], we were able to analyze the stationary position of the lens or IOL, and therefore to study the long term stability of different IOL designs [4]. The new device (Dynamic Purkinje-meter) has been re-designed with significant modifications. It allows video recording (50 Hz) of the Purkinje images of the eye and the capture during saccadic eye movements (9° amplitude) induced by two flickering fixation LEDs placed in a central and a peripheral position with respect to the objective-camera axis. Flickering frequency can be switched to 1, 0.5 or 0.33 Hz. In order to investigate the dependence of stability on the direction of the eye movement, the peripheral positions of the flickering LEDs included four possible orientations (nasal, temporal, inferior and superior). When the lens (or IOL) suffers from wobbling, a quick oscillation of Purkinje images PIII and PIV (from anterior and posterior lens surfaces) can be observed immediately after a change of gaze. Stability is assessed by fitting the relative movement of PIII and/or PIV with respect to PI (reflection from the anterior corneal surface) to the solutions of a classical dumped harmonic oscillator system:

$$\frac{d^2\vartheta}{dt^2} + 2\sigma\omega_0\frac{d\vartheta}{dt} + \omega_0^2\vartheta = 0$$

where ϑ is the relative movement of PIV (or PIII) with respect to PI (converted into gaze angle units); *t* represents time; σ is the damping ratio and ω_0 is the undamped angular frequency of the movement. and ω_0 are the fittings parameters of the model.

Results
Figure 1 shows an example of the procedure to obtain σ and ω_0 in four different pseudophakic subjects (empty red circles represents the experimental data from the wobbling effect after a 9 degrees eye movement; black solid lines show fittings to the damped harmonic oscillator model).

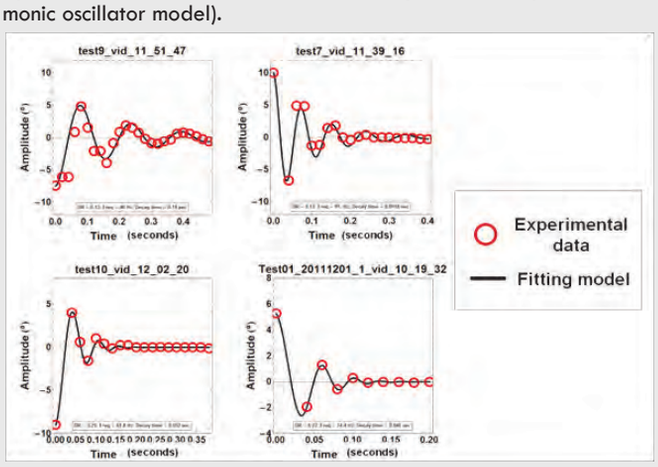

Fig. 1. Examples of fitting the wobbling effect to a damped harminc oscillator model in 4 different pseudophakic subjects

Stability can be characterized by three parameters. The "damping ratio" value (σ) determines how much the amplitude of the oscillations is reduced by the system. Damping ratios ≥ 1 means that wobbling is not present (the ideal situation in this case) and null values means that the system oscillates without dumping. The "undamped frequency" (ω_0) indicates the tendency of the system to oscillate. And the "decay time"

$$\tau = \frac{1}{\sigma\omega_0}$$

combines both previous parameters to define a characteristic time as the amplitude decays by a factor 1/e from its maximum value.

Conclusions
A new instrument to determine lens stability has been developed and successfully tested. It may be useful for a wide range of future studies.

References

[1] Physical forces involved in pseudophacodonesis and iridodonesis. KW Jacobi, WS Jagger, *Graefe's Archive for Clinical and Experimental Ophthalmology,* **216**, 49-52,1981.
[2] Saccadic lens instability increases with accommodative stimulus in presbyopes. LHe, WJ Donnelly III, SB Stevenson, A Glasser. *Journal of Vision,* **10(4)** 2010.
[3] Instrument for measuring the misalignments of ocular surfaces. J Tabernero, A Benito, V Nourrit, P Artal. *Optics Express*, **14**, 10945-10956, 2006.
[4] Impact of intraocular lens haptic design and orientation on decentration and tilt. A Crnej, N Hirnschall, Y Nishi, V Gangwani, J Tabernero, P Artal, O Findl, *Journal of Cataract and Refractive Surgery,* **37**, 1768-1774, 2011.

[5686]

NOTES

12:30-12:45

Accommodating intraocular lens using a controllable liquid-liquid interface

V.V. Molebny; Institute of Biomedical Engineering, Kiev, 03187 (UA).
Email: molebny@gmail.com

Summary
Engineering problems are discussed of an accommodating IOL based on changeable curvature of the interface between immissible liquids with different refraction indices and differing wettability. The curvature is controlled using a variable profile of the peripheral walls or a variable wettability.

Introduction
To treat cataract, the crystalline lens is normally replaced with an artificial IOL, the simplest one being monofocal with no accommodation. Bifocal or multifocal IOLs simulating the accommodation by two or more foci result in reduced contrast sensitivity. An improvement can be achieved by an accommodating IOL. An optic-shift accommodating IOL having moving parts is restricted in the range of accommodation to about two diopters. A fluidic IOL with flexible film between media still meets difficulties of being driven by an accommodative mechanism becoming more brittle after the surgery.
We propose a solution with no flexible film between the media (V.V. Molebny, *Patent Appl. Ukraine*, 201115460, Dec. 27, 2011). The lens is created by an interface of two or more immissible liquids having different refraction and different wettability.

Discussion
The concept of altering interface curvature between immissible liquids is illustrated in Fig. 1. Changing the tilt α of the surface along the line, crossing the points *A* and *B*, results in varying the radius of curvature of the interface surface from *R* (in *a*) to *R'* (in *b*). Note that the contact angle θ is not changed (being the same in *a* and *b*).

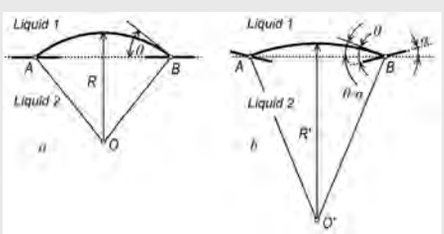

Fig 1. Concept of interface curvature control

An example of a surface of rotation with variable curvature is shown in Fig. 2. The generatrix is rotated around the optical axis along the directrix. In the simplest case, the directrix is a circle. The generatrix is a second or higher-order curve, and can be convex or concave. One of the liquids should be hydrophobic, the other - hydrophilic. The liquids should have different refraction to create a lens at their interface.

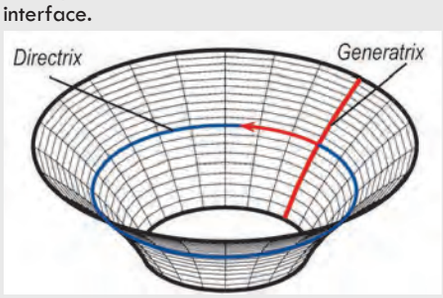

Fig 2. Surface with variable curvature

There can be several combinations of hydrophobic-hydrophilic, higher-lower refraction index, concave-convex wall surface. Positive and negative lenses can be created. Negative lens can be used only if the total optical power (including the outer windows) is high enough, and the variations of the optical power is used for accommodation adjustment. An example of a convex wall surface and liquid parameter combination, forming a positive lens, is shown in Fig. 3. In the relaxed state (left), the interface between the hydrophobic liquid with a higher refraction and the hydrophilic liquid with a lower refraction is at the level *AB* and has the curvature ***S***. When the eye comes to the accommodated state, the accommodation mechanism and the design of the IOL act in such a way that hydrophobic liquid having higher refraction is pumped into the main reservoir moving the level of the interface to the position *A'B'* (right drawing) where it alters the curvature from ***S*** to its higher value ***S'***, thus refocusing the eye on near vision.

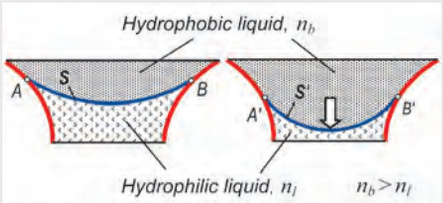

Fig 3. Altering the curvature of the interface with lens filling

Another solution is to make the surface of the periphery wall with the wettability varying along the generatrix being constant along the directrix. In such design, the generatrix can be simply a straight vertical line.
Varying wettability can be produced by a deposited monolayer with imprinted nanocraters (10 - 50 nm) with corresponding distribution of their size or/and density. Carbon nanotubes sized 30 nm - 6 μm can produce the surface with similar parameters.

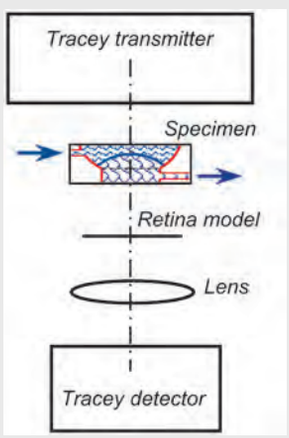

Fig 4. IOL specimen study with a modified ray tracing aberrometer

The IOL can be designed with more than one interface having a core, anterior and posterior layers. Customizing the profile of the periphery walls can result in customized aberrations of the IOL to compensate for the corneal aberrations.
We investigated an IOL prototype with a modified ray tracing aberrometer shown in Fig. 4. To exclude the errors induced in the back pass, we separated the transmitting and detecting parts of the Tracey aberrometer. After passing the specimen, parallel beams from Tracey transmitter are projected on the thin scattering screen mimicking the retina. Tracey detector is stand alone being positioned behind an additional lens having the focal distance corresponding to the human eye.
The specimen under investigation is made of PMMA with the peripheral walls in the form of sphere and the central aperture transparent for the probing Tracey beams. The specimen has the anterior and posterior windows. Delivery and outflow of the immissible liquids are provided through the side channels and syringe needles. A range of liquid pairs was tested, as well as sphere and central aperture diameters were varied. The higher sphere diameters give rise to spherical component of aberrations, which, by the way, can be compensated by a corresponding thickness distribution of the anterior and/or posterior windows.

Conclusions
A new accommodating IOL controlled by a liquid-liquid interface and bio-activated by a residue accommodation mechanism is described with its prototype having been tested. The tests confirmed the feasibility of the proposed approach with acceptable level of induced spherical aberrations and showed the ways of their compensation for larger apertures.

[5708]

NOTES

Room: Clinton Auditorium

12:45-13:00

Extension of vision depth-of-field by corrective lenses with angular modulation of the optical power

K. Petelczyc[1], K. Kakarenko[1], I. Ducin[1], A. Czerwiński[1], Z. Jaroszewicz[2,3], A. Kołodziejczyk[1], M. Sypek[1]; [1]Faculty of Physics, Warsaw University of Technology, Koszykowa 75, 00662 Warsaw (PL); [2]Institute of Applied Optics, Kamionkowska 18, 03805 Warsaw (PL); [3]National Institute of Telecommunications, Szachowa 1, 04894 Warsaw (PL).
Email: krzys137@if.pw.edu.pl

Summary
Small depth-of-field (DOF) becomes a significant problem when the eye's focus becomes constant (presbyopia, aphakia). We present a new method of the DOF extension by means of contact or intraocular lenses with the angularly modulated optical power. Imaging effects show that such idea can be successfully applied.

Introduction
The growing number of problems in communities concerns the vision impairment or its total loss. Thus the purpose of the research presented in the article is to increase the quality of life of the modern society.
Due to the natural aging processes in the human body the ability of the eye accommodation decreases and the use of spectacles is the simplest and the most popular method of vision correction. Many patients are required to wear two types of glasses – one for far vision, the other for near vision (i.e. to read). In this case, glasses with progressive lenses offer the possible solution, although many people find it uncomfortable. Aging of crystalline lens makes it more diffusing leading to cataract. It forms a clouding in a crystalline lens of the eye, which reduces the sharpness of vision. In the case of a cataract the only effective method is a surgical extraction of the eye lens what makes accommodation impossible.

Discussion
The main idea of the Light Sword Optical Element (LSOE) is modulation of its optical power that varies with the angular coordinate in the polar coordinate system. Correction of the human eye by the LSOE causes some aberrations which limit contrast transfer of the eye optical system and makes some blur, tilt and astigmatism (on meridian dependent on object distance) On the other hand the use of the LSOE provides proper sharpness of retina images. Computer simulations in the simplified Gullstrand #2 relaxed eye model including PSF, Strehl ratios, MTF and optotypes' imaging (Fig. 1) were performed recently. They clearly illustrated usefulness of the LSOE for the presbyopia compensation. Unlike to well known multifocal lenses the geometry of correction based on angular modulation is independent of pupil size changes and the use of the LSOE provides uniform quality of imaging for a whole range of object distances [1].
In the present contribution we show some new experimental results, particularly with the use of ophthalmological criteria such as optotype chart imaging. We also analyse imaging contrast obtained in the experimental arrangement. Our experiments were performed in the optical setup modelling an eye. We used three models of the LSOE fabricated in different forms as the diffractive binary-phase element, the high-order kinoform and the photosculpture structure. We analyzed limitations of elements and compared their imaging properties. Obtained images give an evidence that the vision acuity in the case of such correction, could be sufficient for functional tasks.

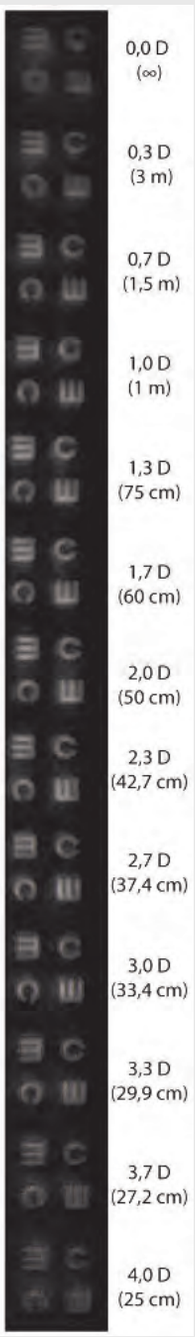

Fig. 1
Computer simulation of vision corrected by the LSOE

Conclusions
The presented DOF extension seems to be very flexible. The LSOEs may be used as corrective element in a form of contact or intraocular lenses. Hence such structures can be potentially implemented in a case of two most common defects of the human eye: presbyopia and cataract.

References
[1] K. Petelczyc, S. Bará, A. Ciro Lopez, Z. Jaroszewicz, K. Kakarenko, A. Kolodziejczyk, and M. Sypek, "Imaging properties of the light sword optical element used as a contact lens in a presbyopic eye model," Opt. Express **19**, 25602-25616 (2011)

[5729]

13:00-14:00 Lunch break UCD Main Restaurant

14:00-15:30
POSTER SESSION I & COFFEE BREAK
Room: Exhibition area

15:30-18:30
RETINAL IMAGING AND PHOTORECEPTOR ANALYSIS
Session Chair: H. Ginis, University of Crete (GR)

15:30-16:00 **INVITED TALK**

Adaptive Optics Imaging of the Retina

S.A. Burns, Toco Y Chui, D.A. VanNasdale, Z. Zhong, A.E. Elsner; Indiana University (US).

Adaptive Optics Imaging has become a powerful modality for looking at the properties of the living retina. In many ways however, we are just starting to tap the ability of adaptive optics to make precise measurements of the properties of the eye. In the current presentation we will concentrate on two unique features we have been pursuing. The first is the use of a programmable, steerable imaging system which allows us to very rapidly collect data from large regions of the retina as well as to program the scan mode in real time to measure blood flow velocity on a cellular basis. The second feature is the ability to control the degree of confocality of the imaging system within a session, allowing measurements of the scattering behavior of retinal features and optimization of the mode of imaging for specific structural properties. Using these techniques we have successfully imaged relatively large extents of the retina to characterize the sampling mosaic of the photoreceptors, measured the speed of blood flow within the vasculature and used the angular scattering of blood and subretinal deposits to improve clinical imaging.

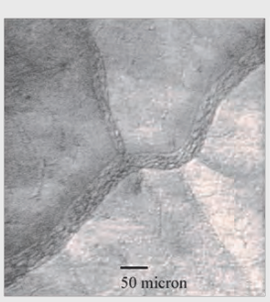

Fig. 1.
Image based on angular scattering of light from the retina. This image was obtained in 1/30 of a second and shows individual cells within a capillary as well as the laminar distribution of cells in slightly larger vessels.

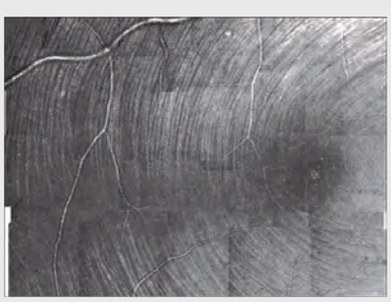

Fig. 2.
Example of montaged images of the nerve fiber layer along the horizontal raphe of an eye. The fovea is towards the right center of the montage

[5747]

16:00-16:15

Pupil apodization in scanning retinal imaging

B. Vohnsen[1], B. Lochocki[1], D. Rativa[2], C. Vela[1]; [1]AOI Group, School of Physics, University College Dublin, Dublin 4 (IE); [2]Dep. Electronics and Systems, Universidade Federal de Pernambuco, Recife (BR).
Email: brian.vohnsen@ucd.ie

Summary
Together with wavefront control, apodization can be used to modify the entrance or exit pupil in scanning retinal imaging allowing extra control of spot size and beam properties at focus. Annular apertures can enhance transverse resolution but the impact of remnant aberrations stresses the need for a compromised solution.

Introduction
The relationship between light incident on the eye and the corresponding retinal image is essentially that of a Fourier transform apodized by the pupil. Controlling the spatial distribution of *phase* in the pupil plane allows, e.g., for optimization of the intensity PSF incident on the retina by reducing the impact of aberrations. Likewise, controlling the spatial distribution of incident field *amplitude* in the pupil plane can be used to control the angle-of-incidence on the retina as utilized when characterizing the Stiles-Crawford effect of the first kind with a Maxwellian source and when probing photoreceptor directionality with fundus imaging [1] and scanning laser ophthalmoscopy [2]. Spatial amplitude control can also be used to suppress unwanted angular components of light, facilitating imaging of photoreceptor cones and rods of a given diameter, and indeed as an extra parameter that can control the size of the probing light spot at the retina [3].
The best of both worlds would require perfect spatial control of both the amplitude and phase at any given instant but a compromise is sought that can facilitate imaging and photoreceptor analysis without hindering its experimental realization. Here, we report our findings analyzing different pupil apodizations in conjunction with experimental findings using an in-house build confocal scanning laser ophthalmoscope where remnant system aberrations are below $\lambda/10$ RMS across the full pupil prior to adaptive optics wavefront correction.

Discussion
An increased pupil size provides higher transverse resolution and a reduced depth of focus in the absence of aberrations. Using a centred annular aperture for the incoming beam reduces the impact of low-angular components and diminishes the width of the central Airy disc in the PSF although at the cost of an increased off-axis ringing. This resolution enhancement is accompanied by an increased depth-of-focus that may favour light coupling to the elongated photoreceptors.

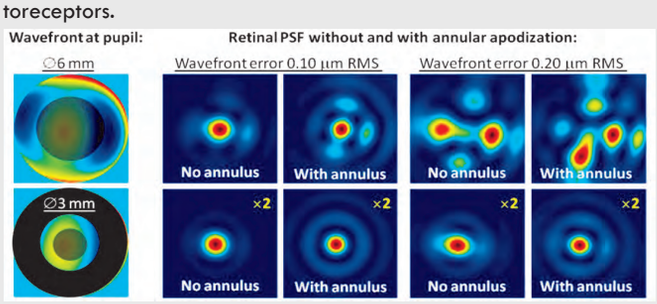

Fig 1. Simulated case of the PSF generated with a 6 mm and a 3 mm pupil respectively and different amounts of remnant (uncorrected) aberrations. In either case the central stop used to generate the annular beam covers 60% of the full pupil diameter. The pupil wavefront images show the wavefront and the location (transparent grey) of a central stop used for the apodization. The retinal PSF images for the smaller 3 mm beam have been magnified by a factor of 2 to ease comparison with the former.

Remnant aberrations across the annular aperture may hamper the successful reduction of the probing light spot in the PSF [3]. Thus, one would either need to reduce the aberrations below a certain threshold or block out those parts of the incident wavefront that when added would deteriorate the beam quality at the focus. The resulting PSF is insensitive to apodization misalignments and to rotationally-symmetric aberrations (defocus, spherical aberration) but highly influenced by other uncorrected aberrations [4]. Examples of wavefronts with the corresponding PSFs are shown in Fig. 1 for two different diameters of the incident beam. As can be seen the impact of remnant aberrations is substantially less once the beam diameter has been significantly reduced. This shows that although not reaching the utmost in terms of transverse resolution an annular beam may be highly practical in a clinical setting to enhance the resolution with simple means. In this contribution we discuss these findings in relation to recent experimental results for the authors' eyes.

Conclusions
We find that apodization of the incident beam can be used to shrink the size of a probing light spot facilitating retinal imaging of smaller structures. However, remnant aberrations may complicate the realization which suggests that a valid compromise is to use a narrower incident beam thereby benefitting more from the use of the annulus without increasing the demands for accurate wavefront correction. Such an approach may ultimately be more clinically relevant.

References
[1] A. Roorda and D. Williams, Optical fiber properties of individual human cones, *J. Vision* **2**, 404-412 (2002)
[2] D. Rativa and B. Vohnsen, Analysis of individual cone-photoreceptor directionality using scanning laser ophthalmoscopy, *Biomed. Opt. Express* **2**, 1423-1431 (2011)
[3] B. Vohnsen and D. Rativa, Ultrasmall spot size scanning laser ophthalmoscopy, *Biomed. Opt. Express* **2**, 1597-1609 (2011)
[4] B. Vohnsen and D. Rativa, Promises and limitations of wavefront corrections with annular apertures using scanning laser ophthalmoscopy, *8th International Workshop on Adaptive Optics for Industry and Medicine* (Murcia, Spain 2011)

[5779]

16:15-16:30

Positional sensitivity to microstimuli detected in the human retina

W.M. Harmening[1], W.S. Tuten[1], A. Roorda[1], L.C. Sincich[2]; [1]Univ. of California, Berkeley, School of Optometry, CA 94720 (US); [2]Univ. of Alabama at Birmingham, Dept. of Vision Sciences, AL 35294 (US).
Email: harmening@berkeley.edu

Summary
In retinal ganglion cells and in thalamic neurons, light sensitivity peaks when small stimuli land on cone photoreceptors rather than in between. Here we show that this positional sensitivity is detectable psychophysically in humans, supporting the idea that the cone mosaic ultimately sets the limit for visual resolution.

Introduction
The rod and cone photoreceptors of the retina provide a continuous tiling for capturing photons in the eye, albeit with different sensitivity between the two photoreceptor classes. At photopic luminance levels in the retinal periphery, when only cones are expected to play a role in active vision, one might expect that sensitivity to light will be lower in the rod-filled spaces between cones compared to the cones themselves. This was shown previously with recordings of primate retinal ganglion cells and lateral geniculate nucleus neurons [1, 2]. Here we examine whether this positional sensitivity decrement can also be demonstrated at the perceptual level in humans using intensity threshold psychophysics.

Methods
We used a multi-wavelength adaptive optics scanning laser ophthalmoscope (AOSLO) for imaging the cone mosaic [3]. Stimulus delivery to selectable locations was achieved by real-time stabilization of fixational eye movements [4]. The light source was a super-continuum laser whose output was bandpass filtered to provide an infrared imaging wavelength of 842±25 nm, and a visible stimulation wavelength of 543±11 nm that minimized the sensitivity difference between L and M cones. Residual light leak through the system produced a background of ~70 cd/m², which effectively eliminated any rod contribution during these experiments. Subjects were 3 males

with normal color vision. The task required fixation on a small spot produced by a white LED presented at 4°-5° eccentricity. While fixating, subjects reported seeing or not seeing a 3.6 µm (45 arcsec) square flashed during one video frame. We used a self-paced QUEST algorithm to measure threshold after 22 trials at one location. Trial sets were randomly interleaved, with the stimulus placed either on a cone or in the space next to it. For each type of location, threshold was measured 5 times. Cones were selected for stimulation in the infrared channel. Because of chromatic dispersion caused by the ocular media, delivering light to a selected cone required that longitudinal and transverse chromatic aberration was corrected prior to any psychophysical trials [5]. Subjects used a bite-bar to quell pupil motion relative to the instrument beams.

Results

In all subjects, cones were spaced ~8 µm apart, consistent with spacing measured anatomically at 4° eccentricity. We estimated the stimulus diameter by first convolving the stimulus geometry (3.6 µm square) with the diffraction-limited pointspread function of a 6 mm pupil, and then averaging this convolved profile across the actual delivery locations recorded for all 22 trials of each threshold measurement. This measure incorporated stimulus delivery errors. The trial-averaged stimulus diameter ranged from 3.7 to 4.0 µm in its full-width at half-height (Fig. 1a).

Luminance intensity thresholds for stimuli targeted to the cone centers varied between cones. Thus, we compared the off-cone location thresholds to the thresholds for the on-cone conditions (Fig. 1b). All off-cone locations yielded higher mean thresholds than on-cone locations, with an average ratio of 1.3 (range: 1.03-1.64). In 6 of 10 cones tested, the threshold was significantly higher for the off-cone location ($p < 0.05$, one-tailed t-test).

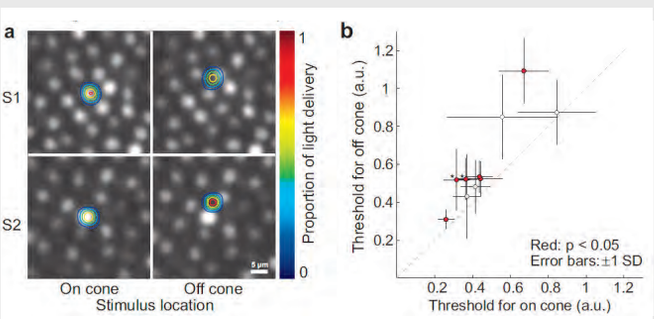

Fig.1 **(a)** Example cumulative light delivery contour plots for stimulus locations in two subjects. **(b)** Sensitivity thresholds comparing stimulus locations (on vs. off a targeted cone).

Discussion

Although the trial-averaged stimulus diameter suggests that photon delivery can be restricted to one cone, it nevertheless remains possible that the intensity of light required to reach threshold resulted in multiple cones being stimulated due to local intra-retinal scatter. Thus, even for the on-cone condition, we have no direct evidence that stimulation of only a single cone suffices for perceptual threshold. With this caveat in mind, the results suggest that thresholds are lowered when more light lands on a single cone than when it lands in its coneless surround.

Given the decrements seen in the responses of single neurons in the retina and thalamus to off-cone stimuli [1,2], it appears that the crenulated sensitivity of the retinal periphery is detectable at multiple stages of the visual system, at least up to the level of perception. Despite the fact that the retina evolved without diffractionlimited optics in front of it, our results are consistent with the idea that the underlying retinal circuitry is sensitive to positional changes smaller than the receptor spacing itself.

Support

DFG Ha 5323/2-1, NIH EY021642, EY019566, EY014375, EY007043

References

[1] Sincich, L.C., Zhang, Y., Tiruveedhula, P., Horton, J.C. & Roorda, A. Nature neuroscience **12**, 967-9 (2009).
[2] Field, G.D. et al. *Nature* **467**, 673-7 (2010).
[3] Zhang, Y., Poonja, S. & Roorda, A. *Optics letters* **31**, 1268-1270 (2006).
[4] Arathorn, D.W. et al *Optics express* **15**, 13731-44 (2007).
[5] Harmening, W. M. Tiruveedhula, P., Roorda, A. & Sincich, L.C. **submitted**, (2012).

[5703]

16:30-16:45

Imaging Photoreceptor Structure in Retinitis Pigmentosa and Usher Syndrome: Results and Challenges

J. Carroll[1,2], P. Godara[1], R.F. Cooper[2], V. Williams[1], P. Summerfelt[1], J.E. Kim[1], D.P. Han[1], D.V. Weinberg[1], K.E. Stepien[1], A. Dubra[1,2], T.B. Connor[1]; [1]Medical College of Wisconsin, Department of Ophthalmology, Milwaukee, WI, 53226 (US); [2]Marquette University, Department of Biomedical Engineering, Milwaukee, WI, 53201 (US).
Email: jcarroll@mcw.edu

Summary

Adaptive optics imaging allows visualization of photoreceptor structure in the living human retina. For some diseases, such imaging holds promise for improving the efficacy of emerging treatments through patient selection and evaluation of treatment efficacy. Realization of this potential requires careful dissection of disease-specific challenges to assessing photoreceptor structure with adaptive optics imaging.

Introduction

Inherited retinal degenerations (including retinitis pigmentosa and Usher syndrome) are characterized by the progressive death of rod and cone photoreceptors, with associated vision loss. One of the challenges in these disorders is the reliable assessment of photoreceptor structure and function. Adaptive optics imaging has emerged as the tool of choice in defining the cellular phenotype in inherited retinal degenerations, in many cases permitting visualization of subclinical photoreceptor damage. Each disease brings with it unique challenges in obtaining the highest quality images of the photoreceptor mosaic. For example, patients with achromatopsia often have severe nystagmus and are photophobic. Patients with retinitis pigmentosa can have media opacities and cystoid macular edema (CME). Patients with Best's disease can have sub-retinal changes that alter the normal alignment of photoreceptors. In some cases, these complications can be addressed through altering the imaging protocol, while in other cases they represent significant barriers. In either case, it is important to carefully dissect the disease-specific challenges to assessing photoreceptor structure with adaptive optics imaging. These results provide the basis for a more tempered and realistic interpretation of images along with guidance in developing new systems that overcome existing barriers.

Discussion

Methods – We recruited 9 patients with retinitis pigmentosa and 3 patients with Usher syndrome. Blood samples were collected and sent for analysis by EyeGene and/or The John and Marcia Carver Nonprofit Genetic Testing Laboratory. To assess outer retinal lamination, all patients were imaged using spectral domain optical coherence tomography (OCT). Images of the foveal and parafoveal photoreceptor mosaic were obtained using an adaptive optics scanning light ophthalmoscope (AOSLO). *Results* – OCT imaging showed classic peripheral thinning in all patients, with a highly variable degree of preserved central macular structure. AOSLO imaging showed rapid degradation of the photoreceptor mosaic at the transition zone, corresponding to the dissipation of the hyper-reflective photoreceptor layers on OCT. Within the transition zone, cones took on an abnormal appearance, making interpretation of the images difficult. CME was present in some patients, and as reported previously, this also interferes with visualization of the photoreceptor mosaic.[1] Beyond transition zone, the RPE mosaic appeared visible, consistent with previous reports from patients with cone dystrophy.[2] Within

the RP patients, a complete, contiguous foveal cone mosaic of normal density was visible in all but the most advanced patient. Surprisingly, in all three Usher patients we observed a disrupted foveal cone mosaic of reduced density, in stark contrast to the RP patients (see Figure 1).

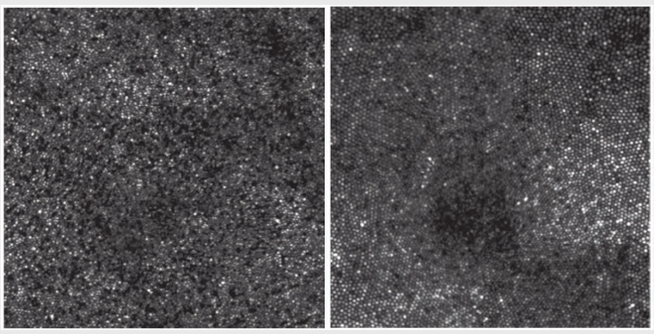

Fig. 1 Foveal montage images (~2° x 2°) from a patient with Usher syndrome (left) and a patient with adRP (right).

Conclusions

High-resolution imaging of the photoreceptor mosaic reveals pronounced differences between RP and Usher patients, at least in our population. In addition, we demonstrate a range of limitations for interpreting such images, and discuss strategies to mitigate these limitations. Despite some difficulties in imaging this patient population, we believe that the ability to visualize photoreceptors in RP and Usher disease should provide sensitive outcome measures for emerging trials, as recently demonstrated by Talcott *et al*. [3].

References

[1] J. Duncan, Y. Zhang, J. Gandhi, C. Nakanishi, M. Othman, K.E.H. Branham, A. Swaroop, A. Roorda, *Investigative Ophthalmology & Visual Science*, **48**, 3283-3291, 2007.

[2] A. Roorda, Y. Zhang, J. Duncan, *Investigative Ophthalmology & Visual Science*, **48**, 2297-2303, 2007.

[3] K.E. Talcott, K. Ratnam, S.M. Sundquist, A.S. Lucero, B.J. Lujan, W. Tao, T.C. Porco, A. Roorda, J.L. Duncan *Investigative Ophthalmology & Visual Science*, **52**, 2219-2226, 2011.

[5756]

16:45-17:00

Cellular-resolution imaging of macaque retinas with an adaptive optics retinal camera designed for humans

E. Odlund[1], K. Azartash[2], L. Vabre[1], B. Lamory-Bardet[1], N. Chateau[1]; [1]Imagine Eyes, 18 rue Charles de Gaulle, 91400 Orsay (FR); [2]Allergan, Inc., 2525 Dupont Drive, Irvine, CA 92612 (US).
Email: eodlund@imagine-eyes.com

Summary

This research focused on evaluating the capabilities of imaging macaque retinas at the microscopic scale using a compact adaptive optics (AO) retinal camera designed for humans.

Introduction

In recent years, numerous AO retinal imaging systems have advanced retinal imaging and research. The potential for clinical research when imaging the human retina at a cellular scale using AO has been documented [1].

The interest in using non-human primates, such as macaques, is widely accepted and studies have already been presented on AO imaging on rhesus monkeys [3, 4]. In the current study and for the first time, we have used the compact AO camera (rtx1, Imagine Eyes, France) developed for use on humans to image the retinas' of cynomolgus monkeys (macaca fascicularis). Retinal areas of 4x4 degrees were imaged on five individuals of ages ranging from 3-18 years. The monkeys' eyes were dilated and contact lenses were used to keep the cornea hydrated. The monkeys were positioned to allow translational movements in all directions so that the retina could be imaged at wide eccentricities, up to the optic nerve head, and beyond. The cone photoreceptor density was calculated at various retinal eccentricities.

Discussion

The retinal camera proved to be perfectly adapted for imaging of macaque retinas, including photoreceptors as well as other retinal features such as the optic nerve head. At higher retinal eccentricities, rod photoreceptors were observed. Thanks to appropriate image processing, the cone/rod distribution was clearly visualized. The presence of retinal blood vessels in the center of the fovea was also noted, as opposed to the case of humans.

The results from the cone counting showed an expected density profile as a function of the retinal eccentricity, as well as a good reproducibility between images acquired at different times.

Conclusions

AO imaging enables an unprecedented precision in terms visualizing details of the retina, allowing early detection and precise follow-up of the progression of retinal diseases. The encouraging results from the use of this technology for imaging of macaque retinas opens up for promising future applications of AO in areas such as pharmacology.

References

[1] M. Zacharria, B.Lamory, and N. Chateau, *Nature Photonics,* **5** (1):24–26, 2011

[2] A.S. Vilupuru, N. V. Rangaswamy, L. J. Frishman, E. L. Smith III, R.S. Harwerth, and A. Roorda, *J. Opt. Soc. Am. A,* **24**(5):1417-1425, 2007

[3] J.J. Hunter, B. Masella, A. Dubra, R. Sharma, L. Yin, W. H. Merigan, G. Palczewska, K. Palczewski, and D. R. Williams, *BioMed OptExpr.*, **2**(1):139-148, 2011

[5777]

17:00-17:15

Symmetry of inter-cone photoreceptor distance between fellow eyes

M. Lombardo[1,] G. Lombardo[2,3], D. Schiano Lomoriello[1], M. Rosati[1], P. Ducoli[1], S. Serrao[1]; [1]Fondazione G.B. Bietti IRCCS, Via Livenza 3, 00198 Rome (IT); [2]CNR-IPCF Unit of Support Cosenza, LiCryL Laboratory, University of Calabria, Ponte Pietro Bucci, 87036, Rende (IT); [3]Vision Engineering, Via Adda 7, 00198 Rome (IT).*
***Email:** mlombardo@visioeng.it

Summary

The cone spacing follows a symmetrical distribution in the parafoveal region of fellow eyes in the same subject. A systematic distribution of the parafoveal cones between fellow eyes may provide an anatomical basis for the involvement of the photoreceptor layer in the first step of binocular spatial sampling.

Introduction

Data on populations of healthy eyes are fundamental in characterizing the density, distribution and appearance of normal retinal photoreceptor cells. The analysis of cone photoreceptor spatial distribution could also give a new information on the physical aspects of visual sampling.

Previous laboratory work [1,2] have previously characterized the cone photoreceptor density distribution in small populations of normal eyes. With the exception of the peak cone density data, which suffers from limited resolution of the smallest cones in most of the cases, even when adaptive optics (AO) is used, the *in vivo* measurements of cone density have shown good agreement with histologic data from cadaver eyes [3,4].

So far, no comparison of the cone photoreceptor spatial distribution between fellow eyes has been published, with the exception of a single cadaver eye study [5].

In the present study, we investigated the symmetry of inter-cone distance between fellow eyes in a population of young healthy subjects.

Discussion

A flood-illumination compact AO ophthalmoscope, the *rtx1* (Imagine Eyes, Orsay, France), was used to image the retina in 16 healthy

Room: Clinton Auditorium

volunteer subjects. Details of the AO system has been described elsewhere [5].
Inter-cone distance (*ICD*, μm) was estimated at 250-, 420-, 760- and 1300-μm eccentricities from the foveal center reference point along the nasal and temporal meridians in both eyes of each subject. *ICD* was calculated within a 50 x 50 μm window from identified cone center considering that the photoreceptors were hexagonally arranged, as previously described [5]. Each image was converted to micrometers using model eye parameterized by the biometry measurements from each eye obtained with the IOL Master (Zeiss, CA, USA) [5].
The mean ICD increased from approximately 4.80 ± 0.40 μm to approximately 9.20 ± 0.93 μm from 250- to 1300-μm eccentricity respectively. The increase of *ICD* was symmetrical along the nasal and temporal meridians of fellow eyes, as shown in figure 1. No differences in *ICD* values were found at any eccentricity between the nasal and temporal meridians of fellows eyes (ANOVA, $P>0.05$). A high degree of intraclass correlation was found (F-test, $P<0.001$) between the same retinal eccentricity locations along the nasal and temporal meridians of fellow eyes.

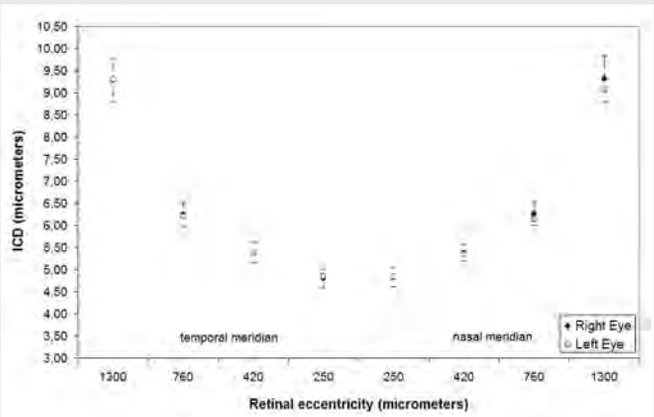

Fig. 1 ICD distribution along the nasal and temporal meridians of fellow eyes. The error bars indicate ± 1 SD.

Conclusions
The bilateral symmetry of microscopic anatomical properties of the cone photoreceptors may have direct consequences for visual function. The highly ordered and systematic architecture of the cone mosaic in the parafoveal region between fellow eyes could be the result of an evolutionary process creating appropriate location information for binocular spatial sampling.

References
[1] T.Y.P. Chui, H. Song, and S. Burns, "Individual variations in human cone photoreceptor packing density: variations with refractive error," Invest Ophthalmol Vis Sci 49, 4679-4687 (2008).
[2] K.Y. Li, P. Tiruveedhula, and A. Roorda, "Intersubject variability of foveal cone photoreceptor density in relation to eye length," Invest Ophthalmol Vis Sci 51, 6858-6867 (2010).
[3] C.A. Curcio, K.R. Sloan, R.E. Kalina, and A.E. Hendrickson, "Human photoreceptor topography," J Comp Neurol 292, 497-523 (1990).
[4] C.A. Curcio and K.R. Sloan, "Packing geometry of human cone photoreceptors: variation with eccentricity and evidence of local anisotropy," Vis Neuroscience 9, 169-180 (1992).
[5] M. Lombardo, S. Serrao, P. Ducoli, and G. Lombardo, "Variations in the image optical quality of the eye and the sampling limit of resolution of the cone mosaic with axial length in young adults," J Cataract Refract Surg, in press (2012).

[5575]

NOTES

17:15-17:30

Simultaneous Multiple-depths *en-Face* Optical Coherence Tomography Imaging of the Retina

J.A. Rogers, A.Gh. Podoleanu; Applied Optics Group, School of Physical Sciences, University of Kent, Canterbury (GB).
Email: ap11@kent.ac.uk

Summary
Active recirculating loops are employed in each arm of a low coherence interferometer to provide simultaneously *en-face* (*ef*) optical coherence tomography (OCT) images from several depths. Sufficient good signal to noise ratio simultaneously generated *ef*–OCT images from 6 to 8 depths in the retina are demonstrated.

Introduction
The ability to measure multiple points in depth simultaneously or at least near simultaneously is one of the inherent advantages of a method like OCT. While the advent of commercially available ophthalmic spectral domain OCT systems has made it possible to capture large amounts of data quickly, for interpretation the resulting images are usually displayed in either *en-face* or in cross sectional planes. In a previous report [1], we have shown that the combination of multiple delay lines employed in both the reference and object arms of an interferometer may be used to acquire *ef*–OCT images from multiple depths in the tissue. Till now, we reported hardware developments only, and images from Drosophila embryos. Here we demonstrate that it is possible to use the concept of multiple recirculation loops to simultaneously capture multiple *ef*–OCT images from several depths within the retina *in vivo*.

Experimental set-up
Key to the new configuration presented in Fig. 1 is the use of recirculation loops in both reference and sample arm. To compensate for the losses due to the beam-splitters, isolators and launchers (structure made of a fiber optic positioner and a microscope objective (MO)), identical semiconductor optical amplifiers (SOA) have been incorporated in both loops. In this way multiple depths can be interrogated that are separated by the difference between the lengths of the two loops. This optical path difference is adjustable by displacing the launchers in each arm relatively to each others. The number of roundtrips and the depth in the sample are encoded on frequency by using an acousto – optic frequency shifter (AOFS) in each recirculation loop and driving them with sinusoidal signals at different frequencies, F1 and F2. The multiple of the difference of these frequencies, $\Delta F = |F2-F1|$ is equal to the multiple of round trips in the two recirculation loops. In the object arm, a XY galvanometer scanner pair operating at 500 Hz line rate and 2 Hz frame rate were used to produce a 500 x 500 pixel image (10 degree field). The system has enabled simultaneous capture of eight *ef*-OCT images from the retina *in vivo*. Signal to noise was sufficient to image the retina across all planes with adjustable spacing between imaging planes.

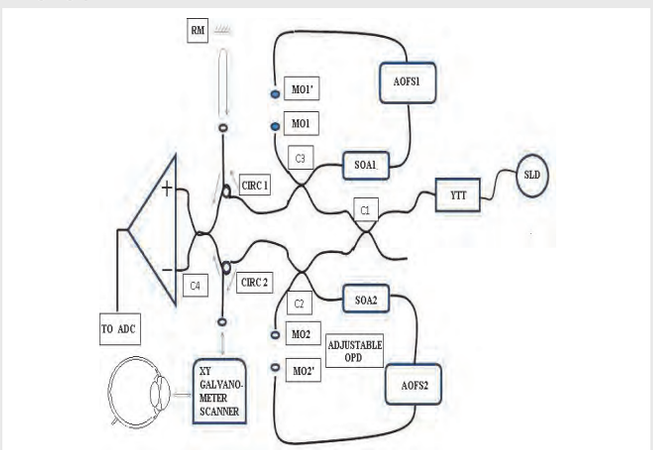

Fig. 1. Layout of multiple paths OCT configuration. Light from a superluminescent diode (SLD) at 1050 nm is amplified by an Ytterbium fibre amplifier (ytt) that contains isolators on the input and output (not shown). This source light is then split by the first single

mode coupler C1 that divides the light into a reference loop (containing SOA1 and AOFS1) and object loop (containing SOA2 and AOFS2) via couplers C2 and C3. The outputs from each loop are sent to the eye and a reference mirror (RM) via fibre optic circulators (CIRC1, CIRC2) and combined at the 50/50 coupler C4. The analogue to digital circuit (ADC) records the signal in synchronism with the signals driving the XY-transversal scanners. For each frame stored, multiple frames are generated, a frame for each spectral window corresponding to a multiple of ΔF.

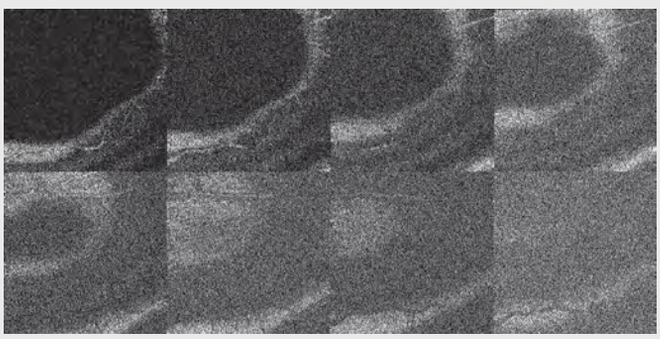

Figure 2. 8 *eF*-OCT images from retina, obtained in the time for one frame, of 0.5 s.Different structures are visualised in each frame.

Multiple planes *ef*-OCT images are captured, all with pixel to pixel correspondence, as shown in fig. 2. The time for each pixel captured is 2 microseconds. The separation between successive *ef*-OCT images is adjustable and for the purposes of the demonstration was set at 75 microns (in air). Due to multiple passes through the limited bandwidth SOAs, and the limited bandwidth of the SLD source used, the axial resolution of each channel was between 30 and 50 microns.

Conclusions

This is the first use of multiple recirculating paths in an ophthalmic OCT system. We are working on improving the efficiency of light in the higher roundtrip orders. This method is scalable to at least 0.2 microseconds pixel rate which could potentially provide images of 250 x 250 pixel images at 80 fps (using faster XY-scanners and without taking into account SNR considerations). The simultaneous capture feature of this type of imaging may be useful for differential measurements in the eye.

Acknowledgment

Acknowledgement: J. Rogers and A. Podoleanu acknowledge the support of the Engineering and Physical Sciences Research Council of the UK, grant EP/H004963/1. A. Podoleanu also acknowledges the support of the European Research Council, grant 249889.

References

[1] Liviu Neagu, Adrian Bradu, Lisha Ma, James W. Bloor, and Adrian Gh. Podoleanu, Optics Letters, (Vol. 35, No. 13, 2296-2298, 2010).

[5695]

17:30-17:45 STUDENT PRESENTATION

Light focusing by photoreceptor cell nuclei

Z. Błaszczak[1], M. Kreysing[1,2], J. Guck[1,3]; [1]Department of Physics, Cavendish Laboratory, University of Cambridge, J.J. Thompson Avenue, Cambridge, CB2 0HE (GB); [2]Systems Biophysics, Ludwig-Maximilians-Universität München, Amalienstr. 54, D-80799, München (DE); [3]Biotechnoglogy Center, Technische Unviersität Dresden, Tatzberg 47/49, 01307, Dresden (DE).

Email: zb225@cam.ac.uk

Summary

Photoreceptor cell nuclei in the retina show species specific chromatin distributions. Specifically, nocturnal animals invert the conventional nuclear architecture in their rods. We show experimentally and through computer simulations that this difference in nuclear architecture has a profound effect on the light transmission properties of the nuclei.

Introduction

Evolutionary pressure has resulted in a vertebrate retina that is inverted [1]. This seems to be an unfortunate design allowing incident light to become scattered and scrambled before it reaches the photoreceptors. But, surprisingly, some of the cells making up the retina have been suggested to also double as optical elements. Radial glial cells and photoreceptor outer segments, for example, have waveguiding properties which allow light propagation with reduced loss due to scatter [2,3]. Here we present a new example of a retinal optical element that can be found in nocturnal animals.

Rods of nocturnal animals have a nuclear architecture that is strikingly different to the architecture found in almost all eukaryotic cells. As was shown in [4] the chromatin distribution inside rod nuclei is different in nocturnal and diurnal animals. For nocturnal animals, the lightly packed euchromatin forms a shell around a core made of heterochromatin; this is an inversion of the conventionall pattern of euchromatin in the centre and heterochromatin on the outside of the nucleus.

Euchromatin and heterochromatin have different densities of DNA and proteins and hence different refractive indices. Since the nuclei do not have any absorbing pigments, it is their refractive index that determines how light interacts with the nucleus. Thus it is reasonable to suspect that the inversion of the chromatin distribution leads to a change in the optical properties of the nucleus. We investigate this idea by using computer simulations and wide field microscopy to look at the near field light distribution for single rod nuclei of mice, rabbits (nocturnal animals) and pigs (diurnal animals).

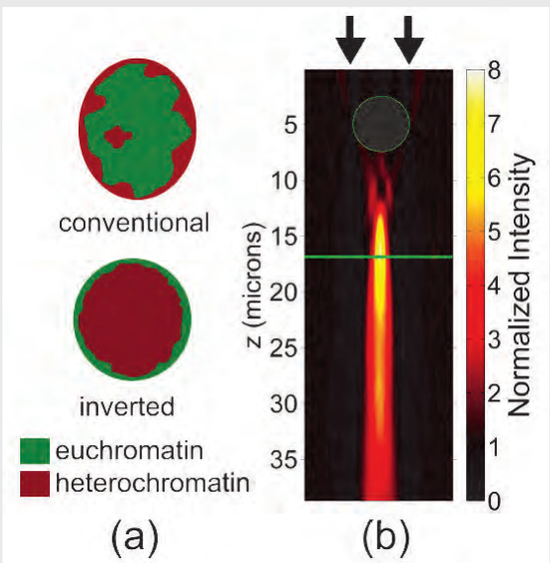

Fig.1: (a) Schematic drawing of the nuclear architecture of inverted and conventional nuclei. (b) XZ reconstruction of the light field around a mouse nucleus. Green circle indicates the nucleus position and has diameter of 5 μm.

Results and Discussion

Finite difference time domain (FDTD) simulations based on interferometric phase measurements and core-shell models of the rod nuclei predicted a lens-like behaviour of the inverted nuclei and a diffraction-like light scattering from the conventional nuclei [4, 5].

These predictions have now been confirmed experimentally using a simple and novel method of capturing light field distributions of micron-sized objects. The method uses wide field microscopy and optical scanning in the axial direction to create a three dimensional intensity map of the light propagating through a sample. Cross sectional reconstructions also allowed determining the effective focal length of the nuclei as well as a simple way of visually comparing simulation results to experiments.

Inverted nuclei were found to act like converging lenses able to effectively focus light and reduce lateral scatter. Conventional nuclei showed a reduced focusing ability, with an effective focal length twice that of inverted nuclei and a near field light distribution more reminiscent of diffraction from a slit.

The evolutionary advantage of a focusing nucleus becomes clear when one considers the nuclei as part of the outer nuclear layer (ONL) which in nocturnal animals can be up to 10 nuclei thick. Our simulations demonstrate that an ONL filled with inverted nuclei shows considerably less light scatter and mixing of light between the columns than an ONL made up of conventional nuclei.

Room: Clinton Auditorium

Results and Discussion
Finite difference time domain (FDTD) simulations based on interefe-rometric phase measurements and core-shell models of the rod nuclei predicted a lens-like behaviour of the inverted nuclei and a diffrac-tion-like light scattering from the conventional nuclei [4, 5].
These predictions have now been confirmed experimentally using a simple and novel method of capturing light field distributions of micron-sized objects. The method uses wide field microscopy and optical scanning in the axial direction to create a three dimensio-nal intensity map of the light propagating through a sample. Cross sectional reconstructions also allo-wed determining the ef-fective focal length of the nuclei as well as a simple way of visually comparing simulation results to expe-riments.

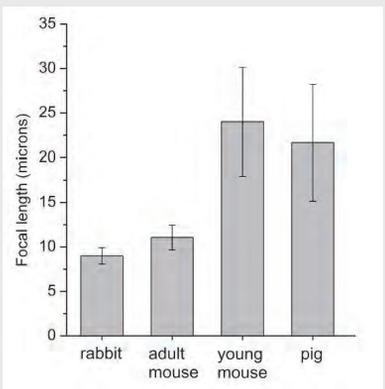

Fig. 2: Graph showing difference in the effective focal lengths of rod nuclei of three species.

Inverted nuclei were found to act like converging lenses able to ef-fectively focus light and reduce lateral scatter. Conventional nuclei showed a reduced focusing ability, with an effective focal length twice that of inverted nuclei and a near field light distribution more reminiscent of diffraction from a slit.
The evolutionary advantage of a focusing nucleus becomes clear when one considers the nuclei as part of the outer nuclear layer (ONL) which in nocturnal animals can be up to 10 nuclei thick. Our simulations demonstrate that an ONL filled with inverted nuclei shows considerably less light scatter and mixing of light between the co-lumns than an ONL made up of conventional nuclei.

Conclusion
We looked at the optical consequences of an inverted nuclear archi-tecture of rod cells as is observed in nocturnal animals. Computer simulations and experiments agree that the inversion results in a new optical element inside the retina enhancing light propagation through the outer nuclear layer.

References
[1] Lamb, T. D., Collin, S. P., and Pugh, E. N. Nature Reviews Neuros-cience 8, 960–76 December (2007).
[2] Franze, K., Grosche, J., Skatchkov, S. N., Schinkinger, S., Foja, C., Schild, D., Uck-ermann, O., Travis, K., Reichenbach, A., and Guck, J. PNAS 104(20), 8287–92 May (2007).
[3] Enoch, J. M. J. Opt. Soc. Am. 53, 71–85 (1963).
[4] Solovei, I., Kreysing, M., Lanctˆot, C., K¨osem, S., Peichl, L., Cre-mer, T., Guck, J., and Joffe, B. Cell 137, 356–368 April (2009).
[5] Kreysing, M., Boyde, L., Guck, J., and Chalut, K. Optics Letters 24(15), 2639–41 August (2010).

[5670]

17:45-18:00 STUDENT PRESENTATION

Estimation of the ocular point spread function by retina modeling

N. Meitav, E.N. Ribak; Department of Physics, Technion – Israel Institute of Technology, Haifa 32000 (IL).
Email: nizanm@tx.technion.ac.il

Summary
Retinal imaging often suffers from blurring aberrations. With knowl-edge of the blurring point spread function (PSF), better images can be reconstructed by deconvolution techniques. We demonstrate a method to enhance the contrast of retinal cells by estimating the ocular PSF. This is done by finding the cells' positions and their inten-sity distribution, and using these as a model for the image.

Introduction
Ocular aberrations in the eye can be corrected, among other meth-ods, by adaptive optics. In addition to this major improvement, re-duction of the blurring is often achieved by image deconvolution methods. The instantaneous PSF can be estimated from the wave front measurement. When the PSF is immeasurable, the method of choice is blind deconvolution: an initial conjecture of the PSF is im-proved by constraint-based algorithms, as well as the reconstructed image [1,2]. However, these methods are often easily biased by the initial guess, which may lead into poor image reconstruction.
In this work a method to estimate the PSF out of cells in the retinal image is demonstrated. This is achieved by taking advantage of our knowledge of the main retinal feature: it is made of photoreceptors (except for the occasional blood vessel).

Discussion
The cells' model is constructed by finding the cells' positions in the image and replacing each such cell by a circular disc. The discs di-ameter is determined by the half-height width of their averaged radial intensity profile, and the intensity of each disc is determined from the radial average of each cell. The cells' model is then used as the intensity distribution of the object, in order to estimate the ocular point spread function. Figure 1(a) presents a part of an input image taken without adaptive optics correction, but after resolution en-hancement by weighted shift-and-add [3], and its corresponding PSF estimation (Fig. 1(b)). We used the estimated PSF as the degrada-tion element in a minimum mean square error filtering (Wiener filter). Figure 1(c) and Fig. 1(d) show the reconstructed image and the com-parison of the power spectra of both images. In the magnified re-constructed image we see cells of two sizes, probably cones and rods, although the smaller cells are almost irresolvable. We marked with an arrow a structure of a big cell surrounded by these smaller cells. This structure is compatible with the rods-cones photoreceptors arrangement in the corresponding retinal layer [4,5].

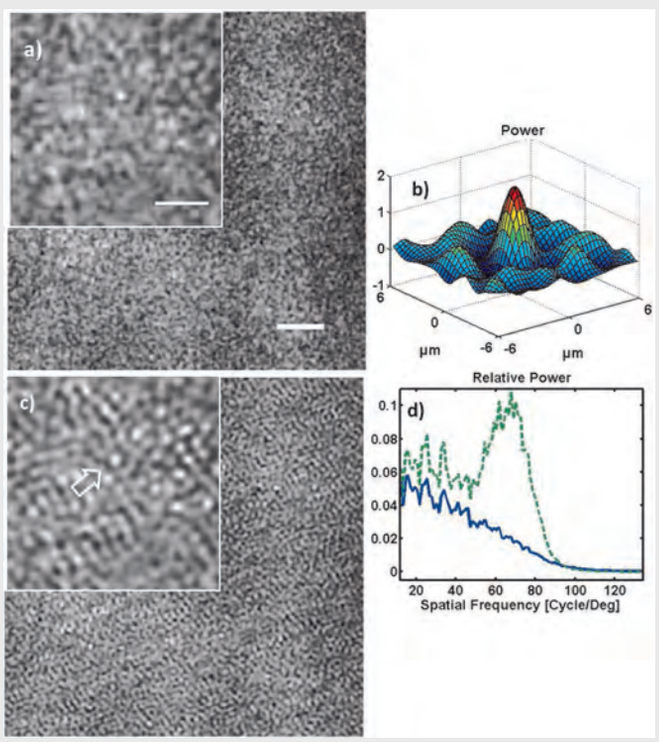

Fig. 1.
PSF estimation process and Wiener image reconstruction. Top row: section of input image and estimated PSF. Bottom row: reconstructed image and power spectra of the image (solid) and the reconstruction (dashed). Scale bars, 30 μm and 15μm for the large and small fields of view (insets).

Conclusions
We present a method to estimate the point spread function of a retinal image. By using the spatial and intensity distribution of cells in retinal layer, a model of the image can be constructed and the PSF can be estimated. In the absence of a measured PSF in these areas,

the estimated PSF can be used to enhance the visibility of cells. Since this method is based on identification of cells, the PSF estimation is expected to be better when using more resolved images as an input.

References

[1] G. R. Ayers and J.C. Dainty, "Iterative blind deconvolution method and its applications", *Opt. Letters* **13**, 547-549 (1988)

[2] L. Blanco and L. M. Mugnier, "Marginal blind deconvolution of adaptive optics retinal images", *Opt. Express* **19**, 23227-23239 (2011).

[3] N. Meitav and E. N. Ribak, "Improving retinal image resolution with iterative weighted shift-and-add", *J. Opt. Soc. Am. A* **28**, 1395-1402 (2011).

[4] N. Doble, et al., "In vivo imaging of the human rod photoreceptor mosaic", *Opt. Lett.* **36**, 31-33 (2011).

[5] A. Dubra, et al., "Noninvasive imaging of the human rod photoreceptor mosaic using a confocal adaptive optics scanning ophthalmoscope", *Biomedical Opt. Express* **2**, 1864-1876 (2011).

[5733]

18:00-18:30

Discussion: Ideal adaptive optics for imaging and analysis of the eye

Discussion leader:

S.A. Burns, Indiana University, School of Optometry (US)

NOTES

NOTES

Room: Clinton Auditorium

09:00-10:30
VISUAL ACUITY, ADAPTATION, AND THE STILES-CRAWFORD EFFECT
Session Chair: R. Blendowske, Hochschule Darmstadt (DE)

09:00-09:30 INVITED TALK

Visual hyperacuity and optical superresolution

G. Westheimer; Division of Neurobiology, 144 Life Sciences Addition University of California, Berkeley, CA 94720-3200 (US).
Email: gwestheimer@berkeley.edu

Once it is realized that some spatial visual thresholds, such as those for vernier alignment, can be a small fraction of the classical Rayleigh resolution limit, the optical and information-theoretical consequences have to be faced. Transferring discussion into the spatial-frequency domain, in which the diffraction limit is embodied in the cut-off frequency, makes it clear that no physical principles are violated. Neither are any of the modern practices of *optical* or *diffractive superresolution* utilized, which employ clever stratagems to shift high-frequency target components into the passband of an imaging device and hence require sophisticated procedures for object reconstitution. On the other hand, the discipline of *geometrical superresolution*, seeking to overcome barriers to image-information retrieval imposed by the structure of the detecting apparatus, shares some ground with the task of understanding the processes involved in hyperacuity responses. Categorical differences between the physical/engineering and the neural/perceptual modes of approach merit recognition.

[5677]

09:30-09:45 STUDENT PRESENTATION

Analysis of the Stiles-Crawford effect of the first kind with tuneable interference gratings

S. Castillo, B. Vohnsen; Advanced Optical Imaging Group, School of Physics, University College Dublin, Dublin 4 (IE).
Email: sara.castillo@ucd.ie

Summary
Holographic phase maps have been generated with a spatial light modulator creating two coherent Maxwellian point sources at the observer's pupil. A reduction in visibility is studied in relation to wavefront slope at the retina for different amplitude distributions of the two sources and linked to the Stiles-Crawford effect of the first kind.

Introduction
In 1933, W. S. Stiles and B. H. Crawford reported on a reduction in visibility when light enters the eye close to the pupil rim [1]. This effect, known as the Stiles-Crawford effect (SCE) of the first kind, is due to waveguiding by the photoreceptor cones and thereby their angular sensitivity [2]. The SCE can be characterized by a Gaussian curve , $\eta = 10^{-\rho_{SCE} r^2}$ where η is the visibility, r is the distance between the pupil point of maximum visibility and the entrance point of the light, and ρ_{SCE} is the characteristic directionality factor.
The goal of this work is to study how this effect changes with the wavefront slope at the retina when two coherent beams are projected onto the retina simultaneously. For that purpose, a range of holographic phase maps were generated on a spatial light modulator (SLM) creating two coherent Maxwellian point sources with a desired intensity distribution at the pupil of the subject; i.e., with an intensity ratio $\alpha = I_2/I_1$ as shown in Fig.1 for any given value of r.

Discussion
A He-Ne laser (633nm) was filtered and expanded to fill the SLM with a homogeneous collimated beam. Holographic phase maps generated with the SLM were used to create two coherent Maxwellian point sources; corresponding to the $\pm 1^{st}$ diffraction orders (0^{th} and further orders were blocked). Each phase map was associated with a specific α value (α_{theory}).
Three observers, with normal vision and dilated pupil, were examined with the setup. A series of phase maps were projected onto the retina by the two Maxwellian points entering the pupil with 4 different α values and 5 pupil distances, r. The experiment was repeat a total of 4 times for each of the subjects. The Maxwellian sources were made rotate (~10Hz) in the pupil plane to reduce the impact of speckles.
The experimental results, as an average for the three subjects, are shown in Fig.1, where the points represent the measurements and curves are the fit for every α value. These curves have been fitted to a Gaussian function $\eta = 10^{-\rho_{eff} r^2}$ similar to the standard SCE but with an effective directionality factor (ρ_{eff}) that is related to ρ_{SCE} [3] and the α parameter as follows:

$$\frac{\rho_{eff}}{\rho_{SCE}} = \frac{1+\alpha-2\sqrt{\alpha}}{1+\alpha+2\sqrt{\alpha}} \quad . \qquad (1)$$

Eq. 1 allows us to estimate the experimentally-realized α parameter (α_{exp}) and compare it with the one used when generating the phase maps (α_{theory}).

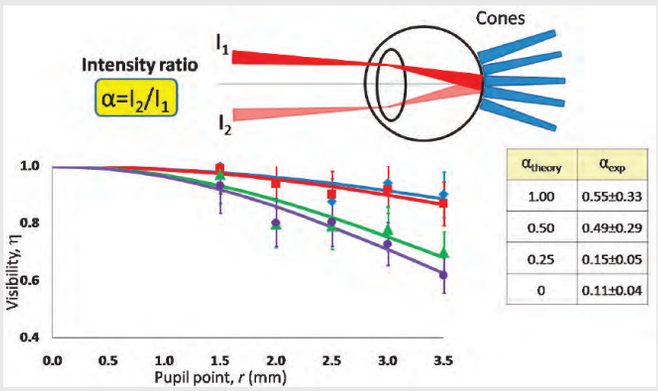

Fig. 1 A schematic drawing representing the human eye and two Maxwellian sources with intensities I_1 and I_2. Below, average of the experimental results for three subjects.

Conclusions
The SCE visibility has been analyzed in a novel way using an SLM to create adjustable (intensity and phase) interference fringes. Some deviations from the numerical analysis were due to the impossibility of completely cancelling I_2 for α=0 as well as fluctuations of α when the phase images were rotated.

Acknowledgements
This research has been realized with financial support from Science Foundation Ireland grant 08/IN.1/B2053 and Stokes award 07/SK/B1239a. Special thanks to Mr. B. Lochocki for his help in realizing this work.

References
[1] W. S. Stiles and B. H. Crawford, "The luminous efficiency of rays entering the eye pupil at different points" Proceedings of the Royal Society of London B: Biological Sciences **112**, 428-250 (1933)
[2] B. Vohnsen, "Photoreceptor waveguides and effective retinal image quality" J. Opt. Soc. Am. A **24**, 597-607 (2007)
[3] B. Vohnsen and D. Rativa, "Absence on an integrated Stiles-Crawford function for coherent light" Journal of Vision **1**, 1-10 (2011)

[5744]

NOTES

09:45-10:00

Impact of Spherical Aberration and Stiles Crawford Apodization on Refractive Error

R. Xu, A. Bradley, L.N. Thibos; Indiana University, School of Optometry, Bloomington, IN 47405 (US).
Email: bradley@indiana.edu

Summary
Using a computational model, we find that, in the presence of spherical aberration, refractive error varies with spatial frequency, and that this effect can be moderated by the inclusion of Stiles Crawford pupil apodization. High spatial frequency image modulation is maximized with a near paraxial focus, while low spatial frequency modulation is more biased toward the pupil periphery and thus affected more by Stiles Crawford apodization.

Introduction
Because human eyes are aberrated, there is no single spherical lens that will correct the refractive error at all parts of the pupil. Most human eyes have significant levels of spherical aberration (Thibos, Ye et al. 1997), which makes the pupil margins up to 3 diopters more myopic than the pupil center. This myopic shift is *not* observed in subjective refractions with increasing pupil size, possibly because the Stiles Crawford Effect (SCE) attenuates the visual impact of marginal rays (e.g. efficacy drops to less than 24% at the edge of an 7 mm diameter pupil). Subjective refractions appear, therefore, to be determined by the central, hyperopic regions of the pupil.
Since clinical refractions generally employ small, high spatial frequency (SF) targets, and experimental studies show that high SF refractions are consistently more hyperopic than low SF refractions (Green and Campbell 1965), it is possible that the central bias of clinical refractions reflects the high spatial frequency content of the small letter test and not the central pupil bias caused by SCE.

Methods and Results
We used computational optics to examine the role of stimulus spatial frequency and SCE apodization on objective refractions (e.g. target vergence (TV) that optimizes either image modulation at a given SF, or width of the point spread function). Figure 1A shows radially-averaged MTFs for a model eye with C_4^0=+0.4 microns of Zernike spherical aberration (SA) and a 7 mm diameter pupil (plus SCE). Each MTF is generated with a different state of focus: TV that minimizes wavefront rms (C_2^0=0), TV that focuses paraxial rays (C_2^0= SQRT(15) C_4^0), and TV that maximized image modulation at 1.7, 5.2, 10 or 30 cpd. The refractive errors measured by these optical criteria vary by about 1 D, and reveal considerable differences in what could be considered the best focused MTF for this model eye. The impact of spatial frequency on measured Rx for a fixed eye is symmetric for the case of + and – 0.4 microns of SA in Figure 1B. In the presence of +SA, the Rx that achieves maximum modulation in the image drifts to hyperopia as SF increases, and the converse is true for negative SA. The 30 cpd Rx is close to a paraxial refraction, and maximum image modulation is achieved with zero C_2^0 at 3.5 cpd. Interestingly, for very low SFs, Rx is myopic in the presence of +SA.
In Figure 2 we systematically vary the level of SA from +0.6 to -0.6 microns and evaluate the impact of SCE. The Rx that maximizes image modulation at 30 cpd closely follows the Seidel Rx (Fig 2A), and is almost unaffected by SCE apodization. However, at 2 cpd, +SA introduces myopia, and this refraction change is attenuated by SCE apodization. We found that the VSOTF refractions (Thibos, Hong et al. 2004) looked very similar to the 30 cpd refractions (compare Fig 2A and B). However, when employing a metric based on width of the PSF (HWHH), we found that +SA introduced significant myopia as can be observed with stigmatoscopy in the unaccommodated eye.

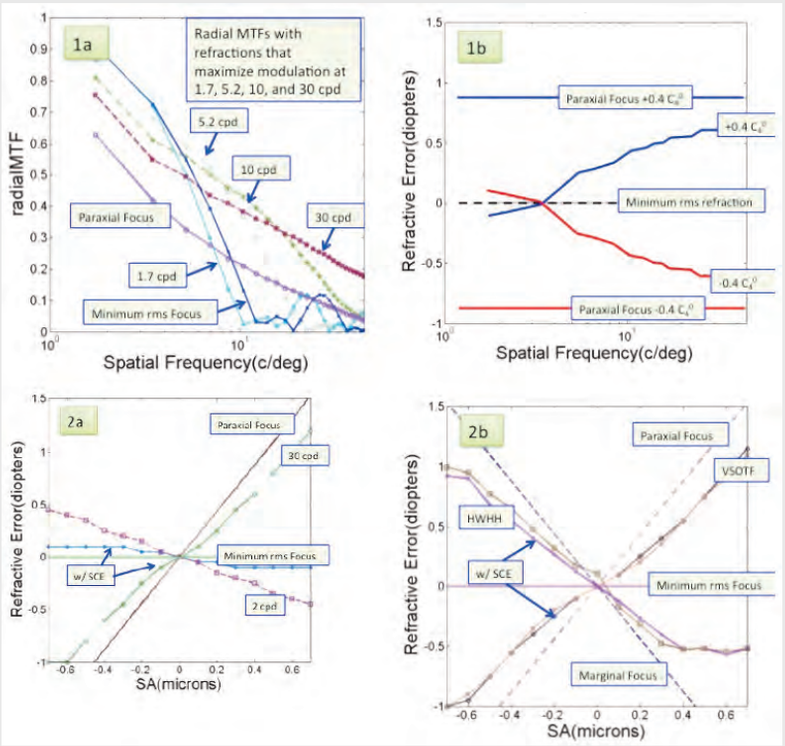

Conclusions
A paraxial bias to the Rx of human eyes is not necessarily due to SCE apodization, but may be caused by a high SF bias in the subjective refraction.

References
[1] Green, D. and F. Campbell (1965). "Effect of focus on the Visual Response to a Simusoidally Modeulated Spatial Stimulus." JOSA ***55***(9): 1154-7.
[2] Thibos, L. N., X. Hong, et al. (2004). "Accuracy and precision of objective refraction from wavefront aberrations." J Vis ***4***(4): 329-51.
[3] Thibos, L. N., M. Ye, et al. (1997). "Spherical aberration of the reduced schematic eye with elliptical refracting surface." Optom Vis Sci ***74***(7): 548-56.

[5765]

10:00-10:15

Refractive error sensing in natural multifocal eyes

R. Navarro[1], V. Fernández-Sánchez[2], N. López-Gil[2]; [1]ICMA, Consejo Superior de Investigaciones Científicas & Universidad de Zaragoza, Zaragoza, 50009 (ES). [2]Grupo de Ciencias de la Visión. Universidad de Murcia. 30100 Murcia (ES).
Email: rafaelnb@unizar.es

Summary
Several examples of eyes with multifocal wavefronts are analyzed by comparing subjective and aberrometric refraction. These multifocal eyes are analyzed using a generalized refractive error sensing method. Our results suggest an important effect on the refraction caused by inhomogeneous pupil transmittance (SCE or vignetting.)

Introduction
In some eyes subjective refraction may differ more than 1 D from objective refraction obtained by aberrometry or autorrefractometry. Usually these eyes present wavefront errors larger than average (in particular coma and/or spherical aberration). Here, our goal was to assess the hypothesis that these important discrepancies in these highly aberrated eyes might be explained by their multifocal properties. In normal eyes, the prevalence of these cases is not high. We identified 8 out of 178 eyes (~5%) from a previous study [1]. However the prevalence in post-surgical eyes is expected to be much higher. The analysis was based on refractive error sensing [2],

Room: Clinton Auditorium

which was generalized to account for multifocal wavefronts, as well as to include the effect of possible irregular and/or non-uniform transmission pupils (Stiles-Crawford effect, etc.).

Discussion

The study was focused on the above mentioned 8 eyes, which showed differences greater than 1 D between subjective and objective equivalent sphere, S_e. S_e was obtained subjectively by standard subjective refraction and also by a more precise custom Badal system. For the objective refraction we used retinoscopy, autorefractometer (Canon T1000) and aberrometer (irx3, Imagine Eyes). In what follows we present one example of bifocal eye, which showed the maximum discrepancy of nearly 2.5 D between subjective and objective refraction. This case is especially interesting, since there are two different possible explanations for such a large difference. The left panel of Fig. 1 shows the distribution of equivalent sphere across a 4.9 mm pupil diameter, showing values ranging from -5 to -9 D. The right panel shows the frequency histogram of that distribution under three hypothetical situations. Red line corresponds to the histogram of the plain aberrometric measure which implicitly assumes a perfect circular pupil with uniform transmission. This histogram shows two peaks separated by more than 2.5 D, which is indicative of a bifocal wavefront. Nevertheless, the peak on the right is dominant as it shows Se = -5.8 D. The blue histogram simulates the effect of pupil vignetting by the upper eye lid. This simulation was included, since this phenomenon was actually observed in this subject. For that purpose we assumed that the area of the pupil above the dashed line was blocked by the eye lid. The resulting (blue) histogram is totally different, now showing a single peak, which is much closer to the value of the subjective refraction (Se=-8.2 D). The green histogram represents a second possible explanation. It was computed by weighting the data points according to the Stiles-Crawford effect (SCE). Here we used standard nominal values, except for the fact that we shifted the SCE peak downwards (its position is indicated by the cross on the left panel.). As expected, the decentered SCE yields an intermediate situation: The two peaks remain but their relative heights changed so that now the dominant peak is the left one (S_e =-8.2 D).

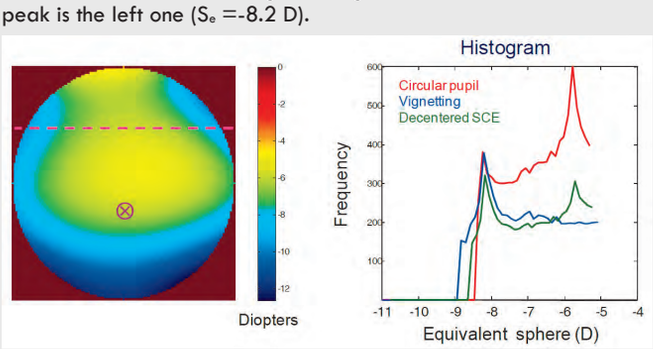

Fig. 1. Distribution of equivalent sphere across the pupil of a bifocal eye (left), and frequency histograms (right) computed assuming a uniform circular pupil (red), vignetting of the upper part (blue) and a decentered SCE (green).

The other cases analyzed so far exhibit two or even three peaks, which means that there are two or three possible refractions. One of these peaks is always close to the subjective refraction. Their relative heights depend on the position of the SCE peak.

Conclusions

A small percentage of normal eyes show bifocal wavefronts, with power differences greater than 1 D (or even 2.5 D in some cases), which are typically associated to high values of HOA. These bifocal eyes often show important discrepancies between subjective and objective refraction. Our results suggest that these discrepancies may appear because aberrometric methods ignore the inhomogeneous effective pupil transmittance. The generalization of refractive error sensing proposed here seems suitable to obtain the refraction in these multifocal eyes. It may be especially relevant for postsurgical eyes, which often present high levels of HOA, and hence may show multifocal wavefronts.

References

[1] N.López-Gil, V.Fernández-Sánchez, L.N.Thibos and R.Montés-Micó."Objective Amplitude of Accommodation Computed from Optical Quality Metrics Applied to Wavefront Outcomes", J.Optom., 2, 223-234(2009).

[2] R. Navarro, "Refractive error sensing from wavefront slopes", J. Vision, 10(13):3, 1–15 (2010).

Supported by grant FIS2011-22496 (Spain)

[5666]

10:15-10:30 STUDENT PRESENTATION

Classification Method to Test Natural Adaptation to the High Order Aberrations of the Eye

L. Sawides[1], C. Dorronsoro[1], P. de Gracia[1], M. Vinas[1], A. Haun[2], E. Peli[2], S. Marcos[1]; [1]Instituto de Optica, CSIC, Madrid (ES); [2]Schepens Eye Research Institute, Massachusetts Eye and Ear, Harvard Medical School, Boston, MA (US).

Email: lucie@io.cfmac.csic.es

Summary

Vision appears to be adapted to the overall amount of blur produced by the ocular high order aberrations (HOA) of an individual's eye. We investigated, using a patterns classification psychophysical paradigm, whether the internal norm of blur is also set to specific orientations of HOA of the eye, under the same overall blur level. We found a lower level of adaptation to individual blur orientation than previously found for overall blur.

Introduction

Several studies have demonstrated short- and long-term aftereffects in the perception of blur after adaptation to sharpened or blurred images, either optically or by computational filtering [1, 2]. Moreover, Adaptive Optics (AO) has proved to be an effective tool for control and manipulation of subject's aberrations and has allowed testing neural adaptation to ocular aberrations in a variety of ways [3-5]. In a recent study we have found that neural adaptation to the wave aberrations characterizing an individual's eye was mostly predicted by the overall amount of natural blur [6]. On the other hand, a prior study had shown that subjects perform better with their natural aberrations than with 90°-rotated versions of the same aberrations [4].

In the current study, we directly investigated subjects' adaptation to their own aberration patterns. We used a psychophysical technique, inspired by the classification image method. An observer's responses to noisy stimulus features over sets of stimuli were inter-correlated, and the observers' perception was estimated from how they weighted the stimulus features to reach their responses [7-8]. In the current experiment, we extracted close matches to subjects' aberration features from the average of the best perceived images of a series of images blurred with the same blur magnitude (Strehl Ratio, SR) but different HOA patterns. The images were generated by convolution with Point Spread Functions (PSFs) estimated from scaled versions of 100 real HOA patterns from a population. The blur of all scaled images in the series matched the SR of each observer. Judgments of perceived blur were measured in four observers with a 2AFC procedure, under full-corrected ocular aberrations using a custom AO system. Five hundred pairs of images, presented in blocks of 100 pairs, were displayed sequentially on a CRT monitor. Both images in the pairs were blurred with differently oriented and randomly selected HOA patterns. Observers judged, in 6 graded responses (according to the level of confidence), the image that appeared in better focus from each pair. The images judged as better focused were identified as Positive, the other as Negative responses. In addition, the graded responses were weighted to perceptually rank the HOA patterns. The PSFs of the positive and negative images were averaged (with the corresponding weights) in order to extract the relevant features (orientation) of the subject's encoded blur. The average PSFs were correlated with the subject's own PSF.

Results

Correlations between the subject's PSF and the PSF corresponding to the 10 highest ranked positive and negative images were estimated,

both on average and individually. Figure 1A shows an example of the 10 best individual positive and negative PSFs, as well as the averaged positive and negative, for subject S4, who showed a more horizontally oriented natural PSF. In general, the negative PSFs were oriented more vertically.
We found (figure 1B) that the correlation of the averaged positive PSF was consistently higher than the averaged negative PSF. This tendency was stronger when the correlations were performed with the individual PSFs. The subject's PSF correlated more with the Positive classified image (r=0.46 on average across the 10 best positive) than with the negative (r=0.34 on average across the 10 higher negatively ranked). The difference between the Positive and Negative classified image (in relation with the subject's PSF) was significant for all subjects (t-test, p<0.02).

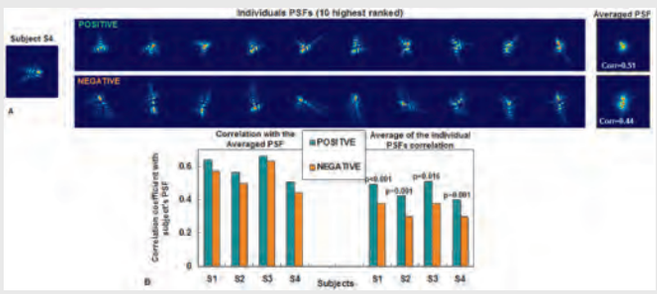

Fig. 1 A: Example of the 10 best individual positive and negative PSFs as well as the averaged positive and negative PSFs for subject S4. B: Correlations between the subject's PSF and the PSF corresponding to the 10 best positive and negative responses considered both individually (right) and on average (left).

Conclusion
While our results did show some bias for in favour of individual blur orientation, subjects reveal relatively high tolerance to blur produced by different orientations in the HOA. The codification of internal blur seems to be driven by the overall level [6] of blur and to a lesser extent by blur orientation.

References
[1] M.A. Webster et al., *Nature Neuroscience,* **5,** 839-40, 2002
[2] K. Pesudovs, *Journal of refractive surgery,* **21,** 144-147, 2005
[3] R. Sabesan & G. Yoon, *IOVS,* **51,** 3835-9, 2010
[4] P. Artal et al., *J Vis*, **4**, 281-7, 2004
[5] L. Sawides et al., *J Vis* **11**, 1-11, 2011
[6] L. Sawides et al., *PLoS One,* **6**, 2011
[7] A.J. Ahumada. *Perception*, **26** (Suppl. 18), 1996
[8] B.L. Beard & A.J. Ahumada, *Proceedings of SPIE, Human Vision & Electronic Imaging*, **3299**, 79-85, 1998

[5692]

10:30-11:00 Coffee break

11:00-13:00
ABERRATIONS AND WAVEFRONT SENSING
Session Chair: V. Nourrit, University of Manchester (GB)

11:00-11:15
Night myopia explanation in terms of different stimuli configuration between day and night
N. López-Gil[1], S.C. Peixoto-de-Matos[2], J.M. González-Méijome[2], L. Thibos[3]; [1]Grupo de Ciencias de la Visión. Universidad de Murcia. 30100 Murcia (ES); [2]Clinical & Experimental Optometry Research Lab. Center of Physics (Optometry) - School of Sciences. University of Minho- Braga (PT); [3]School of Optometry, Indiana University, IN (US).
Email: norberto@um.es

Summary
Subjective refractive error is influenced by stimulus configuration. Stimuli typically encountered at night leave the eye in a more myopic state compared to daytime targets.

Introduction
Night myopia is a tendency for eyes to become near-sighted in dim illumination. Astronomers were the first to describe this phenomenon [1] as a need for correcting lenses of negative power to improve viewing of the stars. The phenomenon gained considerable importance during the Second World War because of the crucial need to visually detect points of light at sea or in the night sky [2].
A variety of visual mechanisms have been invoked by previous investigators to account for night myopia, including under-corrected myopia [3], Purkinje shift, dark focus, spherical aberration (SA), and accommodation [4]. However, little attention has been paid to the nature of the visual stimulus used to elicit the phenomenon. Our study investigated the effect of stimulus configuration and contrast on night myopia.

Methods
We ran two related experiments. In the first one, the equivalent sphere (M) of 17 subject was measured objectively (Gran Seiko autorefractor, WAM5500) and subjectively (custom-made Badal optometer) when the subjects looked at either a standard optometric chart (ETDRS letter chart) or a small white LED on a black background. In the second experiment we compared the objective and subjective M-values using different combinations of luminance for the LED and the background. The experiment was performed in both eyes of a subject with C(4,0)=0.26 μm for 6 mm pupil.

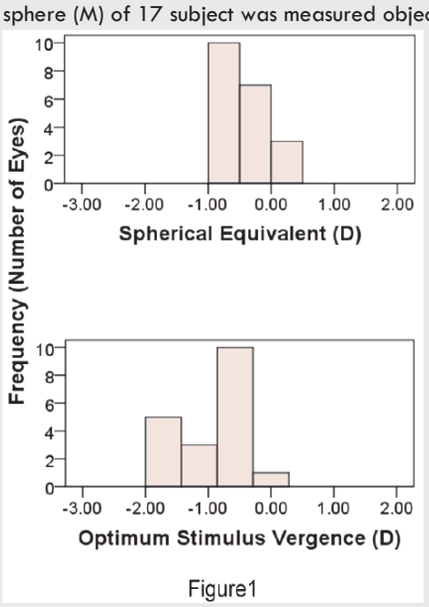

Figure1

Results
The upper part of Fig. 1 shows the histogram of the difference in M value between LED and the letter chart obtained subjectively in the first experiment. The lower part of Fig. 1 shows the histogram of the difference in M obtained objectively. Both histograms show a myopic shift of the M value of the LED with respect the letter chart. A negative correlation with R^2=0.55 was found between the presence of spherical aberration in the eye and the larger difference between the LED and the letter M-value.

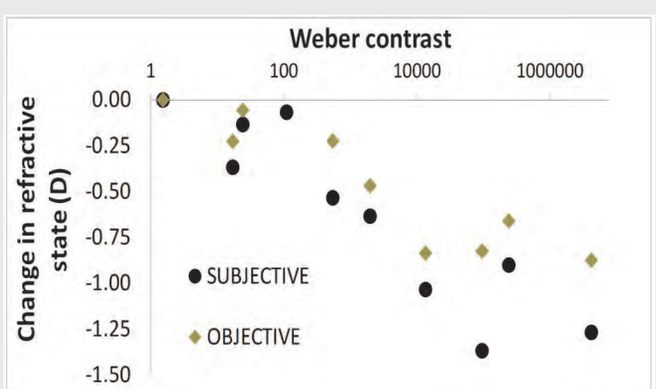

Fig. 2 shows the change in the refractive M-value when the Weber contrast between the LED and its surround increased. Small M-values were found low values of Weber contrast. However, when contrast was larger than 300, the subjective difference was larger than 0.5 D (more myopic for the LED).

Conclusions
Spherical equivalent of the eye was in mean 0.9 D more negative for high contrast objects (as a LED or a start) than for extended

Room: Clinton Auditorium

objects (such us a letter chart) with a lower contrast value. Approximately half of the manifest increase in myopia for the nighttime stimulus (LED) was due to increased accommodation. The remaining half represents changes in refractive state that affect the balancing of higher order aberrations with defocus to optimize retinal image quality.
The results indicate that when contrast between the object and its surround is large enough, the young eye is able to appreciate the spread of the PSF generated by high order aberrations such as spherical aberration. The accommodation of the eye (which minimizes SA value) as well as the balance of SA with negative defocus lead the eye in a myopic state which could be interpreted as a night myopia.

References

[1] Levene JR (1965). Nevil Maskelyne, F.R.S., and the Discovery of Night Myopia. Notes and Records of the Royal Society of London 20, 100-108.
[2] J. M. Otero, L. Plaza & F. Salaverri . Journal of the Optical Society of America, 39, 167-172, 1949.
[3] W. N. Charman. Ophthalmic and Physiological Optics, 16, 474-485, 1996.
[4] R. B. Rabbetts and E. E. A. Mallen. Accommodation and near vision. The inadequate-stimulus myopias.. 'Bennet & Rabbetts' Clinical Visual Optics', ed. Rabbetts RB, (Butterworth Heinemann Elsevier, London, 2007).

[5682]

11:15-11:30

Myopic eye analysis using Hartmann Shack sensor: Evaluating centroid detection methods for Poisson noise dominant spots

A. Vyas; Advanced Optical Imaging Group, University College Dublin, Dublin (IE).
Email: vyas@iiap.res.in

Summary
Poisson noise leads to focal spots with different shapes and sizes in a Hartmann Shack wavefront sensor (HSWS). Through Monte Carlo analysis, we highlight the significance of simple CoG and IWC algorithms over intense IWCoG and MFC algorithms in analysing myopic eye aberrations with dominant Poisson noise.

Introduction
Noise affects the focal spot pattern while using a Hartmann Shack wavefront sensor (HSWS), leading to individual subaperture spots of random shapes and sizes [1, 2]. Monte Carlo analysis was performed to evaluate the performance of various centroid detection methods, namely, (a) centre of gravity (CoG), (b) weighted centre of gravity (WCoG), (c) Iteratively weighted centre of gravity (IWCoG), (d) matched filtered centroiding (MFC), and (e) Intensity Weighted Centroid (IWC) estimation methods [3], while sensing myopic eye aberrations at different levels of Poisson noise. Random wavefronts representative of myopic eye aberrations were statistically generated from real Zernike moment measurement statistics [4]. A detailed analysis is presented for the case of wavefronts corresponding to myopic eye. We conclude that computationally faster IWC and CoG algorithms can be used instead of slower IWCoG and MFC in the case of HSWS spots with dominant Poisson noise. This analysis is useful in optimizing the computations involved.

Discussion
Poisson noise is one of the important intensity dependent noise concern in ocular aberration analysis applications and is often taken into consideration for numerical studies and understanding. The detected HSWS spots have been reported to be having different shapes and sizes [5]. In such a case, it is important to employ a centroid detection algorithm that is more or less stable towards changing spot size and shape for maintaining high wavefront reconstruction accuracy.
The Monte Carlo simulations used to evaluate different centroid detection methods involved four steps: 1. simulation of wavefronts similar to the myopic eye aberrations [4] (wavefronts were simulated statistically using the correlation matrix of 28 Zernike coefficients for myopic eyes of 41 individuals) 2. simulation of displaced HSWS spots 3. reconstruction of wavefronts 4. comparison of simulated wavefronts with reconstructed wavefronts.

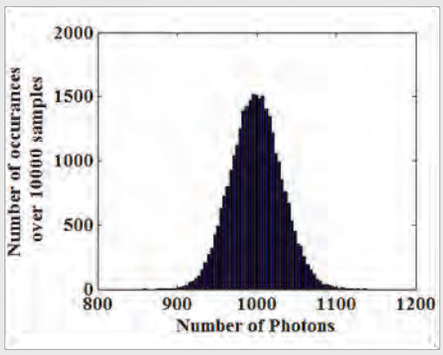

Fig 1.
Histogram of 10000 Poisson random numbers simulated for the case of 1000 photons for one subaperture

We used the zonal reconstruction method for calculation of the wavefronts from the local slope estimates. On an average, the simulated spots occupied 5.5 pixels (measured at 1/e of the maximum intensity). One hundred (10×10) subapertures were used for wavefront sensing. A single subaperture occupies 10×10 pixels on the HSWS detector. Number of samples used in Monte Carlo simulations is 1000. The usefulness of the MFC and IWCoG for aberration analysis of the eye was pointed out on several occasions. Here, we define Noise amplitude as the amplitude of readout noise and background included in the simulations. From Fig. 2, it can be noted that at low noise amplitude and high Poisson noise, CoG and IWC algorithms perform as good as advanced centroiding methods like IWCoG and MFC algorithms. Even at greater noise levels (Noise Amplitude = 500), if the number of photons per subaperture are high enough (above 750 photons/subaperture/frame), IWC and CoG algorithms are enough to detect the location of the HSWS spots (see last plot in Fig. 2). Also, the measured standard deviations in the measurement of wavefront reconstruction accuracy for CoG, IWC, MFC and IWCoG are 0.0687, 0.0627, 0.0591 and 0.0609 respectively for the case where the Noise Amplitude is 500 and number of photons per subaperture per frame is 1000. Since the deviation for CoG and IWC is very small, they can be safely used for centroiding in this case.

Conclusions
In Poisson dominant noise case, it is computationally efficient to use CoG and IWC algorithms which are simpler compared to MFC and IWCoG algorithms. The wavefront reconstruction accuracy is high enough in case of IWC and CoG algorithms at low background noise independent of the number of photons per subapertures per frame.

References

[1] Vyas A, Ellerbroek B, Roopashree M. B, Andersen D. R, and Prasad B. R, "Evaluation of the performance of centroiding algorithms with varying spot size: case of WFS calibration for the TMT NFIRAOS", OSA Technical Digest, paper ATuA1.
[2] Vyas, A., Roopashree, M.B., Prasad, B.R., "Performance of Centroiding Algorithms at Low Light Level Conditions in Adaptive Optics," Advances in Recent Technologies in Communication and Computing, 2009. ARTCom '09. International Conference on, vol., no., pp.366-369, 27-28 Oct. 2009.
[3] Akondi Vyas, M. B. Roopashree and B. Raghavendra Prasad, "Advanced Methods for Improving the Efficiency of a Shack Hartmann Wavefront Sensor", in Topics in Adaptive Optics, Robert K. Tyson (Ed.), InTech, 2012.
[4] J. Schwiegerling. "Statistical Generation of Normal and Post-refractive Surgery Wavefronts," Clin. Exp. Optom. 92, 223-226 (2009).
[5] Pedro M. Prieto, Fernando Vargas-Martín, Stefan Goelz, and Pablo Artal, "Analysis of the performance of the Hartmann–Shack sensor in the human eye." J. Opt. Soc. Am. A 2000; 17: 1388-1398.

[5683]

11:30-11:45

Optimized Microlens-Array Geometry for Hartmann-Shack Wavefront Sensor

O.G. Oliveira[1], D.W. de Lima Monteiro[2], R.F.O. Costa[2] ; [1]Medipha-cos Ltd., R&D Department, Av. Cristovam Chiaradia, 777 Buritis, Belo Horizonte/Minas Gerais, 30575-815 (BR); [2]Universidade Federal de Minas Gerais, OptMAlab, DEE/UFMG, Av. Antonio Carlos, 6627 Pampulha, BeloHorizonte/Minas Gerais, 31270-010 (BR).
Email: otavio@otaviogomes.com

Summary
This work presents the fabrication and test of a microlens array for Hartmann-Shack wavefront sensor, which was optimized, in terms of its geometry, to be applied to the ophthalmic context. Results demonstrate that arrays with fewer suitably located microlenses can yield reconstruction errors as small as regular arrays.

Introduction
The Hartmann-Shack (H-S) wavefront sensor is a core component of major aberrometers, used in the assessment of the visual quality of the eye, academic research and clinical diagnosis. The microlens array is an important element in the H-S sensor, responsible for sampling the aberrated wavefront into light spots on the focal plane. The position of each light spot relates to the average tilt of the wavefront over the respective microlens. These spot-position coordinates are then used in the modal reconstruction to approximate the wavefront topology with a combination of orthogonal basis functions, such as Zernike polynomials. The wavefront reconstruction error describes the deviation of the reconstructed wavefront from the reference one.
Soloviev and Vdovin [1] have discussed the positions of microlenses in the array influence the reconstruction error of the Hartmann-Shack sensor. They demonstrated that random arrays could generate smaller reconstruction errors than regular arrays.
Based on this work, Oliveira and De Lima Monteiro [2] proposed a numerical optimization method that uses genetic algorithm to find the position of the microlenses in the array that minimizes the reconstruction error. The numerical optimization was carried out for an aberration statistics containing 20 Zernike terms, which is presented by Porter *et al.* [3]. The authors demonstrated that optimized arrays with 10 and 16 microlenses could yield reconstruction errors as small as those generated by rectangular 25- and 36-microlens array.
In the present work, the optimized 10- and 16-microlens arrays and the rectangular 16- and 36-microlens arrays are fabricated and tested with an aberration from the used statistics. Then, the arrays are compared to a hexagonal 127-microlens array, which is commercially available.

Discussion
Llorent *et al.* [4] emphasized the importance of specifying an optimal microlens-array geometry to be used in ophthalmology. They stated that besides determining an optimal microlens-array geometry for a specified number of microlenses, it is also desirable to determine arrays with a smaller number of microlenses, preserving the reconstruction error magnitude. With the optimization procedure described in [2], it was possible to find such arrays with smaller number of microlenses, as it was the case for the 10- and 16-microlens optimized arrays.

Fig. 1 Molds produced in silicon.

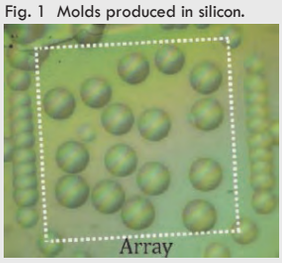

Fig. 2 16-microlens optimized array.

Four arrays were fabricated: optimized 10- and 16-microlens arrays and rectangular 16- and 36- microlens arrays. The fabrication consisted in two basic steps: production of molds and replication. In the first step, the molds were produced in silicon by anisotropic KOH etching. The arrays were designed in order to be inscribed in a 6mm-diameter, circular light-beam and the microlenses had a diameter of 530µm. Fig. 1 shows a picture of the produced molds. In the second step, the molds were replicated in a photopolymer (NOA 61). The liquid polymer was placed on top of the molds and cured under ultraviolet light. Then, it was detached from the molds. Fig. 2 shows a picture of the final result for the 16-microlens optimized array.
An optical setup was constructed to measure optical aberrations introduced by transparent media using Hartmann-Shack method. Preliminary tests were performed with an arbitrarily generated aberration, which was produced by curing a drop of the photopolymer on top of a cover glass. The fabricated arrays were tested and compared with the results generated by a commercial 127-microlens, hexagonal array, adopted as reference. The results corroborated with the predicted numerical ones [2]. In particular, the optimized 16-microlens array and the reference presented results significantly correlated, which was assessed by Pearson`s correlation coefficient.
In the final version of this work, it will be presented results on the fabrication and test of an aberration from Porter`s statistics, using the technique proposed by De Lima Monteiro *et al.* [5]. This aberration will be tested with both the optimized and rectangular arrays.

Conclusion
The obtained results are very encouraging as regards application of optimized microlens arrays in systems where the wavefront statistics are known. The optimization of the microlens array for a given aberration statistics, such as that for ophthalmology, may produce benefits such as reduction in the wavefront reconstruction error and processing time; the last favors real-time wavefront-measurement systems.

References
[1] O. SOLOVIEV, G. VDOVIN, Optics Express, **13,** 9570-9584, 2005.
[2] O. G. OLIVEIRA, D. W. DE LIMA MONTEIRO, Opt Laser Eng, **49,** 521-525, 2011.
[3] J. PORTER *et al.*, JOSA A, **18,** 1793-1803, 2001.
[4] L. LLORENTE *et al.*, JOSA A, **24**, 2783-2796, 2007.
[5] D. W. DE LIMA MONTEIRO, *et al.*, Optics Express, **11**, 2244-2252, 2003.

[5671]

11:45-12:00

A signal-to-noise ratio for the study of the mean squared wavefront estimation error in eye aberrometry

E. Pailos[1,2], J. Arines[1], S. Bara[1]; [1]Universidade de Santiago de Compostela, Area de Optica, Facultade de Optica e Optometria, Santiago de Compostela, 15782, Galicia (ES); [2]National University of Ireland Galway, Applied Optics Group, School of Physics, Galway (IE).
Email: salva.bara@usc.es

Summary
We propose a definition of the signal-to-noise ratio of a slope wavefront sensor in ocular aberrometry. This magnitude allows us to express the noise propagation term of the estimation error in more useful units. We evaluate the estimation error for several SNR, a given sensor configuration, and a statistical model of the aberrations.

Introduction
The mean squared estimation error σ_{err}^2 is an useful metric in wavefront sensing, as it allows the optimisation of the parameters of both the sensor and the estimator (e. g., the number of subpupils of a slope sensor or the number of retrieved modes). This magnitude is the squared difference between the actual and the estimated wavefronts, averaged over the whole pupil and over the realizations of the wavefront.
Let $\mathbf{a}$, $\hat{\mathbf{a}}$ be the vectors of coefficients of the actual and estimated wavefronts. With some assumptions (an orthonormal basis, uncorrelated signal $\boldsymbol{\mu}$ and noise $\boldsymbol{\nu}$ vectors of a slope wavefront sensor, zero-

Room: Clinton Auditorium

mean noise whose components have the same variance σ_v^2 at all subpupils and are uncorrelated, a linear modal estimator) [1, 2]:

$$\sigma_{err}^2 = \text{trace}\left[(\mathbf{I}-\mathbf{RA})\mathbf{C_a}(\mathbf{I}-\mathbf{RA})^T\right] + \sum_{i=M+1}^{M'}\langle a_i^2\rangle + \sigma_v^2\,\text{trace}\left[\mathbf{RR}^T\right] \quad (1)$$

Here $\mathbf{Ca}$ is the correlation matrix of the actual coefficients, <> is an ensemble average, $\mathbf{A}$ is the sensor matrix, $\mathbf{R}$ is the estimation matrix, $\mathbf{I}$ is a M x M' identity matrix, M' is the number of modes of the true wavefront (formally ∞), and M the number of estimated modes. According to Eq. (1), σ_{err}^2 is the sum of a term due to the bias in the M estimated modes, a term equal to the error contribution of the non -estimated modes (truncation error), and a term stemming from the noise propagation.

In principle, it is required to assign values to σ_v^2 in order to compute σ_{err}^2. A better approach is to express σ_v^2 in terms of the signal-to-noise ratio of the sensor (SNR). We define this magnitude as SNR $=\Sigma_\mu^2/\sigma_v^2$, where Σ_μ^2 is the 'sensor signal'. A suitable choice for $\Sigma_\mu^2$is to average the squared noiseless measurements μ_s^2 over the K wavefront realizations, the two $\{x, y\}$ slope directions, and the N subpupils:

$$\Sigma_\mu^2 = \frac{1}{2N}\frac{1}{K}\sum_{s=1}^{2N}\sum_{k=1}^{K}\mu_s^2(k) = \frac{1}{2N}\text{trace}\left[\langle\boldsymbol{\mu}\boldsymbol{\mu}^T\rangle\right] = \frac{1}{2N}\text{trace}\left[\mathbf{AC_aA}^T\right] \quad (2)$$

In Eq. (2) we use that $\boldsymbol{\mu} = \mathbf{Aa}$. The noise propagation term of σ_{err}^2 can be easily expressed as a function of the intuitive and physically meaningful SNR just defined.

Discussion

To evaluate σ_{err}^2 we need to know the actual $\mathbf{Ca}$ matrix. The experimental matrices $\mathbf{Ca}$ available are affected by a bias arising from modal coupling and noise propagation [3]. In addition, they only provide information for a limited number M of estimated modes, whereas the accurate computation of σ_{err}^2 demands the inclusion of higher order correlations. To overcome these problems, we built a model for $\mathbf{Ca}$ assuming: (a) an exponential decay for the variances of each Zernike radial order n [4] and (b) several degrees of cross-correlation of the Zernike coefficients.

We computed σ_{err}^2 for a Hartmann-Shack sensor with different SNR and 145 square microlenses of side 0.133 (in pupil radius units). $\mathbf{R}$ was the least-squares matrix, built with a sensor model assumed to be correct. Figure 1 plots σ_{err}^2 and its three terms vs. the maximum estimated radial order, n_{max}, for a $\mathbf{Ca}$ matrix with uncorrelated coefficients and SNR =20. The truncation error dominates for low n_{max}, while the noise propagation dominates for high $n$max. The bias term is of little importance in this case; this result was also obtained for a $\mathbf{Ca}$ matrix with fully cross-correlated elements. There is an optimal number of estimated modes which minimises σ_{err}^2: n_{max} =6 (M =27).

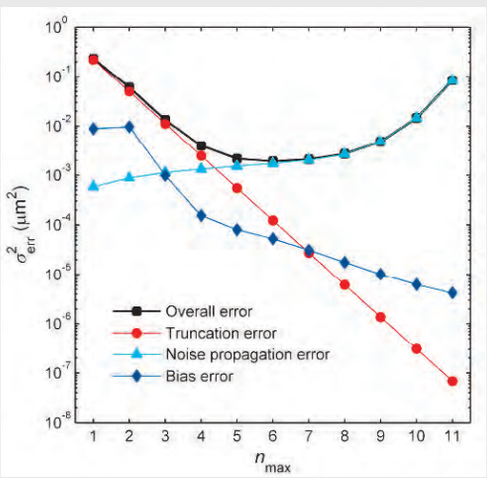

Fig 1. Estimation error σ_{err}^2 and its three terms vs. the maximum estimated radial order for SNR =20

Conclusions

The SNR defined depends on the aberrations statistics, the sensor configuration, and the noise variance. The noise propagation term of the estimation error can be conveniently parametrised by this magnitude. Finally, the computed curves of the estimation error show that, for each SNR and for the aberration statistics assumed, it is possible to find an optimal number of estimated modes.

Work supported by the Spanish MICINN, grant FIS2008-03884. J. Arines acknowledges support from the Isidro Parga Pondal Programme 2009 (Xunta de Galicia) and E. Pailos from Science Foundation Ireland, grant No 07/IN.1/I906.

References

[1] L. Diaz-Santana, G. Walker, and S. X. Bara, *Opt. Expr.*, **13**, 8801, 2005
[2] G. Dai, *J. Opt. Soc. Am. A*, **13**, 1218, 1996
[3] S. Bara, P. Prado, J. Arines, and J. Ares, *Opt. Lett.*, **31**, 2646, 2006
[4] L. N. Thibos, X. Hong, A. Bradley, and X. Cheng, *J. Opt. Soc. Am. A*, **19**, 2329, 2002

[5675]

12:00-12:15

Fixation Quality with a Bessel Beacon in an Adaptive Optics System

E.M. Daly[1], A.J. Lambert[2], J.C. Dainty[1]; [1]Applied Optics, National University of Ireland Galway, Galway(IE); [2]School of Engineering and IT, UNSW@ADFA, Canberra ACT 2600 (AU).
Email: a.lambert@adfa.edu.au

Summary

Active optics may be used to shape the beacon in an adaptive optics (AO) system. It therefore becomes possible to present to the subject a beacon which, because of ist structure, may be easier to fixate upon than the traditional narrow spot.

Introduction

We have previously investigated active shaping of the beacon for use in our ophthalmic AO system [1], and we showed that a Bessel beacon [2] does allow for good closure of the AO loop. When conducting these experiments it was noticed that the Bessel beam was, perhaps, more easy to fixate upon. If this were the case, it might offer some respite for ophthalmic examination of subjects who have limited attention spans or stability issues, such as those suffering from Down's syndrome for example. Before considering such clinical effects, we here examine the quality of fixation for a healthy subject and the effects that may have on system performance.

Discussion

Using the AO system which has the addition of active optics in the beacon creation path as described in Ref [1], we seek to consider the temporal variances of the subject's aberrations. The subject's pupil was dilated and 20s of open loop wavefront measurements were obtained for each trial. The nominal frame rate was 64 Hz with 24 samples across the 6mm pupil. A spatial light modulator (SLM) in the beaconcreation path was used either flat (producing a spot on the subject's retina of ~40μm diameter) or with a phase profile to create a Bessel beacon at the retina. 10 trials were performed with each configuration to allow for averaging. The wavefront was reconstructed using the OSA standard for labeling of Zernikes [3]. Blinks were removed manually from the time series before calculating the power spectral density (PSD) of individual Zernike terms using the Lomb-Scargle periodogram [4,5] over the frequency range 0.05-26 Hz with 500 evenly spaced samples. In Fig 1 we show the PSD of OSA J=1 and 2 tip and tilt terms combined, and J=7 and 8 y and x coma terms combined.

For this initial experiment, the subject's myopia was partially corrected in the wavefront sensing path using a Badal, but the beacon creation suffered without this correction. However, the Bessel beacon observed from the retina, while not perfect, exhibited the immunity to defocus that it possesses. The subject reported the concentric ring pattern associated with the Bessel beam was blurry. The expected

ring pattern is shown, imaged from an artificial eye in Fig 1(a). Subsequent experiments will correct this with a chirp contribution to the SLM in addition to the Bessel phase modulation.
Nevertheless, differences are evident in the PSD derived from the time series aberration data. Examples are shown in Fig1(b), for tip-tilt (J1,2) and coma (J7,8), with flat and Bessel phase on the SLM. Apart from the vertical offset, it appears that the curves differ in slope at lower frequencies between the two beacons. Fitting the ranges (0.05-2 Hz) and (2-26Hz) separately yields the slopes listed in Table 1, indicating less change in the slopes with frequency for the Bessel beacon.

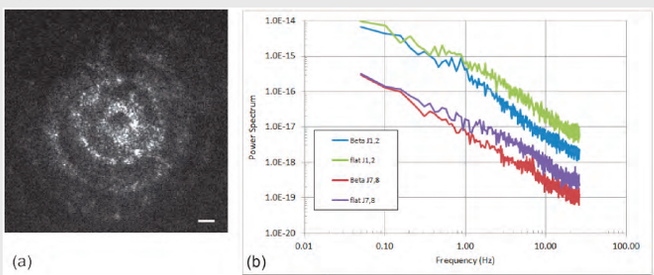

Fig 1. (a) The Bessel beacon (for Beta=0.02 pixels-1) as imaged on the retina of an artificial eye, scale bar = 25 μm. (b) Spectral power on a log-log scale averaged over all runs for the Bessel beacon, versus that generated by having a traditional beacon using a flat SLM, for a human subject.

OSA J	Trad. Low Freq	Bessel Low Freq	Trad. High Freq	Bessel High Freq
1 (Tip)	-1.08	-1.21	-1.56	-1.57
2 (Tilt)	-0.7	-1.17	-1.51	-1.43
7 (Coma-y)	-1.04	-1.44	-1.30	-1.19
8 (Coma-x)	-0.95	-1.18	-1.52	-1.39

Table 1: Slope fitting to the PSD in Fig 1(b) in the low and high frequency ranges. Units (Hz-1).

The difference between these results warrants further experimentation with more subjects, and evaluation of systemic variation. We will present these results and deduce any evidence upholding the premise that the Bessel beacon aids fixation.

Acknowledgements
This work was supported by Science Foundation Ireland grant SFI/07/IN.1/1906, and the Australian Research Council DP110102018. The authors wish to thank Dr. Conor Leahy of NUI Galway for Matlab code for calculation of the PSD.

References

[1] A.J. Lambert, E.M. Daly, E. deLestrange and J.C. Dainty, *Journal of Modern Optics*, **58**, 1716-1728 (2011).
[2] J Davis, J Guertin, D Cottrell, *Applied Optics*, **32**, 6368-6370 (1993).
[3] L. N. Thibos, R. A. Applegate, J. T. Schwiegerling, R.Webb, *Vision Science and Its Applications*, Vol. 35 of Trends in Optics and Photonics Series, V. Lakshminarayanan, ed. (Optical Society of America, 2000), pp. 233-244.
[4] N. R. Lomb, Astrophys. & Space Sci., **39**, 447-462 (1975).
[5] J. D. Scargle, Astrophys. J., **263**, 835-853 (1982).

[5687]

12:15-12:30

Calibration of a commercial anterior segment OCT instrument for accurate corneal topography

D. Siedlecki[1], S. Ortiz[2], S. Marcos[2]; [1] Wroclaw University of Technology, Institute of Physics, Wroclaw, 50370 (PL); 2Consejo Superior de Investigaciones Cientificas, Instituto de Optica, Madrid, 28006 (ES).
Email: Damian.Siedlecki@pwr.wroc.pl

Summary
We implemented successfully a recently introduced [1,2] method for calibration of Optical Coherence Tomography (OCT) setups on a purely commercial OCT instrument. The accuracy of the method was tested on the optical surfaces of spherical shape and a human cornea in vivo.

Introduction
Fan (or field) distortion occurs inherently in OCT as a result of the 2-mirror scanning configuration. In a recent work we have demonstrated the correction of fan distortion in a custom-developed OCT system in laboratory conditions [1,2,3]. Upon correction of fan distortion, topographic measurements of optical surfaces (spherical and aspheric) were obtained within 1% of those produced by non-contact profilometry. Corneal topographies in patients were comparable to those obtained from state-ofthe-art techniques (Placido Disk Videokeratography and Scheimpflug imaging). In the current study, we have implemented a similar method of fan distortion estimation and correction on a commercial OCT instrument (Copernicus HR®, Optopol Technology, a member of Canon Group, Zawiercie, Poland), including its built-in scanning protocols.
Custom algorithms of signal denoising, contrast enhancement and surface shape recognition [1,2,3], written in Matlab, were applied to the cross-sectional OCT images captured with the device. Figure 1a shows an of a cross-section obtained from a flat optical surface (IR filter). A set of those images was used for estimation of the magnitude of the fan distortion, as presented in the Figure 1b.

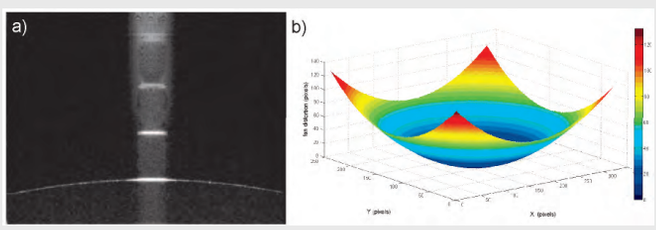

Fig. 1. Cross-section (320x1010 pixels) of a flat optical surface; 240 of such images were used for estimation of the magnitude of 3-D fan distortion of the commercial OCT device.

Subsequently, the estimated fan distortion was used to correct the three dimensional images from spherical surfaces of known radii of curvatures (Figure 2) and a cornea in vivo (Figure 3).

Discussion
Correcting for fan distortion improved by more than 20% the estimation of the surface radii of curvature. The mean deviation from the retrieved shape from the nominal surface is less than the axial resolution of the device (2.5μm). Results of in vivo corneal topography measurements show great improvement in comparison to the topography without correction. The estimated corneal radius of curvature from OCTbased topography is similar to that obtained from standard Placido Disk videotopography obtained in the same eye (8.17 vs 8.18 mm), although the topography maps show some discrepancies, perhaps due to low signal-to-noise ratio, particularly in the periphery.

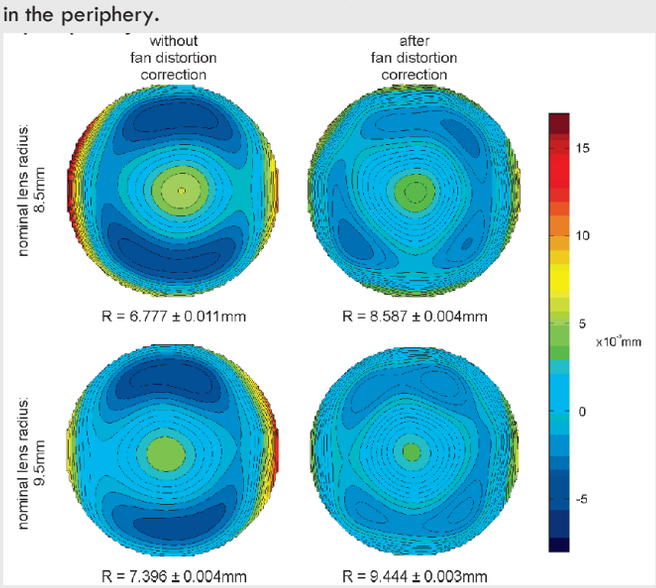

Fig. 2 Estimated topographies of spherical surfaces without and with fan distortion correction

Room: Clinton Auditorium

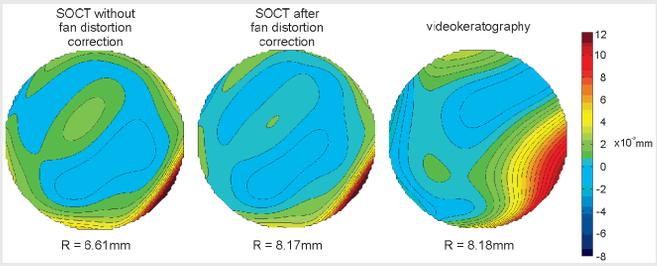

Fig. 3 Estimated corneal topography in vivo without and with fan distortion correction compared to the corneal topography measured by videokeratography

Conclusion

We showed that custom procedures of calibration may be successfully implemented in commercial OCT devices, leading to accurate and quantitative surface topography.

References

[1] S. Ortiz, S.Marcos, D. Siedlecki, C. Dorronsoro, Spanish patent application No P201130685, Priority: 29/04/2011

[2] S. Ortiz, D. Siedlecki, L. Remon, S. Marcos, *Applied Optics*, 48, 6708–6715 2009

[3] S. Ortiz, D. Siedlecki, P. Pérez-Merino, N. Chia, A. de Castro, M. Szkulmowski, M. Wojtkowski, S. Marcos, *Biomedical Optics Express*, 2, 3232-3247 2011

[5761]

12:30-12:45

Shape of the posterior cornea described by Zernike polynomials: influence of anterior corneal shape and central reference point

T. de Jong[1], M.T. Sheehan[2], S.A. Koopmans[1], N.M. Jansonius[1]; [1]Department of Ophthalmology, University Medical Center Groningen, University of Groningen (NL); [2]National University I reland-Galway, Galway (IE).

Email: t.de.jong03@umcg.nl

Summary

When fitting the posterior corneal surface with Zernike polynomials, the central reference point can be the apex of either the anterior or the posterior cornea. We determined (1) the effect of the choice of the central reference point and (2) the correlation between corresponding Zernike coefficients of both corneal surfaces.

Introduction

For optical modeling of the eye it is essential to have a good representation of the corneal shape. This shape is usually described with Zernike polynomials [1]. For fitting Zernike polynomials to the elevation data of the anterior cornea, taking its apex as central reference point seems the most intuitive choice. However when looking at the posterior side of the cornea, one could choose between the apex of either the posterior or the anterior corneal surface. The posterior apex could be a good choice if one is just interested in the posterior corneal shape, while the anterior apex seems a more logical if it comes to optical modelling.

The aim of this study was to determine the effect of the central reference point on the fitting of Zernike polynomials to the elevation map of the posterior cornea as obtained with the Pentacam (Oculus) using standard alignment. The correlation between corresponding Zernike coefficients for the anterior and posterior corneal shape was studied as well. After all, if the Zernike coefficients describing both corneal surfaces are known to be highly correlated, the need to determine the posterior corneal shape separately would diminish.

Methods

Thirty right eyes of 30 healthy subjects were measured with the Pentacam. The subjects had no history of ocular disease or refractive surgery. For the comparison of the reference systems, Zernike polynomials were fitted to the raw height data of the posterior cornea using both the (1) anterior and (2) posterior corneal apex as the origin. The corresponding anterior cornea was fitted as well for determining the correlation. The comparisons were made for the coefficients for defocus (z_2^0), astigmatism (z_2^{-2} and z_2^2), coma (z_3^{-1} and z_3^1) and spherical aberration (z_4^0). All surface fitting was performed with Matlab (v7.10.0 R2010a, Mathworks, Nattick, MA, USA), for Zernike polynomials up to the 8th order (45 terms) over an 8 mm diameter.

Results

Typically the apex of the posterior corneal surface was, considering a plane tangential to the apex itself, displaced by 0.1 mm from the apex of the anterior cornea (range 0.07 to 0.18 mm). The direction of this shift was between 207 and 243 degrees from the apex of the anterior cornea (that is, inferotemporal direction).

The influence of the choice for the central reference point on the Zernike coefficients describing the posterior corneal shape was significant for all Zernike terms, but only relevant for the coma terms ($P<0.001$; Table 1). The correlation between the Zernike coefficients of the anterior corneal surface and their corresponding coefficients for the posterior corneal surface (Table 2) appeared to be independent of the chosen central reference point. For each Zernike polynomial a strong correlation is shown, especially for the defocus term (z_2^0).

	Anterior cornea	Posterior cornea		
Zernike coefficient (n=30 OD)	mean +/- st. dev. (µm)	Anterior apex origin mean +/- st. dev. (µm)	Posterior apex origin mean +/- st. dev. (µm)	Paired difference mean +/- st. dev. (µm)
Defocus (z_2^0)	-313 ± 11.7	-395 ± 18.6	-394 ± 18.7	-0.62 ± 0.85
Astigmatism (z_2^{-2})	+1.00 ± 1.79	+2.22 ± 3.90	+2.38 ± 3.90	-0.17 ± 0.24
Astigmatism (z_2^2)	-3.84 ± 3.56	+13.4 ± 5.91	+13.4 ± 5.91	+0.24 ± 0.23
Coma (z_3^{-1})	-0.15 ± 1.26	+0.65 ± 2.38	-0.39 ± 2.45	+1.03 ± 0.62
Coma (z_3^1)	+1.46 ± 1.18	+1.73 ± 2.40	+2.56 ± 2.18	-0.83 ± 0.42
Spherical (z_4^0)	-4.33 ± 0.91	-8.28 ± 2.63	-8.19 ± 2.60	-0.09 ± 0.11

Table 1: The mean +/- st. dev. values for the coefficients of six Zernike polynomials for the corneal shape of the anterior surface, posterior surface centered on the anterior apex and posterior apex. Also the paired difference between the Zernike coefficients for both central reference points is shown.

Zernike coefficient (n=30 OD)	Anterior apex origin	Posterior apex origin
Defocus (z_2^0)	0.947	0.947
Astigmatism (z_2^{-2})	0.789	0.793
Astigmatism (z_2^2)	0.775	0.774
Coma (z_3^{-1})	0.779	0.718
Coma (z_3^1)	0.781	0.795
Spherical (z_4^0)	0.775	0.769

Table 2: Correlation coefficients between the Zernike coefficients fitted on the anterior cornea and posterior cornea with the anterior apex and posterior apex as central point respectively.

Discussion

A small shift of reference system will lead to relevant changes in some but not all Zernike coefficients that describe the posterior corneal shape. The high correlation of lower order Zernike polynomials was reported earlier [2]. They reported a correlation between the anterior and posterior corneal surface of 0.943, 0.721 and 0.849 for the defocus (z_2^0) and astigmatism (z_2^{-2} and z_2^2) terms respectively, which agrees well with our findings. Furthermore we did not find any significant difference regarding the correlation of Zernike coefficients for the anterior and posterior surfaces when comparing the choice of the fitting origin. The correlation between corresponding Zernike coefficients suggest that, depending on the accuracy needed, measuring the posterior surface of the cornea might be redundant for normal healthy eyes.

References

[1] J. Schweigerling, J.E. Greivenkamp, J.M. Miller, *J Opt Soc Am A*, **Vol 12**, pp 2105-2213, 1995.

[2] D. Mas, J. Espinosa, B. Domenech, J Perez, H Kasprzak and C. Illueca, *Ophthalmic Physiol Opt,* **Vol 29**, pp 219-226, 2009.

[5748]

12:45-13:00 STUDENT PRESENTATION

Look-up table of quadrics applied to corneal topography

J. Espinosa[1,2], A.B. Roig[2], J. Pérez[1,2], D. Mas[1,2], C. Illueca[1,2];
[1]University of Alicante, IUFACyT, San Vicente del Raspeig - Alicante, 03690 (ES); [2]University of Alicante, Dept. Optics, Pharmacology and Anatomy, San Vicente del Raspeig - Alicante, 03690 (ES).
Email: julian.espinosa@ua.es

Summary
We present a new look-up table method to convert acquired corneal data from reflected Placido rings to curvature radii. The technique avoids extrapolating corneal data and overcomes the difficulty with the lack of symmetry of projected rings and provides a better description of the corneal morphology.

Introduction
The information in obtaining a corneal topography using a commercial device usually is hidden, in spite of being of interest for researchers. In previous works [1,2], the authors detailed the algorithms and procedures to obtain the curvature data of cornea. Radial distances from Placido rings were related to the correspondent local curvature radii through a set of calibration curves (look-up table method). If the method was able to distinguish and classify l rings, then lookup tables contained L calibration equations on the form $R = m_l + n_l$, where R are the mean radial distances measured for calibration balls of curvature radius C in the $l = 1, \ldots, L$ different labeled rings. Mean radial distance was computed as an arithmetic mean of distances obtained after transforming from Cartesian to polar coordinates and this averaging introduces quite uncertainty.

Espinosa et al. [1] proposed obtaining a calibration equation, alternatively to that set of calibration curves in [2]. They considered three variables, the independent variables L, corresponding to the ring's label, C, the curvature radius, and R, the radial distance of each ring, which was set as the radius obtained from least square fitting them to a circle. The radial distance of each reflected ring on a surface depends of both the curvature radius of the surface and the ring's label as $R=(a\,l+b)C$. Coefficients a and b could be obtained through least square fitting of computed radial distances. In order to compute the curvature radius $C(x,y)$ at each pixel at a distance $R_{(x,y)}$ from center, and being part of a reflected ring L, we have

$$C(x,y)=\frac{R(x,y)}{(a\,l+b)} \qquad (x,y)\in Ring_l \qquad (1)$$

Discussion
Equation (1) introduces a dependence of radial distance with the ring's label. Moreover, it is a unique calibration equation, alternatively to the set of curves in [2]. However, when we compute both a and b parameters in the calibration process, we do not take into account the indetermination in the radial distance R. This radial distance is obtained from a fitting of Cartesian sampled data to a circle. Therefore, the assignment of a unique radial distance to each ring interpolates data sampled in a Cartesian grid.
The indetermination in the radii of fitted circles depends both on the ring's label and the curvature radius of the theoretical eye used in the calibration. This is an intrinsic inconvenience to the method which comes from the sampling of an image with polar symmetry, the reflected rings, with a Cartesian grid, the CCD array of the camera. Therefore, we reformulate the problem from the beginning. From equation (1), it is clear that the curvature radius is proportional to the radial distance. In order to avoid the above exposed interpolation of data, we look for a calibration equation directly considering all measured data.
If we perform the expansion of

$R = m_l + n_l$, we get $x^2+y^2=m_l^2C^2+2m_ln_lC+n_l^2$,

an expression with terms in a similar way to a quadric equation. Therefore, as an initial general case, we consider that curvature radii and spatial coordinates of captured reflected rings are related following a quadric surface in the Euclidean space which may be compactly written in vector and matrix notation as

where $v_l = \{x_l, y_l, C\}$ are row vectors containing the coordinates of data of each l ring or edge for each calibration surface of curvature radius is the transpose of v_l, D_l are 3x3 matrices, E_l are 3-dimensional row vectors and F_l are scalar constants. Expression (2) provides a calibration equation for each ring as
Curvature radii and (x_l, y_l) coordinates of data for each l ring are least-squares fitting to (3), thus providing a look-up table of quadrics. The method overcomes the interpolation of Cartesian data so it improves the morphological description of corneal surface.

Results
Figure 1 and Table 1 show results for the fitting of ring l=16.

a	40.78 (38.99, 42.57)	***f***	3.01 (2.67, 3.34)
b	40.88 (39.09, 42.68)	***g***	1.10 (0.70, 1.41)
c	-0.08 (-0.13, -0.04)	***h***	-26.16 (-28.04, -24.29)
d	-0.35 (-0.39, -0.31)	***k***	92.43 (85.47, 99.38)
e	-0.11 (-0.14, -0.07)		

Table 1. Parameters and confidence bounds in brackets of the fitting to (5)

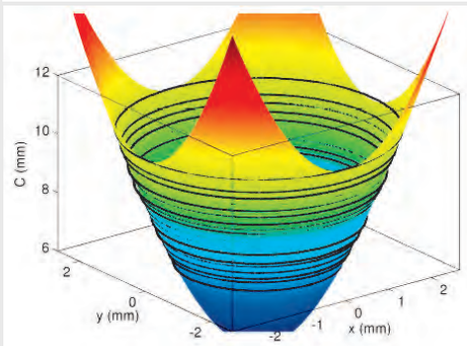

Fig. 1. Data and surface resulting from the fitting

References
[1] J. Espinosa, A.B. Roig, D. Mas, C. Hernández and C. Illueca, *Proc. SPIE Photonics Europe*, 2012.
[2] D. Mas, M.A. Kowalska, J. Espinosa and H. Kasprzak, *J. Mod. Opt.*, **57**, 94-102 2010.

Aknowledgements
Thanks to Spanish Ministerio de Ciencia e Innovación through the project FIS2009-05639-ET and BIA2011-22704, the Generalitat Valenciana through the project PROMETEO/2011/021 and the University of Alicante through the project GRE10-09. A.B. Roig thanks Fundación Cajamurcia the grant "Beca de investigación Cajamurcia 2010"

[5668]

13:00-13:45 Lunch break & Pick-up lunch bags

14:00-18:00 Social Programme

18:30-21:00 Conference Dinner

NOTES

Room: Clinton Auditorium

09:00-10:30
OCULAR SCATTERING MECHANISMS AND ANALYSIS
Session Chair: B. Pierscionek, Kingston University (GB)

09:00-09:30 **Invited talk**

Intraocular scattering - measurement and analysis

G.M. Perez; Laboratorio de Óptica. Universidad de Murcia, 3 0100 (ES)
Email: gperez@um.es

Summary
Intraocular scattering has remained as an elusive phenomenon in terms of objective assessment. A new method allowing direct and accurate measurement of the light scattering in the living human eye will be presented.

Introduction
Light scattering is an inherent consequence to light propagation through media with local variations in the refractive index [1]. In the eye, light propagates through different mediums, from the tear film to the retinal layers, and the magnitude of intraocular scattering will correlate with the overall optical inhomogeneity of the ocular mediums.
Furthermore, when the optical properties of the eye become disruptively modified by ocular diseases, like cataracts [2] or tear film inhomogeneity [3], an appropriate estimation of the intraocular scattering may arise as a useful diagnosis tool to assess the severity of the ocular pathology.
Many different methodologies have been proposed to estimate the amount of scatter in the living human eye, based both in subjective [4] and objective approaches [5]. An accurate characterization of intraocular scattering would improve the description of the eye's optical properties and how do they change in concomitance with ocular diseases. On other hand, and since scattered light is spread all over the retina, there is an interest in terms of the inherent visual degradation induced [6].

Discussion
In that context, a new objective methodology for estimating intraocular scattering will be presented in this talk [7]. The approach consists in projecting on the retinal fundus illuminated disks with angular dimensions ranging from 0 to 9.1 degrees (radius), and then recording the images after reflection and double-pass through the eye's optics. A custom analysis of the apparent radiant intensity at the center of each recorded disk provides with a wide angle point-spread function (Fig.1).
By using different wavelengths in the illumination path of the device, information regarding the chromatic dependence of intraocular scattering is also obtained. Examples of application of the technique in real eyes with different amount of scatter artificially induced will be presented (Fig. 2).

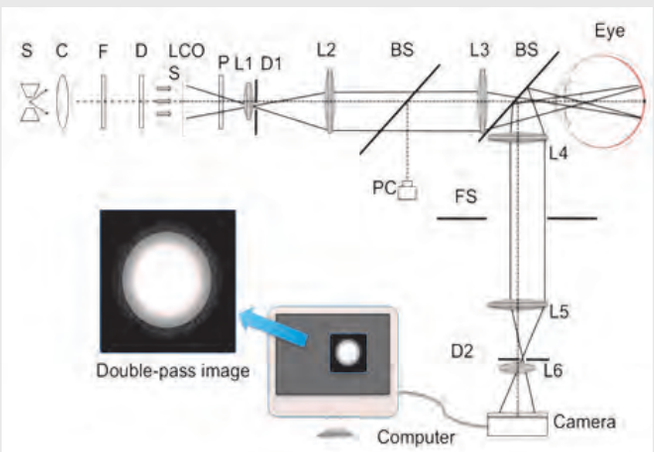

Fig. 1. Experimental setup. S, light source; C, collimating lens; F, green filters; D, diffuser; LCOS, liquid crystal spatial light modulator; P, linear polarizer; L1–L6, lenses; D1 and D2, diaphragms; BS, beam splitters; PC, pupil camera; FS, field stop.

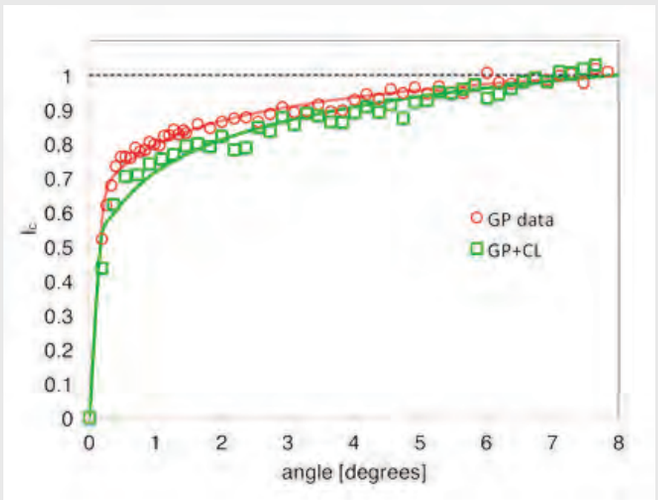

Fig. 2. Experimental data on the radial integral of the PSF for one eye under two experimental conditions: no CL (red symbols) and wearing a CL with moderate scattering.

Conclusions
The new method allows the direct, accurate, and in vivo, measurement of the effect of intraocular scattering. The procedure is sensitive enough to detect differences in the light scatter intensity between normal healthy eyes in vivo and may be a step toward the comprehensive optical evaluation of the optics of the human eye.

References
[1] H. van de Hulst, Light scattering by small particles, New York: Dover , 1981.
[2] P. Artal, A. Benito, G. Perez, E. Alcon, A. De Casas, J. Pujoil and M. J.M., *Plos One,* **vol. 6**, no. 2, 2011.
[3] Benito, G. Perez, S. Mirabet, V. Meritxell, J. Pujol, J. Marin and P. Artal, *Journal of Cataract and Refractive Surgery,* **vol. 37**, no. 8, pp. 1481-7, 2011.
[4] T. van den Berg and J. IJspeert," *Applied Optics,* **vol. 31**, pp. 3694-3696, 1992.
[5] G. Westheimer and J. Liang, *Investigative Ophthalmology and Vision Science,* **vol. 35**, no. 5, pp. 2652-2657, 1994.
[6] J. Zuckerman, D. Miller, W. Dyes and M. Keller, *Investigative Ophthalmology,* pp. 213-224, 1973.
[7] H. Ginis, G. Perez, J. Bueno and P. Artal, *Journal of Vision,* **vol. 12**, no. 3, pp. 1-10, 2012.

[5690]

09:30-09:45

A new optical instrument for the optical measurement of intraocular scattering using modulated visible light

H.S. Ginis[1], O. Sahin[1], G.M. Pérez[2], J.M. Bueno[2], P. Artal[2]; [1]Institute of Vision and Optics, University of Crete, 71003 (GR); [2]Laboratorio de Optica, Universidad de Murcia, 30100 (ES).
Email: ginis@ivo.gr

Summary
A novel instrument for the measurement of intraocular scatter was developed. The instrument is based on the double-pass principle and builds on previous experience [1] with extended light sources. The validation of the method using an artificial eye and diffusers as well as preliminary measurements in human eyes are presented.

Introduction
The purpose of this study was to develop a new optical instrument based on the double-pass principle that utilises a spatio-temporally modulated visible light source and signal processing in the Fourier domain to detect light scattering in three angular domains ranging from 1 to 12 degrees.
The instrument is a variation of a double-pass instrument that has been used to characterize cataracts [2] and tear film irregularities [3]. In this instrument a

specially designed source is projected onto the retina. This source comprises four concentric annular diffusers back-illuminated by an array of 97 high-brightness LEDs (530±10 nm). The LEDs corresponding to each diffuser are modulated at different frequencies ranging from 1 to 3 kHz. An annular diaphragm conjugated with the pupil plane allows light to enter the eye through an annulus with internal and external diameters of 4.5 and 5.5 mm respectively. The eye is aligned by means of a pupil camera. The retinal image of the largest of the diffusers subtends a radius of 12 deg. Light reflected from the fundus is limited by a circular diaphragm conjugated with the pupil plane (concentric to the illumination annulus) so that the incoming and outgoing beams do not overlap. A pinhole conjugated with the retinal plane allows the light corresponding to the central15 -arcmin of the retinal image to be detected by a photomultiplier tube. The Fourier transform of the photomultiplier signal reveals the contribution of each annulus and therefore the average intensity of scattered light between the corresponding angles. The system's sensitivity was evaluated by means of an artificial eye and previously calibrated diffusers. The duration of the exposure and signal sampling is 300 msec.

Discussion

The system was capable of measuring the intensity of scattered light in three different regions (0.5-2, 3-5 and 6-12 degrees of visual angle). The sensitivity was better that 0.1 log units of the equivalent straylight parameter -log(S)- for the three angular regions that were investigated. Preliminary measurements on human eyes are presented.

Conclusions

An instrument to measure intraocular scattering based on the double-pass method with improved illumination and detection schemes has been developed and validated in an artificial eye model. A high sensitivity was demonstrated by using diffusers that create comparable scatter to that expected in healthy young eyes. The system is compact and could be of use in future clinical applications.

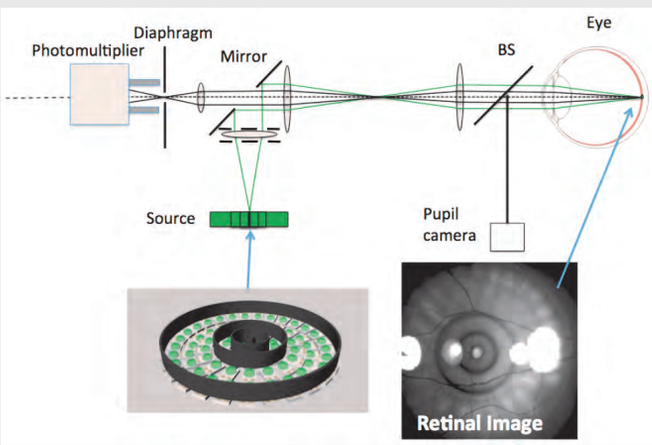

Fig 1. Schematic of the Experimental setup.

References

[1] H. Ginis, G. Perez, J. Bueno and P. Artal, *Journal of Vision,* **vol. 12**, no. 3, pp. 1-10, 2012.
[2] P. Artal, A. Benito, G. Perez, E. Alcon, A. De Casas, J. Pujoil and M. J.M., *Plos One,* **vol. 6**, no. 2, 2011.
[3] A. Benito, G. Perez, S. Mirabet, V. Meritxell, J. Pujol, J. Marin and P. Artal, *Journal of Cataract and efractive Surgery,* **vol. 37**, no. 8, pp. 1481-7, 2011.

Acknowledgement

"Ministerio de Educación y Ciencia", Spain (Grant FIS2010-14926) and "Fundación Séneca", Murcia, Spain (grant 04524/GERM/06) and by EU , ITN OpAL (PITN-GA-2010-264605).

[5763]

09:45-10:00 STUDENT PRESENTATION

Comparison of forward light scatter estimations using Hartmann-Shack spot patterns and C-Quant

P.B. Lopez, H. Radhakrishnan, V. Nourrit; University of Manchester, Faculty of Life Sciences, Manchester, M13 9PL (GB).
Email: pablo.benitolopez@manchester.ac.uk

Summary

We developed and implemented a method to extract an estimation of forward light scatter from the Hartmann-Shack (HS) spot patterns of an irx3 wave front aberrometer (Imagine eyes). After validation with a model eye, the method was used in 33 healthy patients and results compared to those obtained with a psychometric method (C-Quant). On the contrary of the results reported in a similar study, no correlation was found between the measurements produced by the two techniques.

Introduction

The objective estimation of intraocular forward light scattered (FLS) is a difficult issue. In this context, various studies suggested extracting a measure of FLS from the analysis of HS spot patterns (hartmanngrams). Several wave front sensors have been developed for applications in ophthalmology/optometry, and therefore the development of a numerical tool that could extend the range of applications of commercial wave front sensors presents a strong interest. The purpose of this study was to develop such a tool to process hartmanngrams from an irx3™ (Imagine Eyes) wave front sensor and to compare the associated results to those obtained with the C-Quant straylight meter. The C-Quant is a subjective method but that has been shown to provide repeatable and reliable measures of retinal straylight. The C-Quant has also been used in numerous clinical studies.

Discussion

We developed and implemented a HS metric based on previously reported methodology [1, 2]. The method was first validated using a model eye An aerosol was sprayed on the lens of the model eye to generate various levels of scattering. A good correlation was observed ($R=0.94$, $P<0.01$) between the density of droplets on the lens and the scatter value extracted from the hartmangramms. Measurements with both methods (HS-based and C-Quant) were then obtained in 33 healthy participants (mean age of 38.9±13.1 years old; min=24, max=62). The mean C-Quant values for participants were in agreement whose those reported in the literature for healthy subjects (mean±SD: 0.87±0.18). However no relationship was found between the two set of data ($R=0.04$, $P>0.01$).

Conclusions

The lack of correlation between HS and C-Quant results are in opposition with those reported in an earlier study[2] based on 6 eyes. This lack of correlation could be related to technical details (e.g. use of a different commercial wave front sensor). It may however be a consequence that both instruments are intrinsically different in design and objectives. The C-Quant is a subjective method that is really assessing large angle scattering while the HS is an objective method more sensitive to information in a narrow angle around the PSF. This lack of correlation (i.e. with a measure of visual performances) may limit the clinical use of a HS-based metric for FLS.

References

[1] Donnelly Iii, W. J., K. Pesudovs, et al. (2004). "Quantifying scatter in Shack-Hartmann images to evaluate nuclear cataract." Journal of Refractive Surgery 20(5): S515-S522.
[2] Cerviño, A., D. Bansal, et al. (2008). "Objective measurement of intraocular forward light scatter using Hartmann-Shack spot patterns from clinical aberrometers. Model-eye and human-eye study." Journal of Cataract and Refractive Surgery 34(7): 1089-1095.

[5755]

Room: Clinton Auditorium

10:00-10:15 STUDENT PRESENTATION

Quantification of human corneal grafts transparency

O. Casadessus[1], L. Siozade Lamoine[1], G. Georges[1], C. Deumié[1], L. Hoffart[2]; [1]Institut Fresnel, UMR 7249, CNRS, Université d'Aix-Marseille, Ecole Centrale Marseille, Domaine Universitaire de Saint Jérôme, 13397 Marseille cedex 20 (FR); [2]Service d'ophtalmologie, Hôpital la Timone, APHM, Université d'Aix-Marseille, 264 rue Saint Pierre, 13 385 Marseille Cedex 5 (FR).
Email: olivier.casadessus@fresnel.fr

Summary
In clinical and graft sorting applications, the transparency of cornea is only subjectively qualified. This study aims to bring tools to achieve the quantification of the transparency. It is based on a multiscale analysis of the microstructure (by optical coherence tomography) and of the macroscopic scattering properties of the tissue.

Introduction
With a transmission coefficient over 90% in the visible spectrum, the main function of the cornea is to transmit light inside the eye. This unique property of a tissue in the human body (along with the crystalline lens) is due to an absence of blood vessels and a very regular organization of the corneal bulk [1]. Indeed, the thicker part of the cornea, the stroma, is composed of 2µm-thick lamellas that are made of collagen fibrils, regularly aligned in each lamella, ensuring the good transmission of the light throughout the tissue with few losses due to scattering [2].
In the case of an edema development, the cornea swells because of a abnormally high hydration. This involves a disorganization of its internal structure and an increase of the light scattering, leading to cornea haziness [3, 4]. In this paper, angular resolved scattering properties are analyzed and are combined with three-dimensional micrometric imaging (by full-field optical coherence tomography) in order to bring tools to quantify the corneal transparency.

Discussion
Human corneal grafts were used for this study. Their edematous state was modified using osmotic solutions and controlled through graft thickness measurements.
On the one hand, the "macroscopic" scattering properties relatively to the degree of swelling were studied. An experimental device allows a measurement with an angular resolution of up to a few hundredths of a degree and a dynamics of six decades (from a lambertian sample to noise level) [5]. The measurements were performed in the reflected half-space (the only one accessible in in-vivo conditions), allowing a detailed analysis of scattering properties (including the identification of scattering sources). From these measurements, an integral parameter is then related to the transparency aspect of the tissue, providing an indicator for transparency quantification with consideration of the backscattered light only (as shown in figure 1).

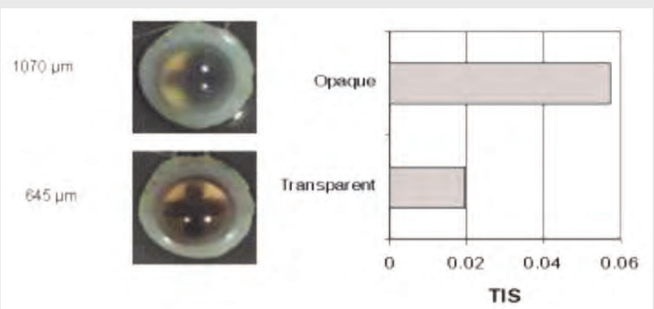

Fig. 1: Total backscattering scattering (TIS) as a function of graft thickness compared to their transparency degree.

On the other hand, the tissue microstructure modifications as a function of swelling were imaged by full-field optical coherence tomography (OCT). The experimental device allows a spatial resolution of 1 micrometer in the three directions of space with a sensitivity of about 80 dB [6]. When the cornea swells, lamellas in the stroma disjoin themselves and "lakes", corresponding to liquid infiltrations, appear within the tissue. Their localization and size are function of edema degree. The figure 2 shows a corneal graft with two different edema states: without any edema, stroma cells (keratocytes) can clearly be seen but when edema develops the organization is modified and heterogeneities are observed.

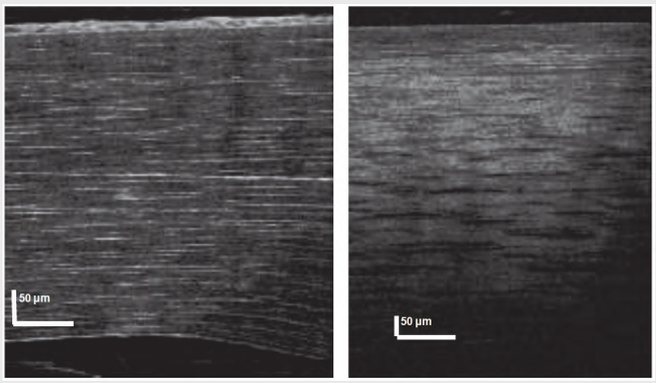

Fig. 2: Cross-sectional images of a non edematous (left) and edematous corneal graft (right).

Combining both techniques allows the observation of the scattering behavior of the graft with the evolution of microscopic structures within the tissue. Numerical modeling enables to link both aspects and to propose a quantitative appreciation of the influence of lakes development over the light scattered by the cornea.

Conclusions
Transparency loss, and more generally scattered intensity, increases in corneal graft as a function of swelling, but the phenomenon itself remains complicated to describe in relation with the corneal structure. However, the consideration of micrometric scale inhomogeneities and their evolution in edematous tissues offers scattering behaviors in agreement with the experimental ones, and enables the possibility of a quantification of the transparency.

References
[1] D. M. Maurice, *J. Physiol.*, **136**, 263-286, 1957.
[2] T. Nishida, *Cornea, Volume 1: Second Edition*, (Elsevier/Mosby, 2005).
[3] R. A. Farrell, R. W. Hart, *J. Opt. Soc Am.*, **59**, 766-774, 1969.
[4] G. B. Benedek, *Appl. Opt.*, **10**, 459-473, 1971.
[5] G. Latour, G. Georges, L. Siozade-Lamoine, C. Deumié, J. Conrath, L. Hoffart, *J. of Appl. Phys.*, **108**, 053104, 2010.
[6] G. Latour, G. Georges, L. Siozade-Lamoine, C. Deumié, J. Conrath, L. Hoffart, *J. Biomed. Opt.*, **15**, 056006, 2010.

[5707]

10:15-10:30

Possible origin of black spots in interferometric measurements of tear film surface

H.T. Kasprzak[1], D.T. Szczęsna-Iskander[1], D. Mas[2]; [1]Wrocław University of Technology, Institute of Physics, Wrocław, 50-370, (PL); [2]University of Alicante, Department of Optics, Alicante (ES).
Email: henryk.kasprzak@pwr.wroc.pl

Summary
During interferometric measurements of tear film surface, one can observe clear black, round spots in the image. This effect has not been fully explained. We aim to shade some light on this phenomenon and propose to explain it as vortices on the tear film surface. The full paper will provide model calculations of this effect.

Introduction
In our experiments on tear film surface stability, recorded by Twyman-Green or shearing interferometers we observed dark and round spots, with a diameter of about 0.2 - 0.5 mm [1]. In particular, inside larger spots no fringes are visible and the area is darker while in smaller spots a local weaker contrast of fringes is observed. Fringes deflection inside those spots indicate a very small depth of tear film cavity inside the spot area, in order of few micrometers or less. Figure 1 shows an example of an interferogram with a dark

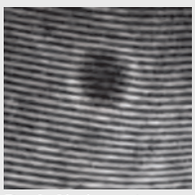

Fig. 1. Black spot in inter-ferogram of the tear film.

spot. Spots are also clearly visible by an examined person on its retina, in a refracted beam. However, they are not observable in scattered or not well collimated illumination. The form of spots is relatively stable between blinks however, on some interferograms we noticed that spot can disappear very fast. Figure 2 presents three interferograms from a sequence, with fast disappearing black spot, having about 0.5 mm in diameter.

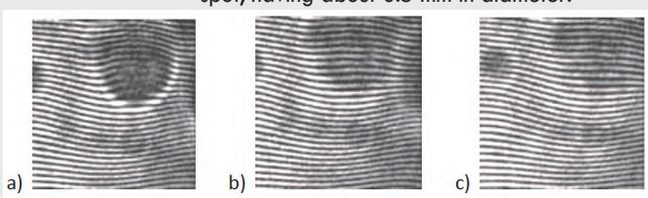

Fig. 2. Fast disappearing of the black spot within 0.28s.

Time between the frame a) and c) is 0.28 s. Also, it can be concluded from the fringe deflection inside the spot, that the cavity decreased its depth during disappearing and finally becomes almost smooth.

In our opinion, the phenomenon could be related to the fast fixation eye movements, namely tremor. The tear film covering corneal surface takes place in this movement, and rotational component of the tremor [2] can produce vortices in the tear film. Similar vortices and their fast disappearing can be clearly visible on a surface of moving, shallow water. To verify this approach we numerically modeled 40 000 rays reflected and refracted on the spherical refractive surface ($R = 7.8$ mm) with local, round cavities, having half-depth diameter of 0.4 mm and the central depth in order of single micrometers. Calculations were carried out in MATHCAD 15.

Result of modeling

Figure 3 shows 3D plot of considered cavity surface, described by:

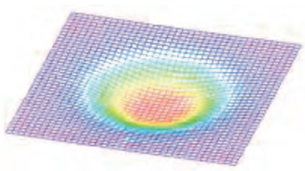

Fig. 3. 3D plot of modeled surface.

$$z(x,y) = \frac{1}{a \cdot \cosh\left(b \cdot \sqrt{x^2 + y^2}\right)}.$$

Figure 4 presents result of ray tracing after reflection from the spherical surface with three cavities. Central depth of cavities was equal to 1, 2 and 4 μm, and the half-depth diameter was the same and equal to 0.4 mm. The

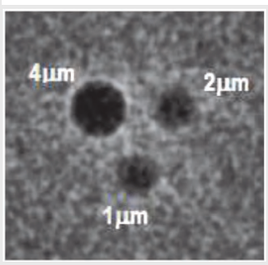

Fig. 4. Density of rays reflected from the spherical surface having three cavities with different depth.

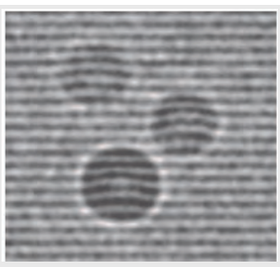

Fig. 5: Modeled rays reflected from the surface with overlapped numerically generated fringes.

image after ray tracing procedure was smoothed and converted into a negative. It can be seen that visibility of dark spots depends on their central depth. Additionally one can see bright ring around the spot, similarly to those observed in our experiments. This modeling shows that image of collimated, reflected rays from the optical surface is very sensitive to its irregularities. Similar methods that have been used in optics from long time are called Schlieren imaging.

The next step was calculating the shape of interference fringes after reflection of the plane wavefront from such disturbed, spherical surfaces. Result of this calculation was then overlapped on previous results of ray tracing. Figure 5 shows an example of both calculations overlapped with each other. The similarity of this image with experimentally obtained interferogram is striking. Visibility of modeled dark spots depends also on the fringe deflections within spots. Results of presented calculations can be useful to better understand the kinetics of the corneal surface, especially the influence of tremor and the roll of lipid layer in the tear film surface stability.

References

[1] D.H. Szczęsna, H.T. Kasprzak, J. Jaroński, A. Rydz and U. Stenevi, Acta Ophthalmol. Scand, **85**, 202, 2007.

[2] S.B. Stevenson, A. Roorda, Correcting for miniature eye movements in high resolution scanning, laser ophthalmoscopy. Proceedings of SPIE, **5688**, 145, 2005.

[5781]

10:30-11:00 Coffee break

11:00-13:00

ACCOMMODATION, PRESBYOPIA AND VISUAL IMPAIRMENT

Session Chair: L. Lundström, KTH, Royal Institute of Technology (SE)

11:00-11:15

Retinal Image Quality During Accommodation

L. Thibos[1], J. Martin[1], T. Liu[1], A. Bradley[1], D. Diaz-Muñoz[2], N. López-Gil[2]; [1] School of Optometry, Indiana University, Bloomington, IN, 47405 (US); [2]Grupo de Ciencias de la Visión. Universidad de Murcia. 30100 Murcia (ES).

Email: thibos@indiana.edu

Summary

We reject the classical model of accommodative lead and lag when subjects perform a demanding visual task. Despite changes in ocular aberrations and pupil size during accommodation, accommodative error is negligible and retinal image quality is near maximum provided visual acuity remains high.

Introduction

According to classical models of accommodation, the human eye typically accommodates too much for distant targets ("accommodative lead") and too little for near targets ("accommodative lag"). Between these two extremes, accommodative response is proportional to stimulus vergence but the constant of proportionality is less than one. This model implies that accommodative errors are the rule rather than the exception and consequently the quality of the retinal image is typically suboptimal. Conversely, the model implies quality of the retinal image is optimal for only that singular, intermediate stimulus vergence where accommodative error is reduced to zero as "lead" changes sign to become "lag".

One implication of this classical model of accommodation is that human spatial vision is almost always sub-optimal because focusing errors cause retinal image quality to be sub-optimal for almost all states of accommodation. We aimed to test this prediction experimentally by measuring visual acuity while simultaneously assessing the refractive state of the eye using wavefront aberrometry.

Methods

Wavefront aberrations were measured for 10 young adult eyes while simultaneously viewing the smallest resolvable letters on an acuity chart (552nm) located at various distances (Fig.1). A control condition used phenylephrine to inhibit pupil constriction during accommodation. Retinal image quality was computed from the aberration data (adjusted to 552nm) using unbiased scalar metrics [1]. For any given state of accommodation, the refractive state of an eye is defined as the target vergence that optimizes retinal image quality. Accommodative error is the difference between the actual target vergence and the optimum target vergence.

Room: Clinton Auditorium

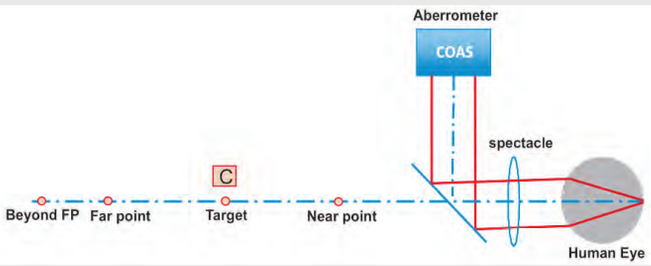

Results

Experimental measurements for a typical observer are shown in Fig. 2, for which the abscissa is target vergence (in diopters) and the ordinate is refractive state (in diopters). Ideal, error free accommodation is indicated by the dashed 1:1 (Ref) line. The subject's visual acuity measured at each state of accommodation (solid black curve) oscillates around the required criterion of 0 logMAR for target vergences in the approximate range -2 to -5 D. Acuity declines rapidly (logMAR increases) for more distant targets and therefore we conclude the far point lies 50 cm from this eye. Refractive state determined by two unbiased metrics (PFSc = fraction of pupil area for which wavefront quality is good, VSOTF = visual Strehl ratio) is nearly constant for targets beyond the far-point, indicating accommodation is fully relaxed. As the target approaches the eye from the far point, the eye's refractive state changes accordingly. Unlike the classical model's prediction, the slope of this linear portion of the accommodation curve is 1 and the two curves lie near the ideal 1:1 line. A small lag in refractive state relative to target vergence is consistent with a small depth of field that allows good acuity to be maintained over a range of target vergences.

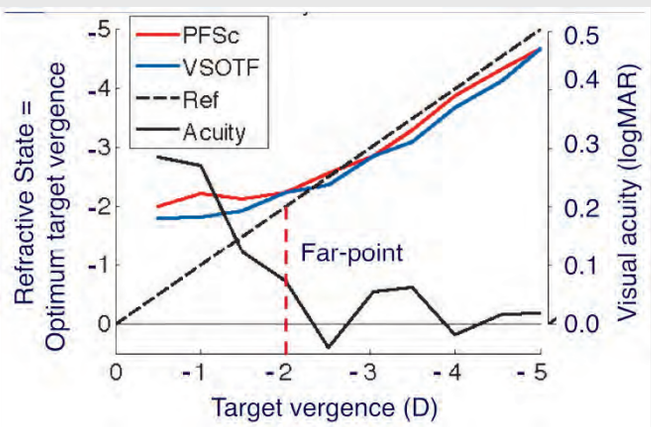

Discussion

Recent reports [2,3] describing the effect of spherical aberration on accommodation errors have suggested a need to abandon the notion that the 1:1 accommodation curve is ideal. Our approach shows this essential reference line need not be abandoned, provided refractive state is defined as the optimum target vergence for maximizing image quality. For refractive state data on the 1:1 line, optimum target vergence equals the actual target vergence, indicating neither image quality nor visual acuity can be improved by refocusing the target. This is to be expected if the subject is given a demanding visual task requiring accurate accommodation.

References

[1] Martin, J., Vasudevan, B., Himebaugh, N., Bradley, A., & Thibos, L., *Vision Res,* ***51***, 1932-1940, 2011.

[2] Plainis, S., Ginis, H.S., & Pallikaris, A., *J Vision,* ***5*** (5), 466-477, 2005.

[3]Buehren, T. & Collins, M.J., *Vision Res,* ***46***, 1633-1645, (2006).

[5758]

11:15-11:30 STUDENT PRESENTATION

Measuring accommodative response with a double-pass system.

M. Aldaba, M. Vilaseca, F. Díaz-Doutón, M. Arjona, J. Pujol;
Universitat Politècnica de Catalunya, CD6, 08222 (ES).
Email: aldaba@cd6.upc.edu

Summary

In our aim of measuring accommodative response with a double-pass system, we developed a method based on maximizing the retinal image quality. After confirming the suitability of the double-pass technique for measuring the accommodative response, an extended group of patients with a wide age range was measured.

Introduction

Firstly the suitability of the double-pass based method for measuring the accommodative response was studied, by comparison with Hartmann-Shack measurements. A custom-built set-up that combines double-pass and Hartmann-Shack techniques was used for this purpose. The measurement procedure consisted of a through focus scanning in the range from +0.5 to -0.5 diopters (D) in 0.125-D steps for every accommodative stimulation, recording double-pass images at each step and a Hartmann-Shack image at the central point of the scanning. In the case of the double-pass technique, the accommodative response was calculated aiming at the best double-pass image, whose vergence was then associated with the accommodative response value. In Hartmann-Shack measurements, the accommodative response was measured as the defocus maximizing the retinal image quality. Double-pass and Hartmann-Shack measurements were compared in 10 patients with a mean age (± standard deviation [SD]) of 27.90 ± 2.33 years (range: 23 to 31 years), a mean subjective spherical refraction of -0.50 ± 1.45 D (range: +0.75 to -3.00 D), a mean subjective astigmatic refraction of -0.30 ± 0.20 D (range: 0.00 to -0.50 D) and a mean best corrected visual acuity of 1.16 ± 0.08 (range: 1.00 to 1.20). Patients were corrected according to their subjective refraction, had monocular vision and were instructed to focus on a fixation test during measurements. Accommodation was stimulated from 0 to 5 D using a push-up method, in steps of 1 D.

In the second part of the study accommodative response was measured with the double-pass system in a wide age range. 84 patients were enrolled in this study, with a mean age of 34.55 ± 12.04 years (range: 15 to 55 years), a mean subjective spherical refraction of -0.99 ± 1.72 D (range: -8.00 to +3.00 D), a mean subjective astigmatic refraction of -0.46 ± 0.46 D (range: 0 to -1.75 D) and a mean best corrected visual acuity of 1.13 ± 0.10 (range: 0.9 to 1.2). The measurement procedure was similar to that described above. Accommodative stimulus-response curve, total accommodation played in role, pupil diameter evolution and the retinal image quality evolution with accommodation were studied.

Discussion

When comparing double-pass and Hartmann-Shack accommodative response measurements we found good agreement between both techniques, with a mean absolute difference of 0.05± 0.24 D and a statistically significant (p<0,001) linear correlation with a Pearson coefficient of 0.966. Bland and Altman analysis also highlighted small differences between techniques, and no statistically significant differences were found (p=0.822) by means of the paired sample t test. From this data we concluded the suitability of the double-pass system to measure accommodative response as the results were in concordance with the widely used Hartmann-Shack method [1].

The extended population study highlighted lower total accommodative response values than those measured with subjective techniques [2], especially in old patients. As it has been previously shown [3], subjective techniques overestimate accommodative response, mainly due to the depth of field. The accommodative stimulus-response curve in young patients (<35 years) showed lower accommodative errors than those previously published in the literature using objective techniques [4]. This could be due to the fact that measurements are based on retinal image quality. As it has been suggested [5,6] certain amount of defocus could be used to enhance the retinal image quality, and with some measuring techniques this defocus can be confused with accommodative error. Since double-pass measure-

ments are based on retinal image quality and not on defocus, this cannot be a source of error in our results. Patients older than 35 years showed a sudden decrease in the accommodative response, as also pointed out by other authors [7]. As widely reported in the literature [8] there is a pupil constriction with accommodation, and we found no clear differences with age in this near response. The optical quality seemed to decreased with accommodation, although the differences between accommodated and unaccommodated eye were not statistically significant.

Conclusions

We have shown the suitability of double-pass for measuring the accommodative response by its comparison with the Hartmann-Shack technique. The results in the extended population highlighted differences with subjective techniques, which overestimate the accommodative response due to the depth of field. The accommodative stimulus-response curve results also emphasized the importance of taking into account the retinal image quality in the measurements, as conventional objective methods underestimate the response.

References

[1] M. Aldaba, M. Vilaseca, F. Díaz-Doutón, M. Arjona, J. Pujol, Vision Research, accepted.
[2] J.A. Mordi, K.J. Ciuffreda, Vision Research, 38, 1643, 1998.
[3] D.M. Win-Hall, A. Glasser, Journal of Cataract and Refractive Surgery, 34, 774, 2008.
[4] M.P. Cacho, A. García, J.R. García, A. López, Optometry and Vision Science, 76, 650, 1999.
[5] S. Plainis, H.S. Ginis, A. Pallikaris, Journal of Vision, 5(5), 466, 2005.
[6] T. Buehren, and M.J. Collins, Vision Research, 46, 1633,2006.
[7] M. Kalsi, G. Heron, W.N. Charman, Ophthalmic and Physiological Optics, 21, 77, 2001.
[8] S. Kasthurirangan, A. Glasser, Vision Research, 46, 1393, 2006,

[5705]

11:30-11:45

Quantifying performance of accommodative intraocular lenses with 3-D anterior segment OCT

S. Marcos[1], S. Ortiz[1], P. Pérez-Merino[1], J. Birkenfeld[1], S. Durán[2], I. Jiménez-Alfaro[2]; [1]Instituto de Optica, CSIC, Madrid (ES); [2]Fundación Jiménez-Díaz, Madrid (ES).

Email: susana@io.cfmac.csic.es

Summary

We used a custom-developed anterior segment spectral Optical Coherence Tomography system (sOCT) provided with quantification tools to fully image threedimensionally the anterior segment of the eye in patients implanted with an accommodative intraocular lens (A-IOL) for different accommodative demands, and to quantify the 3-D biometrical changes pre/post operatively and as a function of accommodation. These measurements allow, for the first time, fully quantitative 3-D analysis of A-IOLs designed to move inside the eye.

Introduction

The ultimate solution for presbyopia (the age-related loss of accommodation) should restore the dynamic focusing capability of the young crystalline lens. A-IOLs are therefore a promising solution for the restoration of accommodation. Today, only one A-IOL has been approved by the USA Food and Drug Administration: the Crystalens (Bausch and Lomb, Rochester, NY)[1]. This lens is expected to move axially in response to the cilliary muscle, which would produce a force onto hinged haptics and displace the lens towards the cornea upon compression by the cilliary muscle (and relaxation of the zonulae). Much of the direct in vivo visualization of the crystalline lens implanted in patients has been obtained through Ultrasound Biomicroscopy [2] although the invasiveness of the procedure, lack of reliable fixation, and relatively poor quality and low resolution of the captured images make quantification challenging. Most of the information regarding performance of Crystalens comes from clinical evaluations of the near vision function (which may be masked by depth of focus)[3]. Overall, data regarding the performance of this lens are conflicting, with some studies reporting some accommodation capacity, while others do not find that the lens performs differently (in terms of functional accommodation) than a monofocal lens. An excellent tool for assessing the compliance of the Crystalens with the ideal mechanism of operation is Optical Coherence Tomography. Although with sOCT the haptics of the lens (and the zonulae, cilliary processes, etc…) are generally blocked by the iris, ideally the lens can be imaged in 3-D with high-resolution and speed. However, to date, this technique has not been widely used for 3-D biometry, primarily due to the lack of axial range (to image the entire anterior segment), and more importantly, because the OCT images suffer from distortions (fan and optical distortion, resulting from the scanning architecture and refraction by preceding ocular components) [4,5].

We have developed procedures for 3-D imaging, merging and analysis of the corneal and lens pre- and post-operatively in patients implanted with Crystalens AIOLs. A custom developed sOCT was used to image the anterior segment (cornea and crystalline lens/IOL) in patients implanted with AIOLs. Images were automatically merged, using the peripheral corneal region and iris for registration. Denoising volume clustering, edge detection and segmentation algorithms, and distortion correction were developed and applied. Patients were imaged before and after surgery under relaxed accommodation and 1.25 and 2.5-D of accommodative effort. 3-Dl 4-surface real-eye models were obtained. Biometrical parameters such as A-IOL location with respect to the pre-operative lens, and A-IOL displacement as a function of accommodation were estimated.

Discussion

Full 3D quantitative images of the anterior segment were obtained, which allowed 3D pre- and post-operative biometry in patients implanted with A-IOLs (see example in Fig.1). The A-IOL center fell 100 !m behind the pre-op natural lens equator. Interestingy, with accommodation, lenses moved from 400 !m from the cornea (opposite to expected shift) to 180 um towards the cornea. In many cases, A-IOLs tilted (rather than axially displaced) with an increased accommodative demand.

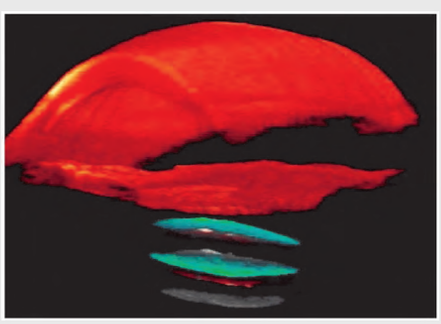

Fig. 1:
Merged 3-D OCT image for an eye implanted with a Crystalens A-IOL, for three accommodative demands. The lens moved backwards with accommodation. Green: relaxed accommodation; Red: 1.25 D accommodative demand; Gray: 2.5 D accommodative demand

Conclusion

Full 3-D sOCT is a powerful tool to assess performance of AIOLs. In general, the Crystalens A-IOL does not function as attempted: axial shifts were too small to produce functional accommodation, moved in the opposite direction or tilted.

Acknowledgements

FIS2008-02065 and FIS2011-25637; EURHORCs-ESF EURYI-05-102-ES; ERC-2011-AdG-294099

References

[1] US FDA. http://web.archive.org/http://fda.gov/cdrh/mda/docs/p030002.html
[2] Marchini G, et al. J Cataract Refract Surg. 2004; 30: 2476-82.
[3] Alió JL, et al.. J Cataract Refract Surg. 2010; 36: 1656-64.
[4] Ortiz S, et al. Opt Express. 2010; 18: 2782-96.
[5] Ortiz S, et aBiomed Opt Express. 2011; 2: 3232-47.

[5680]

Room: Clinton Auditorium

11:45-12:00

Binocular Adaptive Optics Visual Analyzer to optimize optical solutions for presbyopia

S. Manzanera, E.J. Fernández, C. Schwarz, J. Tabernero, P.M. Prieto, P. Artal; Laboratorio de Óptica, Instituto Universitario de investigación en Óptica y Nanofísica (IUiOyN), Universidad de Murcia, Campus de Espinardo, 30100 Murcia (ES).
Email: silmanro@um.es

Summary
We describe an instrument based on adaptive optics that allows wave-front aberration manipulation and visual testing simultaneously in both eyes. This instrument, called binocular adaptive optics visual analyzer possesses an enormous potential for both basic and applied vision experiments. As an example, its application to optimize different optical solutions to presbyopia will be described.

Introduction
Adaptive optics visual simulators [1], or vision analyzers, consists of an adaptive optics device to manipulate ocular wave-front aberrations combined with a visual testing unit. These instruments have proved to be an important step forward in fundamental Vision research [2] and in testing and designing of new ophthalmic optical devices [3,4].
While the first generation of this instrument was designed to work monocularly, more recent versions allow binocular visual testing [5,6]. Since daily life visual activities make use of both eyes, the new binocular version of the visual analyzer extends the range of application of these instruments. As an example of the application, we studied the induced depth of focus and the stereoacuity produced by two solutions to correct presbyopia: monovision, a classical approach where one eye is set for distance vision and the other for near vision and the recent concept of small aperture corneal inlays implanted unilaterally.

Methods
The BAOVS allows for modifying the magnitude and phase of the eye's complex pupil in both eyes simultaneously. It incorporates a programmable phase modulator using liquid crystal on silicon technology for wave-front shaping and an additional liquid crystal intensity modulator located at the exit pupils plane of the system. This permits the full manipulation of the eye's complex pupil function in diameter, shape, transmission and phase. Figure 1 shows a schematic diagram of the setup. A pico-projector is used to present the different visual test to the subject. The liquid crystal modulator in amplitude, the modulator in phase and the eye's pupil plane are optically conjugated. To make this possible for both eyes simultaneously a periscope system composed of a right angle prism and two flat mirrors in front of each eye are employed. Ocular wave-front aberration measurements are performed by means of a Hartmann-Shack sensor which uses the light from an infrared laser. A beam-splitter is used to illuminate the eye and a flip mirror is placed in the path whenever an aberrations measurement is carried out. The prototype can be also equipped with a stimulus generator based on a pair of high luminance micro-displays (not shown in figure 1). Each display is independently projected over its corresponding eye, still simultaneously, creating retinal disparity. For characterizing stereopsis, a three-needle test is programmed. Subjects underwent a series of forced choice and adjustment test under the induced optical conditions binocularly. A direct comparison of the performance under conditions is obtained. This allows the selection of the optimum situation for each subject.

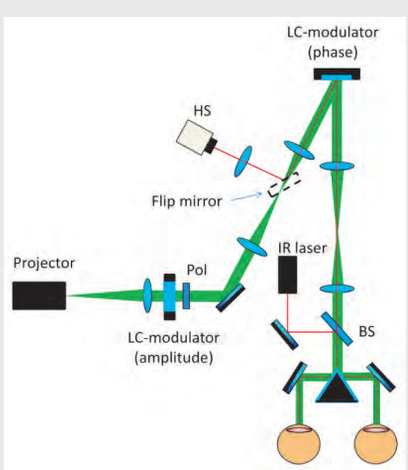

Fig.1:
schematic diagram of the BAOVA.

Conclusions
We have developed and built a new generation of adaptive optics visual analyzers that allows full control over the complex pupil, amplitude and phase, simultaneously on both eyes. The instrument's capabilities have been proved comparing the performance of monovision and small aperture corneal inlays. While binocular depth of focus can be similar, the small aperture provided a superior stereoacuity than monovision due to a reduced retinal disparity.

References
[1] E. J. Fernández, S. Manzanera, P. Piers, and P. Artal, J. Refract. Surg. 18, S634 (2002).
[2] P. Artal, L. Chen, E. J. Fernández, B. Singer, S. Manzanera,and D. R. Williams, J. Vis. 4, 281 (2004).
[3] S. Manzanera, P. M. Prieto, D. B. Ayala, J. M. Lindacher, and P. Artal, Opt. Express 15, 16177 (2007).
[4] J. Tabernero, C. Schwarz, E. J. Fernandez, and P. Artal, Invest. Ophthalmol. Vis. Sci. 52, 5273 (2011).
[5] E. J. Fernández, P. M. Prieto, and P. Artal, J.Opt.Soc.Am.A. 27, A48 (2010).
[6] C. Schwarz, P.M. Prieto, E.J.Fernandez, P. Artal, Opt. Letters, 36, 24, 4779-4781 (2011).

[5772]

12:00-12:15

Interocular Differences in Visual Latency Induced by Reduced-Aperture Contact Lenses or Corneal Inlays for Presbyopia

S. Plainis[1], D. Petratou[1], T. Giannakopoulou[1], H. Radhakrishnan[2], I.G. Pallikaris[1], W.N. Charman[2]; [1]Institute of Vision and Optics, University of Crete, Heraklion (GR); [2]Faculty of Life Sciences, University of Manchester, Manchester (GB).
Email: neil.charman@tesco.net

Summary
Although monocular use of small aperture optics in the form of a corneal inlay or contact lens may improve intermediate and near binocular acuity of presbyopes, the associated inter-ocular differences in retinal illuminance result in differences in visual latency and the Pulfrich effect.

Purpose
To explore the interocular differences in the temporal responses of the eyes induced by the monocular use of small-aperture optics designed to aid presbyopes by increasing their depth-of-focus.

Methods
Monocular and binocular pattern reversal visual evoked potentials (VEPs) were measured at a mean photopic field luminance of 30 cd/m^2 in 7 normal subjects with either natural pupils or when the non-dominant eye wore a small-aperture hand-painted opaque soft contact lens (aperture diameter 1.5, 2.5 or 3.5mm, or an annular opaque stop of inner and outer diameters 1.5 and 4.0 mm respectively; supplied by Cantor & Nissel Ltd, Brackley, UK). Responses were also measured with varying stimulus luminance (5, 13.9, 27.2 and 45 cd/m^2) and a fixed 3.0 mm artificial pupil. The Pulfrich effect was also measured under the same conditions.

Results
Mean natural pupil diameters were 4.7 and 4.4 mm under monocular and binocular condition respectively. The small-aperture contact lenses reduced the amplitude of the P100 component of the VEP and increased its latency (Fig.1). Inter-ocular differences in latency rose to about 20-25 ms when the pupil diameter of the non-dominant eye was reduced to 1.5 mm. The measurements with fixed pupil and varying luminance suggested that the observed effects were explicable in terms of the changes in retinal illuminance produced by the restrictions in pupil area. This was supported by the Pulfrich measurements.

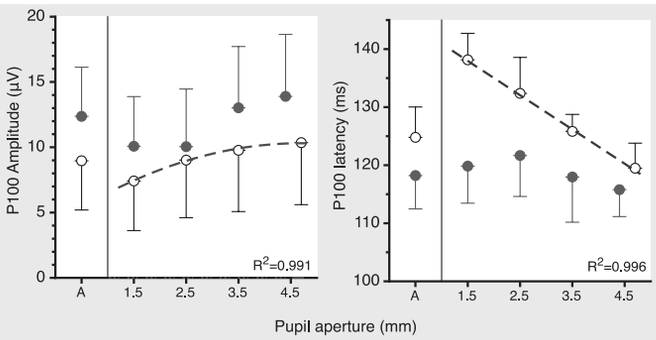

Fig.: 1 Mean amplitude (left) and mean latency (right) of the VEP P100 component from seven observers as a function of the central aperture of the contact lens (used in the non-dominant eye) under binocular (filled circles) and monocular (open circles) stimulation. The data for the largest pupil aperture is for the unobstructed natural pupil condition, The bars indicate ±1 SD. The dashed lines form second order (left) and linear (right) regressions. The "A" in x-axis represents the "annular" lens (4.0 mm diameter opaque pupil with a central 1.5 mm aperture)

Conclusions

The anisocoria induced by small-aperture approaches to aid presbyopes produces marked interocular differences in visual latency. The literature of the Pulfrich and related effects suggests that such differences can lead to distortions in the perception of relative movement and, in some cases, to possible hazard in practical situations such as driving

[5688]

12:15-12:30

Driving with Monocular Bioptic Telescope: Strabismus Might Affect Hazard Detection with the Fellow Eye

A. Doherty, A. Bowers, E. Peli; Schepens Eye Research Institute, Massachusetts Eye and Ear, Harvard Medical School, Boston, MA (US).
Email: eli.peli@schepens.harvard.edu

Summary

Bioptic telescopes are commonly used by visually impaired patients who frequently also have strabismus. Strong ocular dominance in strabismus may result in suppression of the non-dominant eye and therefore affect the ability of this eye to detect hazards outside of the telescope view when the dominant eye is viewing through the telescope. Strabismic participants had reduced fellow-eye detection with the bioptic on a patterned background; non-strabismics did not.

Introduction

Bioptic telescopes are small spectacle-mounted telescopes enabling people with reduced visual acuity to see details of distant objects. Some countries permit the use of these telescopes when driving [1, 2]. When looking through a **monocular** telescope, part of the scene is covered by the magnified field of view, creating a 'ring scotoma' around that view. However, the area covered by the ring scotoma should be seen by the fellow eye. The differences between the images seen by the telescope eye and fellow eye, which fall on corresponding retinal areas, may cause rivalry or suppression in complex visual conditions such as driving [3]. This could affect the ability of the fellow eye to detect potential hazards while spotting through the telescope. Our previous study [4] of visually impaired participants **without** strabismus found no evidence of suppression of the fellow eye when detecting objects on uniform and patterned backgrounds with a monocular bioptic telescope. However, the strong ocular dominance in strabismus could result in suppression of the non-dominant fellow eye's view. About 60% of drivers with bioptic telescopes have congenital ocular conditions, such as albinism and nystagmus that result in reduced visual acuity and are frequently associated with strabismus.

We evaluated the effect of strabismus on fellow-eye detection ability using the same methodology as our previous study [4]. Nine patients with strabismus and 6 with reduced visual acuity but no strabismus participated. A dichoptic perimeter [5] was used to present suprathreshold stimuli to each eye separately. The telescope ring scotoma was mapped by presenting the stimulus to the telescope eye only. Participants then performed a series of detection tests under binocular viewing conditions with stimuli presented to the fellow eye only within the area of the ring scotoma. Fellow-eye detection rates were evaluated with and without a bioptic on a uniform and patterned background, while participants performed a passive (looking at a cross) or active (reading letters) viewing task.

Results

While there was no overall difference in fellow-eye detection rates between strabismic and nonstrabismic participants (88% vs 92%, p=0.542), there was a significant interaction between strabismus and background. Strabismic participants showed a greater reduction in detection rate from the uniform to the patterned background (97% to 70%) than nonstrabismic participants (95% to 87%; p=0.022; Figure 1A). Furthermore, on the patterned background, strabismic participants had lower detection rates with than without the bioptic (p=0.029), while detection rates for nonstrabismic participants were not significantly different with and without the device (p=0.764; Figure 1B).

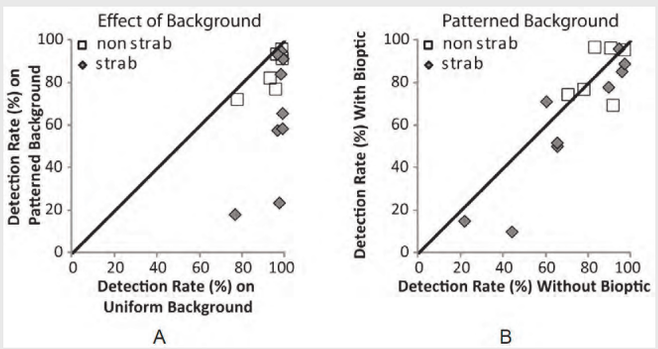

Fig. 1 A): Scatter plot showing fellow-eye detection rates for each participant on the uniform and patterned backgrounds. B): Scatter plot showing fellow-eye detection rates on the patterned background with and without the bioptic.

Conclusion

In the USA, patients with congenital vision loss are more frequently fitted with bioptic telescopes for driving than older patients with acquired vision impairment. This is sensible as they are younger and better adapted to their vision loss. While the ring scotoma has been raised as a concern by people opposed to driving with bioptic telescopes, the effect of strabismus has never been considered. We are not convinced that the ring scotoma is important when using monocular telescopes. However, if it is shown to matter, then strabismus will have to be considered in selecting patients for this rehabilitation device.

References

[1] B.J.M. Melis-Dankers, et al., *Vis. Imp. Res.*, **10**, 7-22, 2008.
[2] E. Peli & D. Peli, *Driving With Confidence: A Practical Guide to Driving With Low Vision*, (World Scientific, Singapore, 2002).
[3] R. Blake, *Brain and Mind*, **2**, 5-38, 2001.
[4] A.L. Doherty, et al., *Arch. Ophthalmol.*, **129**, 611-617, 2011.
[5] R.L. Woods, et al., *J. Biomed. Optics*, **15**, 1-13, 2010.

[5699]

NOTES

Room: Clinton Auditorium

12:30-12:45 STUDENT PRESENTATION

Peripheral Contrast Sensitivity Function with Adaptive Optics

R. Rosén, L. Lundström, S. Winter, A.P. Venkataraman, P. Unsbo; Royal Institute of Technology, Dept of Applied Physics, 106 91 Stockholm (SE).
Email: robert.rosen@biox.kth.se

Summary
We present a system with adaptive optics and a psychophysical procedure for peripheral vision that is capable of determining the peripheral contrast sensitivity function (CSF) while simultaneously correcting higher order aberrations. This study reports peripheral CSFs for resolution and detection as well as data on the aliasing zone.

Introduction
Understanding peripheral visual function has practical implications for research on myopia development and for treatment and diagnosis of patients with central visual field loss. CSF is an important tool for such understanding. Many earlier determinations of peripheral CSF, e.g. the study by Johnston[1], did not correct for peripheral refractive errors, and as a result the reported CSFs differ substantially from those presented by Thibos et al.[2] They found, using one principal subject, a large peripheral aliasing zone. At 30° eccentricity their subject had a CSF for detection with a distinctly different shape than that for foveal vision with a long tail to high spatial frequencies; whereas the CSF for resolution had a sharp cutoff-point. Therefore, foveal and peripheral CSF could not be related by only spatial scaling, neither for detection nor for resolution.
The purpose of the current study is to determine if the earlier results regarding the shape of the peripheral CSF can be verified on several different subjects, with different correction levels. Foveally, correction of higher order aberrations using adaptive optics have improved CSF at high but not low spatial frequencies.[3] However, in the periphery a larger amount of higher order aberrations, particularly coma, exists. We have earlier found improvement in peripheral low contrast acuity with adaptive optics correction for subjects with large amounts of higher order aberrations (Rosén R, et al, IOVS 2012;53:ARVO E-Abstract 3587). In the current study we measure the peripheral CSF with Gabor gratings using an adaptive Bayesian procedure at 12 spatial frequencies in the 20° nasal visual field for three subjects, both for detection and resolution with best refractive correction and full adaptive optics correction.

Discussion
The adaptive optics system was capable of running in continuous closed loop throughout the whole psychophysical procedure and corrected the peripheral higher order aberrations down to a residual root mean square of 0.1 µm at 5 mm pupil. The system was robust and small head movements in the chin rest and blinking did not affect correction stability. The CSF results of the three subjects can be seen in Figure 1. We replicated the finding by Thibos et al of an aliasing zone and a peripheral resolution acuity with a sharp cutoff-point. For resolution, the CSF was below 2 for spatial frequencies above 6 cycles/degree. The peripheral detection CSF had a long high-frequency tail and maximal spatial frequency around 15 cycles/degree. As we have found earlier, the visual benefits of adaptive optics correction depended on the subject's initial amount of higher order aberrations.

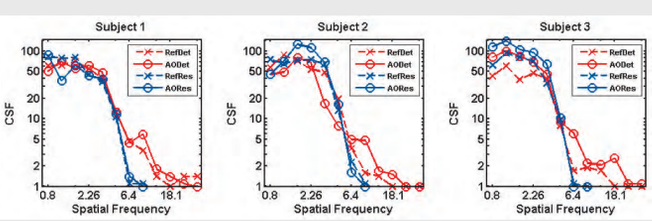

Fig. 1. Peripheral contrast sensitivity in the 20° nasal visual field for the three subjects. Shown are both resolution (res) and detection (det) with optimal refractive correction (Ref) and adaptive optics correction (AO). With optimal refractive correction, the amount of higher order aberrations at 5 mm pupil was 0.2 µm for subject 1, 0.3 µm for subject 2 and 0.9 µm for subject 3.

Careful assessment of peripheral CSF is primarily limited by the long time it takes to conduct the experiment. As a result, its use is not widespread for measuring peripheral visual function and studies usually rely on acuity measurements at specific contrast levels. However, if the shape of the curve is known a priori, psychophysical routines could be developed to estimate the specific parameters of the curve at all contrasts and spatial frequencies simultaneously. Such routines have been developed for the foveal CSF[4] and could be adapted for peripheral measurements.

Conclusions
Adaptive optics can be used to study peripheral CSF with aberrations corrected. The shape of the peripheral CSF curve is similar when comparing different subjects and correction levels; both for detection and resolution. It is therefore be possible to make use of quicker algorithms that utilize the knowledge of this shape.

References
[1] A. Johnston, *J. Opt. Soc. Am. A,* **4**, 1583-1593, 1987
[2] L. N. Thibos, D. L. Still, A. Bradley, *Vision Res,* **36**, 249-258, 1995
[3] P. de Gracia, S. Marcos, A. Mathur, A. A. Atchison, *Journal of Vision,* **11**, 1-10, 2011
[4] L. A. Lesmes, Z-L. Lu, J. Baek, T. D. Albright, *Journal of Vision,* **10**, 2010

[5750]

12:45-13:00

Peripheral refraction out to 60 degrees from fixation using the Hartmann-Shack technique

D.A. Atchison, A. Mathur; School of Optometry & Vision Science and Institute of Health & Biomedical Innovation (AU).
Email: d.atchison@qut.edu.au

Summary
We made measurements on the right eyes of 30 adults using a Hartmann-Shack aberrometer. We identified a refraction pattern to add to Rempt et al.'s 1971 scheme, with characteristics of both their types IV and I, that we call type IV/I.

Introduction
Rempt *et al.*1 measured retinoscopic refractions at 0, ±20, ±40 and ±60° angles along the horizontal visual field. They divided their "skiagrams" into five patterns. The type I pattern had hypermetropic (positive) shifts into the periphery for both horizontal and vertical meridians (Fig. 1a), and the type IV pattern had myopic shifts for the horizontal meridian and hypermetropic shifts for the vertical meridian (Fig. 1e). Type II was intermediate between type I and IV (Fig. 1b), with a hypermetropic shift for the vertical meridian into the periphery and little change in the horizontal meridian into the periphery. Type III was asymmetric, consisting of the type I pattern on one side of the field and the type IV pattern on the other side (Fig. 1c). Type V showed little change of the refraction into the periphery along the vertical meridian and a large myopic shift into the periphery along the horizontal meridian (Fig. 1f).

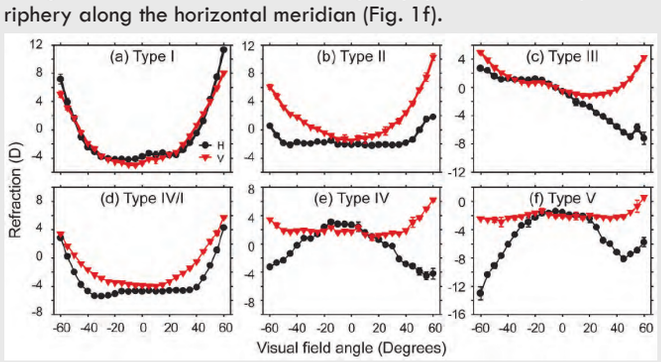

Fig. 1. Examples of skiagram types. Negative angles correspond to the temporal visual field

One feature of large angle peripheral refraction studies that has not received a lot of attention is the tendency for the refraction to

move in the hypermetropic direction, particularly the horizontal refraction, at large angles2,3. Here we report measures of peripheral refraction out to 60° along the horizontal visual field in the cycloplegged eyes of 30 participants with a range of refractions.
We used a modified COAS-HD Hartmann-Shack aberrometer along the horizontal visual field in 5° steps (Fig. 2). A two lens relay system was built to enable fixation at the targets mounted on the wall 3 m away. An average of 3 measurements was taken as the refraction for each field angle. Second-order Zernike aberration coefficients were used to determine horizontal and vertical refraction components at 555 nm, for 3 mm elliptical pupils.

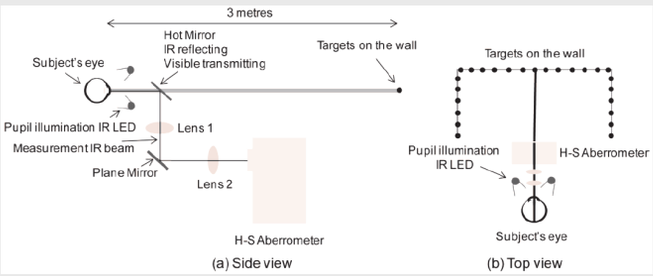

Fig. 2. Setup of aberrometer

Discussion
We categorised refraction patterns according to Rempt et al's scheme. Some participants showed a rapid hypermetropic shift towards the edge of the field and we introduced a new Type IV/I group that shows the characteristics of type IV out to an angle of between 40° and 50° before behaving like type I. subjects fitted this pattern, which we placed between III and IV (Fig. 1e). Nine of 30 and 8/30 subjects fit type IV/I and IV respectively, with smaller numbers in the other groups Comparing the participant groups and without applying any statistics, the trend is for a shift from type I to type V as refraction moves from myopia to hypermetropia, consistent with the trend reported by Rempt et al. (see Table).

Refraction Group	Peripheral Refraction Pattern						Total
	I	II	III	IV/I	IV	V	
myopes	3	1	3	2	1	1	11
emmetropes	0	1	2	7	2	1	13
hypermetropes	0	0	0	0	5	1	6
total	3	2	5	9	8	3	**30**

Conclusion
A sizable minority of eyes have a horizontal field peripheral refraction pattern that is a combination of Rempt et al.'s type IV and type I patterns, having the characteristics of type IV (relative hypermetropia along the vertical meridian and relative myopia along the horizontal meridian) out to an angle of between 40° and 50° before behaving like type I (both meridians show relative hypermetropia).

References
[1] F. Rempt et al. Ophthalmologica, **162**, 1-10, 1971
[2] M. Millodot. Am J Optom Physiol Opt, **58**, 691-695, 1981
[3] J. Gustafsson et al. Ophthal Physiol Opt, **21**, 393-400, 2001
[4] D.A. Atchison et. al. Optom Vis Sci, **87**, 823-832, 2006

[5780]

13:00-14:00 Lunch break UCD Main Restaurant

14:00-15:30
POSTER SESSION II & COFFEE BREAK
Room: Exhibition area

NOTES

15:30-17:00
MULTIPHOTON IMAGING AND ANALYSIS OF THE EYE
Session Chair: J. Carroll, Medical College of Wisconsin & Marquette University (US)

15:30-16:00 **Invited talk**

Two-photon imaging of the retina

J.J. Hunter[1A,B], R. Sharma[1B,C], B. Masella[1B,C], L. Yin[1B], W.H. Merigan[1A,B], G. Palczewska[2], K. Palczewski[2,3], D.R. Williams[1A,B,C]; [1]University of Rochester, [A]Flaum Eye Institute, [B]Center for Visual Science, [C]The Institute of Optics, Rochester, NY, 14642 (US); [2]Polgenix, Inc., Cleveland, OH, 44106 (US); [3]Department of Pharmacology, Case Western Reserve University, Cleveland, OH, 44106 (US).
Email: jhunter@cvs.rochester.edu

Summary
In vivo two-photon fluorescence imaging of the retina has the potential to not only provide images of cellular structure, but also probe retinal function in the healthy and diseased eye. Progress has been made to overcome the many obstacles to transferring this technique from imaging *ex vivo* retina to safely imaging the retina in the living eye.

Introduction
Microscopic imaging of the retina can provide insight into retinal structure and function at the cellular scale in the normal and diseased eye. Although many of the molecules involved in visual function are intrinsically fluorescent, the anterior optics of the living human eye are opaque to the wavelengths required for single photon fluorescence excitation. By using considerably longer excitation wavelengths, two-photon fluorescence imaging has the potential to access these otherwise unreachable fluorophores and provide intrinsic contrast for imaging a number of retinal structures. In addition, two-photon imaging has the potential to image retinal cell classes that have evolved to be transparent to visible light, and are therefore invisible with other imaging modalities. We have used an adaptive optics scanning laser ophthalmoscope (AOSLO), to overcome the challenges of eye motion and poor optical quality to obtain two-photon fluorescence images from the living monkey [1] and mouse [2] retina.

Discussion
Both naturally occurring intrinsic fluorophores and non-native extrinsic fluorophores may now be imaged with two-photon fluorescence in the living eye. The specific intrinsic fluorophores imaged *in vivo* in photoreceptors are as yet unknown, although they are most likely molecules involved in metabolism (e.g. NADH) or the visual cycle (e.g. retinoids or bisretinoids) [3]. In *ex vivo* retinal samples, intrinsic fluorescence can be observed in all retinal layers, suggesting the potential to visualise these cells in the living eye. Furthermore, by varying the excitation wavelength and/or emission bandpass there is potential to investigate multiple fluorophores and thereby probe different cellular functions [4].
Because it allows imaging at infrared wavelengths that do not directly excite photoreceptors, two-photon fluorescence imaging is ideal for studying retinal function. Beyond imaging the intrinsic fluorescence of retinoids and metabolites, extrinsic fluorophores can be used to quantify changes in cellular dimensions associated with visual stimulation, or to study neuronal function using calcium indicators such as G-CaMP.

Conclusion
Two-photon fluorescence imaging of both intrinsic and extrinsic fluorophores may provide great insight into retinal structure and function in the living eye.

References
[1] J.J. Hunter *et al.*, *Biomedical Optics Express*, **2**, 139-148, 2011
[2] R. Sharma *et al.*, *IOVS*, ARVO e-Abstract 5600, 2012
[3] C. Chen *et al.*, *Biophysical Journal*, **88**, 2278-2287, 2005
[4] G. Palczewska *et al.*, *Nature Medicine*, **16**, 1444–1449, 2010

[5787]

Room: Clinton Auditorium

16:00-16:15

Multimodal multiphoton imaging (THG-SHG-2PEF) of the human cornea

N. Olivier[1], G. Latour[1], F. Aptel[2,3], A. Deniset-Besseau[1], J.-M. Legeais[3], K. Plamann[2], M.-C. Schanne-Klein[1], E. Beaurepaire[1]; [1]Lab. for Optics and Biosciences, Ecole Polytechnique, CNRS, INSERM, 91128 Palaiseau (FR); [2]Laboratoire d'Optique Appliquée, ENSTA ParisTech, 91761 Palaiseau (FR); [3]Lab. Biotechnologie et Œil, Univ. Paris V, Hôpital Hôtel Dieu, 75181 Paris (FR).
Email: emmanuel.beaurepaire@polytechnique.edu

Summary
We evaluate the combination of third-harmonic generation (THG), second-harmonic generation (SHG), and two-photon-excited fluorescence (2PEF) for ex vivo imaging of intact human corneas, with particular emphasis on understanding THG contrast mechanisms.

Introduction
Non-invasive optical methods that enable *in situ* visualization of tissue components are of particular relevance in ophthalmology. Nonlinear microscopy is attractive for obtaining virtual biopsies because it can provide several complementary modes of contrasts. We evaluate the combination of third-harmonic generation (THG), second-harmonic generation (SHG), and two-photon-excited fluorescence (2PEF) for imaging intact human corneas, with particular emphasis on understanding THG contrast mechanisms [1-2].

Results
Imaging was performed on a custom-built laser scanning THG-SHG-2PEF microscope. Simultaneous THG/SHG imaging was performed with 1200 nm excitation and trans-detection of both signals. Simultaneous 2PEF/SHG imaging was performed with 730 nm or 860 nm excitation, usually with epidetection of the 2PEF signal and trans-detection of SHG.
Nonlinear signals can be detected over entire freshly excised corneas. 2PEF imaging reveals intracellular fluorescence. SHG imaging probes the distribution of stromal collagen lamellae organization. THG imaging reveals tissue morphology, including the epithelium and endothelium structure [1]. A stromal THG signal is also observed at the interfaces between collagen lamellae, resulting from changes in anisotropy direction. Cellular and anisotropy-related THG signals can be distinguished using polarization-resolved imaging [2]. Typical images of unstained epithelium and stroma are shown in the figure below.
Multimodal imaging provides a detailed description of several key corneal components. We note that coherent nonlinear images (THG and SHG) rely on specific contrast mechanisms, and that their interpretation requires a careful analysis. We discuss the contrast mechanisms in these images, based on our previous studies [3-5].

Conclusion
Our data show that combined THG-SHG-2PEF microscopy is a very effective method for evaluating corneal microstructures in intact tissue, which should prove appropriate for studying corneal and glaucoma physiopathologies.

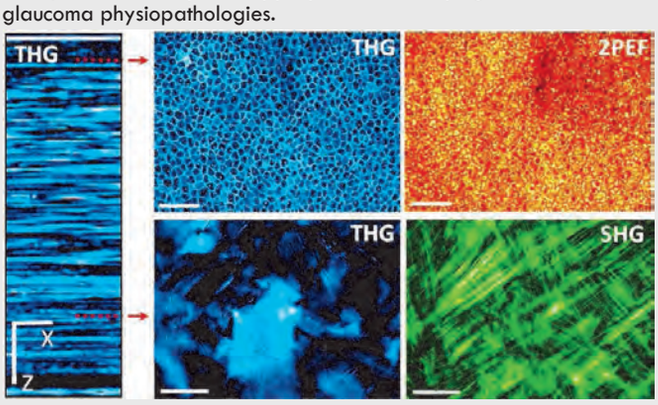

Fig.: Multimodal THG-SHG-2PEF imaging of excised human corneas at different depths. The left panel is a XZ reprojection of an image stack acquired in XY geometry. Scale bars: left: 20 µm (X) and 100 µm (Z) – right: 50 µm.

Acknowledgments
Human cornea specimens were obtained under permission from the Banque Française des Yeux (French Eye Bank), Paris. This work was partly supported by the Délégation Générale pour l'Armement and by the Fondation de la Recherche Médicale.

References
[1] Olivier et al, Opt Express 18, 5028 (2010).

[5674]

16:15-16:00

In vivo polarization-resolved SHG imaging of the corneal microstructure

G. Latour[1], I. Gusachenko[1], L. Kowalczuk[2], I. Lamarre[1], M.-C. Schanne-Klein[1]; [1]Ecole Polytechnique - CNRS – INSERM U696, Laboratory for Optics and Biosciences, 91128 Palaiseau (FR); [2]ENSTA ParisTech - Ecole Polytechnique – CNRS, Laboratory for Applied Optics, 91128 Palaiseau (FR).
Email: gael.latour@polytechnique.edu

Summary
We used polarization-resolved SHG microscopy in unstained human corneas to determine the orientation of the nanometer-sized collagen fibrils in the stromal lamellae, even though backward SHG images were spatially homogenous. We then implemented this technique *in vivo* to map the stromal microstructure in rat corneas.

Introduction
Multiphoton microscopy has been shown to be a promising method for obtaining virtual biopsies in unstained corneas[1]. In particular, forward Second Harmonic Generation (F-SHG) images exhibit striated features that reveal the orientation of collagen fibril within lamellar domains. Nonetheless, backward SHG (B-SHG) images provide no structural information about these nanometer-sized fibrils because of different phase-matching conditions, which is a strong limitation for *in vivo* imaging.
To overcome this limitation, we implemented polarization-resolved SHG microscopy[2]. Polarization resolved techniques are indeed highly sensitive to the submicrometer distribution of anisotropic structures within a sample, much below the optical resolution, as routinely exploited in ellipsometry measurements. We showed that polarization-resolved SHG enables mapping the orientation of sub-micrometer scale collagen fibrils at each depth in human corneas[3]. Comparison with numerical simulations confirmed that our experimental approach probes accurately the direction and heterogeneity of the collagen architecture[4]. We also performed *in vivo* SHG imaging of rat corneas and demonstrated structural imaging of corneal stroma without any labelling and despite the vital movements of the animal.

Results and discussion
We first imaged rat-tail tendons to characterize the linear propagation effects that may affect polarization-resolved SHG imaging of thick anisotropic collagen tissues2. We verified that there is no diattenuation of the incident excitation in the cornea which results in reliable polarization-resolved measurements at any depth4.
We studied 7 human corneas, obtained from the French Eye Bank (BFY, Paris, France), which were unsuitable for transplantation. F-SHG images exhibited striated spatial features, while B-SHG images were nearly homogeneous at the micrometer scale and did not provide any structural information about the corneal stroma (see Figure 1). However, polarization-resolved F-SHG and B-SHG signals enabled the determination of the orientation of collagen fibrils within the lamellar domains
because collagen fibrils exhibit a larger SHG signal (resp. smaller SHG signal) when aligned parallel (resp. perpendicular) to the incident linear excitation field. Together with the orientation, the SHG anisotropy parameter $\rho=\chi_{xxx}/\chi_{xyy}$ was measured all along the depth of the cornea. The orientations determined by this method showed a good agreement with the orientations of the striated features in the F-SHG images, which confirmed that F-SHG images directly reveal the orientation of the collagen fibrils in stromal lamellar domains. Moreover, the orientations determined by polarization-resolved

SHG imaging were consistent for F-SHG and B-SHG signals. It showed that polarization-resolved SHG microscopy is a robust and effective technique to determine the orientation of sub-micrometer-sized collagen fibrils.

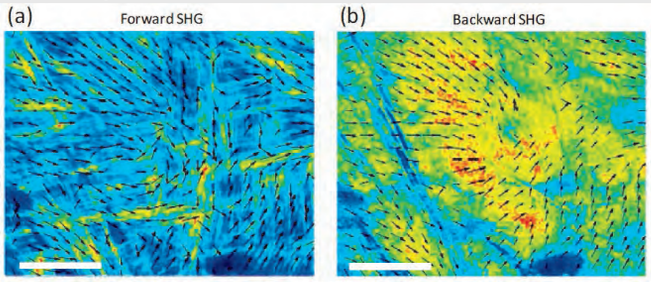

Fig. 1: (a) Forward and (b) backward SHG imaging of human cornea. Fibrils orientation is calculated from polarization-resolved SHG and plotted with overlayed arrows. Scale bar: 50 µm.

Moreover, we evaluated the accuracy of SHG polarimetry at the interface between two lamellae. The axial resolution of SHG imaging is indeed close to the thickness of the lamellae that are stacked along the depth of corneas and most images have contributions from two adjacent lamellae with different orientations. To address this question, we performed numerical calculations accounting for the Gouy phase shift that results in quadrature phase shifted contributions on both sides of the focal plane4. We obtained an excellent agreement with experimental results, which showed that ρ probes heterogeneities of the fibrillar collagen organization within the focal volume and that the orientations are accurately determined at any depth.
Finally, we performed *in vivo* polarization-resolved SHG microscopy in anesthetized Wistar rats and successfully retrieved the orientation of collagen fibrils despite the vital movements[3].

Conclusion
Our study showed that polarization-resolved SHG microscopy is a valuable imaging technique to probe the sub-micrometer architecture of cornea. Moreover, our demonstration of *in vivo* polarization-resolved SHG microscopy opens great opportunities for further biomedical studies.

Acknowledgments
We acknowledge the French Eye Bank for the supply of the corneoscleral discs. G. Latour was supported by RTRA-Triangle de la Physique and Fondation de France and L. Kowalczuk was supported by the ANR TechSan 025 NOUGAT.

References
[1] F. Aptel, N. Olivier, A. Deniset-Besseau, J.-M. Legeais, K. Plamann, M.-C. Schanne-Klein and E. Beaurepaire, *Invest. Ophthalmol. Vis. Sci* **51**, 2459 (2010)
[2] I. Gusachenko, G. Latour, M.-C. Schanne-Klein, *Opt. Express* **18**, 19339 (2010).
[3] G. Latour, I. Gusachenko, L. Kowalczuk, I. Lamarre, and M.-C. Schanne-Klein, *Biomed. Opt. Express* **3**, 1 (2012).
[4] G. Latour, I. Gusachenko, L. Kowalczuk, I. Lamarre, and M.-C. Schanne-Klein, in *Proc. SPIE* **8226** 8226-46 (2012)

[5696]

16:30-17:00
Discussion: Can we separate optical from neural effects?

Discussion leader:
D. Atchison, Queensland University of Technology (AU)

17:00 **EOS Student Award**

17:15 **End of EOS Topical Meeting**

NOTES

Room: Exhibition area

POSTER SESSION I:
Monday, 20 August | 14:00 - 15:30 CEST

EMVPO2012_5432_001

Clinical measurements: entries of factor matrices of the dioptric power matrix

H. Abelman, S Abelman; School of Computational and Applied Mathematics, University of the Witwatersrand, Johannesburg, Private Bag 3, Wits, 2050 (ZA).
Email: *Herven.Abelman@wits.ac.za*

Summary
Many observed and measured ophthalmic quantities symbolized on an annotated optical cross and expressed in principal meridional form are characteristic of, belong to, or have been "zoomed in from" their dioptric power matrix and are represented by its eigenvalues and -vectors. We explain how to zoom in holistically from their information-laden power matrix to powers and associated meridians, measureable in the clinic, and zoom out back to this matrix for distinct meridians that are perpendicular or not. Nonsingular matrices containing eigenvalues and –vectors are some of the factors of the dioptric power matrix that make the process reversible.

Introduction
Eyes that reveal an effective difference in the curvature of the meridians of the refracting media will manifest astigmatism. Ametropia along meridians of greatest and least curvature, at right angles to one another for continuous surfaces, can be compensated using characteristic, paraxial, task-specific information. All other meridians are then simultaneously compensated except in cases of irregular astigmatism.

Discussion
Matrices are more universal in that they can disclose information for not only principal meridians and can also contain information on irregular astigmatism. As members of a vector space, matrices are processed in most cases and their entries are unique for powers expressed in all the clinical, but ambiguous ways.

Conclusion
Our analysis quantifies uneven corneal surfaces left by a laser during refractive surgery where irregular astigmatism results. An asymmetric dioptric power matrix is characteristic of the uneven surface created by the laser. Scalar power and regular astigmatism are also present.

References
[1] Long WF. Am J Optom Physiol Opt **53**, 27-33, 1976.
[2] Keating MP. Am J Optom Physiol Opt **58**, 1154-1160, 1981.
[3] Anton H, Rorres C. Elementary Linear Algebra: Applications Version. Drexel University: John Wiley & Sons; 2010.
[4] Harris WF. Optom Vis Sci **74**, 349-366, 1997.
[5] Abelman H. Ophthal Physiol Opt **26**, 426-30, 2006.
[6] Zalevsky Z, Ben Yaish S, et. al. Optics Express **15**, 10790-10803, 2007.
[7] Wang M, Irregular Astigmatism: Diagnosis and Treatment. New Jersey: Slack Incorporated; 2008.
[8] De Stefano VS, Melo Junior LAS, et al. Arq Bras Oftalmol **73**, 363-6, 2010.

NOTES

EMVPO2012_5561_002 STUDENT PRESENTATION

Spherocylindrical error for oblique gaze regarding the position of the center of rotation

S. Perchés, F. Palos, V. Collados, J. Ares; Universidad de Zaragoza, Departamento de Física Aplicada, Zaragoza, 50009 (ES).
Email: sperches@unizar.es

Summary
In this work, the influence of the position of the center of rotation of the eye (CRE) on the performance of a set of monofocal spherical lenses is analyzed. The aim was to determine whether the customization according to the CRE contributes to improve the visual quality for oblique gaze (40 degrees). Results indicate that the negative lenses are the most sensitive to the choice of the CRE value.

Introduction
In recent years, the arise of computer numerically controlled (CNC) [1] fabrication technology has allowed the launch to the market of ophthalmic lens designs customized to different wearing conditions. At the same time, to close the loop, different measuring devices of these visual parameters (vertex distance, Galve angle, pantoscopic tilt …) have also been developed. However, at the present moment, the real visual quality gain of these products is not well established. One of the parameters involved in the design of customized ophthalmic lenses is the position of CRE. In this work, we try to find rules of thumb about the situations in which customization can be more suitable than conventional lenses. We evaluate the influence of the CRE customization on the vision quality in oblique gaze (40 degrees) regarding the power and base curve of the lenses.
Conventional ophthalmic lenses were designed with back vertex powers ranging from +8 to -10 D in 2 D steps with spherical geometry and several base curves. For each design, the spherocylindrical error for oblique direction of gaze was computed for different CRE positions (20, 27 and 35 mm measured from the back vertex of the lens).
The calculations were performed by two different methods:
1) Analytical calculation using Coddington´s equations [2]
2) Calculation using a Ray tracing commercial software (OSLO® Light 6.1, Lambda Research Corporation)

In order to evaluate the obtained results, a 0.5 D of spherocylindrical error was selected as threshold value. As a consequence, two different groups were determined: the ones that achieve errors lower than the threshold were considered as well behaved lenses, being the other ones considered as bad behaved lenses.

Discussion
The two analysis methods show differences in results. The reason is that the analytical calculation considers third-order and thin lens approach. Therefore, the method based on numerical ray tracing was the most accurate when computing the spherocylindrical error. Regarding the obtained results by numerical ray trace we have seen that, in general, the negative lenses are more sensitive to the choice of the CRE value than the positive lenses studied.
More particularly, we have also seen that the negative lenses made with base 2 are the exception to this general trend. In fact, the negative lenses made with base 2 have values of spherocylindrical error below 0,5D for all the powers and CRE studied.
It was also outstanding, that the low and median power positive lenses (between 2D and 4D) made with high base curve (6-8 D) have error are well behaved lenses regardless of the CRE of the patient. Nevertheless, the high power positive lenses (between 6D and 8D) have error values above 0,5D regardless of CRE and base curve manufactured. Determine whether high power positive lenses can be benefited for CRE customized aspherical designs must be a subject for further researching.

Conclusions
By ray tracing techniques is possible to estimate the spherocylindri-

cal error for ophthalmic lenses for oblique gaze.
Our analysis allows us to select the best base curve for each power as a function of the center of rotation of the eye.
On the one hand, we have seen that negative lenses are the most sensitive to the choice of the CRE value. However it is possible to find one quite well behaved spherical lens design for each CRE.
On the other hand, we have also seen that the high power positive spherical lenses are bad behaved for oblique gaze regardless the CRE and base curve selected.

Reference

[1] D.J. Meister, "*Free-Form Surfacing Technology Makes Possible New Levels of Optical Sophistication for Spectacles*". Refractive Eyecare for Ophthalmologists 9(6), 29-32 (2005)
[2] J. Landgrave, J. Moya-Cessa, "Generalized Coddington equations in ophthalmic lens design," J. Opt. Soc. Am. A13, 1637-1644 (1996)

EMVPO2012_5564_003

Effects of contrast, cut-off spatial frequency and phase of the OTF on visual acuity and subjective image quality score

R. Legras[1], A.P. Sansot[1], G. Vandermeer[2], Y. Nochez[2], R. Navarro[3]; [1]Université Paris-Sud, Laboratoire Aimé Cotton, Orsay, 91405 (FR); [2]Université François Rabelais, Faculté de médecine, Tours, 37000 (FR); [3]Consejo Superior de Investigaciones Científicas & Universidad de Zaragoza, ICMA, Zaragoza, 50009 (ES).
Email: richard.legras@u-psud.fr

Summary
We evaluated the separated effects of a loss of contrast, sharpness, phase and a pure defocus on high-contrast tumbling-E visual acuity (VA) and subjective quality of image, by means of an adaptive optics visual simulator.

Introduction
Retinal images suffer from optical blur, given by the Optical Transfer Function (OTF). Its modulus (the MTF) expresses the loss of contrast and sharpness (cut-off spatial frequency, COF), whereas its phase describes spatial shifts between frequencies (phase shift). These are the main factors affecting optical image quality, and hence they induce a loss of visual acuity and quality of vision.

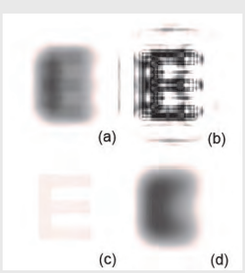

Fig 1. Example of image degradations: (a) pure defocus, (b) phase shift, (c) contrast and (d) cut-off spatial frequency

The aim of this experiment was to evaluate the effects of these three factors (contrast, cut-off frequency and phase) separately. The COF is a scalar variable, but contrast and phase are 2D functions in general. To somehow convert them to scalar variables, the contrast was assumed constant within the frequency interval $0 < f <$ COF; the phase of the OTF was that of a pure defocus, given in diopters. In this way a synthetic OTF was obtained combining that phase with a MTF, which was a cylinder with radius COF, and height given by the contrast (plus a delta function at $f = 0$).
We calculated the appearance of images on 5 -mm pupil diameter, degraded either by a loss of contrast (i.e. 1; 0.5; 0.25; 0.12 and 0.06) or by a lower cut-off spatial frequency (i.e. 50; 25; 12 and 6 c/deg) or by the phase shifts (i.e. 0.05; 0.10; 0.25; 0.5; 0.75; 1; 1.25; 1.5 diopters of pure defocus for 5 mm pupil). As a reference, these synthetic degradations were compared to that caused by pure defocus (modulus and phase), for the same diopters. These types of degradations are illustrated figure 1.

Discussion
We measured these effects on degraded high-contrast tumbling-E visual acuity and on subjective score. Five subjects, aged between 22 and 40 years, scored three times the quality of each simulated image (three 0.4 logMar letters) using a continuous 5-items grading scale according to the ITU recommendations [1]. Their visual acuities under the various conditions were also measured three times. To limit the degradation due the observer's eye optics, the simulated images were viewed through a dynamic correction of aberrations (CRX1TM, Imagine Eyes) and an artificial pupil of 3mm. They were displayed on an EmaginTM micro display coupling with a colour filter ensuring a monochromatic light (i.e. 550 ± 50nm).
The averaged intra-individual standard deviation (SD) was 0.03 logMar and 0.15 grade, the larger difference of SD between subjects and type of degradation was observed with image quality score. The averaged inter-individual SD was 0.03 logMar and 0.27 (dimensionless) grade. These SD were largely under clinical significant difference (i.e. 0.1 logMar and a difference of grade of 1).
Figure 2 illustrates the loss of visual acuity and the subjective score as a function of type of image degradation. We normalized the results to obtain respectively the best and worst VA corresponding to the best and worst score for the defocus condition (see figure 2a).
When lowering the COF, only the sharpness of the letter is degrading (see figure 1d)

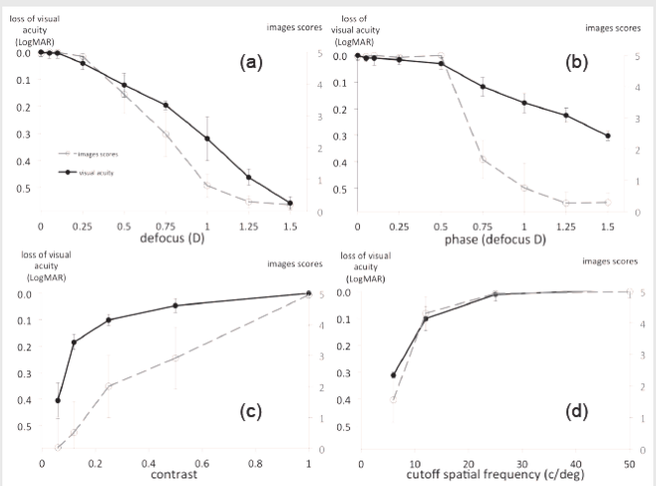

Fig 2: Visual acuity loss and subjective score as function of defocus (a), phase shift (b), contrast (c) and cut-off spatial frequency (d).

Conclusions
The cut-off frequency induces a comparable loss of VA and subjective score. However, a loss of contrast or phase shift appeared to have a more detrimental effect on VA than on subjective score. Considering a given loss of VA, we are subjectively more affected by a phase shift or loss of contrast than by a loss of sharpness (lower COF) or a pure defocus error.

References

[1] ITU-R, Methodology for the subjective assessment of the quality of televisionpictures, Recommendation ITU-R BT, 500-506, 1974-2002.

EMVPO2012_5570_004

The changes of shape of the human cornea with age

R. Navarro[1], J.J. Rozema[2], M.-José Tassignon[2]; [1]ICMA, Consejo Superior de Investigaciones Científicas & Universidad de Zaragoza, Zaragoza, 50009 (ES); [2]Department of Ophthalmology. Antwerp University Hospital, Wilrijkstraat 10, 2650 Edegem (BE).
Email: rafaelnb@unizar.es

Summary
The shape of the aging cornea was studied in a group of 407 normal eyes. The most significant changes found were: a small increase of the curvature, eccentricity and irregularity of the anterior surface with age. For both the anterior and posterior surfaces the misalignment with the keratometric axis increased with age.

Introduction
There are several studies on the mean corneal shape based on fitting the surface topography to a given model. The most popular models divide the surface elevation S into a regular basis surface, B (with a straightforward optical interpretation, such as spheres, conicoids, 3 axes ellipsoids or biconics) plus a residual R = S – B which

accounts for local irregularities and departures from the basis surface B. It is also common to fit the residual to a Zernike polynomial expansion. In an earlier study [1] the geometry and optical properties of the mean cornea were analyzed using a general 3-axis ellipsoid, so that we could determine the position *(x0, y0, z0)* and orientation *(α, β, γ)* of the optical axis in the 3D space. The strength of that B model was patent as it provided significant lower fitting errors than standard (canonical) models. Here we apply a similar approach to a larger set (407 corneas), covering a wide range of ages (4 - 79 years) [2]. The measurements were taken with a Scheimpflug system (PentacamTM) which provides topographies of both front and back surfaces [3]. The B model was also improved and generalized to a general biconic defined by 10 parameters: apex radii (R_{Max}, R_{min}), conic constants (Q_{Max}, Q_{min}) plus position and orientation in space. The residual R was analyzed by a 8th order Zernike polynomial expansion.

Discussion

The RMS residual (fit error) shows marked differences between the anterior ($<RMS_{ant}>$ = 5.7 μm) and posterior ($<RMS_{pos}>$ = 14.6 μm) surfaces (S_{ant} and S_{pos}). This suggests that the biconic is a good model but only for the anterior surface. Interestingly, this residual slightly increases with age for S_{ant} but shows the opposite trend for S_{pos}. Fig. 1 shows the evolution of the horizontal (β) and vertical (α) angles between the biconic and keratometric axes. The linear regression shows a clear trend to increase both angles (misalignment) with age. Even though the predictability is poor due to a high intersubject variability, such trend has a high statistical significance (p-values 0.0236 and 0.0033 for β_{ant}, and β_{pos}; and even lower p-values for α). In addition there is a clear misalignment between S_{ant} and S_{pos} of ~2.5° for both angles. Similar plots were obtained for radii, conic constants and apex coordinates for both surfaces. The radii of the anterior surface were found to decrease slightly but significantly ($P < 0.01$) with age ($<R_{Max}>_{ant}$ = 7.85 - 0.0047·age mm; $<R_{min}>_{ant}$ = 7.70 - 0.0040·age), as well as the conic constant along the meridian of maximum curvature for both surfaces ($<Q_{min}>_{ant}$ = -0.30-0.0025·age; $<Q_{min}>_{pos}$ = - 0.55 -0.0024·age). Several parameters, on the other hand, remained constant with age, such as the apical radii of the back surface ($<R_{Max}>_{pos}$ = 6.27 ± 0.26 mm; $<R_{min}>_{pos}$ = 5.92 ± 0.30 mm); the conic constant along the axis of minimum curvature for both anterior and posterior surfaces ($<Q_{Max}>_{ant}$ = -0.38 ± 0.13; $<Q_{Max}>_{pos}$ = -0.49 ± 0.14 mm) do not change significantly with age; and Euler angle γ, corresponding with the astigmatism axis, which on average is close to vertical, but shows a large intersubject variability.

The statistical analysis presented so far is somewhat preliminary in the sense that it is based on the complete set without removing outliers. Nevertheless, it is worth noting that this will probably affect the exact values of parameters, but the main trends and conclusions are expected to be basically the same.

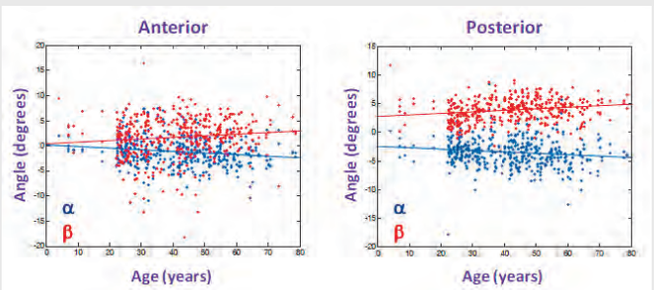

Fig 1. Changes of Euler angles (α,β) of the best fit biconic with age, for the anterior (left) and posterior (right) corneal surfaces.

Conclusions

These results confirm previous findings, such as the increase of the corneal power, or the tendency of the cornea to become more prolate with age [3]. In addition, the biconic model permits to identify that the conic constant has a maximum change along the meridian of maximum curvature (no change in the orthogonal one). A new finding (to our knowledge) is that our results suggest a significant progressive tip/tilt of the optical axis of the (best fit) biconic with age, for both anterior and posterior corneal surfaces.

References

[1] R. Navarro, L. Gonzalez, and J. L. Hernandez-Matamoros, "Optics of the average normal cornea from general and canonical representations of its surface topography," J.Opt. Soc. Am. A 23, 219–232 (2006).
[2] J. J. Rozema, D. A. Atchison and M. J. Tassignon, "Statistical Eye Model for Normal Eyes", Invest. Ophthal. Vis. Sci., 52, 4525-4533 (2011).
[3] M. Dubbelman, V.A.D.P. Sicam, G.L. Van der Heijde, "The shape of the anterior and posterior surface of the aging human cornea", Vision Res. 46, 993–1001 (2006).
Supported by grant FIS2011-22496 (Spain)

EMVPO2012_5669_005 **STUDENT PRESENTATION**

Alternative Methodology for Intraocular Lenses Characterization

F.T. Amaral, D.W. de Lima Monteiro, Universidade Federal de Minas Gerais - UFMG, Department of Electrical Engineering, Belo Horizonte, MG, Av. Antônio Carlos 6627, 31270-010 (BR).
Email: felipetayer@ufmg.br

Summary

This paper presents an optical setup for an alternative methodology to characterize intraocular lenses using a Hartmann-Shack wavefront sensor. The methodology is based on the ANSI Z8030 Standard and aims to simplify the procedure therein presented, allowing complete IOL characterization by a single measurement.

Introduction

The use of intraocular lens (IOL's) implants has increased in the past few years, and their designs have improved considerably alongside. Patients' vision quality after the crystalline lens replacement depends on the IOL topography, which can be assessed by wavefront analysis. This has become a very popular technique in the ophthalmology field.

The ANSI Z8030 Standard [1] proposes a method for IOL characterization that uses an optical setup with a wavefront sensor. However, this method is slow and complex requiring successive measurements and the acquisition of a large amount of data to run an optimization process that enables complete IOL characterization.

This paper proposes an optical setup based on the ANSI Standard, also deploying a conventional wavefront sensor, and an alternative methodology for the complete IOL characterization with a single measurement. It is expected that this methodology is simpler and faster than the ANSI method, besides reducing the overall opticalsetup cost when compared to commercial solutions. The measurement time is important, especially when characterizing the lenses in production lines.

Discussion

The Standard ANSI Z8030 establishes a procedure for monofocal and toric refractive IOL characterization, where optical topographies are quantified in terms of Zernike Polynomials and their respective coefficients (C_n^m) [2]. The method recommended by ANSI consists of a point laser source, the IOL under test, and relay lenses to ensure that the wavefront on both the IOL and wavefront sensor planes exhibit identical phase profiles. The effective power (spherical equivalent), or the effective focal length can be determined through systematic measurement of the wavefront radius of curvature as a function of source position.

The optical setup established by the Standard has an encoder position sensor to measure the laser source position related to a reference point. The IOL spherical equivalent power (C_2^0) is determined by successive measurements of the IOL

curvature (wavefront sensor) as a function of its position (encoder) from a point source created by a laser through a pinhole. The optical setup proposed here has a precision opto-mechanical component to remove the IOL from the optical path. The characterization procedure consists in measuring the wavefront twice, i.e. when the IOL is positioned at focal length from the point source, and when the IOL is removed from the optical path. The wavefront resulting from the difference between the two measurements contains the most significant IOL topographical data, decomposed in Zernike polynomials, including that related to the IOL spherical equivalent power (C_2^0). The

optical setup also has a caliper to measure the point source distance to the IOL position allowing the direct determination of IOL focal length ($f_{caliper}$). The IOL focal length is also calculated from the measured term (C_2^0)(f_{calc}) [1], and the difference between $f_{caliper}$ and f_{calc} determines the focal-length measurement error.

Results

Although the setup is rather generic, we have chosen as a proof of concept seven PMMA IOL's manufactured by Mediphacos Ltda. All of the IOL's had been previously characterized with a commercial equipment, compliant to the ANSI Standard. Table 1 shows the measured dioptric power by the commercial equipment (DP_{ANSI}) and by the new methodology (DP_{NEW}), and the calculated dioptric power from the measured radius of curvature and the central thickness (DP_{CALC}) [3]. The radii of curvature and the central thicknesses were measured by another commercial equipment, Brassiola, and by a digital micrometer, respectively.

Table 1. IOL dioptric powers measured by the commercial equipment and by the new methodology.

#	DP_{ANSI} [D]	DP_{NEW} [D]	DP_{CALC} [D]
1	22.50	22.34	22.12
2	22.42	22.42	22.11
3	22.52	22.76	22.10
4	25.66	25.11	25.09
5	25.64	25.28	25.07
6	25.62	25.07	25.07
7	25.73	25.94	25.07

The standard ANSI Z8030 establishes the tolerances for the measured IOL spherical dioptric power, which is ±0.4D. The dioptric power error is the difference between the measured dioptric powers (DP_{ANSI} and DP_{NEW}) and DPCALC. All measurements with the commercial equipment obtained dioptric power errors larger than 0.4D. Measurements with the new methodology resulted in dioptric power errors larger than 0.4D only for IOL's 3 and 7 (0.42D and 0.66D respectively). It is important to highlight that DP_{CALC} is the nearest dioptric power to the actual values. Measurements of cylindrical power, longitudinal spherical aberration and MTF will be presented in the full version of this paper, where the influence of the dioptric value for IOL's 3 and 7 will also be evaluated based on the general lens deviation from spherical.

Conclusion

The optical setup for IOL characterization presented in this paper provides more information about the IOL, such as MTF curves and a two-dimensional map for spherical aberration, besides being a potentially lower cost alternative in comparison to the existing commercial solutions. With the new methodology, IOL's are completely characterized by a single measurement, eliminating the somewhat complex and numerous steps proposed by the Standard ANSI Z8030. The characterization process provides fundamental characteristics of IOL's that directly impact patient's vision quality. High amplitude of the higher order aberrations also provides important information regarding their manufacturing quality.

References

[1] THE ACCREDITED COMITTEE Z80 FOR OPTHTALMICS STANDARDS. American National Standard for Ophthalmics - Toric Intraocular Lenses. 2010. (Z8030).

[2] NOLL, R. J. Journal of the Optical Society of America, v. 66, n. 3, p. 207-211, 1976.

[3] HECHT, E. Optics. India: Pearson Education, 2003.

EMVPO2012_5672_006

Theoretical evaluation of different corneal models for the correction of presbyopia by laser refractive surgery

R.G. Anera, A. Alarcon, J.R. Jimenez, M. Soler; Laboratory of Vision Sciences and Applications, Departamento de Óptica, Universidad de Granada, Granada, 18071 (ES)

Email: rganera@ugr.es

Summary

Theoretical comparison of a Q-optimized aspheric corneal model and two multifocal corneal models designed to correct presbyopia by laser refractive surgery. For each model we evaluated the visual quality, the ablation profiles and the postsurgical asphericity.

Introduction

Corneal ablation by laser has become a steadily more common treatment for presbyopic patients. The objective of this work is to compare theoretically one Qoptimized aspherical model (similar to the one proposed in monovision for expanding depth of focus in the eye corrected for near vision, optimizing the Q value [1]) and two multifocal corneal models: a central model (CM), with a central corneal zone for near vision and a peripheral zone for distance vision, and a peripheral model (PM), with a central zone for distance vision and a peripheral zone for near vision [2,3].
The models were optimized with the aim of achieving the best visual quality possible both for distance and near vision, considering two different near addition values: +1D and +2.5D. The analysis was made using the Liou-Brennan eye model [4] and ray tracing with the commercial optical-design software ZEMAX. To assess the visual quality, we calculated the Neural Sharpness (NS), determined by the Point Spread Function [5].

Discussion

Our results show that the peripheral model requires a greater ablation depth (Fig 1). Furthermore, the ablation depth significantly increases as the near addition power rises. Both the central model as the aspheric model has negative asphericities on average, as well as negative spherical aberration. However, both the asphericity as well as the spherical aberration take positive values in the peripheral model. Also, the peripheral model presents a higher value for wavefront aberrations.

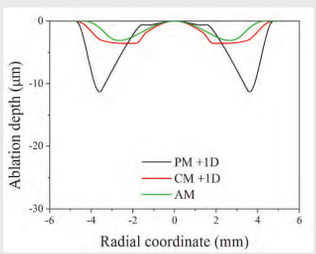

Fig 1. Ablation profiles (Near addition power +1D)

Despite the differences found, our results show that both multifocal models provide approximately the same visual quality Fig 1. Ablation profiles (Near addition power +1D) and respond similarly with respect to the variations in the pupil, though opposite. Our results indicate that the Q-optimized aspheric model is feasible only with small additions. For large additions, the aspheric model, even for very negative asphericities, behaves in a completely monofocal way. In all the models analysed, we found that whatever was gained in the quality of the near vision was lost in the distance vision and vice versa. Therefore, although it is possible to improve visual quality in near vision of a subject with presbyopia, this will always bear the cost of worsening distance vision.

Conclusions

The multifocal cornea with central near zone provides better results since it requires less ablated corneal surface area, permits higher addition values, presents more stable visual quality with pupil-size variations and lower high-order aberrations.

References

[1] A. Alarcón, R.G. Anera, C. Villa, L. Jiménez del Barco, R. Gutierrez, *J. Cataract Refract. Surg.*, **37** (9), 1629-1635, 2011

[2] A. Alarcón, R.G. Anera, M. Soler, L. Jiménez del Barco, *J. Refract. Surg.*, **27** (11), 833-836, 2011

[3] A. Alarcón, R.G. Anera, L. Jiménez del Barco, J.R. Jiménez, *J. Biomed. Opt.*, **17** (1), 018001, 2012

[4] H.L. Liou, N.A. Brennan, *J. Opt. Soc. Am. A*, **14** (8), 1684-1695, 1997

[5] L. Chen, B. Singer, A. Guirao, J. Porter, D.R. Williams, *Optometry Vis. Sci.*, **82** (5), 358-369, 2005

NOTES

EMVPO2012_5679_007 STUDENT PRESENTATION

Effect of the lens histology in optical aberrations

A. Gargallo[*1], *J. Arines*[1,2], *E. Acosta*[1]; [1]*Universidade de Santiago de Compostela, Departamento de Física Aplicada, Facultade de Física, Campus Vida, Santiago de Compostela, 15782 (ES);* [2]*Universidad de Zaragoza, Departamento de Física Aplicada, Facultad de Ciencias, Zaragoza, 50009 (ES).*
email: *ana.gargallo@usc.es

Summary
We studied the influence of the suture planes in the generation of lens optical aberrations for Y-shaped branched lenses. Measurements of optical aberrations for bovine, ovine and porcine lenses were performed with a point diffraction interferometer. We found a high degree of correlation between the orientation of lens sutures and the axis of non-symmetric aberrations.

Introduction
The primary aim of this work is to study correlations between the lens histological structure and the orientation of non-symmetric aberrations. To do this, we used a modified point diffraction interferometer (PDI) to measure optical aberrations. This technique has been proved to have enough dynamic range to accurately provide aberrations of eye lenses [1]. We analyzed three representative species with Y-suture branches (bovine, ovine and porcine) 10 lenses for each one. Lenses were measured within a glass cell filled with supplemented Medium 199 plus solution to prevent fast degeneration (cataracts and breaking of the sutures) and with the anterior face leaning over a ring in order to minimize deformations of the lens [2]. When excised from the globe, lenses were marked in order to locate the vertical suture, allowing us to know the orientation of the lens with respect to the eye.

Discussion
For all 30 measured lenses, phase provided by tracking interferometric fringes was fit to a Zernike polynomial expansion. The number Zernike polynomials used for the fit was chosen by taking into account the minimum number polynomials minimizing the root mean square error of the phase. Thus we found that porcine lenses need 16 Zernike polynomials for the best fit, 25 for the ovine and 37 for the bovine. This adjustment provided us synthetic inferograms that fit with real ones (figure 1).

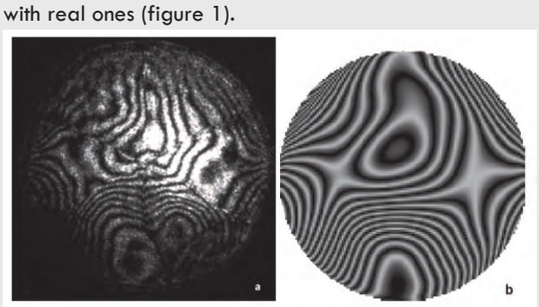

Fig. 1: real interferogram (a) and reconstructed interferogram (b) of a bovine lens.

The mean value for the main aberrations as well as the corresponding standard deviation for the measured lenses is shown in figure 2. For the three species we observed significant amounts of primary and secondary astigmatism and coma; high order spherical aberrations as well as trefoil. On the one hand we found that the amount of each type of aberration differs quantitatively from one species to another.

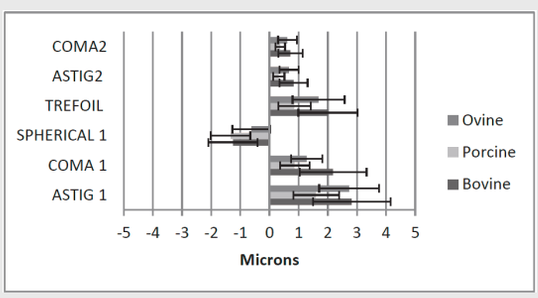

Fig. 2: main value of main aberrations with their standard deviation

On the other hand, we have found that in all species the axis of non symmetric aberrations was systematically oriented with one of the Y suture branches (figure 3), nevertheless, in opposition to what we expected there is neither privileged suture ruling aberration's axis neither correspondence of different aberrations with the same suture.

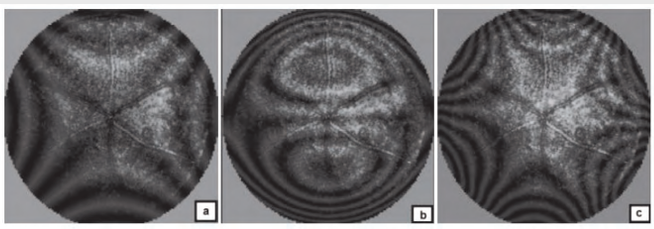

Fig. 3: Superposition of the lens suture image with different interferograms generated with the estimated Zernike components of the lens aberrations (primary astigmatism (a), primary coma (b) and trefoil (c)) in a bovine lens.

Conclusion
Despite the fact that the amount of aberrations of crystalline lenses differs quantitatively in the three studied species (ovine, porcine and bovine), our results show a significant correlation between suture planes orientation and lens non-symmetric aberration axis. This result points at the lens sutures as the histological origin of the most significant non-symmetric aberrations of the lens (astigmatism, coma and trefoil) in mammal eyes with Y-suture branches.

References
[1] E. Acosta, *et.al.*, *Ophthal. Physiol. Opt*, **29**, 235-246, 2009.
A. Gargallo, *et. al.*, Proc. of SPIE Vol. 8001 800138-1.

EMVPO2012_5685_008

Investigation of Hartmann Shack and curvature sensors in quantifying aberrations of the myopic eye

M.B. Roopashree[1], *A. Vyas*[2], *S. J. Weddell*[3], *B. Raghavendra Prasad*[1]; [1]*Indian Institute of Astrophysics, II Block, Koramangala, Bangalore (IN);* [2]*Advanced Optical Imaging Group, University College Dublin, Dublin, Ireland (IE);* [3]*University of Canterbury (NZ).*
Email: vyas@iiap.res.in

Summary
The pros and cons of using a curvature wavefront sensor (modal reconstruction) ahead of a Hartmann Shack wavefront sensor (zonal vector matrix multiply reconstruction method) in analysing myopic eye aberrations is investigated via Monte Carlo simulations.

Introduction
Myopic eye aberrations are dominated by lower order Zernike aberrations. Carrying out an analysis that gives an insight into the optimal wavefront sensing device for quantifying these aberrations is worthwhile. Here, the performance of Hartmann Shack wavefront sensor (HSWS) is studied in comparison with the curvature sensor with the aim of minimizing the wavefront sensing error and increasing the consistency of reconstruction.

Discussion
The Monte Carlo simulations with HSWS involved four steps: 1. simulation of wavefronts similar to the myopic eye aberrations [1] (wavefronts were simulated statistically using the correlation matrix of 28 Zernike coefficients for myopic eyes of 41 individuals) 2. Simulation of displaced HSWS spots 3. Reconstruction of wavefronts and 4. Comparison of simulated wavefronts with reconstructed wavefronts. We used the zonal reconstruction methods (vector matrix multiply and Fourier) for calculation of the wavefronts from the local slope estimates [2]. On an average, the simulated spots occupied 5.5 pixels (measured at 1/e of the maximum intensity). One hundred (10×10) subapertures were used for sensing. A single subaperture occupies 10×10 pixels on the HSWS detector. The number of myopic wavefront samples used in Monte Carlo simulations is 1000. In the analysis, we assumed that there is no background noise, i.e., the signal to noise ratio is very high; hence a simple center of gravity algorithm was used for sensing [3].

The first two Monte Carlo simulation steps for the curvature sensor are the same as those for HSWS. The third step involves the simulation of the extra focal and intra focal images. The intra focal image is subtracted from the extra focal image to estimate low-order Zernike aberrations. As opposed to the HSWS, the second derivative of the wavefront is used, where the intensity distribution from both defocused images is used to compute phase perturbations. The wavefront is reconstructed by the calculation of Zernike modes using the linearity of the Radon transform. This method has been used to estimate multiple wavefronts using a mixed modal/zonal approach for wide-field prediction of the spatially-variant point spread function [4]. The results of the Monte Carlo simulations performed on the curvature sensor are summarized in Fig. 1.

We find that the HSWS depends strongly on the wavefront reconstruction algorithm used and the number of subapertures used for sensing (see Fig. 2). The curvature sensor depends largely on the number of Zernike modes used for reconstruction (see Fig. 3). Overall, the consistency of reconstruction using the HSWS is lower than that for the curvature sensor, while reconstructing 1000 randomly simulated myopic aberrations. The mean reconstruction accuracy of the HSWS is 0.79 with a three-sigma value of 0.19, whereas the mean for the curvature sensor (5 Zernike moments) is 0.96, with the three-sigma value of 0.08.

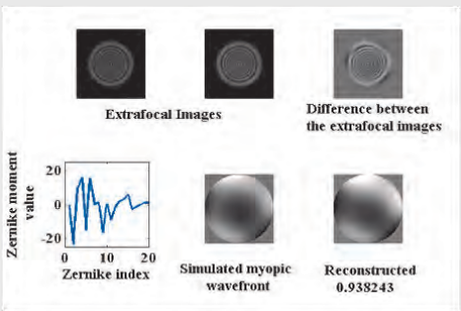

Fig. 1. Curvature sensor simulation results

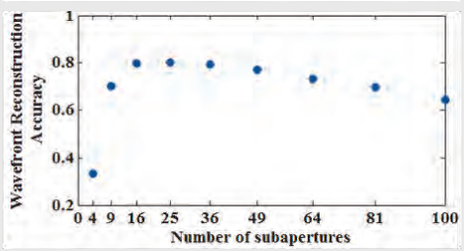

Fig. 2. HSWS reconstruction and subapertures

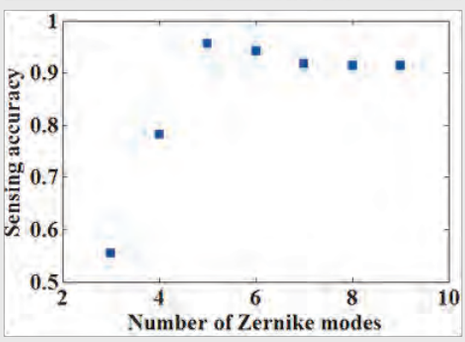

Fig. 3. Curvature sensor: dependence on Zernike modes

Conclusions

The performance of the HSWS depends on the choice of the number of subapertures and the wavefront reconstruction method used, whereas the curvature sensor depends on the number of Zernike modes used for representing the aberration. It is shown that for sensing aberrations with dominant lower orders, the curvature sensor is a more reliable wavefront sensor when compared to the HSWS. Also, the use of 5 Zernike modes for sensing these aberrations is sufficient to reconstruct efficiently in the case of the curvature sensor.

References

[1] J. Schwiegerling. "Statistical Generation of Normal and Post-refractive Surgery Wavefronts," Clin. Exp. Optom. 92, 223-226 (2009).

[2] W. H. Southwell, "Wave-front estimation from wave-front slope measurements," J. Opt. Soc. Am. 70, 998-1006 (1980)

[3] Akondi Vyas, "Myopic eye analysis using Hartmann Shack sensor: Evaluating centroid detection methods for Poisson noise dominant spots," 6th EOS Topical Meeting on Visual and Physiological Optics, UCD, Dublin, Ireland.

[4] S. J. Weddell and R. Y. Webb, "Reservoir computing for prediction of the spatially-variant point spread function", Selected Topics in Signal Processing, J. IEEE, 2008.

EMVPO2012_5694_009 **STUDENT PRESENTATION**

Non-rotational, aspherical models of the human optical system

S. Giovanzana[1], H.T. Kasprzak[2], Ş. Ţălu[3]; [1]University of Milan-Bicocca, Milano, 20125 (IT); [2]Wroclaw University of Technology, Visual Optics Group, Wroclaw, 50-370 (PL); [3]Technical University of Cluj-Napoca, Discipline of Descriptive Geometry and Engineering Graphics, Cluj-Napoca, 400641 (RO).

Email: lol_740@hotmail.com

Summary

The aim of this work is to define 3D non-rotational models for human cornea and lens. Hyperbolic cosine based function is used for the cornea and parametric model is used for the lens modelling. We combine, implement and evaluate these models with a 3D ray-tracing to fully analyse the human eye model.

Introduction

With new modern imaging techniques (e.g. Optical Coherence Tomography [1], Magnetic Resonance Imaging [2]), 3D images of the internal structure of the eye can be more easily acquired, explored, visualized and interpreted.

Our purpose is to create a 3D non-rotational model against the most known rotational model that do not consider the well known toricity of the structures of the eye (e.g. cornea and lens).

Discussion

The basis of this work is the Navarro eye model [3], since it uses conic surfaces along with constant refraction indices, that at this stage we think are more convenient then a GRIN model for the lens. We use the hyperbolic cosine type function [4] to modelise the corneal surfaces, in cylindrical coordinate system:

$$x = \rho\cos(\theta)$$
$$y = \rho\sin(\theta) \qquad (1)$$
$$z = \frac{\sqrt{r_x^2\cos^2(\theta)+r_y^2\sin^2(\theta)}}{3\left(p_x^2\cos^2(\theta)+p_y^2\sin^2(\theta)\right)}\left[\cosh\left(\sqrt{\frac{3\rho^2\left(p_x^2\cos^2(\theta)+p_y^2\sin^2(\theta)\right)}{r_x^2\cos^2(\theta)+r_y^2\sin^2(\theta)}}\right)-1\right]$$

where r_x and r_y are apex radii of curvature, p_x and p_y are shape coefficients respectively in x and y directions.

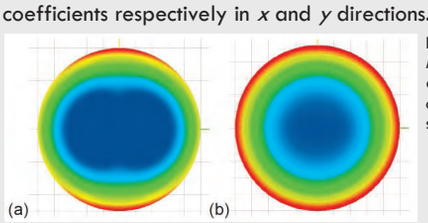

Fig 1. Maps of values of minimal (a) and maximal (b) radius of curvature of external corneal surface

The parameters used in computational model are: $r_x = 7.82$ mm and $p_x = 0.9096$, $r_y = 7.72$ mm and $p_y = 0.9111$.

The lens instead is modelised using a parametric model [5, 6], which is changed along, to be non-rotational in a spherical coordinate system:

$$x = R_{eq,x}\sin(\theta)\cos(\varphi)$$
$$y = R_{eq,y}\sin(\theta)\sin(\varphi) \qquad (2)$$
$$z = \frac{\left[b_0+b_{1,x}\theta^2+b_{3,x}\theta^4\right]\cdot\left[b_0+b_{1,y}\theta^2+b_{3,y}\theta^4\right]}{\sqrt{\left[b_0+b_{1,x}\theta^2+b_{3,x}\theta^4\right]^2\cdot\sin^2(\varphi)+\left[b_0+b_{1,y}\theta^2+b_{3,y}\theta^4\right]^2\cdot\cos^2(\varphi)}}\cos(\theta)$$

where R_{eq} is the equatorial radius, and b_i are coefficients linked to the geometry ($t = 4$ mm, $R_{eq,x,y} = 5.044$ mm) and optics ($R_{ant,x} = 10.05$ mm, $R_{ant,y} = 10.20$ mm, $q_{ant} = -3.1316$ $R_{post,x} = -5.85$ mm, $R_{post,y} = -6$ mm) of the lens.

These models are generated using the Navarro data for *y* direction [3], taking into account, just as computational example, 0.50 D astigmatism with-the-rule for the cornea and against-the-rule for the lens in the *x* direction.
The models are imported into CAD (Rhinoceros) software, and surface curvature analysis is performed for the cornea (Fig 1) and for the lens (Fig 2).
A ray-tracing plug in is created along, to trace rays from infinite parallel to *z*-axis into the eye.
Refraction index are taken as for Navarro eye model [3].
Intersection points with the retina are then collected and analysed in a point spread function plot (Fig 3).

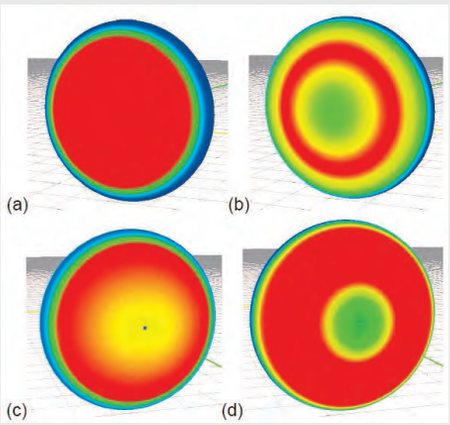

Fig 2.
Lens anterior minimum (a) and maximum (b) radius of curvature. Lens posterior minimum (c) and maximum (d) radius of curvature

Conclusions
A first approach for 3D non-rotational, aspherical models are presented. Both models for the human cornea and the lens are created from data collected only in *x* and *y* directions. In particular the lens model is generated only with geometrical and optical constraints with no need of any numerical method for creation of the surface.

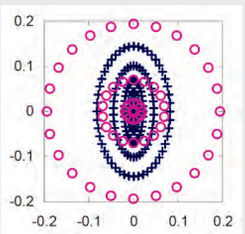

Fig 3.
Spread point functions of Navarro (dot) and a 3D (cross) eye model on the retina

References
[1] S.R. Uhlhorn, D. Borja, F. Manns, J.M. Parel, *Vision Res.,* **48,** 2732-2738, 2008.
[2] E. Hermans, et al, *Invest. Ophth. Vis. Sci.,* **50 (1),** 281-289, 2009.
[3] R. Navarro, J. Santamaria, J. Bescos, *J. Opt. Soc. Am. A,* **2,** 1273-1281, 1985.
[4] H.T. Kasprzak, E. Jankowska-Kuchta, *J. Mod. Opt.,* **43 (6),** 1135-1148, 1996.
[5] S. Giovanzana, et al, *J. Mod. Opt.,* **58(19-20),** 1770-1780, 2011.[6] S. Giovanzana, Ș. Țălu, *J. Mod. Opt.,* **59 (1),** 26-34, 2012.

EMVPO2012_5698_010 STUDENT PRESENTATION

Chromatic Null Screen corneal topographer with three LCD´s

M.I. Rodríguez-Rodríguez[1,2], A. Jaramillo Núñez[1], R. Díaz Uribe[2]; [1]Instituto Nacional de Astrofísica, Óptica y Electrónica, Apdo. Postal # 51, Puebla, Pue., 72000 (MX); [2]Universidad Nacional Autónoma de México, Centro de Ciencias Aplicadas y Desarrollo Tecnológico, Apdo. Postal # 70-186, C.P. 04510 (MX)

Summary
The use of chromatic null screens with three LCD's in a triangular prism setup for measuring the shape of human corneas is proposed. Some experimental results obtained with calibration spheres and preliminary images obtained with real corneas are presented.

Introduction
A new technique has been developed during recent years for the testing of very fast aspheric surfaces similar to corneal surfaces with null screens [1]. The essential idea consists of designing a screen with a set of spots in such a way that the image reflected by the test surface gives a perfectly ordered arrangement if the test surface is perfect; assuming that the ideal shape of the surface to be evaluated (reference surface) is known, the spots on the screen can be easily computed. This technique has the advantage that it does not need any additional optical element with a specific design to correct the aberrations of the system under test. The test with screens has a great similarity with the Hartmann [2] test, but it differs in several aspects; for instance, it does not require a point source or a screen with holes used to select rays. A common aspect to both testing methods and to all those methods that measure the slope of the wavefront is that the quantitative evaluation is made by means of a numerical integration process. The proposed null screen is now displayed on LCD flat screens instead of a traditional printed cylindrical null screen [1,3]. Several configurations can be used for testing with LCD's; in this paper; however, we propose the use of three LCD's forming a triangular prism, to measure the shape of the human corneas. A detailed description of the design of null screens in a triangular prism array of LCD's is found in Ref [4]. In this paper a color codification of the spots in the screen is made as suggested by Beltrán-Madrigal [5]. There are other proposed devices which use a color code, but the bright spots are fixed in position, color, shape and size [6]. Some experimental results obtained with calibration spheres used to simulate the corneal surface will be presented.

Materials and Methods
The null screen for the measurement was built with three LCD's in a triangular prism arrangement as described in Ref [4]. A new device was built to be used in corneal topography. A CCD camera with a 110mm focal length lens was used to capture the reflected spot images. In Fig. 1, the experimental setup is shown as well as the image obtained for a 6.37 mm ROC steel ball and the first image obtained with a real cornea; in these images about 150 measuring points are shown just as a proof of principle, but, by reducing the size of the spots and their separation, many more measuring points can be included. With this device the position of the drop-shaped spots on the LCD´s in three dimensions can be programmed, with the obvious advantage that the null screen can be appropriately modified to include a different number of spots or to change between a square and radial spots array or an arrangement of lines, included a Placido-like screen; this allows the measurement of different radii of curvature and shapes of the cornea. The color code is such that for a given spot, no other nearby spot has the same color, simplifying the correspondence between object and image spots, which becomes difficult for corneas with severe deformations.

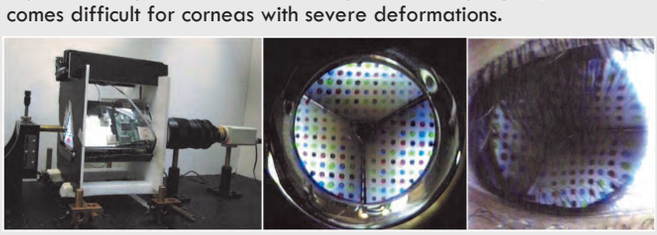

(a) (b) (c)

Fig1. a) Schematic setup for testing with chromatic null screens, using an arrangement of LCDs forming a triangular prism. Images obtained with this setup are: b) The test surface is a 6.37 mm. ROC, steel ball, and c) Image on a real cornea.

Conclusions
A novel corneal topographer based on three flat LCD's in a triangular prism arrangement is proposed. The setup and preliminary images obtained with this device have been shown. The corneal shape reconstruction can be performed with various methods, such as ray tracing or Fourier methods. The non-uniform background illumination can be improved easily by software, so this is not an essential drawback.

Acknowledgment
Financial support "grant PAPIIT DGAPA-UNAM No: IT101912" is gratefully acknowledged.

References
[1] Díaz-Uribe, R. and Campos-García, M., "Null-screen testing of fast convex aspheric surfaces," Appl Opt, **39**, 2670–2677 (2000).
[2] D. Malacara-Doblado and I. Ghozeil, "Hartmann and other screen tests", in [*Optical Shop Testing*], Third Ed., D. Malacara, ed. (Wiley, 2007), 361-394.
[3] Moreno-Oliva, V. I., Campos-García, M., Bolado-Gómez, R. and Díaz-Uribe, R., "Point shifting in the optical testing of fast aspheric concave surfaces by a cylindrical screen", Appl Opt, 47, 644–651 (2008).
[4] Rodriguez-Rodriguez, M., Jaramillo-Nunez, A., and Díaz-Uribe, R. "Dynamic Point Shifting in Null Screen Videokeratometry," Proc. of SPIE Vol. 8011, 80119H, 2011 SPIE.
[5] Beltrán-Madrigal, J. and Díaz-Uribe, R. "Progress in the design of chromatic null screens to test cylindrical parabolic concentrators," Proc. of SPIE Vol. 8011, 80111R, 2011 SPIE.
[6] Victor A. Sicam, Harry de Vries, Maarten Huijbregtse and Michiel Mensink, "Image Processing of Irregular Corneas in Color-coded Multiple-point-source Corneal Topography (CMCT)", ARVO Meeting Abstracts April 22, 2011 52:4189 - D933.

EMVPO2012_5710_012 **STUDENT PRESENTATION**

Expected Visual Acuity and Depth of Focus with spherical and aspheric Intraocular Lenses

F. Alba-Bueno[1], F. Vega[1], M.S. Millán[1], R. Navarro[2]; [1]Universitat Politècnica de Catalunya (UPC), Department of Optics and Optometry, Barcelona (ES); [2]ICMA, Consejo Superior de Investigaciones Científicas & Universidad de Zaragoza, Zaragoza (ES).

Summary
Expected visual acuity (VA) and depth of focus (DOF) of both spherical and aspheric intraocular lenses (IOLs) are calculated from the in vitro Modulation Transfer Function. The resulting VAs were similar for both types of design but DOF were larger in eyes implanted with spherical IOLs.

Introduction
Intraocular lenses (IOLs) implantation is a common procedure in cataract surgery that has been greatly improved over the last decades. Several studies have shown that the average normal human cornea has a positive spherical aberration (SA). In young eyes, this SA is partially compensated by the negative SA of internal optics [1]. However, spherical IOLs also present a positive SA, thus further degrading retinal image quality. Alternatively, IOLs with aspheric surfaces may compensate corneal SA [2] but they may also reduce de depth of focus (DOF) [3]. The standard way to describe the in vitro optical imaging quality of IOLs is the Modulation Transfer Function (MTF), but non-standard designs (such as multifocal IOLs) may require other additional measurements [4]. In this work we propose to use the same magnitudes utilized to assess visual performance, such as visual acuity (VA) and the Contrast Sensitivity Function (CSF) also to report the results of optical bench measurements of IOLs. In particular, here we compare the VA and DOF predicted from in vitro measurements of spherical versus aspheric IOLs obtained on a model eye.

Discussion
The IOLs are placed on a model eye built according to the ISO standard requirements except for the artificial cornea, which induces an amount of positive SA similar to the natural human cornea. The MTF is firstly obtained for each IOL at the best image plane (0 Diopter defocus), for large (4.3 mm) and small (2.4 mm) IOL pupils. The through-focus MTF was then measured for different amounts of defocus (in steps of 0.1D). The expected CSF is then obtained as the product of the optical MTF and a generic Neural Transfer Function (NTF) [5]: CSF = (MTF)x(NTF). The predicted VA (in cycles per degree) is obtained as the cut-off frequency of the CSF. Note that the VA obtained in this way is the prediction for the particular model eye used (which includes the IOL) and a generic neural system. Figure 1 compares the through-focus VA for two IOL models, one spherical (upper panel) and one aspheric (lower panel). At the best image plane (0D) and for the two pupil diameters (2.4 and 4.3 mm) both IOLs present values higher than 30cpd (equivalent decimal VA of 1.0). Furthermore, for the small pupil both IOLs show peak values of 60cpd (VA of 2.0), which mean that the VA will be only limited by the Nyquist frequency of the cone mosaic. The spherical IOL shows a lower VA for the larger pupil. On the contrary, the aspheric IOL shows almost no difference between small or large pupils, but at the cost of a lower DOF. The DOF values (Table 1) are obtained from the bandwidths of these curves at the frequencies of 25cpd and 15cpd (equivalent to decimal VAs of 0.8 and 0.5, respectively) according to the limits for normal and mild vision loss, respectively, given by the World Health Organization.

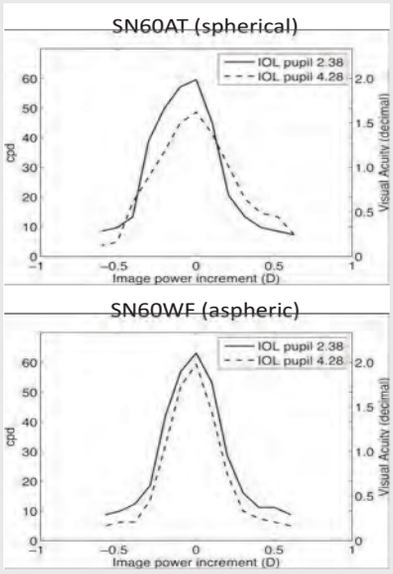

Fig. 1: Potential visual acuity for each lens and IOL pupil as a function of defocus

	IOL pupil (mm)	Sph.*	Asph.*
25cpd (VA 0.8)	2.38	0.56D	0.50D
	4.28	0.59D	0,42D
15cpd (VA 0.5)	2.38	0.69D	0.67D
	4.28	0.84D	0.54D

Table 1: Depth of focus of each IOL for visual acuities of 0.8 and 0.5 (decimal).

Conclusions
A simple method is proposed to report in vitro measurements of optical performance of IOLs (within model eyes) in terms of expected visual quality (VA and CSF) by considering a generic neural response (NTF). The results obtained so far agree with previous clinical studies [6], in which no statistically significant difference in VA was found between patients implanted with spherical and aspheric IOLs. The non-compensated SA in the spherical IOL causes a moderate reduction of VA only for large pupils.

Bibliography
[1] P. Artal, A. Guirao, E. Berrio, and D. R. Williams, "Compensation of corneal aberrations by the internal optics in the human eye," *J Vis* **1**, 1–8 (2001).
[2] J. T. Holladay, P. A. Piers, G. Koranyi, M. van der Mooren, and N. E. S. Norrby, "A new intraocular lens design to reduce spherical aberration of pseudophakic eyes," *J Refract Surg* **18**, 683–91 (2002).
[3] S. Marcos, S. Barbero, and I. Jiménez-Alfaro, "Optical quality and depth-of-field of eyes implanted with spherical and aspheric intraocular lenses," *J Refract Surg* **21**, 223–35 (2005).
[4] F. Vega, F. Alba-Bueno, and M. S. Millán, "Energy distribution between distance and near images in apodized diffractive multifocal intraocular lenses," *Investigative Ophthalmol & Vis Sci* **52**, 5695-5701 (2011).
[5] M. A. Losada, R. Navarro, and J. Santamaría, "Relative Contributions of Optical and Neural Limitations to Human Contrast Sensitivity at Different Luminance Levels," *Vision Research* **33**, 2321–36 (1993).
[6] K. M. Rocha, E. S. Soriano, W. Chamon, M. R. Chalita, and W. Nosé, "Spherical aberration and depth of focus in eyes implanted with aspheric and spherical intraocular lenses: a prospective randomized study," *Ophthalmol* **114**, 2050–54 (2007)

NOTES

EMVPO2012_5715_013 STUDENT PRESENTATION

Zernike vs Bessel Circular Functions in Visual Optics

J.P. Trevino[1], J.E. Gomez-Correa[1], Robert Iskander[2], S. Chavez-Cerda[1]; [1]Instituto Nacional de Astrofísica, Optica y Electrónica. Depto. De Optica, Apdo. Postal 51/216, Puebla, Mex. 72000 (MX); [2]Institute of Biomedical Engineering and Instrumentation, Wroclaw University of Technology, Wybrzeze Wyspianskiego 27, 50-370 Wroclaw (PL).*
***Email:** trevinojp@inaoep.mx

Summary
We present a comparison between the Zernike Circle Polynomials and the Bessel Circular Functions to approximate any surface defined in a circular domain for applications in Visual Optics.

Introduction
It is well known that the Zernike Circular Polynomials (ZCP) are the standard functions used to represent wavefront aberrations and corneal topography in Visual Optics. This is due since the ZCPs form a complete set of orthogonal functions defined in the unit disk [1]. Completeness of the ZCPs set means that any arbitrary function defined in a disk can be represented as a linear combination of ZCPs:

$$W(r,\theta) = \sum_{n,m}^{\infty} a_n^m Z_n^m(r,\theta). \quad (1)$$

In practical cases only a finite number of terms are needed to obtain an approximation within an acceptable error. The ZCPs originate as solutions of a rotationally symmetric partial differential equation (RS -PDE) [2]:

$$\nabla^2 u(x,y) + \alpha\left(x\frac{\partial}{\partial x} + y\frac{\partial}{\partial y}\right)^2 u(x,y) + \beta\left(x\frac{\partial}{\partial x} + y\frac{\partial}{\partial y}\right) u(x,y) + \gamma u(x,y) = 0. \quad (2)$$

A suitable choice of the parameters α and β and boundary conditions for the solutions $u(x,y)$ leads to the ZCPs. A different choice of values for the same parameters leads to the Bessel Circular Functions (BCFs) $B_n^m(r,\theta) = J_n^m(r)\Theta_m(\theta)$ that are also orthogonal and complete in the unit disk. In this sense, they can also be used to represent arbitrary functions in a circular domain as a linear combination, $W(r,\theta) = \sum_{n,m}^{\infty} b_n^m B_n^m(r,\theta)$. In this work we present the BCFs and make a comparison with ZCPs on approximating surfaces defined in the unit disk.

Discussion
Dealing with Eq. (2) as a Sturm-Liouville problem requires that $\beta = 2\alpha$. Setting $\alpha = -1$ and $\beta = -2$ and imposing the boundary condition that the radial component of the solutions be equal to unity along the edge of the unit disk, i.e. $R(r=1)$ yields that the solutions are the set of ZCPs $Z_n^m(r,\theta)$ [2]. Since the parameters α and β are somewhat arbitrarily chosen, a different selection of parameters is acceptable as long as they are related by $\beta = 2\alpha$. The choice $\alpha=\beta=0$ leads to the Helmholtz equation, whose solution in polar coordinates is the set of BCFs. The radial component is a Bessel function of the first kind and their boundary conditions are $u(r=1,\theta) = 0$. As mentioned before, ZCPs and BCFs are complete and orthogonal sets and thus, candidates to expand arbitrary functions within the unit disc, see Fig. 1.

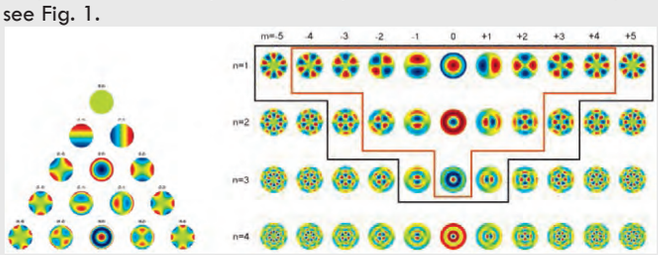

Fig. 1: ZCP(left) and BCF (right) up to n=3.

The ordering scheme of the BCFs is rather different to that of ZCPs and is related to the parameter γ. Such scheme for the BCFs is shown in table (1). In general the approximation error of the BCFs is of the same order as that for ZCPs. Comparing their performance we found that if the surfaces contain low frequencies, the ZCPs perform better. On the other hand, BCFs can perform better where there are discontinuities in the derivatives.

m= / n=1	9	8	7 27	6 21	5 17	4 11	3 7	2 5	1 3	0 1	1 2	2 4	3 8	4 12	5 16	6 20	7 26	8	9
2			43	9 37	8 31	6 25	5 19	4 13	3 9	2 6	3 10	4 14	5 18	6 24	8 32	9 38	44		
3			53	49	45	9 39	8 33	7 29	6 23	4 15	6 22	7 28	8 34	9 40	46	50	54		
4			59	57	55	51	47	41	8 35	7 30	8 36	42	48	52	56	58	60		

Table 1. Ordering scheme of the BCFs.

Conclusions
We presented the BCFs as an alternative basis to approximate surfaces in the circular disk. We compared them with the ZCPs and found that they perform similarly. However, we found that if the surfaces contain low frequencies, the ZCPs perform better, while BCFs can perform better when there are discontinuities in the derivatives as in the case of the Rand surface.

References
[1] Max Born and Emil Wolf. *Principles of Otptics.*Cambridge University Press, seventh (expanded) edition, 1999.
[2] B. R. A. Nijboer. *The Diffraction Theory of Aberrations.* PhD thesis, University of Groningen, 1942.

NOTES

EMVPO2012_5728_014

Corneal Topographer Based on Null-Screen Testing

A. Estrada-Molina[1], M. Campos-García[1], R. Díaz-Uribe[1], M. Ramírez-Ortiz[2];[1]Universidad Nacional Autónoma de México, Centro de Ciencias Aplicadas y Desarrollo Tecnológico, C.P. 04350 (MX); [2]Hospital Infantil de México Federico Gómez, Servicio de Oftalmología, C.P. 06720 (MX).
Email: amilcar.estrada@ccadet.unam.mx

Summary
The motivation behind the design and construction of a corneal topographer was to develop a portable device that can be used with neonates and infants as also with patient that not can be seated in an upright position or those who do not cooperate during the topographic study.

Introduction
Our portable topographer has essentially the same components of the commercial topographers based on the Placido rings: luminous pattern (null screen [1-4]), camera lens, CCD detector, a dedicated laptop, etc., but to differences of these, it was designed to have a compact fashion and a light weight so that the use of it in the clinical practice with neonates, infants and patients that not can be seated in an upright position or those who do not cooperate during the corneal topography measurements to be more easier to perform (see Fig 1). The topographer presented here removes the skew ray ambiguity present in the topographers based on the Placido rings, because there is a one-to-one correspondence between points on the null screen and the image plane. Therefore, the direction of the incident and reflected ray can be obtained and the direction of the surface normal is calculated easily by using of the Reflection Law. Eventually, a height map can be computed by numerical integration of the surface normal as suggested by Díaz-Uribe [5].

Fig 1.
Example of use of the topographer proposed in the clinical practice

Discussion
Fig 2 are the first images obtained with the topographer, it displays some problems that must be solved before to obtained the corneal topography measurements, for example; lashes should be removed by using image processing because are source error. Excessive tearing in the eye some points projected on the cornea can not to display, etc. An important issue to consider is that if the cornea is misalign respect to the optical axis of the topographer and it is not in the correct position on the z-axis when the image was captured, even so we can perform the evaluation, just have to find the defocus and misalignment to correct the results obtained.

Conclusions
We have proposed a corneal topographer to use potentially with neonates and infants. This topographer solves some problems presented in pediatric corneal topography.

Acknowledgement
We acknowledge to DGAPA-UNAM for the financial support of this project, through the grant PAPIIT No: IT101912. Also, Amilcar Estrada-Molina thanks to the CEP-UNAM because granted him a doctorate scholarship.

References
[1] R. Díaz-Uribe and M. Campos, *Appl. Opt.* **39**, 2670-2677 (2000).
[2] M. Campos-García, R. Bolado-Gómez and R. Díaz-Uribe, *Appl. Opt.* **47**, 849-859 (2008).
[3] M. Campos-García, R. Díaz-Uribe and Fermín Grandos-Agustin, *Appl. Opt.* **43**, 6255-6264 (2004).
[4] V. I. Moreno-Oliva, M. Campos-García, R. Bolado-Gómez and R. Díaz-Uribe, *Appl. Opt.* **47**, 644-651 (2008).
[5] R. Díaz-Uribe, *Appl. Opt.* **39**, 2790-2804 (2000).

EMVPO2012_5731_015 STUDENT PRESENTATION

Imaging quality of multifocal intraocular lenses. Automated assessment setup.

L. Remón[1], A. Calatayud[1], J.A. Monsoriu[1], W.D. Furlan[2];[1]Centro de Tecnologías Físicas, Universitat Politècnica de València, Camino de Vera s/n, 46022 Valencia (ES); [2]Departamento de Óptica, Universitat de València, Dr. Moliner 50, 46100 Burjassot (Valencia) (ES).
Email: lauremar@upvnet.upv.es

Summary
A new technique for the assessment of the optical quality of multifocal intraocular lenses (MIOLs) under monochromatic and polychromatic illumination is presented. The system provides the MTF of the lens under test for different axial positions of the object in a totally automated procedure.

Introduction
Multifocal intraocular lenses (MIOLs) are the most frequent approach used by ophthalmologists for the surgical treatment of cataract. The performance of these lenses has been reported in the literature in numerous objective studies performed both *in vivo* and *in vitro* [1-2]. Particularly, to assess the optical quality of MIOLs several experimental setups were designed in which the Point Spread Function (PSF) and/or the Modulation Transfer Function (MTF), measured for the far and the near focus, are the essential merit functions. However, information about the depth of focus is missed if measurements are restricted to these cases. The Defocus Transfer Function (DTF) is a useful tool to evaluate the optical performance for all levels of defocus [3]. In this work, we describe a new technique for the assessment of MIOLs response. The system provides the trough-focus MTF (modulus of the DTF) of the lens under test in a totally automated procedure.

Methods
The MIOL is placed in a wet cell with saline solution and the model eye includes a cornea lens and pupils of different diameters. To assess the throughfocus MTF, the object plane is axially displaced with a step motor to generate the different vergences. For each position of the object, the retinal image is stored and analyzed. We employed an object test consisting on a binary grating of 5 lp/mm (that corresponds to an object of size 20/40 in a visual acuity letter chart). The MTF of the eye was evaluated by measuring the contrast degradation of its image. This image is pre-processed dividing it by a *background* image with no object in the setup in order to avoid the errors introduced by the eventual non uniform illumination of the object. The movements of the translation stage and the processing of the retinal images were programmed in LabView ®.

Results
The performance of the apparatus is tested with two commercial MIOLs: ReZoom (refractive) and Tecnis (diffractive). We study the influence of both chromatic aberration and the pupil size on the MTF. Three different chromatic filters (490 nm, 560 nm and 630 nm) were used in this study. The through-focus MTF plots a pupil diameter: 4.2 mm, without cornea shows that the efficiency of each focus is highly dependent on the wavelength for both lenses.
The through-focus MTF for monochromatic light (560 nm) and two different pupil sizes (2.7 mm and 4.2 mm), with the cornea lens in the model eye shows that the far focus MTF for the ReZoom with pupil size 2.7 mm is better than the one corresponding to Tecnis. The opposite happens for a 4.2 mm pupil. Moreover, the MTF for the Tecnis has approximately the same value for the near and far focus for both pupil diameters.

Conclusion
We have designed a precise and robust optical method for testing diffractive and refractive MIOLs. The system is based on an image forming system that allows measuring the trough the focus MTF (the MTF for different axial positions of the object) in an automated way. The potentiality of the setup is demonstrated by the assessing two commercial MIOLs of different characteristics. The system is modular and therefore versatile, for example, different artificial corneas (i.e.; aspheric) and different pupil diameters can be used in the model eye.

References

[1] V. Portney, *"Optical testing and inspection methodology for modern intraocular lens,"* J. Cataract. Refract. Surg. 18, 607-613 (1992).
[2] S. Barbero, S. Marcos, and I. Jiménez-Alfaro, "*Optical aberrations of intraocular lenses measured in vivo and in vitro,"* J. Opt. Soc. Am. A 20, 1841-1851 (2003).
[3] J. Schwiegerling and J. Choi, "Application of the polychromatic defocus transfer function to multifocal lenses," J. Refract Surg. 24, 965-969 (2008).

EMVPO2012_5742_016 **STUDENT PRESENTATION**

Automatic Selection and Registration of Adaptive Optics (AO) corrected Best Quality Retinal Images

G. Ramaswamy, Ni. Devaney; Applied Optics, School of Physics, National University of Ireland Galway (IE).
Email: Nicholas.devaney@nuigalway.ie

Summary
In this work, we report on a study into the registration and selection of sequences of retinal images obtained with an Adaptive Optics system, the *rtx1* from Imagine Eyes. The images may be divided into two classes; those focused on the photoreceptor layer and those focused on the nerve fiber/blood vessel layer. We compare alrgorithms for registration (including correction of rotation) and the measurement of image quality for both of these image classes.

Introduction
In this work the retinal image sequences were obtained using a commercial AOassisted fundus imager; the rtx1 from Imagine Eyes[1]. The sequences have residual image motion (translation and rotation) and show variations in image quality. Our goal is to enhance the final image quality by accurately registering and selecting the best images. The first step in our processing is to correct for uneven image illumination, and we use a Wavelet analysis approach for this. The next step is to measure the quality of the individual images before selecting the best images for registration.

Image Quality Metrics
The quality of the images varies due to variations in uncorrected aberrations, and blurring due to rapid eye motion. It is required to automatically reject poor quality frames. We have studied the application of several image quality metrics, including Image variance or contrast, entropy, frequency domain kurtosis and image sharpness. The latter is defined by [2]:

$$\Gamma_{D1}[I]=\frac{1}{12}(I-\gamma I_0)^{\beta}$$

where the γ and β parameters can be varied depending on the scene content.

Image Registration
We tested different approaches to image registration. In the case of photoreceptor images, we have developed a 'peak-tracking' approach based on centroiding several cone photoreceptors. It was also possible to accurately correct for image rotation using the Matlab Imtransform routine. For the images containing nerve fibers or blood vessels we have found phase correlation to be most robust. The shift (x_0,y_0) between two images f and f' is found from the cross power spectrum defined as:

$$\frac{F(\xi,\eta)F'(\xi,\eta)}{|F(\xi,\eta)F'(\xi,\eta)|}=e^{j2\pi(\xi x_0+\eta y_0)}$$

where F and F' are the Fourier transforms of the images f and f'[3]. We have examined different approaches to correcting nerve fiber/vessel images for rotation, including log-polar and radon transforms. Fig. 1 shows average images centered on the fovea obtained by registration using phase correlation (left) and registration combined with de-rotation using conetracking. The image on the right has higher contrast, especially around the edges.

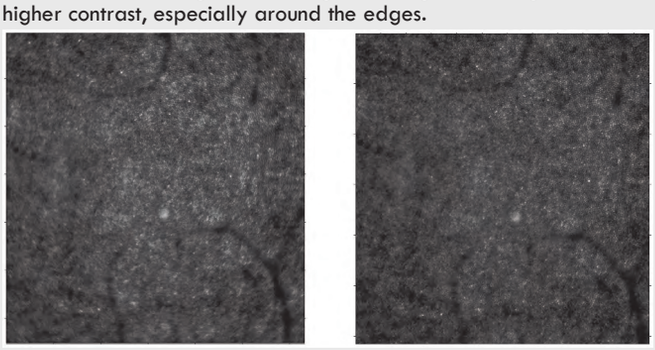

Fig 1. Left; AO image of fovea obtained by registering using phase correlation (left) and registering and de-rotating using cone tracking (right).

Conclusion
We have investigated techniques to select high quality retinal images and to precisely register them, correcting for both residual translation and residual rotation. We intend to apply these techniques to a large dataset of retinal images in order to investigate how they can enhance the detection of retinal pathologies.

Acknowledgement
The authors would like to thank Science Foundation Ireland (SFI) for financial support and Dr. Marco Lombardo for providing the retinal image data set.

References

[1] C.Viard et. al, *BiOS*, 12, 3, 788509.1-10, 2011.
[2] J.R.Fienup, and J.J.Miller, JOSA, 20,4,609-620,2003.
[3] B.S.Reddy and B.N.Chatterji, IEEE Transactions on Image Processing, 5, 8, 1266-1271, 1996

EMVPO2012_5746_017 **STUDENT PRESENTATION**

Singular Optical fields used to calculate Wavefront aberrations

J.E. Gómez-Correa, J.P. Trevino, S.E. Balderas-Mata, S. Chávez-Cerda; Instituto Nacional de Astrofísica, Óptica y Electrónica, Departamento de Óptica, Apdo. Postal 51/216, Puebla, Pue. México 72000 (MX).
Email: jgomez@inaoep.mx

Summary
We investigate the non-paraxial effects inside the whole eye including the gradient index crystalline. Using standard parameters of the human eye for the refractive index and the curvatures of the different surfaces, an exact ray tracing was performed in a pupil of 8 mm and we construct and propagate through the retina the corresponding wavefront.

Introduction
Non-paraxial exact ray tracing in optical systems leads to the concept of caustics also known as singular optical fields. A caustic can be defined as the envelope of intersection points between adjacent rays and it is related to zones with higher irradiance [1]. The crystalline could be modeled using a gradient refractive index (GRIN) lens with a certain geometry, whose refractive index varies in two different ways. The first variation $n_a(z,r)$ goes from the anterior surface to a fixed distance z_m on the optical axis, where it reaches its' highest value. The second variation $n_p(z,r)$ goes from this point to the posterior surface of the crystalline [2]. Using this information in the ray equation the paths of each ray can be calculated. Once the rays trajectories are calculated at a given plane their associated wavefront con be obtained and propagate using wave optics.

Discussion

The refractive index of the lens could be mathematically modeled by a fourth degree polynomial. The first variation is represented by n_a and the second n_p:

$$n_a(z,r) = n_0 + n_1 r^2 + n_2 r^4 + n_3 z + n_4 z^2 + n_5 z^3 + n_6 z^4 \quad (1)$$

$$n_p(z,r) = n_{max} + n_1 r^2 + n_2 r^4 + n_{3,2} z + n_{4,2} z^2 + n_{5,2} z^3 + n_{6,2} z^4, \quad (2)$$

where, r is the radial distance, z is the longitudinal, n_0 is the refractive index of the surface before the lens, n_{max} is the refractive index at the distance z_m, and n_i are the refractive coefficients [2]. Using the paraxial approximation, a simplified model of the gradient refractive index could be obtained, in this model only the radial direction varies. This is shown in equation (3).

$$n(r) = n_0 + n_1 r^2 \quad (3)$$

When the Eikonal equation is solved with the refractive index given by eq. (3), the solutions have a sinusoidal type with an amplitude that depends on n_1. If n_1 is very small, then the variations are small too and the solutions inside the lens will be approximately straight lines.

We first investigated the paraxial case based in eq. (3). A human eye was built based on the geometric parameters given in [3] and performed an exact ray tracing considering that the cornea and the aqueous humor have constant refractive indexes, and that n_1 is of the order of 10^{-3}. The results are shown in Fig.1A.

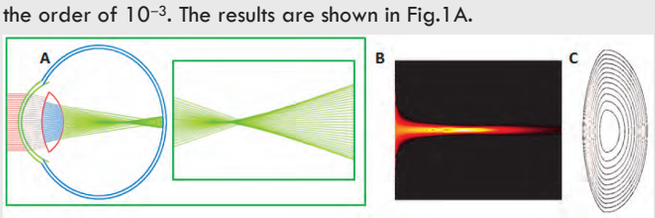

Fig. 1: A: Exact ray tracing through the whole optics of the eye and zoom of the ray tracing. B: Wavefront reconstructed from optical path in ray tracing and corresponding wavefront propagation. C: Graded Refractive Index of the lens, divided into fore and back distributions.

Once the exact ray trace is done, and considering that the optical paths are the same, it is easy to propagate the corresponding wavefront from the lens to retina, obtaining the propagation caustic in the sagittal plane, Fig. 1B. This caustic provides information about the eye's aberrations. We will present the whole and detailed non-paraxial analysis using the refractive indices given by eqs. (1) and (2), whose iso-indicial behavior is shown in Fig. 1C.

Conclusions

We have shown the possibility of investigating the non-paraxial effects in the human eye. Performing an exact ray tracing including the gradient index of crystalline we first obtain the ray trajectories. Then we construct and propagate the corresponding wavefront characterizing the imaging characteristics of the optical wave field at every plane from the crystalline to the retina.

References

[1] J. F. Nye, *Natural focusing and fine structure of light*, (IOP, London,1999).
[2] Alexander V. Goncharov and Chris Dainty, *J. Opt. Soc. Am. A,* **24**, 2157-2174.
[3] David A. Atchison and George Smith. *Optics of the human eye,* (Butterworth Heinemann, Edinburgh, 2000).

NOTES

EMVPO2012_5751_018

Improving retinal image via descattering for the detection of diabetic retinopathy

G. Russell[1], J. Oakley[2], N. McLoughlin[3], V. Nourrit[3]; [1]Health Intelligence Ltd, Saxon House, Moston Road, Sandbach, Cheshire, CW11 3HL (GB); [2]The University of Manchester, School of Electrical and Electronic Engineering Manchester, M13 9PL (GB); [3]The University of Manchester , Faculty of Life Sciences, Manchester M13 9PL (GB).
Email: Vincent.Nourrit@manchester.ac.uk

Summary

A new method to automatically improve the quality of retinal image degraded by media opacities is presented. Results suggest that the method could be beneficial for the diabetic retinopathy screening process.

Discussion

The quality of a retinal image can be significantly degraded by media opacities. This is turn can limit the diagnostic potential of such images. In some cases an image is considered unassessable by retinal graders and this can delay the detection of vision threatening pathologies.

In this context, we developed and implemented a method to automatically reduce the degradation due to intraocular scattering. 305 images that had previously been graded as unassessable by retinal graders, were reprocessed using our new algorithm and then reassessed by a second grader.

Of the images tested 5 images, from 5 patients, were deemed assessable after processing, allowing for the recognition of pathological features that were previously undetectable. One of these was a case of referable maculopathy. No clinical information was lost in the processed image and no spurious information added.

Conclusion

This method has the potential to improve the retinal screening process by offering a rapid means of enhancing retinal images that are otherwise unassessable. This will also help reducing the costs encored by follow up slit lamp biomicroscopy examination.

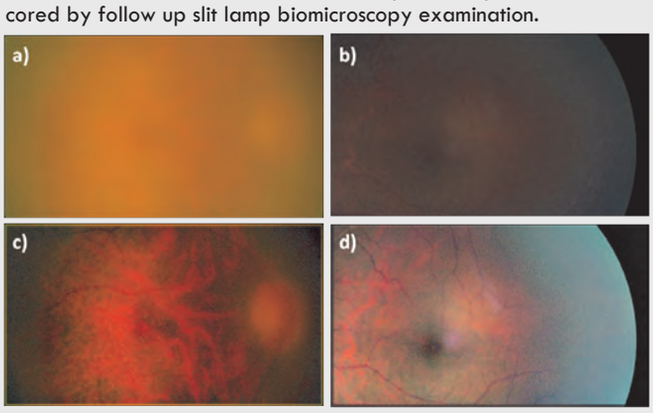

Fig. 1: a) and b)Two images recorded through a media poorly transparent. c) and d) respectively images a) and b) after "descattering".

NOTES

EMVPO2012_5752_019

3D Modeling and reconstruction of human corneal surface using superellipsoids

Ș. Țălu[1], S. Giovanzana[2], M. Țălu[3], I.V. Petrescu-Mag[4]; [1]Technical University of Cluj-Napoca, Faculty of Mechanics, Discipline of Descriptive Geometry and Engineering Graphics, Cluj-Napoca, 400641 (RO); [2]University of Milan-Bicocca, Milano, 20125 (IT); [3]University of Craiova, Faculty of Mechanics, Department of Applied Mechanics, Craiova, 200512 (RO); [4]SC Bioflux SRL, 54 Ceahlau St., Cluj-Napoca, 400488 (RO).
Email: mihai_talu@personal.ro

Summary
The present study provides a new geometric model for representation and reconstruction of the 3D human corneal surface using superellipsoids, based on an explicit spatially parameterization method of the cornea characteristics.

Introduction
Over the past few decades, 3D computational image modeling and reconstruction methods of the human corneal surface have received significant attention in human vision studies and ophthalmology [1 - 5]. In these fields, the superquadrics and extended superquadrics can be used due to their flexible shape description in terms of topological changes and for their efficient 3D computer graphic representation [6]
Superellipsoids can be used to model a wide range of geometric shapes and can be expressed by a spherical product of a pair of such superellipses [7]:

$$r(\eta,\omega)=s_1(\eta)\otimes s_2(\omega)=\begin{bmatrix}\cos^{\varepsilon_1}\eta\\ a_3\sin^{\varepsilon_1}\eta\end{bmatrix}\otimes\begin{bmatrix}a_1\cos^{\varepsilon_2}\omega\\ a_2\sin^{\varepsilon_2}\omega\end{bmatrix}=\begin{bmatrix}a_1\cos^{\varepsilon_1}\eta\cos^{\varepsilon_2}\omega\\ a_2\cos^{\varepsilon_1}\eta\sin^{\varepsilon_2}\omega\\ a_3\sin^{\varepsilon_1}\eta\end{bmatrix},\ -\frac{\pi}{2}\le\eta\le\frac{\pi}{2};\ -\pi\le\omega\le\pi. \quad (1)$$

The a_1, a_2, a_3 parameters are scaling factors along the three coordinate axes. ε_1 and ε_2 are derived from the exponents of the two original superellipses.
The shape of the superellipsoid cross section parallel to the [*xoy*] plane is determined by ε_1, while the shape of the superellipsoid cross section in a plane perpendicular to the [*xoy*] plane and containing *z* axis is determined by ε_2.
A superellipsoid is defined as the solution of the general form of the implicit equation [7]:

$$\left(\left(\frac{x}{a_1}\right)^{2/\varepsilon_2}+\left(\frac{y}{a_2}\right)^{2/\varepsilon_2}\right)^{\varepsilon_2/\varepsilon_1}+\left(\frac{z}{a_3}\right)^{2/\varepsilon_1}=1. \quad (2)$$

All points with coordinates (*x*, *y*, *z*) that correspond to the above equation lie on the surface of the superellipsoid. This is a compact model defined by only five parameters that permits to handle a large variety of shapes. The exponent functions are continuous to ensure that the superellipsoid model deforms continuously and thus has a smooth surface. This form provides an information on the position of a 3D point related to the superellipsoid surface, that is important for interior/exterior determination [7]. We have an inside-outside function $F(x, y, z)$:
$F(x, y, z) = 1$ when the point lies on the surface;
$F(x, y, z) < 1$ when the point is inside the superellipsoid;
$F(x, y, z) > 1$ when the point is outside.

Discussion
Computational modeling of the 3D human corneal surface was performed using the Madsie Freestyle 1.5.3 application [8] based on a corneal surface database [6].

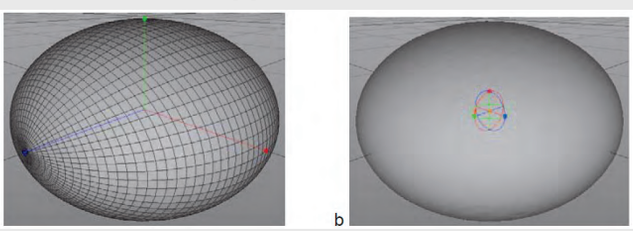

Fig 1. Image of a 3D human corneal surface in Madsie Freestyle 1.5.3 application with the next values for superellipsoid: $r_1 = 1$; $r_2 = 0.8$; $r_3 = 1$; $n_1 = 64$; $n_2 = 64$; $e_1 = 1$; $e_2 = 1$. The parameters are: radius X (r_1) - the radius of the ellipsoid along the X-axis; radius Y (r_2) - the radius of the ellipsoid along the Y-axis; radius Z (r_3) - the radius of the ellipsoid along the Z-axis; stacks (n_1) - the number of segments along the Z-axis; slices (n_2) - the number of radial segments around the ellipsoid; stack exponent (e_1) - the shape of the ellipsoid; slice exponent (e_2) - the shape of the ellipsoid.

In order to maintain the advantages of model controllability and compactness, we determined the optimal superellipsoid parameters that are able to provide a better approximation and to minimize the error function. This model allows us to calculate the corneal parameters. To test the geometrical computation, the parameters for superellipsoids were chosen from a 3D human anterior corneal surface database [6]. This model has also been tested in 3D reconstruction of the human corneal surface from two orthogonal preprocessed images and demonstrated good agreement with computerized measurements.

Conclusions
This geometric model can be applied in solid modelling, mesh generation and simplified volumetric - finite element analysis applications, biomechanical behavior of the cornea, in corneal refractive surgery and human vision studies.

References
[1] H. Burek, W. Douthwaite, *Ophthal Physiol Opt.,* **13**: 68-72, 1993.
[2] H.T. Kasprzak, E. Jankowska-Kuchta, *J Modern Opt.,* **43**: 1135-1148, 1996.
[3] H.T. Kasprzak, D.R. Iskander, *Ophthal Physiol Opt.,* **26**: 602-609, 2006.
[4] T. Bhabhrawala, *Shape recovery from medical image data using. Extended superquadrics*. Doctoral thesis, Buffalo, New York, USA, 2004.
[5] Ș. Țălu, M. Țălu, *IFMBE Proceedings*, **26**: 291-294, 2009.
[6] M. Țălu, Ș. Țălu, S.D. Țălu, R. Shah, *IFMBE Proceedings*, **36** (**4**): 252-255, 2011.
[7] A. Jaklic, A. Leonardis, F. Solina, *Segmentation and Recovery of Superquadric. Computational imaging and vision*. Kluwer Academic Publishers, Dordrecth, The Netherlands, 2000.
[8] Madsie Freestyle 1.5.3, at http://www.madsie.com/.

EMVPO2012_5757_020 STUDENT PRESENTATION

Defocus-corrected determination of the Stiles-Crawford effect of the first kind

B. Lochocki, B. Vohnsen; University College Dublin, School of Physics, AOI Group, Dublin 4 (IE).
Email: benjamin.lochocki@ucdconnect.ie

Summary
The Stiles-Crawford effect of the first kind has been determined across the visible spectrum while correcting defocus subjectively in the authors' eyes. The obtained results show the distinct influence of chromatic aberrations and the role they play when light impinges on cone photoreceptors.

Introduction
The Stiles-Crawford effect of the first kind (SCE) describes a reduced visibility when a light beam's entry into the eye is shifted towards the edge of the pupil [1] and has commonly been attributed to photoreceptor waveguiding. The visibility function η of the SCE across the pupil is subjective characterized by a wavelength-dependent directionality factor $\rho(\lambda)$ of the cone photoreceptors and usually fitted to the following equation:

$$\eta(x,\lambda)=10^{-\rho(\lambda)(x-x_0)^2} \quad (1)$$

where x_0 is the peak of the visibility function and x is the pupil entrance point.
Analysis of the SCE is commonly done using white light or a fixed wavelength and aberrations are commonly neglected due to the Maxwellian illumination. In 2007 Vohnsen has shown that defocus may influence the amount of coupled light into the photoreceptors [2]. Therefore a defocus-corrected SCE setup has been developed to minimize its impact on the determination of the SCE.

Discussion
We determined the SCE in the author's eyes: BV(43y, right eye) and BL(32y, left eye) using a bipartite Maxwellian setup measuring ac-

ross the visible spectrum at eleven wavelengths. Our setup includes automated control of wavelength, bandwidth, colour and intensity adjusted by the subject. To obtain the defocus correction a combination of a negative achromatic lens and a current-controlled tunable positive lens (Optotune™) was placed in front of the eye. The subject compares the brightness of a bipartite field when one beam is traversing the pupil and the subject adjusts the brightness as desired for the best match to the reference field.
For each individual wavelength four across-the-pupil scans were realized whereby the individual defocus correction was linked to the examined wavelength and reducing the impact of chromatic aberrations.

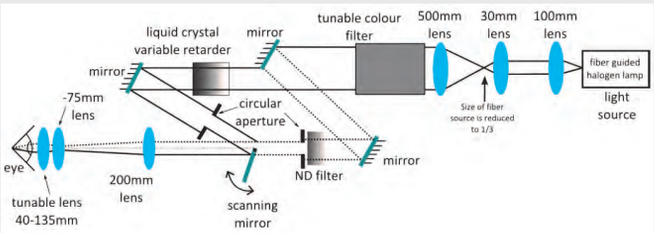

Fig. 1: Schematic of the experimental setup

Measurements of the SCE were taken by compensating defocus errors. All of the obtained results were fitted to the equation:

$$\eta(x,\lambda) = a + b * 10^{-\rho(\lambda)(x-x_0)^2} \quad (2)$$

This fitting equation improves the accuracy of the fit compared to the traditional Gaussian function (see Eq.1).

Conclusions
The results indicate a not negligible impact of aberrations when coupling light into cone photoreceptors where in particular chromatic aberrations need attention. We found a higher directionality factor for both subjects compared to values found by Stiles and Crawford [1] and to our previous measurements done without aberration correction [3].

References

[1] W. S. Stiles and B. H. Crawford. The luminous efficiency of rays entering the eye pupil at different points, *Proceedings of the Royal Society of London. Series B, Containing Papers of a Biological Character*, **112**, 428-450, 1933
[2] B. Vohnsen. Photoreceptor waveguides and effective retinal image quality, *Journal of Optical Society of America*, **24**, 597-607, 2007
[3] B. Lochocki and D. Rativa and B. Vohnsen. Spatial and spectral characterisation of the first and second Stiles-Crawford effects using tuneable liquid-crystal filters, *Journal of Modern Optics*, **58**, 1817-1825, 2011

EMVPO2012_5759_021 **STUDENT PRESENTATION**

Health Risks of Artificial Stereopsis and a Natural Solution

E. Ansbro[1], C. Overhauser[2], Alova[2]; [1]Open University, PSSRI, Milton Keynes (GB); [2]RealView Innovations Ltd, Boyle (IE).
Email: eansbro@realview.ie

Summary
Modern 3d displays exploit our brain's ability to generate a stereooptical image from both eyes. Numerous health risks have been reported, such as fatigue, headaches, nausea, and disorientation. A natural method of depth enhancement is preferred, which allows viewers to dynamically shift between accommodation and vergence.

Introduction
3D displays, and in particular 3D TVs, are intended for immersing viewers' visual faculties with realistic stimuli. This relies critically on properly stimulating their visuoocular processes, while avoiding artificial interferences to their perception when viewing.
In natural viewing, viewers do not just passively perceive. Instead, they dynamically scan the visual scene by shifting their eye fixation and focus between objects at different distances. In doing so, the oculomotor processes of accommodation (eye focus) and vergence (angle between lines of sight of two eyes) must be shifted synchronously to place new objects in sharp focus in the centre of each retina. Accordingly, nature has reflexively linked accommodation and vergence, such that a change in one process automatically drives a matching change in the other.

Discussion
Conventional stereoscopic displays, such as 3D TVs, whether utilizing parallax barrier, lenticular, polarization, shuttering, retro-reflective mirrors, half-silvered mirrors, or multiple projectors, force viewers' visual systems to try to decouple the processes of accommodation and vergence, which are normally synchronized. With these types of artificial stereopsis, viewers must dynamically vary the vergence angle to view objects at different stereoscopic distances. But they must also keep accommodation at a fixed distance – or else the entire display slips out of focus. This unnatural decoupling generates eye strain, headaches, fatigue, dizziness, and nausea, and compromises image quality. Viewers also report being disoriented for up to several hours after watching 3D TVs. These symptoms depend on age, with people under 35 being most strongly affected.

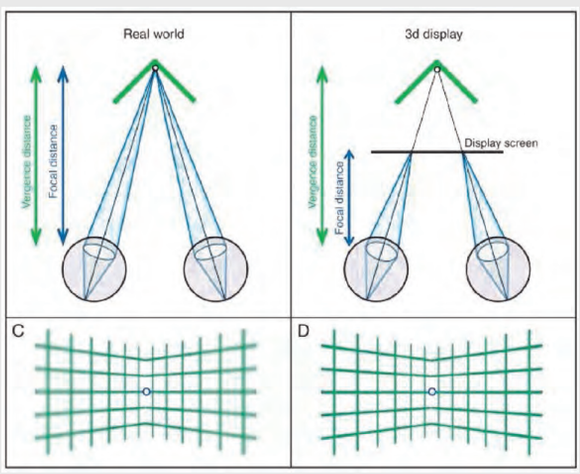

Fig. 1: Virtual 3D requires different vergence and accommodative responses

In an effort to solve this accommodation/vergence mismatch problem, we have developed a screen that is placed in front of an ordinary 2D display. This screen does not require artificially generated images, but utilizes natural depth cues in the image. It allows viewers to focus on objects at different distances in a displayed scene, matching vergence and stereoscopic retinal disparity, thus simulating natural viewing conditions. The focus of individual objects in a scene matches the viewer's stereoscopic retinal disparity, so the cues for ocular accommodation and vergence are congruent. As in natural vision, the viewer brings different objects into focus by shifting accommodation. As the mismatch between accommodation and vergence is decreased, natural viewing conditions are greatly increased.
No adverse side-effects or reactions of any kind have been reported to date.

Conclusions
The health risks of artificial stereopsis are numerous and widespread. A natural alternative is preferred.

References

[1] P.J. Corriveau, R.A. Doherty, S.N. Yang, and J.E. Sheedy, "*Visual Factors in Virtual Three-Dimensional Displays", Stanford Workshop on 3D Imaging*, 2011
[2] David M. Hoffman, Ahna R. Girshick, Kurt Akeley, and Martin S. Banks, "*Vergence–accommodation conflicts hinder visual performance and cause visual fatigue" J Vis.* **8(3):33**,1–3330, 2008
[3] P.A. Howarth, "*Potential Hazards of Viewing 3-D Stereoscopic Television, Cinema and Computer Games: a Review*," *Opthalmic Physiol Opt.*, **31(2)**,111-22, 2011
[4] S.K. Rushton and P.M. Riddell, *Developing visual systems and exposure to virtual reality and stereo displays: Some concerns and speculations about the demands on accommodation and vergence*, *Applied Ergonomics*, **30(1)**, 69-78, 1999
[many more references]

EMVPO2012_5760_022 STUDENT PRESENTATION

Wavefront reconstruction for a thick fundus model using a Shack-Hartmann wavefront sensor

T.Liu, L.N. Thibos; Indiana University, School of Optometry, Bloomington, 47405, (US).
Email: liutao@indiana.edu

Summary
We simulated wavefront aberrometry for a thick-fundus model in which light from a probe beam is reflected by two retinal layers separated axially. Conventional centroid algorithms determined aberrations and mean focus but a global reconstruction method also recovered both focus values associated with both reflecting layers.

Introduction
Conventional Shack-Hartmann (SH) wavefront aberrometry of human eyes assumes light from a retinal beacon is reflected by a single, thin layer of tissue. Based on this assumption, the displacement of spot images formed by a lenslet array may be determined from spot centroids, from which wavefront slope is computed [1]. However, evidence that the fundus is a thick reflector [2, 3] casts doubt on this standard model of wavefront aberrometry. Light reflected from each layer of the fundus will produce a pattern of spots characteristic of the eye's astigmatism and higher-order aberrations, but with different amounts of defocus. The superposition of these multiple images will cause radial elongation of the spots by an amount determined by the axial thickness of the reflector. The centroids of these composite spots would be expected to correspond to the centroid of the axial distribution of light reflected from the fundus, but would not reveal the axial thickness of the reflector. To extract thickness information we turned to a global wavefront reconstruction method [4] that utilizes radial elongation of spots.

Method
A SH simulation program written in Matlab was used to create an artificial image of spot patterns from a wavefront aberration map associated with a single reflecting layer of the retina. The wavefront aberration map was generated by a random process with the same statistical properties as the normal human population [5]. A second image was generated by adding 0.7 diopters of defocus to the same wavefront to simulate a second reflecting layer separated 0.27mm axially from the first layer. Incoherent superposition of the two images yielded a composite "data image" for analysis. The developed global algorithm retrieved both Zernike defocus coefficients for the bi-layers by optimizing axial separation to minimize the difference between the simulated image and original data image. This process was repeated for 100 randomly selected wavefront aberration maps.

Results
A typical example of a composite data image processed by the global algorithm is shown in Fig. 1. Note the subtle radial elongation of individual spots, which is more pronounced near the pupil margin. This pattern of spot elongation is the signature of the bi-layer reflector model. Axial separation of the bi-layer reflectors determined by the global reconstruction algorithm is shown in Fig. 2 for all 100 randomly generated test wavefronts.

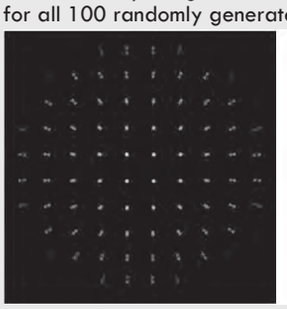

Fig. 1 Processed data image

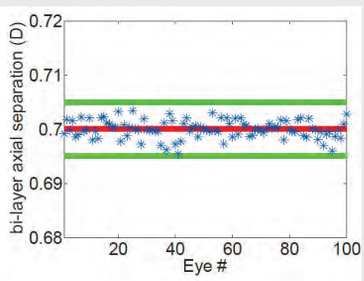

Fig. 2 Recovered axial separation of the bi-layer reflectors

The mean axial separation was 0.7001D, as indicated by the red line. The standard deviations (SD) of the axial separation was 0.0016D, the +/-3 SD are drawn as green line. All the estimated axial separation fall in the +/- 3SD interval, which demonstrates that the derived Zernike defocus arising from the global method agreed with the programmed bi-layer model used to create the data image.
However, the traditional wavefront reconstruction method utilizing centroids could only recover the averaged defocus that corresponds to the midpoint of the bi-layer model.

Discussion
Because the global method is an iterative algorithm, the proper initial value played an important role. While the centroid reconstruction algorithm cannot recover the bilayer axial separation, it does produce a useful initial value for the global method. Although we used a simplified, bi-layer reflector model, the global reconstruction method can be generalized to include multi-layer scenarios.

Conclusions
Axial thickness of a bi-layer fundus reflector is measurable with a global reconstruction method. This result suggests that the thick reflection model plus global algorithm is a promising SH data image analysis tool to be applied in clinical research.

References
[1] J. Liang, B.Grimm, S. Goelz, and J. F. Bille, *J. Opt. Soc. Am. A* ,**11**, 1949,1994
[2] S. A. Burns, S. Wu, F. Delori, and A. E. Elsner, *J. Opt. Soc. Am. A* , **12**, 2329, 1995
[3] W. Gao, R. S. Jonnal, B. Cense, O. P. Kocaoglu, Q. Wang and D. T. Miller, *OPTICS EXPRESS* , **17**, 23085 , 2009
[4] R. C. Cannon, *J. Opt. Soc. Am. A* , **12** , 2031, 1995
[5] L.T. Thibos, *Ophthal. Physiol. Opt.,* **29**, 288–291, 2009

EMVPO2012_5764_023

Selection of a relevant human eye model to study visual performances of corneal inlays

J. Jarosz[1,3], F. Castignoles[3], T. Lépine[1,2], P. Tankam[1]; [1]Laboratoire Hubert Curien (UMR 5516 CNRS), Université de Lyon, Université Jean-Monnet, F-42000, Saint-Etienne (FR); [2]Institut d'Optique Rhône-Alpes, 18 rue Benoît Lauras, F-42000, Saint-Etienne (FR); [3]Presbeasy, Lyon, F-69007 (FR).
Email: thierry.lepine@institutoptique.fr

Summary
We aim at selecting the best eye model in order to deal with presbyopia-correcting corneal diffractive multifocal lenses characterization and optimization. The eye model will enable the analysis of optical performances along with the simulation of surgery-induced changes such as decenter and tilt.

Introduction
A thorough knowledge of the eye is compulsory when one's interests are to design and assess performances of ophthalmic lenses. Various eye models more or less elaborate and accurate have been proposed to model the human eye since Gullstrand number 1 schematic eye in 1909 – [1]. Unlike classic intraocular lenses (IOL), developing phakic IOL and corneal inlays requires a complete modeling of the eye. We present the specifications the eye model must fulfill to yield realistic performances with our corneal lens.

Discussion
The simulations are performed in Zemax®. Our goal is to study corneal diffractive multifocal lenses to correct presbyopia. Regarding the eye model, such an application implies paying special attention to modeling the gradient refractive index distribution and chromatic dispersion of the crystalline lens, the axes of the eye and the pupil decenter. First, we review existing eye models – in particular [2-5], so as to

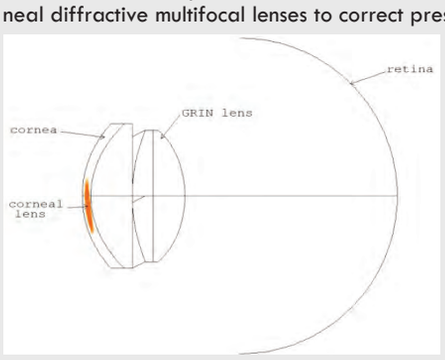

Fig 1. Insertion of the corneal lens within the eye model

select the most appropriate model within our framework. Then, we position the lens within the selected eye model – Fig 1, and present preliminary characterizations of the presbyopia-correcting corneal diffractive multifocal lens whose design was discussed elsewhere – [6].

Conclusion
The selected eye model offers realistic data and enables us to place the corneal lens correctly within the eye and thus study decentering and tilting of the corneal lens as well as providing accurate simulation of the corneal lens positioning. We point out compensation of longitudinal chromatic aberration entailed by the insertion of the corneal diffractive lens and demonstrate our presbyopia-correcting corneal lens efficiency for improvement of near vision performances in terms of modulation transfer function.

References

[1] A. Gullstrand, Appendices II and IV, in *Helmholtz's Handbuch der Physiologischen Optik*, 3rd ed., A. Gullstrand, J. von Kries, W. Nagel, (Voss, Hamburg, 1909)
[2] D.A. Atchison, and G. Smith, *Optics of the human eye*, (Butterworth Heinemann, Oxford, UK, 2000)
[3] H.L. Liou and N.A. Brennan, J. Opt. Soc. Am. A, **14**, 1684-1695, 1997
[4] R. Navarro, F. Palos, and L. González, J. Opt. Soc. Am. A, **24**, 2175-2185, 2007
[5] R. Navarro, F. Palos, and L.M. González, J. Opt. Soc. Am. A, **24**, 2911-2920, 2007
[6] F. Castignoles, M. Flury, and T. Lépine, Opt. Express, **18**, 5245-5256, 2010

EMVPO2012_5766_024 STUDENT PRESENTATION

Individual biomechanical model of the human eyeball

E. Szul-Pietrzak, A. Hachoł, H. Podbielska; Wroclaw University of Technology, Group of Biomeasurements and Biomedical Signals Analysis, Wroclaw, 50-370 (PL).
Email: elzbieta.szul@pwr.wroc.pl

Summary
The aim of this work is to present biomechanical model of the human eyeball created with using the finite element method (FEM). The model takes into account the individual geometry and biomechanical properties of the cornea.

Introduction
Development of numerical methods allows the simulative testing of even the most complicated research problems. Finite element method (FEM) is helping to solve the design, electromagnetic and biomedical issues [1]. The FEM method allows for construction of eyeball model based on individual measurements of the geometry and biomechanical properties for each patient. This method is useful in solving the biomedical problems, because the in vivo measurement of alive objects if very difficult, or even impossible for ethical reasons, or may result in damage of the object. Earlier works on the subject have shown that the modeling of an eyeball using FEM can give interesting results [2-4].

Discussion
The developed model is based on clinical measurements of the real geometrical parameters of the eyeball. Parameters of the anterior eye segment were mapped on the basis of images from the OCT Visante (Carl Zeiss Meditec Ltd, Dublin, CA) (Fig. 1). The length of the eyeball was measured with IOL Master (Carl Zeiss Meditec Ltd, Dublin, CA), and its biomechanical parameters using the Ocular Respondents Analyzer (Reichert, Inc.. Depew, NY, USA).
The influence of diurnal changes in intraocular pressure on deformation of the cornea and the effect of geometrical parameters and corneal biomechanical properties on the error of intraocular pressure measurement with tonometrical method was studied. Displacements in the apex area of up to 0.012 mm/mmHg were observed in the model, whereas in the limbus area they were 0.01 mm/mmHg in the horizontal axis direction and 0.003 mmHg in the vertical axis direction.

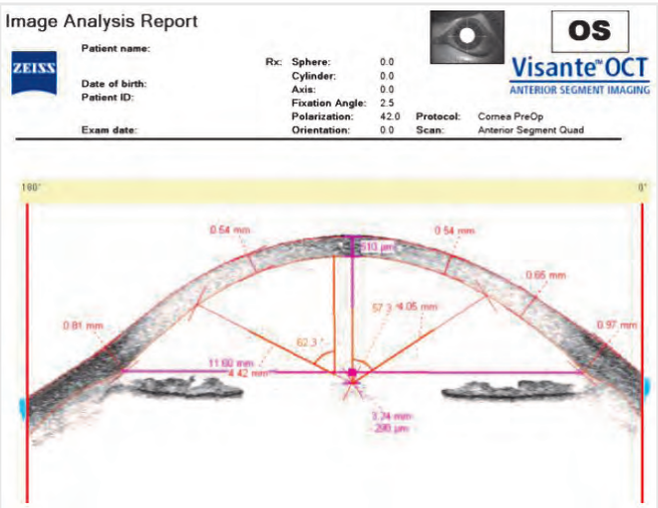

Fig1. Geometry of the anterior eye chamber measured with using of OCT Visante.

Research on the influence of corneal geometry and biomechanical properties have shown a multi-dimensional relationship between the measured value of intraocular pressure and corneal thickness, the radius of the corneal curvature and biomechanical properties When cornea was loaded with pressure of 15 mmHg we observed in our study that the measurement error depends on corneal thickness, radius of the cornea profile and the biomechanical properties and that they are different for different combinations of cornea parameters. For example, when the corneal thickness is equal to 0.650 mm and the radius is equal to 9.5 mm the measurement result is overestimated by about 3.7 mmHg while for the cornea of the same stiffness and thickness but with a radius of 7.0 mm it is overestimated only by about 2 mmHg. In contrast, when cornea is thin and radius of curvature is small, (e.g. 0.45 mm of thickness and 7.0 mm of radius) the result of measurements is lower by 2.5 mmHg from the assumed model pressure.

Conclusions
The developed model enables: (i) to study the impact of the patient's individual eyeball parameters on the cornea deformation under the influence of intraocular pressure changes, (ii) evaluate the influence of geometry and corneal biomechanical properties on accuracy of intraocular pressure measurement and also (iii) can be applied to individualized preoperative procedures for laser refractive surgery.

Acknowledgements
This work was supported by the Ministry of Science and Higher Education (Grant No. N N518406738), by the Wroclaw University of Technology, Wroclaw, Poland.

References

[1] O. C. Zienkiewicz, Internationa Journal for Numerical Methods in Engineering 47, 9-28, 2000
[2] M. Asejczyk-Widlicka, W. Środka, H. Kasprzak, D. Iskander, Optik, 11: 517-52, 2004
[3] A. Hachoł, E. Szul-Pietrzak, E. Pelczar, 6th European Symposium on Biomedical Engineeing, ESBME Greece, Chania, 2008
[4] E. Szul-Pietrzak, A. Hachoł, K. Cieślak, R. Drożdż, H. Podbielska, Journal of Modern Optics, 1-9, 2011

EMVPO2012_5771_026 STUDENT PRESENTATION

Transposing the Stiles-Crawford Effect from Pupil to Retina in Eye Modelling

C. Vela, B. Lochocki, B, Vohnsen; AOI Group, University Dublin College, School of Physics, Belfield, Dublin 4 (IE).
Email: carmen.vela-garcia@ucdconnect.ie

Summary
Effective retinal images for two common eye models have been analysed with the Stiles–Crawford effect introduced directly at the retina rather than at the pupil. The impact of defocus has been analysed on effective retinal images being guided to the visual pigments by photoreceptor cones.

Introduction

The Stiles-Crawford effect of the first kind (SCE) describes a marked reduction in visibility of a narrow beam of light incident near the pupil rim. The directionality of cone photoreceptors is recognised as being the main cause of the SCE1 resulting in a reduced coupling of obliquely incident light at the retina. This angular sensitivity results from the elevated refractive index and elongated structure of cones making them act as biological waveguides and impacting the light propagation towards the visual pigments contained in the outer segments.2-4

Models that simulate optical properties of the human eye are essential to examine refractive optics and visual function. Common eye models and refractive optics are typically analysed using the Modulation Transfer Function, Point Spread Function (PSF) or Strehl Ratio (SR) to evaluate the predicted retinal image quality. Here, the SCE is either ignored or, when included, treated as a Gaussian apodisation of a given directionality across the pupil despite of its retinal origin. In the present work, both (i) a relaxed and (ii) an accommodated Gullstrand schematic eye model5 has been analysed using Zemax™ to propagate the light and evaluate the resulting PSF (intensity, field amplitude and phase) at the retina. The fraction of light incident on the retina that via waveguiding may reach the outer-segment pigments has been estimated using MATLAB™ to project the PSF into a waveguided and thus an effective retinal image. This mapping procedure allows the SCE to be taken into account directly at the retina rather than at the pupil thereby giving a clearer insight of its role in vision.

Discussion

The field incident on the retina ψ_r, as determined by the PSF, can be written in terms of its amplitude and phase distribution as

$$\psi_r(u,v) = \mathrm{A}(u,v)\exp[i\varphi(u,v)] \quad (1)$$

where (u, v_c) refers to any point on the retina. Assuming that each cone is a single-mode waveguide (the approach may easily be generalised to include higher-order modes3,4), a Gaussian mode distribution for each inner segment may be written as

$$\psi_c(\rho) = \sqrt{\frac{2}{\pi\omega^2}}\exp\left[-\frac{\rho^2}{\omega^2}\right], \quad (2)$$

where w is the width of the mode and the amplitude has been normalised. The waveguided effective retinal image, taking the SCE into account directly at the retina, may be expressed as a convolution4

$$T(u_c,v_c) = \left|\iint \psi_r(u,v)\psi_c(u-u_c,v-v_c)\,du\,dv\right|^2 \quad (3)$$

where (u_c, v_c) refers to the retinal location of any given cone photoreceptor aperture.

The PSF obtained in the presence of defocus for the two eye models has been analysed using Eq. (3) to calculate the waveguided PSF and integrated across the retina to find the total waveguided power, P, for a closely-packed arrangement of photoreceptor cones. The results are shown in Fig. 1 that for comparison also shows the corresponding Strehl Ratio of the PSF prior to waveguiding.

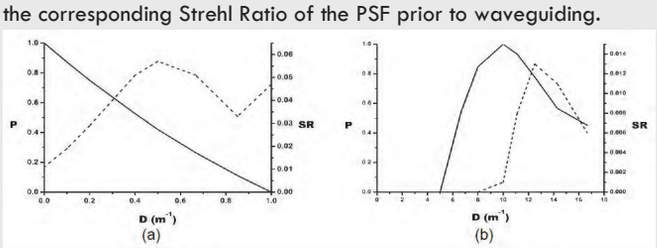

Fig.1 Normalised waveguided power P (solid curve) and the Strehl Ratio (dashed curve) for the relaxed Gullstrand eye model (a) and the accommodated Gullstrand eye model (b) for a pupil diameter of 6 mm in the presence of defocus D at a wavelength of 0.550 μm. The mode width ω for the singlemode photoreceptors was fixed at 2 μm.

Conclusions

The results show that the waveguided power contained in the PSF is influenced by defocus and serves as a better indicator than the Strehl ratio of the best focal plane for both the unaccomodated and the accommodated eye models. For the accommodated eye model the power levels off to about 50% of its peak value at ~10D ± 3D. This suggests that the SCE may provide clues for accommodation at large pupil diameters while still attenuate the visual impact of aberrations in agreement with the pupil apodisation commonly used to represent the SCE.

References

[1] W.S. Stiles and B.H. Crawford, *The luminous efficiency of rays entering the eye pupil at different points*, Proc. R. Soc. London, Ser. B **112**, 428–450, 1933

[2] A.W. Snyder, and C. Pask, *The Stiles–Crawford effect: Explanation and consequences*. Vision Research **13**, 1115–1136, 1973

[3] B. Vohnsen, I. Iglesias and P. Artal, *Guided light and diffraction model of human-eye photoreceptors*. Journal of the Optical Society of America A **22**, 2318–2328, 2005

[4] B. Vohnsen, *Photoreceptor waveguiding and effective retinal images*. Journal of the Optical Society of America A **24**, 597-607, 2007

[5] D. A. Atchison & G. Smith, *Optics of the Human Eye*, (Elsevier Science, Edinburgh, 2006)

EMVPO2012_5778_027

The minimum motion and heterochromatic techniques to differentiate lutein and zeaxanthin macular pigment optical density using CRT and different spectral emission LED light stimuli

M. Ozolinsh[1,2], P. Paulins[1]; [1]University of Latvia, Riga LV1063 (LV); [2]Institute of Solid State Physics, University of Latvia, Riga (LV).
Email: ozoma@latnet.lv

Summary

Heterochromatic flicker and minimum motion techniques are applied to determine effective red-blue isoluminance affected by macular pigment optical density (MPOD) in central retina areas. Light stimuli with discrimination in blue spectral region allow to distinguish changes in optical density of macular pigments lutein and zeaxanthin.

Introduction and Experimental

The decrease of density and consequentially optical density of macular pigment (MPOD) serves as a diagnostic mean for a number of ophthalmological pathologies, particularly as a risk factor for age related macular degeneration (AMD). Macular pigment absorbs light in short wavelength blue spectral range. Thus MPOD can be detected by various optical – both objective and subjective psychophysical techniques. Latter techniques use eye and brain visual pathways as spectral sensitive optical detector and decision maker, and exploit perception facility to process information flow in a unique manner to create various perception illusions. The psychophysical methods of detection of MDOD include heterochromatic flicker photometry and minimum illusory motion photometry [1-3].

We employ a similar motion nulling grating method as proposed by Cavanagh and Anstis [1]. A chromatic CRT generated red-blue grating is displayed sequentially with a neutral luminance grating. The perceptual forward-backward direction of grating drift is dependent on the relative perceived luminance of red and blue components. The same principles are used in a method developed by us where LED are used as visual stimuli. LED emission maximum wavelengths in blue spectrum region can choose in range 445-460 nm, that corresponds to spectrally resolved maxima of light absorption for two types of macula pigments – lutein and zeaxanthin [4].

Conclusions

Replacement of planar CRT screen with a modular LED compound consisting of controllable red, neutral and two types of blue LEDs allows to realize a separate detection of lutein and zeaxanthin macular pigment densities using minimum perceived motion illusion and heterochromatic flicker techniques.

References

[1] S. Anstis, and P. Cavanagh. A minimum motion technique, in Colour vision: Psychophysics and physiology, Acad.Press, London,1983

[2] J. Mellerio, S. Ahmadi-Lari, F.J.G.M. van Kuijk, D. Pauleikhoff, A.C. Bird, and J. Marshall, Cur.Eye Res., 25, 37–47, 2002

[3] J.D. Moreland, Arch.of Biochem.and Biophys., 430, 143–148, 2004

[4] J.van de Kraats, M.J. Kanis, S.W. Genders, and D.van Norren, Invest. Ophthalmol.Vis Sci., 49, 5568–5573, 2008

Room: Exhibition area

POSTER SESSION II:
Wednesday, 22 August | 14:00 - 15:30 CEST

EMVPO2012_5337_028 STUDENT PRESENTATION

Just-noticeable differences for ocular wavefront aberrations

H. Jungnickel[1], D. Weigel[2], H. Babovsky[2], A. Kiessling[2], R. Kowarschik[2], M. Gebhardt[1]; [1]University of Applied Sciences, SciTec Department, 07743 Jena (DE); [2]Friedrich Schiller University, Institute of Applied Optics, 07743 Jena (DE).
Email: *Hendrik.Jungnickel@fh-jena.de*

Summary
Just-noticeable differences (JND) for astigmatism, coma and trefoil were determined using an adaptive optics setup. Lower values of coma than those of astigmatism and trefoil lead to a change in visual impression.

Introduction
In conventional spectacle corrections, residual lower-order aberrations (defocus and astigmatism) and higher-order aberrations (e.g. coma and trefoil) remain. The aim of the study was to find out just-noticeable levels of three selected aberrations in healthy eyes. 28 eyes of 28 subjects participated and were carefully refracted with trial lenses. For determination of JND, an adaptive optics setup including MIRAO 52-e Deformable Mirror and HASO 32 Wavefront Sensor (both Imagine Eyes, Orsay, France) was used. Initially determined values of defocus and astigmatism were corrected (correction A), residual aberrations were measured and additional astigmatism, coma or trefoil was induced by the setup (correction B). Both additional and residual aberration had the same angular orientation. Subjects observed a radial test-pattern (Fig. 1) with non-cyclopleged eyes and an artificial 5 mm pupil. They compared corrections A and B and had to identify the subjective better correction. Magnitude of the aberration for each presentation varied according to the "Best PEST" staircase procedure. JND was found after 30 presentations.

Fig. 1 Radial black-and-white test pattern, diameter 1.0°

Discussion
Median JND was 0.09 µm for astigmatism, 0.06 µm for coma and 0.11 µm for trefoil with a large interindividual spread (maxima 0.635 µm, 0.211 µm and 0.364 µm). Blur was also quantified in units of log VSOTF (visual Strehl ratio based on the optical transfer function). Median reduction was 0.09 log VSOTF for astigmatism, 0.08 log VSOTF for coma and 0.08 log VSOTF for trefoil by increasing up to the respective JND. Compared with the mean values of coma and trefoil in healthy eyes (coma 0.109 µm, trefoil 0.095 µm) [1], it is assumed that coma leads to a noticeable loss in vision quality more often than trefoil. Conversely, this means that coma correction could be helpful in the majority of healthy eyes, whereas trefoil correction would rarely result in an improvement.

Conclusions
Just-noticeable differences are lower for coma than for astigmatism and trefoil. However, there are large differences between the subjects. Thus, the decision to correct more pronounced aberrations (e.g. by wavefront-guided LASIK) should not depend on wavefront measurement results alone. Instead, subjective alignment (e.g. by means of an adaptive optics phoropter) is necessary.

References
[1] T.O. Salmon, and C. van de Pol, *J Cataract Refract Surg*, **32**, 2064-2074, 2006

EMVPO2012_5563_029

Application of multivariate analysis of variance (MANOVA) to distance refractive variability and mean distance refractive state

S. Abelman, H. Abelman; School of Computational and Applied Mathematics, University of the Witwatersrand, Johannesburg, Private Bag 3, Wits, 2050 (ZA).
Email: *Shirley.Abelman@wits.ac.za*

Summary
A 30-year-old female was subjected to 30 autorefractor measurements each taken at various intervals before and after the instillation of Mydriacyl 1% (tropicamide) into her right eye. The purpose of this work is to apply multivariate analysis of variance (MANOVA) to the sample data in order to assess whether instillation of Mydriacyl into the eye affects variability of distance refractive state as well as mean distance refractive state as measured by an autorefractor.

Introduction
The optometrist engaged in research investigates anything that has to do with vision. Refractive state can be regarded as a dynamic quantity. Multiple measurements of refractive state can be determined easily and rapidly on a number of different occasions using an autorefractor. Different types of refractive variation have been found when measuring refractive state using an autorefractor. Repeated measurements of refractive state reveal variability of the refraction. A cycloplegic refraction is the procedure whereby an individual's refractive error is determined while the muscles that control accommodation are paralysed with cycloplegic agents. Although cycloplegic testing is not usually performed with adult subjects, those who overfocus or underfocus could benefit.

Discussion
Let $\mathbf{S}_1$ be the variance-covariance matrix of the mean distance refractive state of the right eye of a 30-year-old female subject 30 minutes before the instillation of Mydriacyl, $\mathbf{S}_2$ the variance-covariance matrix of the mean distance refractive state of the eye just prior to instillation, $\mathbf{S}_3$, $\mathbf{S}_4$ and $\mathbf{S}_5$ the variance-covariance matrix of the mean distance refractive state of the eye 15 minutes, 30 minutes and 60 minutes respectively post instillation.
In five of the seven cases where pairwise hypotheses tests were performed, it is concluded that at a 99% level of confidence there is no difference in variability of distance refractive state before and after cycloplegia. In two of the three cases where MANOVA was applied, there is a significant difference at a 95% and at a 99% level of confidence in both variability of distance refractive state and mean distance refractive state with and without cycloplegia.

Conclusions
The selection of a cycloplegic agent depends on the desired outcome, the characteristics of the subject receiving the drug and the associated risks. A minimum clinical history of each subject should be undertaken in order to avoid potential adverse drug reactions, both systemic and ocular. For example, one of the side effects of Mydriacyl is dry mouth and this could make the subject very uncomfortable and influence his/her responses.
A sample size of 30 measurements per sample is possibly too small. A larger sample of 30-year-old female subjects with a variety of spectacle prescriptions should be subjected to the experimental procedure to draw more concrete conclusions. Possibly a control group should also be included. Subjects can be their own controls. In addition one should also perform the experimental procedure on an equivalent sample of 30-year-old males including a control group. The experimental trial should also be performed on a combined group of 30-year-old males and females with a control group.
One may ask whether Mydriacyl is in fact an effective cycloplegic for paralysis of the ciliary muscle for the duration of this experiment. Cyclogyl would have been more effective, but it takes longer to dissipate. A study using Mydriacyl with autorefraction at near rather than at distance would also be useful to obtain a clearer idea of its

cycloplegic efficacy. The entire experiment could be repeated with different cycloplegics, and the results compared to make the study more comprehensive.

References

[1] Harris WF. Testing hypotheses on dioptric power. *Optom Vis Sci* **69** 835-845, 1992.
[2] Sharma S. *Applied multivariate techniques*. New York: Wiley, 1996.

EMVPO2012_5572_030

Is the iris suitable as a biometric?

D.Rankin[1], B. Scotney[1], P. Morrow[1], B.Pierscionek[2]; [1]University of Ulster, School of Computing and Information Engineering, Cromore Road, Coleraine, BT52 1SA (GB); [2]Faculty of Science Engineering and Computing, Kingston University, Friars Avenue London SW15 3DW (GB).
Email: b.pierscionek@kingston.ac.uk

Summary
The search for reliable biometrics is increasing with global security threats. A biometric must remain consistent throughout a lifetime if it is to be successful for identification purposes. The number of degrees -of-freedom that a biometric has determines its suitability with increased independent dimensions of variation providing a more discriminative biometric. The iris contains around 266 degrees-of-freedom cited which is the greatest of all facial features. However, the iris pattern is complex and the iris is dynamic, with changes in pupil size mediated via the autonomic nervous system in response to internal and external stimuli.

Introduction
This study examined differences in iris texture patterns, whether changes over a short time period can be detected and whether texture differences affect iris identification. Iris images were captured using a Takagi biomicroscope from the left and right eyes of 76 subjects at three sessions with a time interval of three months between each session, from 41 subjects on two occasions at three month intervals and from 2 subjects on two occasions with a six month interval. All subjects were free of ocular pathologies, did not suffer from any systemic conditions and none were on any medications. Primary gaze position was steadied by asking each subject to focus on a fixation target. Stability was verified by the position and size of the first Purkinje image. All irides were graded on texture by two independent observers, into six grades from the finest (Grade 1) to the coarsest (Grade 6). Images were processed and features extracted, using log Gabor filters, to produce binary codes that were matched to determine identification.

Discussion
Most irides were classified as Grades 3 and 4, with the smallest numbers in the extreme (finest and coarsest) groups. Failure to recognise the same iris occurred in around 21% of cases between images taken at three (21.2%) and six month (20.5%) intervals. At three month intervals, changes in iris features from the same individual occurred across all texture grades with the highest proportions in Grades 1, 2 and 6. Results for comparison of images separated by a six month interval showed the highest failure rates to recognise the same iris in Grades 1 and 2.

Conclusions
The complex fibre pattern formation of the iris results in variability in identification with differing failure rates depending on texture. The relatively high failure rates in healthy irides over short time periods suggest that the iris is not stable enough as a biometric.

Reference

Rankin, D., Scotney, B., Morrow, P. and Pierscionek, B.K. Iris recognition failure over time: the effects of texture. Pattern Recognition 45: 145-150 (2012)

EMVPO2012_5667_031

Kinematics of eyelid movement and eye retraction in the blinking

J. Pérez[1,2], J. Espinosa[1,2], A.B. Roig[1], B. Domenech[1,2], D. Mas[1,2]; [1]University of Alicante, Dept. Optics, Pharmacology and Anatomy (ES); [2]University of Alicante, IUFACyT, San Vicente del Raspeig - Alicante, 03690 (ES).
Email: julian.espinosa@ua.es

Summary
A non-invasive technique is used to measure the eyelid closure and simultaneous eye retraction. We have fitted the displacement of the eyelid to an analytical function and have extended the kinematic model to the eye retraction movements. As a result, some dynamic parameters have been presented.

Introduction
Mas et al. [1] presented a non invasive technique for high speed measuring some of the dynamic processes that occur during blinking. The technique allows simultaneously measuring the corneal retraction and the eyelid motion during a spontaneous blink. We propose here an analytical model of the eye blinking including lid movement and ocular retraction. The setup for illuminating, capturing and processing the image of the anterior corneal segment was described in [1]. Briefly, the system consists on a slit lamp and an external fast camera working at 512 fps.
Lid displacement was monitored by studying the saturation of the frames in the sequence. Camera is adjusted to detect the light diffused from the cornea, therefore, light diffused by the eyelid saturates the sensor. By counting the number of saturated pixels in each frame, we can reconstruct the position of the eyelid. Eye retraction is evaluated by analysing a scanning line perpendicular to the inferior part of the cornea. After binarizing the image, cornea is detected from the presence of a white to black border. Pixel to millimetre calibration allows measuring the eye retraction.

Discussion
Upper eyelid motion starts when the Levator Palpebral Superioris muscle (LPSM) is inhibited and the eyelid performs a passive movement downwards. Simultaneous to the LPSM inhibition, the Orbicularis Oculi muscle (OOM) starts a fast contraction thus producing a strong active force. This combination of inhibition and activation of muscular action produces the closure phase of the eyelid. After the action of the OOM, the LPSM starts a restoration force which pulls up the lid to its initial position. Nevertheless, when the OOM action ceases, the upper lid keeps its movement down due to its inertia. The acceleration in the opposite direction makes that the absolute value of the velocity is slowly decreasing until the movement is reversed (Figure 1a).
We divide the blink process in two parts defined by the sign of the eyelid acceleration. The first one, the *active* part, goes from the start to the point of maximum absolute velocity and coincides with the active muscular action. The second part, the *recovery* part, covers the time from the peak velocity to the end of the blinking, being in this part when the forces pull back the lid to its original position. The mechanism for eye retraction inside the orbit is not so well known. Although our method does not permit visualization of the whole eye trajectory, we assume the presence of an *active* and a *recovery* phases. Both eyelid movement and eye retraction are therefore divided in two parts according to the sign of the acceleration, which can be described following (1)

$$X_l^a(t)=\tfrac{1}{12}bt^3(t-2\tau);\quad X_e^a(t)=\tfrac{1}{12}bt^4;\quad X_{e,l}^r(t)=A\exp(-\mu t)\cos(\omega t+\phi) \qquad (1)$$

Parameters *b*, τ, ω and μ represent the strength of the muscle force, its actuation time, frequency of the oscillation and the attenuation constant of the system. Indexes *l* and *e* stand for lid and eye retraction, and *a* and *r* refer to *active* and *recovery* phase, respectively. The fitting function does not have any physical meaning; it is used to determine the instant of maximum absolute velocity, which happens at $t = \tau$.
The lack of data in the eye retraction analysis (Figure 1b) impedes the determination of the point with maximum velocity.

Results and Conclusions

Data from blinking of six subjects have been experimentally fitted to the equations (1). Results (mean ± standard deviation) are shown in (2).

$$b_l=(11.7\pm15.4)\times10^3\,mm/s^4;\quad b_e=(-0.488\pm0.471)\times10^3\,mm/s^4;$$
$$\tau_l=(51.1\pm16.5)\,ms;\quad \mu_e=(17.0\pm2.7)\,s^{-1};\quad (2)$$
$$\mu_l=(10.8\pm2.4)\,s^{-1};\quad \omega_e=(2.2\pm0.9)\,s^{-1};$$
$$\omega_l=(12.5\pm2.6)\,s^{-1};$$

According to Figures 1a and 1b, matching between active and recovery phases occurred at the same time, but, while at that moment the eyelid has started the recovery phase, the eye is still under the effect of a pulling force.

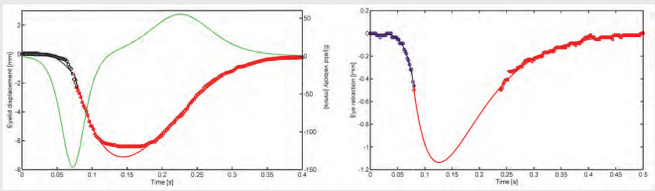

Fig. 1 a)Eyelid position and fitting to the model for one typical case. Green line shows eyelid velocity during blinking. b) Anterior corneal position and fitting to the model for one typical case. The vertical dashed lines marks the link between the two fitting curves (active and the recovery phases).

The method is non-invasive and provides accurate results and can be easily extended to the analysis of contact lens behaviour during blinking, which can be of importance in designing new compensation elements. In addition, obtained parameters can be of interest for analysis of biomechanical modelling of the eye or in neurophysiology due to the deep connection between blinking and neural activity.

References

[1] D. Mas, B. Domenech, J. Espinosa, J. Perez, C., Hernandez, C. Illueca, *Opt. Lett.*, **35**, 1884–1886, 2010.

[2] J. Perez, J. Espinosa, B. Domenech, D. Mas, C. Illueca, *J. Mod. Opt.*, **58**, 1857-1863, 2011.

Aknowledgements

Thanks to Spanish Ministerio de Ciencia e Innovación through the project FIS2009-05639-ET and BIA2011-22704, the Generalitat Valenciana through the project PROMETEO/2011/021 and the University of Alicante through the project GRE10-09. A.B. Roig thanks Fundación Cajamurcia the grant "Beca de investigación Cajamurcia 2010"

EMVPO2012_5673_032

Effects of various combinations of multifocal optics on binocular subjective image quality score

R. Legras[1], G. Vandermeer[2], Y. Nochez[2]; [1]Université Paris-Sud, Laboratoire Aimé Cotton, Orsay, 91405 (FR); [2]Université François Rabelais, Faculté de médecine, Tours, 37000 (FR).

Email: richard.legras@u-psud.fr

Summary

We evaluated the effect of wearing two different multifocal optics (i.e. various combinations of spherical (SA4) and secondary spherical (SA6) aberration) on the left and right eye. This effect was evaluated by measuring binocular subjective image quality score using simulated images calculated from a numerical eye model.

Introduction

The advantage of having two different multifocal optics on the right and left eye has already been used in the correction of presbyopia either by contact lenses or IOL. Spherical aberration (SA4) and secondary spherical aberration (SA6) are often used to compensate presbyopic patients by enlarging the depth-of-focus (DoF). Combinations of SA4 and SA6 of opposite signs appeared to be the most effective in increasing the monocular subjective DoF [1]. The aim of this study was to evaluate the effect of various combinations of spherical (SA4) and secondary spherical (SA6) aberration on each eye on binocular through-focus image quality score.

We used a previously published [2] numerical eye model to calculate the appearance of images viewed through a 4.7-mm pupil diameter and degraded by various combinations of SA4 and SA6 for each proximity from -5-D to 5-D with a 0.125-D step. The calculated point spread functions were convolved with a target corresponding to three 0.4 logMAR high contrast letters.

Binocular vision was simulated by using a 3D system (i.e. NVIDIA video projector) projecting different images on each eye at a 120Hz frequency (i.e. 60Hz per eye).

Through-focus subjective quality of vision was evaluated three times by three subjects, aged between 22 and 28 years old, using a 5 items continuous grading scale following ITU-R 500 recommendations [3] in monocular and binocular condition of vision for each tested conditions (see legend of Figure 1B).

Discussion

Figure 1A shows an example of both monocular and binocular through-focus image scores. Even there was binocular inhibition when different image qualities are viewed by each eye (see figure 1 C, D and E), the general trend of the binocular curve was to follow the best monocular curve. We rarely measured binocular summation in term of subjective vision contrary to what happens with contrast threshold. Ocular dominance appeared to influence the level of inhibition as observed in figure 1 C, D and E. When the best image was viewed by the dominant eye (i.e. plus lens test) the binocular inhibition was limited. This effect was function of the strength of the ocular dominance. The area under the binocular through-focus curve measured between grades 2 and 5 (i.e. a fair or higher subjective image quality) was doubled (i.e. between 1.5 and 2.2 as function of the subject) compared to the area obtained without any multifocal profile (i.e. Naked eye) with a center near (negative SA4 coupling with positive SA6) optical profile on one eye and a center distance (positive SA4 coupling with negative SA6) optical profile on the other eye. Subject 3 seemed to be less sensitive to multifocal profiles.

Conclusion

Our study confirms what is already clinically observed; the use of different profiles on each eye involves a better through-focus quality of vision specially when a center near multifocal design on one eye and a center distance multifocal design on the other eye.

References

[1] Benard and al., Subjective Depth-of-Filed in presence of 4th-order and 6th-order Zernike spherical aberration using adaptive optics technology, J Cataract Refract Surg. 2010 Dec;36 (12):2129-38.

[2] Legras R. and al, A Method for Simulation of Foveal Vision During Wear of Corrective Lenses, Optom Vis Sci. 2004 Sep;81 (9):729-38.

[3] ITU-R, Methodology for the subjective assessment of the quality of television pictures, Recommendation ITU-R BT, 500-506, 1974-2002.

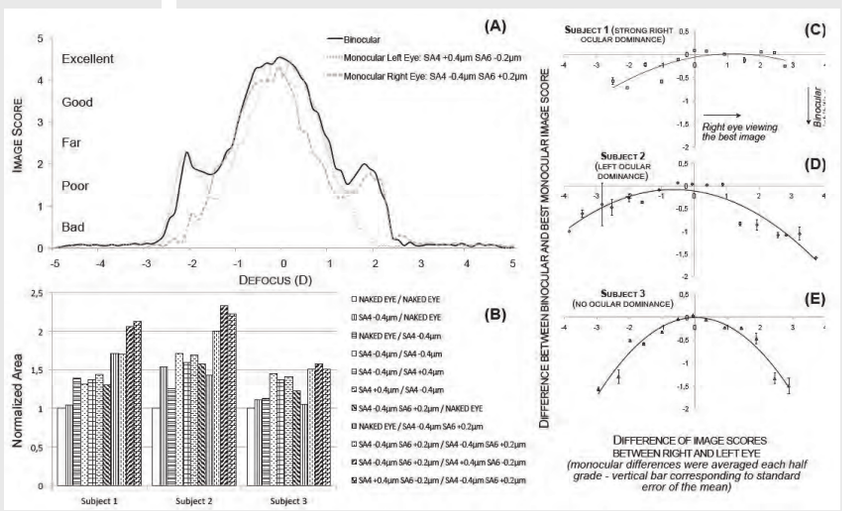

Fig. 1 – **(A)** Example of through-focus curves – **(B)** Comparison of calculated area (i.e. area under binocular through-focus between 2 and 5 normalized by the binocular naked eye area) – **(C, D, E)** Binocular effect (summation or inhibition) as a function of the difference of image quality score between right eye and left eye.

EMVPO2012_5681_033

Variation with the orientation (horizontal - vertical) of a Ronchi achromatic grating in the vision of a color sequence located inside.

J. Montalvá Colomer, I. Tortajada Montañana, M. Aguilar Rico; Universidad Politécnica de Valencia, Escuela Técnica Superior de Ingeniería del Diseño, Valencia, 46021 (ES).
Email: jormonc1@doctor.upv.es

Summary
In this paper we study the value of the Bezold effect produced by a rectangular achromatic grating on the vision of a color sequence (red, green or blue) located inside. According to our results, this value varies with the orientation of the grating, being greater with the horizontal orientation.

Introduction
It is well known that, apart the physical magnitudes of a color test (dominant wavelength, purity and the luminance factor) their psychophysical magnitudes (hue, saturation and lightness) may vary depending on the surrounding colors, variations due mainly to the simultaneous contrast and Bezold effect (assimilation effect, reverse contrast).

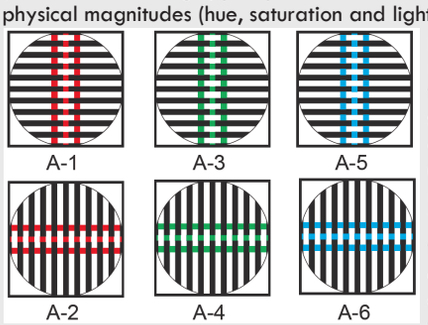

Fig. 1: Tests used. All surrounding gratings are white-black, and sequences are red for A-1 and A-2, green for A-3 and A-4 and blue for A-5 and A-6.

The behaviour of simultaneous contrast is opposite to the reverse contrast occurred when the two colors are altered with high frequency in space that we are observing.
In this paper we have analyzed the vision of a color sequence (red, green or blue) against the background of a rectangular achromatic network (Ronchi) causing the Bezold effect (eB) in the viewing of the sequence.
Without denying the possibility that the expansion effect (eB) can be justified physiologically, as claimed Hurvich and Jameson [1] with the existence of receiver units of various sizes in the area in which the retinal image is formed, we believe this effect can be explained psychologically within the framework of the gestaltian theory, applying not only to the interpretation of the forms and details of the visual scene, but also to their perception of color [2, 3].

Experimental technique
The test used is composed of three parallel rectilinear sequences of a width equal to the separation (1 cm), having as background a rectangular grating with a period of 2 cm, covering a circle of 20 cm in diameter. This circle is circumscribed by a square. The grating, provided achromatic (white - black) comes with two orientations (vertical: horizontal stripes, and horizontal: vertical stripes). Sequences have three variants: red, blue or green, with the stripes perpendicular to the grating (figure 1). Gratings and sequences are generated and printed by computer.
From a distance of 4 meters observers approach the test in 4 intermediate distances: 4, 3, 2 and 1 meters. In each of the distances observers give the value V.
The value V is the opinion of the observer in relation to the visual perception of the central sequence on a scale from 0 to 10. The observer compares the central sequence with the two lateral sequences. The two side stripes are always given a fixed value of 10. The value 0 means that observers do not perceive the central sequence (dissapears). The value 10 means that the central sequence is perceived equal to the laterals. Experiments have involved 4 observers, students aged between 20 and 25. With this value we determine the visual contrast in the distances above, between the central and lateral sequence. With this contrast we quantify the Bezold.

$$\text{Bezold effect} = \frac{10-V}{10} \qquad (1)$$

The chromaticity coordinates of the colors used are red (x=0.58, y=0.36), blue (x=0.29, y=0.36) and green (x=0.37, y=0.48), where Y is about 25 cd/m2.

Results and conclusions
The results obtained by studying the relationship between the value of the Bezold effect produced in the vision of a color sequence (red, green or blue) contained in a rectangular achromatic (β=1) grating and the angular frequency of the grating, taking into account the orientation (verticalhorizontal) tell us:

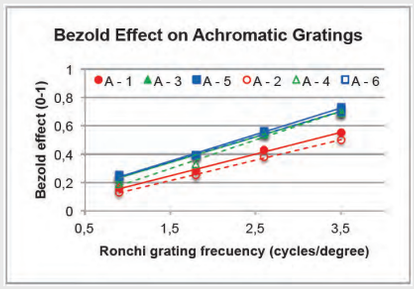

Fig. 2: Graphical relationship between the Bezold effect and the frequency of the grating.

By varying the grating orientation (vertical-horizontal), the Bezold effect produced in the vision of green and blue sequences, undergoes almost negligible variation between high and low frequencies studied in this paper, being higher in the green sequence, with low frequencies (fig. 2). Sequences in red, with all the grating frequencies, the vision of the Bezold effect produced is less than the produced with the blue and green sequences, and nearly constant (0.03 to 0.05). This difference are obtained by varying the grating orientation (vertical-horizontal). The Bezold effect obtained is greater with the horizontal orientation.

References
[1] D. Jameson and L. M. Hurvich, *Annual Review of Psychology,* **40**, 1, 1989.
[2] I. Tortajada, V. Blanca, M. Martínez, and M. Aguilar, *Variation with the contrast and modulation ratio of a achromatic grating on the view of a chromatic periodic test*, presented at the 10th Congress of the International Colour Association, Granada (Spain), 2005.
[3] I. Tortajada, M. Martínez, and M. Aguilar, *Viewing of an achromatic test with chromatic gratings as an adaptation field*, presented at the Interim Congress of the International Colour Association, Stockholm (Sweden), 2008.

EMVPO2012_5697_034

Correlative imaging of corneas from diabetic rats and human donors

G. Latour[1], L. Kowalczuk[2], M. Savoldelli[3], J.-L. Bourges[4], K. Plamann[2], F. Behar-Cohen[3], M.-C. Schanne-Klein[1]; [1]Ecole Polytechnique - CNRS - INSERM U696, Laboratory for Optics and Biosciences, 91128 Palaiseau (FR); [2]ENSTA ParisTech - Ecole Polytechnique – CNRS, Laboratory for Applied Optics, 91128 Palaiseau (FR); [3]Sorbonne Paris Cité, Paris Descartes university, faculty of medicine; AP-HP Hôtel-Dieu, department of ophthalmology; Paris (FR); [4]INSERM UMR872, Centre de Recherche des Cordeliers, Team 17 Physiopathology of ocular diseases; Paris (FR).
Email: gael.latour@polytechnique.edu

Summary
Diabetic rat corneas were observed by *in vivo* confocal reflectance microscopy, *in vivo* SHG microscopy and TEM. This correlative imaging approach highlighted the formation of abnormal fibrillar collagen structures in the Descemet's membrane. These abnormalities were also observed in human corneas from diabetic donors.

Introduction
In this study, we evaluated hyperglycemia-induced effects in the corneas of diabetic rats using a correlative imaging approach. We combined imaging techniques that exhibit different resolutions and modes of contrast, including Second Harmonic Generation microscopy (SHG). SHG microscopy is a multiphoton imaging technique which gives signal at half the excitation wavelength and is highly specific for fibrillar collagen[1,2]. Our study showed that SHG images reveal corneal abnormalities in diabetic rats and human donors with an excellent contrast and that this technique can be implemented for *in vivo* studies[3].

Structural changes in diabetic rat and human corneas
Hyperglycemia-induced effects were studied using the Goto-Kakizaki (GK) rat model that develops spontaneously type 2 diabe-

tes. 9 animals (around one year old) have been used for this study. We compared images from the Descemet's membrane obtained by *in vivo* confocal microscopy and by *ex vivo* multiphoton microscopy in the same corneas (fig. 1). Low hyper-reflective signals were detected in confocal microscopy while strong SHG signals were observed and allowed the spatial characterization of these abnormal structures with a micrometer-scale resolution. Ultrathin sections were then analyzed by Transmission Electron Microscopy (TEM) and correlated to multiphoton images of adjacent sections. Longspacing collagen fibrils (around 120 nm) were observed in TEM images in the same region as SHG signals in multiphoton images.

Corneas from diabetic donors were also studied in collaboration with the French Eye Bank. These corneas were unsuitable for transplantation and could be used for scientific investigations. *Ex vivo* SHG imaging was performed in 6 corneas from diabetic donors and 2 corneas from donors with no identified hyper-glycemia. Corneas from diabetic donors exhibited strong SHG signals in the Descemet's membrane, in contrast to the other ones. These observations were confirmed by TEM using the same correlative imaging approach as in GK rat corneas. These results indicate a correlation between the presence of fibrillar collagen in the Descemet's membrane and the hyper-glycemia of the donors.

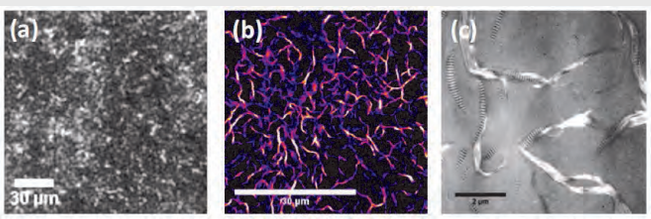

Fig. 1: Correlative imaging of the Descemet's membrane in diabetic rat corneas: (a) *in vivo* confocal reflectance microscopy, (b) SHG microscopy and (c) TEM

In vivo multiphoton imaging

Wistar and GK rats were anesthetized by intramuscular injection and corneas were observed using multiphoton microcopy. We successfully recorded SHG images of the corneal stroma in control and diabetic rats[2]. In the diabetic rat, we observed SHG signals in the Descemet's membrane while no signal was observed in the control rat. These results confirmed the *ex vivo* study and showed that hyperglycemia-induced effects can be observed using *in vivo* SHG microscopy.

Conclusion

Correlative imaging of diabetic GK rat corneas was performed and provided complementary information on hyper-glycemia-induced structural changes in the Descemet's membrane. These abnormalities were also observed in diabetic human donor corneas. SHG microscopy appeared as a highly contrasted technique to highlight these structural abnormalities in unstained corneas because of its structural specificity for fibrillar collagen. Most importantly, *in vivo* SHG imaging of the cornea has been demonstrated, which opens the way to longitudinal studies. Such studies must now be performed to determine the chronology of the formation of these collagen abnormalities compared to the onset of diabetic retinopathy, in order to evaluate whether SHG microscopy could be a diagnosis tool of diabetic retinopathy.

Acknowledgments

We acknowledge the French Eye Bank for the supply of the corneo-scleral discs. G. Latour was supported by RTRA-Triangle de la Physique and Fondation de France and L. Kowalczuk was supported by the ANR TechSan 025 NOUGAT.

References

[1] F. Aptel, N. Olivier, A. Deniset-Besseau, J.-M. Legeais, K. Plamann, M.-C. Schanne-Klein, and E. Beaurepaire, *Invest. Ophthalmol. Vis. Sci* **51**, 2459 (2010)

[2] G. Latour, I. Gusachenko, L. Kowalczuk, I. Lamarre, and M.-C. Schanne-Klein, *Biomed. Opt. Express* **3**, 1 (2012)

[3] L. Kowalczuk, G. Latour, M. Savoldelli, J.-L. Bourges, M.-C. Schanne-Klein, K. Plamann, and F. Behar-Cohen, *ARVO/ISIE 22/300* (2012)

EMVPO2012_5701_035

Monofractal and multifractal analysis in human retinal pathology

Ş. Ţălu[1], S.D. Ţălu[2], S. Giovanzana[3], M. Ţălu[4], I.V. Petrescu-Mag[5]; [1]Technical University of Cluj-Napoca, Faculty of Mechanics, Discipline of Descriptive Geometry and Engineering Graphics, Cluj-Napoca, 400641 (RO); [2]"Iuliu Hatieganu" University of Medicine and Pharmacy, Faculty of Medicine, Department of Surgical Specialties, Cluj-Napoca, 400012(RO); [3]University of Milan-Bicocca, Milano, 20125 (IT); [4]University of Craiova, Faculty of Mechanics, Department of Applied Mechanics, Craiova, 200512 (RO); [5]University of Agricultural Sciences and Veterinary Medicine Cluj-Napoca, 400372 Cluj-Napoca (RO).

Email: simonatalu@yahoo.com

Summary

The aim of this work is to assess the branching patterns of retinal arterial and venous systems in both the normal and the diseased retina using monofractal, multifractal and lacunarity analyses.

Introduction

Computer-aided analysis of the human fundus eye images using the monofractal and multifractal geometry is a part of the detection and diagnosis of retinal diseases [1, 2]. The human retinal microvascular network as an anatomic system is expressed through a variable geometry of vessel shapes and surfaces that cannot be measured properly using Euclidean geometry, but its 3D architecture can be assessed by monofractal, multifractal and lacunarity analyses [2]. Let A be any nonempty bounded subset of R^n (n-dimensional Euclidian space R^n). The fractal dimension gives the scaling between the smallest number of n-dimensional ε boxes needed to cover the set A completely, and the boxes' size ε.

The box-counting monofractal dimension of A is expressed by [3]:

$$D_B(A) = \lim_{\varepsilon \to 0} \frac{\log N_\varepsilon(A)}{\log(1/\varepsilon)} \quad (1)$$

In multifractal analysis, the generalized dimension D_q can be expressed as [4]:

$$D_q = \frac{1}{q-1} \lim_{\varepsilon \to 0} \frac{\ln Z(q,\varepsilon)}{\ln \varepsilon} \quad (2)$$

where: $Z(q, \varepsilon)$ is the partition function; q is a real parameter that indicates the order of the moment of the measure and ε is the size of the boxes used to cover the sample.

The relationship between the $D(q)$ spectrum and the $f(\alpha)$ spectrum is established via the Legendre transformation [4]:

$$f(\alpha(q)) = q\alpha(q) - \tau(q) \quad (3)$$

where

$$\alpha(q) = d\tau(q)/dq \quad (4)$$

and

$$\tau(q) = (q-1)D_q \quad (5)$$

is the mass correlation exponent of the qth order.

The mean ($\bar{\lambda}$ or Λ) from all ε sized boxes at a grid orientation, g, is expressed as:

$$F\lambda = 1 + \lambda \quad (6)$$

$$\Lambda = (\sum [F\lambda])/n \quad (7)$$

where: n is the number of box sizes; and the F stands for "foreground pixels", that signifies lacunarity (Λ) calculated using the count of foreground pixels independently of other considerations.

Discussion

Computational analysis was performed for the human fundus eye images using a retinal database [5, 6] for the following cases: (a) normal subjects; (b) hypertensive retinopathy; (c) peripheral choroidal atrophy; (d) cystoid macular edema; (e) early diabetic retinopathy; (f) choroideremia and (g) chloroquine retinopathy.

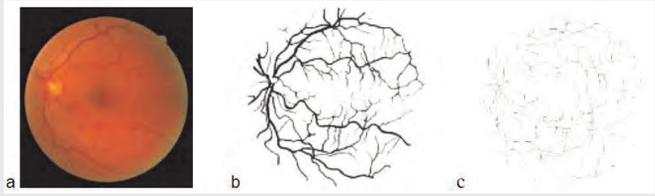

Fig 1. Image of a normal state retinal vessel network: (a) the color image version, (b) the segmented version and (c) the skeletonised version

The monofractal, multifractal and lacunarity analyses were performed, applying the the Image J software with the standard box-counting algorithm, in two cases: 1) for the segmented (seg.) and (2) the skeletonised (skl.) versions (Fig 1). Lastly, all the raw data were exported and analyzed in Microsoft Office Excel. It was found that the monofractal and generalized fractal dimensions D_q of the vascular trees followed a normal distribution. The results were expressed as average ± standard deviation.

Conclusions

The results obtained in multifractal analysis are more accurate than in monofractal analysis. Monofractal analysis is useful in a quick investigation of the healthy and diseased retina, while the multifractal analysis is recommended in a detailed one.

References

[1] V. Lakshminanarayanan, et al, *J. Mod. Opt.*, **50** (**11**), 1701-1703, 2003.
[2] Ș. Țălu, S. Giovanzana, *HVM Bioflux,* **3**(**3**), 205-212, 2011.
[3] K. Falconer, *Fractal Geometry: Mathematical Foundations and Applications*, 2nd Edition, John Wiley & Sons Ltd., 2003.
[4] L. Telesca, et al, *Chaos, Solitons and Fractals*, **18** (**2**): 385-399, 2003.
[5] J.J. Staal, et al, *IEEE Trans. Med. Imaging*, **23** (**4**): 501-509, 2004.
[6] http://www.isi.uu.nl/Research/Databases/DRIVE/.

EMVPO2012_5702_036 STUDENT PRESENTATION

An estimate of the ocular media transmittance using an updated psychophysical method

P. Teikari[1,2], R.P. Najjar*[1,2], K Knoblauch[1,2], D. Dumortier[1,3], P.-L. Cornut[1,2,4], P. Denis[1,5], H.M. Cooper[1,2], C. Gronfier[1,2]; [1]INSERM, U846, Stem Cell and Brain Research Institute, Dept. of Chronobiology, 69500, Bron (FR); [2]University of Lyon, Lyon I, UMR-S 846, 69003, Lyon (FR); [3]ENTPE, 69518-Vaulx-en-Velin (FR); [4]Dept. of Ophthalmology, CHU de Lyon Hopital Edouard Herriot, Lyon (FR); [5]Hôpital de la Croix Rousse, Lyon (FR). *These 2 authors contributed equally to the study.*
Email: petteri.teikari@gmail.com

Summary

An inexpensive psychophysical heterochromatic flicker technique was improved to evaluate human ocular media density. The technique allowed us to estimate the full spectral transmittance of the ocular media. Results were used to correct retinal irradiance for ocular media filtration in a study of melatonin suppression by light [1].

Introduction

Many anatomical and physiological processes in the eye follow a gradual decline with ageing. Although these processes are distinct from alterations of the retina, the consequences for vision may be closely similar. Lens yellowing is one of these phenomenon and gradually leads to the most documented cause of blindness in developed countries: cataract, [2]. The relationship between healthy ageing and ocular lens density has been studied by many groups [3,4]. These studies show a decreased transmission (increased density) of the crystalline lens, especially for short wavelength light.

Psychophysical methods are easy and low cost to implement both in clinical and experimental settings. In our study we evaluated an improved two-wavelength (410 nm vs. 560 nm) scotopic heterochromatic flicker photometry technique that we designed and implemented to assess the age-related changes in ocular media density. Spectral attenuation of the ocular media was approximated by fitting the obtained absorbance difference with an age-dependent human ocular media model of van de Kraats and van Norren [5]. The full spectral attenuation template allowed us to estimate photoreceptor-specific attenuation for each subject. Our technique was compared to a previously described psychophysical technique of absolute threshold detection in the same subjects [3].

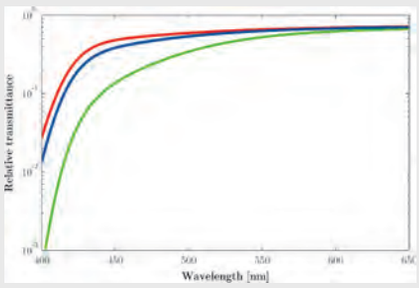

Fig. 1. Relative spectral transmittance of the three age groups using the ocular media model of van de Kraats and van Norren [4]. Young group (red line, 26.7 yrs.); middle age group (blue line, 476. yrs.); and the old group (green line, 65.6 yrs.).

Discussion

Our results show that short-wavelength light absorption by the ocular media correlate well with the age of the subjects (Fig. 1) as shown previously [5,6]. The obtained difference of 0.61 log units in lens density index between the young age group ($age_{mean} \approx 26.7$ yrs.) and old age group ($age_{mean} \approx 65.6$ yrs.) was in accordance with the previous studies.

Inter-individual variability in the ocular media density among the same age-group, especially found in the old age group in our study, has previously been reported [6], supporting the notion that in many cases the use of average values are not indicative of the individual crystalline lens density. While mathematical models have been produced to predict the expected changes in the absorption characteristics of the ageing lens [5,7] they cannot accurately represent the individual variability occurring with real subjects. This is in contrast with the typical pre-retinal absorbance corrections applied using a standardized lens density template [8], for example in studies on perceptual [9] and non-image forming (NIF) visual system [10].

Conclusions

In conclusion, the proposed inexpensive method is able to provide an accurate estimate of the ocular media density that is a distinct improvement compared to the approach of using standardized ocular media templates. Such estimates are of major relevance in studies regarding photoreception were estimation of retinal spectral irradiance is essential. We are currently optimizing the protocol procedure by reducing the dark adaptation time with an intention of eliminating it, making this technique easier to implement for subjects and the experimenters in both research and clinical settings.

To further improve the spectral resolution of the approximation of the ocular media transmittance, additional test wavelengths could be employed. For example a wavelength of 480 nm can be used for non-image forming-related studies [10]. In that case two distinct heterochromatic flicker pair tests (410 nm vs. 560 nm, and 480 nm vs. 560 nm) would be required for each subject providing three points for the curve fitting algorithm [5], thus improving the accuracy of the full spectral attenuation estimate. This method has not yet been done for ocular media using psychophysical methods as for example in measures of macular pigment density [11].

References

[1] R.P. Najjar, P. Teikari, B. Claustrat, P.L. Cornut, P. Denis, H.M. Cooper, C. Gronfier. *Submitted*
[2] R. Michael and A.J. Bron, *Philosophical Transactions of the Royal Society B: Biological Sciences* **366**, 1278 –1292, 2011.
[3] D. van Norren and J.J. Vos, *Vision Research*, **14**, 1237–1244, 1974.
[4] B.R. Wooten, B.R. Hammond and L.M. Renzi, *Ophthalmic & Physiological Optics,* **27,** 321–328, 2007.
[5] J. van de Kraats and D. van Norren, *Journal of the Optical Society of America. A*, **24,** 1842–1857, 2007.
[6] P.A. Sample, F.D. Esterson, R.N. Weinreb and R.M. Boynton, *Investigative Ophthalmology & Visual Science.* **29,** 1306–1311. 1988.
[7] J. Pokorny, V.C. Smith and M. Lutze. *Applied Optics,* **26**, 1437-1440, 1987.
[8] A. Stockman, L.T. Sharpe, C. Fach, *Vision Research,* **39**, 2901–2927, 1999.
[9] N.P. Cottaris, *Journal of the Optical Society of America A,* **20**, 1694–1713, 2003.
[10] W.N. Charman, *Ophthalmic and Physiological Optics,* 23, 181–187, 2003.
[11] J.S. Werner, S.K. Donnelly and R. Kliegl, *Vision Research*, **27**, 257–268, 1987.

EMVPO2012_5711_037 STUDENT PRESENTATION

Assessment of intraocular scattering. Comparative study using several techniques

J.A. Martínez-Roda[1], M. Vilaseca[2], J. C. Ondategui[1], L. Almudi[3], J. Pujol[2]; [1]University Vision Centre (CUV), Technical University of Catalunya (UPC), Terrassa (Barcelona), 08222 (ES); [2]Centre for Sensors, Instruments and Systems Development (CD6), Technical University of Catalunya (UPC), Terrassa (Barcelona), 08222 (ES); [3]Ophthalmology service, Hospital de Terrassa, Terrassa (Barcelona), 08227 (ES).
Email: jmartinez@oo.upc.edu

Summary
In this study we evaluate the intraocular scattering in eyes with nuclear and cortical cataracts by means of several techniques, including the LOCS III classification system, the C-Quant instrument and the OSI parameter. The results show that a correlation exists between the different tested techniques.

Introduction
The evaluation of vision in patients with cataracts is often carried out by means of visual acuity and CS tests. However, there are other more specific procedures such as that based on a compensation comparison method and a flickering glare ring that adds a veil to a central bipartite test determining LogS, an indicator of the straylight produced by the flickering glare ring (C-Quant, Oculus GmbH, Wetzlar-Dutenhofen, Germany)[1][2]. Additional procedures used by ophthalmologist to evaluate cataracts involve the observation of the lens through a slit lamp. The most standardized classification system of this type is the Lens Opacities Classification System III (LOCS III)[3]. In order to obtain an objective assessment of the intraocular scattering, the double-pass technique has also been used. Westheimer and Liang [4] have proposed a combined analysis of double-pass images and subjective measurements to extract information about the scattered light. Artal et al. have recently proposed a new objective scatter index (OSI) calculated from double-pass images to classify cataract patients.[5]
In this study we analyse these parameters over a population with different grades of cataracts, specifically nuclear and cortical, establishing a quantitative comparison between them. Specifically, 37 eyes diagnosed with nuclear cataracts and 31 eyes diagnosed with cortical were included in the study (average age=68.9(±8.3) y/o). Nuclear cataracts were classified from NO1 to NO6 (Opacity) and NC1 to NC6 (Colour). Cortical cataracts were classified from C1 to C5. Patients included in the study did not report any ocular alteration other than the cataract itself. Examinations were performed at "Hospital de Terrassa" (Terrassa). The evaluation included determining the subjective refraction and measuring the visual acuity (VA) with LogMAR chart. Furthermore, cataracts were graded clinically at the slit lamp after dilating the patients' pupils by instilling 0.2 ml of tropicamide (1%) and were classified using the LOCS III. The protocol also included an assessment of intraocular scattering using the C-Quant instrument (LogS) and the OSI parameter, which is determined using a pupil diameter of 4 mm. Every patient was informed of the subject of the study, and a written informed consent obtained, following the tenets of the Declaration of Helsinki.

Discussion
Table 1 shows the mean (±SD) of the VA, the LogS index provided by the C-Quant system and the OSI parameter measured by means of the OQAS instrument (Optical Quality Analysis System, Visiometrics S.L., Spain) of eyes classified regarding the LOCS III scale.

LOCS (N)	VA (±SD)	logS (±SD)	OSI (±SD)	LOCS (N)	VA (±SD)	logS (±SD)	OSI (±SD)	LOCS (N)	VA (±SD)	logS (±SD)	OSI (±SD)
NO2 (2)	-0.16 (0.06)	1.02 (0.01)	1.70 (0.28)	NC2 (2)	-0.16 (0.06)	1.02 (0.01)	1.70 (0.28)	C2 (8)	0.03 (0.11)	1.25 (0.36)	2.29 (1.66)
NO3 (10)	0.06 (0.07)	1.49 (0.32)	3.44 (1.75)	NC3 (13)	0.19 (0.30)	1.34 (0.27)	3.14 (1.66)	C3 (15)	0.14 (0.22)	1.37 (0.26)	4.43 (2.72)
NO4 (17)	0.23 (0.31)	1.31 (0.29)	4.01 (2.62)	NC4 (11)	0.05 (0.11)	1.40 (0.38)	4.13 (2.08)	C4 (8)	0.30 (0.16)	1.44 (0.36)	8.91 (2.84)
NO5 (8)	0.27 (0.17)	1.66 (0.21)	8.16 (3.92)	NC5 (11)	0.31 (0.21)	1.54 (0.18)	6.93 (3.87)				

Table 1: Mean (±SD) of the VA, Log S and OSI for LOCS III classified cataract.

As it can be seen all parameters increase with increasing cataract grade. In addition, OSI and LOCS III show statistically significant correlations (NO: r=0.579, p<0.001; NC: r=0.639 p<0.001; C: r=0.688, p<0.001). Furthermore, for the correlation between LogS and OSI the following data were found (Nuclear: r=0.463, p=0.002; Cortical: r=0.403, p=0.020), whereas if the OSI logarithm is taken into account, better statistically significant correlations are found (Nuclear: r=0.546, p<0.001; Cortical: r=0.504, p=0.003) (see Fig. 1).

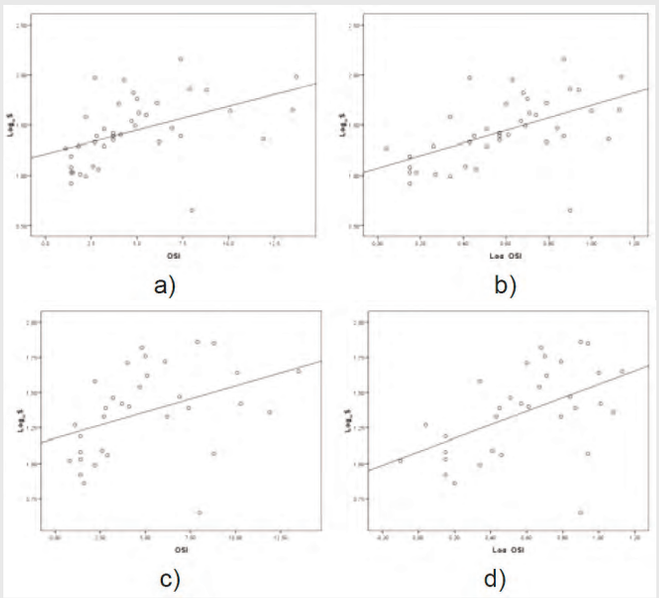

Fig. 1: Correlation between: a) LogS and OSI for nuclear cataract. b) LogS and LogOSI for nuclear cataract. c) LogS and OSI for cortical cataract. d) LogS and LogOSI for cortical cataract.

Conclusions
In this work it is shown that intraocular scattering might be assessed by means of several techniques, which correlate rather well between them when eyes with nuclear and cortical cataracts are considered. The LogS index and the OSI capture the impact of forward scattering, which is responsible for vision degradation; whereas the LOCS III scale is more related to the back-scattered light. Nevertheless, good correlations between variables have been generally found, which demonstrates their usefulness.

References
[1] L. Franssen, J. Coppens, T. van den Berg. *Invest Ophthal Vis Sci.* **47**, 768, 2006.
[2] J.E. Coppens, L. Franssen, L.J. van Rijn, T. van den Berg. *J Biomed Opt.* **11**, 34027, 2006.
[3] L. T. Chylack, J, K. Wolfe, D. M. Singer, et al. *Arch Ophthalmol.* **111**, 831, 1993.
[4] G. Westheimer, J. Liang. *Invest Ophthalmol Vis Sci.* **35**, 2652, 1994.
[5] P. Artal, A. Benito, G. M. Pérez, et al. PLoS ONE. **6(2)**, e16823, 2011.

NOTES

EMVPO2012_5716_038

Accommodative response to Chinese and Latin characters in myopes and emmetropes

L. LLorente[1,2], H. Radhakrishnan[3], A. Hartwig[4]; [1]Carl Zeiss Vision, R&D, Lonsdale, 5160 (AU); [2]Universiti Kebangsaan Malaysia, Faculty of Health Science, Optometry and Vision Science Programme, Kuala Lumpur, 50300 (MY); [3]University of Manchester, Department of Optometry, Manchester, M13 9PL (GB); [4]Hartwig, Heikendorf, 24226 (DE).
Email: Lourdes.llorente@vision.zeiss.com

Summary
We compared the accommodative response using negative lenses of a group of 11 myopes and 10 emmetropes using Chinese and Latin characters as targets. No difference was found in the accommodative response for the characters or between refractive groups.

Introduction
Hyperopic retinal blur, present during accommodation (lag), has been pointed out as a trigger for excessive axial growth in myopic eyes, given that greater accommodative lag has been reported in subjects with high myopia progression rates [1]. On the other hand, accommodation accuracy has been shown to depend on the spatial frequencies present in the accommodation target [2]. Taylor et al. [3] suggested that, due to their greater tolerance to blur, accommodation in myopes might be more inaccurate than in emmetropes when high spatial frequency targets are used. However, they did not find significant differences in the accommodation responses between both refractive groups.
Nevertheless, the combination of responses to the individual frequencies present in a complex target is not necessarily equivalent to the accommodation response to the target itself [4]. Writing characters are a more realistic accommodation target than gratings. Chinese characters present high spatial frequencies that might affect accommodation. In the present study we compared accommodative responses between Chinese and Latin characters.

Methods
Accommodative response to negative lenses (0 to 5D) was measured monocularly with an open field autorefractometer (Shin Nippon SRW 5000, Ajinomoto Trading Inc., Tokyo, Japan) in 11 myopic and 10 emmetropic non Chinese literates. We used three Latin and four Chinese characters (see bottom fig.1) subtending an angle of 55 min arc from the eye as fixation target, presented isolated in a white background and alternated in different order. The regression line for response/stimulus data was obtained for 1 to 5D accommodation stimulus, and the accommodation error index (AEI) [5] was calculated. The slope, AEI and accommodation response values were compared across characters within the same refractive group and across refractive groups for the same characters, using a mixed design ANOVA and the corresponding non parametric tests in the case of AEI.

Results
No significant differences in the accommodative response/stimulus curves slopes (mean±std, 0.75±0.20 for emmetropes and 0.79±0.14 for myopes) or in the accommodative error indices (1.16±0.79 for emmetropes* and 0.75±0.38 for myopes) were found across letters within both groups (fig.1). No significant differences were found for the slopes or AEI between both refractive groups. Although no significant differences were found, the accommodative response for the myopic eyes tended to be greater than that for the emmetropic eyes, which indicates a smaller lag of accommodation for this group (mean lag difference between both groups was 0.28±0.09D across accommodation stimuli, standard deviation across subjects was 0.56 D for the emmetropes and 0.32 D for the myopes).

Discussion
Our results show no difference in the accommodative response between Latin and Chinese characters, so apparently the different features present in both kinds of characters did not influence the accommodative response. However, some factors such as knowledge of the Chinese characters presented could influence the subject towards a more accurate accommodation.

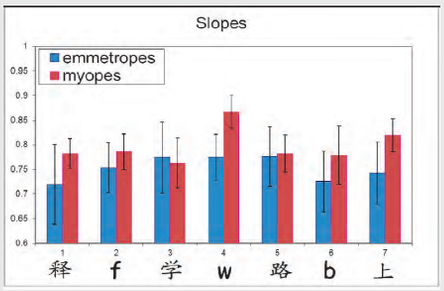

A

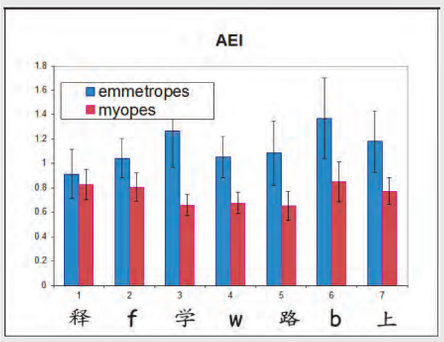

B

Fig.1: slopes (A) and AEI (B) obtained for each character for our emmetropic (blue) and myopic (red) groups.

References
[1] M.L. Abbot, *Ophthalmic and Physiological Optics*,18, 13-20,1998
[2] L.J. Bour, *Vision Research*, 21, 1287-1296, 1981
[3] J Taylor, *Journal of Vision*, 9, 1-14, 2009
[4] W.N. Charman, *Vision Research*, 17,129-139, 1977
[5] K. Chauhan, *Opthalmic and Physiological Optics*, 15,217-221,1995* Following Taylor et al, three unrealistically high AEI values for the emmetropic eyes were assigned the value of 3.

EMVPO2012_5717_039 STUDENT PRESENTATION

Peripheral aberrations and changes in refractive error during one year

A. Hartwig[1], N.W. Charman[1], H. Radhakrishnan[1]; [1] University of Manchester, Faculty of Life Sciences, Manchester, M13 9PL (GB).
Email: andreas.hartwig@firma-hartwig.de

Summary
Peripheral higher order aberrations were analysed in association with refractive error changes as higher order aberrations might have an influence on myopia development. In a group of low progressing myopes and emmetropes peripheral aberrations do interact with refractive error progression during one year.

Introduction
The present study aimed to analyse the possible influence of peripheral higher order aberrations on refractive error progression. As there is evidence that peripheral refraction might have an influence on myopisation [1, 2] there is also a possibility that peripheral higher order aberrations have an impact. Higher order aberrations up to the fourth order, subjective refraction and axial length were measured in 32 myopes and 22 emmetropes. Aberrometry was performed along the horizontal meridian for up to 20 degrees eccentricity using the IRX-3. At the same visit, subjective refraction and axial length were measured. After one year subjective refraction and axial length were measured again.

Discussion
Refractive error progression during one year was 0.04 ± 0.29 D in myopes and -0.12 ± 0.38 D in emmetropes. Axial length increased in myopes by 0.01 ± 0.07 mm and by 0.02 ± 0.07 mm in emmetropes. Peripheral higher order aberrations were fitted with linear trend lines. Correlations between fitting parameters (slope and intercept) and refractive error progression were not significant. A significant correlation was found between the slope of horizontal coma and corneal curvature ($r = 0.34$, $p = 0.02$). In previous work [3] various distributions of horizontal coma along the horizontal me-

ridian were found and it was speculated that corneal asphericity has an influence on the distributions of peripheral horizontal coma. In the present study it was shown that corneal curvature and the slope of horizontal coma are linked. This finding is contrary to that of Mathur *et al.* [4] who could not find a significant correlation between the two parameters. It was found that corneal curvature also correlates with axial length [5]. Therefore the present study might give some further evidence for the involvement of horizontal coma in myopisation as it was discussed by other authors [3, 6, 7].

Conclusions

In the present work no strong evidence was found for the involvement of peripheral higher order aberrations in refractive error development. This is possibly caused by the fact that the progression of refractive error during one year was very low. More emphasis should be drawn to peripheral horizontal coma as a factor influencing myopisation.

References

[1] J. Hoogerheide, F. Rempt, and W.P. Hoogenboom, *Ophthalmologica*, **163,** p. 209-15, 1971

[2] E.L. Smith, 3rd, et al., *Invest Ophthalmol Vis Sci*, **46,** p. 3965-72, 2005

[3] A. Hartwig, I.J. Murray, and H. Radhakrishnan, *Clin Exp Optom*, **in press,** 2011

[4] A. Mathur, D.A. Atchison, and W.N. Charman, *J Vis*, **9,** p. 15 1-12, 2009

[5] C. O'Donnell, A. Hartwig, and H. Radhakrishnan, *Cont Lens Anterior Eye*, **34,** p. 26-31, 2011

[6] R.C. Bakaraju, et al., *Ophthalmic Physiol Opt*, **28,** p. 538-49, 2008

[7] A. Carkeet, et al., *Vision Res*, **42,** p. 1809-24, 2002

EMVPO2012_5730_040 **STUDENT PRESENTATION**

Comparison of Accelerated Corneal Cross-Linking to Standard Cross-Linking using Second-Harmonic Optical Microscopy

R. McQuaid[1,2], J. Li[2], A. Cummings[1], M. Mrochen[3], B. Vohnsen[2];
[1]Wellington Eye Clinic, Beacon Court, Sandyford, Dublin 18 (IE);
[2]AOI-Group, School of Physics, University College Dublin, Dublin 4 (IE); [3]IROC, Stockerstrasse 37, 8002 Zurich, (CH).
Email: rebecca.mcquaid@wellingtoneyeclinic.com

Summary

Cornea collagen lamellar structures were investigated with second-harmonic optical imaging after standard and accelerated cross-linking and compared to reference images for untreated corneas. Knowledge about the fibrilar structure could prove beneficial for in-vivo studies and the measurement of the effect of treatment.

Introduction

Second-Harmonic (SH) imaging allows optical probing of the collagen fibril organization due to its inherent nonlinear optical response contained in the second-order susceptibility tensor.[1-4] Here, backward SH images of fibrils in post-mortem porcine corneas under CXL (Standard cross-Linking)[5] and AXL (Accelerated cross-Linking) conditions respectively will be compared, along with other higher intensities as well as untreated control corneas. Our aim is to investigate morphological and optical changes in the corneal stroma after higher intensity collagen cross-linking in the porcine eyes. Intra-Ocular Pressure (IOP) was controlled throughout experiments to examine its impact on the structural change in the cornea after cross-linking.

Post-mortem porcine corneas CXL treated with 3mW/cm^2 have been compared to AXL corneas treated with 10mW/cm^2 using second-harmonic optical microscopy. Additionally, also the impact of higher intensities 30mW/cm^2 and 100 mW/cm^2 from an Ultra-Violet UV-X™ lamp has been studied. In all cases, the exposure time was adjusted to keep the total UV radiation dose constant at 5.4mJ. SH imaging is used in a reflection geometry to reveal changes in the collagen fibril organization after treatment whilst monitoring and controlling the impact of IOP.

Discussion

Results show that cross-linking has a similar effect on the porcine corneas at all the UV intensities tested. Too low or too high IOP introduce increased back-scattering of the SH signal, as the fibres are stretched to capacity from the increase in pressure. Examples of images obtained are shown in Fig. 1. In the clinic, CXL may take up to one hour per eye causing significant stress to the patient being exposed to the UV light. Higher intensity AXL has shown to be as effective as the standard treatment but this might have a detrimental impact on the corneal collagen fibril ordering as a consequence of the more intense UV radiation. Measurement of IOP during experimentation is beneficial as the stromal collagen morphology changes in response to increasing IOPs. At a normal porcine IOP of 15.2mmHg (±1.8)[6], the structure shows less interweaving, similar to what would be expected in human corneas. To date, there is an absence of experimental studies showing a morphologic change in the stroma after exposure to higher intensity cross-linking. The use of SH imaging has potential for future in-vivo research.

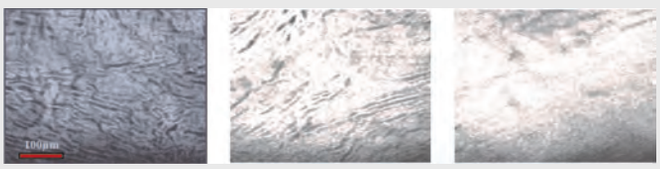

Fig. 1. Second-harmonic reflection images of porcine corneas *with CXL, AXL, and Untreated*respectively. Depth into stroma 100µm. Scale Bar 100µm.

Conclusions

Our research comparing untreated with CXL and AXL corneas indicate a similar fibrilar appearance of the collagen with SH enhancement dots that may be a consequence of crosslinking. It does, however, also indicate that AXL may not actuate as deep into the cornea as CXL possibly due to the finite viscosity of the riboflavin applied during treatment. At increased IOP, the structure is clearly present in the corneas treated with cross-linking, indicative of a higher tensile strength whereas the untreated cornea shows an absence of fibrilar structure. These results suggest that AXL may be as safe and possibly as effective as CXL with no observed cornea damage despite the higher UV-intensity applied.

References

[1] J.M. Bueno, E.J. Gualda EJ, and P. Artal. Analysis of corneal stroma organization with wavefront optimized nonlinear microscopy. *Cornea* 30, 692-701, 2011

[2] N. Morishige, Y. Takagi, T. Chikama, A. Takahara, and T. Nishida. Three-Dimensional Analysis of Collagen Lamellae in the Anterior Stroma of the Human Cornea Visualized by Second Harmonic Generation Microscopy. *Invest Ophthalmol. Vis. Sci.* **52**, 911-915, 2011

[3] N. Morishige, W.M. Petroll, T. Nishida, M.C. Kenney, and J.V. Jester. Non- invasive corneal stromal collagen imaging using two-photon-generated second-harmonic signals. *J. Cataract Refract. Surg.* **32**, 1784-1791, 2006

[4] K.M. Meek, S.J. Tuft, Y. Huang, P.S. Gill, S. Hayes, R.H. Newton, and A.J. Bron.Changes in collagen orientation and distribution in keratoconus corneas. *Invest. Ophthalmol Vis Sci.* 46, 1948-1956, 2005

[5] G. Wollensak, E. Spoerl, and T. Seiler. Riboflavin/ultraviolet-a-induced collagen crosslinking for the treatment of keratoconus. *Am. J. Ophthalmol.* 135, 620-627, 2003

[6] Sheldon Middleton, Porcine Ophthalmology, Elsevier Ltd, 1984; *557-559*.

NOTES

EMVPO2012_5743_041

Demonstration of Digital Holographic Display, Optimized for Human Eye Perception

V. Venediktov[1,2], M. Lyakh[3], A. Sevryugin, M. Solov'ev[2], I. Pasechnik[1]; [1]St.-Petersburg State Electrotechnical University "LETI" (RU); [2]National Research University of Information Technologies, Mechanics and Optics (RU); [3]Intel Labs, St. Petersburg (RU).
E-mail: vlad.venediktov@mail.ru

Summary
We discuss the laboratory prototype of the dynamic holographic display, based on multi-pixel liquid crystal spatial light modulator, optimized for human eye pupil size.
The problem of holographic display, providing real 3D imaging of real or imaginary objects by means of holographic reproduction has a long story of discussion and investigation. Recently the technique was strongly promoted by arrival on the market of the computer-controlled liquid crystal matrix phase arrays. Such elements, in particular that of HOLOEYE Photonics AG (http://www.holoeye.com/) production provide the possibility to record efficient thin phase holograms.
A simple prototype of such system was built for testing (Fig.1). We have used the transmission type element Holoeye LC-2002 with 800x600 pixels resolution and 21x26 mm clear aperture. It was connected by a VGA cable with a personal computer, which had two independent video outputs. Video output was controlled by Holoeye SLM Application Software. The spatial light modulator (SLM) was illuminated by the collimated plain beam of He-Ne laser (633 nm). Beam intensity was adjusted by neutral density filters. The computer hologram has reconstructed the virtual (imaginary) image, which was observed by experimenter eye, positioned at the distance ~1500 mm from this image. For recording the image we have used the high-quality professional digital camera, whose lens pupil size was manually controlled, and a standard CCD camera, connected to the same personal computer.

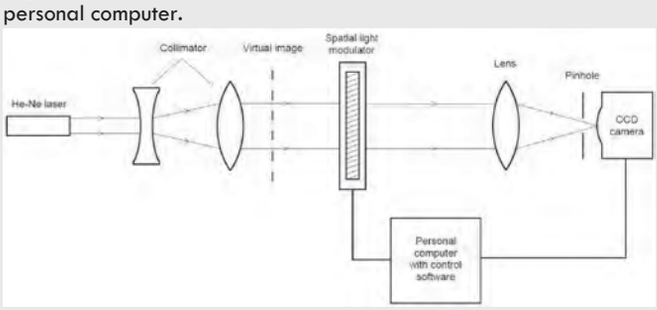

Fig. 1. Setup schematics.

The structure of hologram was calculated with the use of the proprietary code with account for the real human (or photographic lens) pupil diameter of 3-4 mm. From the optical point of view this pupil has served as a field aperture, extracting from the overall diffracted field the proper image, predetermined for observation by eye in this position.

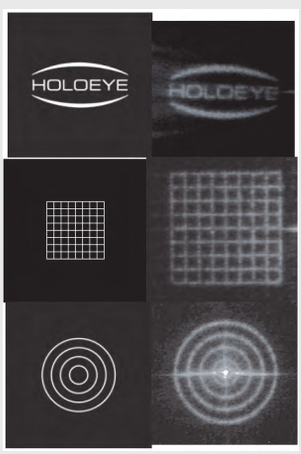

Fig. 2. Build-in test images and results of their hologram reconstruction.

Fig. 3. Pupil size and focusation position influence. The letters were "positioned" at the different distance from the hologram (compare upper right and upper left pictures – some letter images are sharper in upper left picture, while others – in the upper right one). The pupil diameter increase results in image deterioration (bottom)

For initial testing of the experimental setup we have used control software built-in hologram structures. Images were recorded by CCD camera. Some of these images with respective image prototypes are shown on Figure 2. Figure 3 shows images we have recorded during testing pupil size effect. Hologram structure was calculated with the use of the proprietary code with account for pupil diameter of 3-4 mm. The correlation between picture noise level and pupil size is clearly visible. The experiments have confirmed the expected behavior of the system. The camera lens focal length was equal to 170 mm. Another achieved results: All images were viewed by several observers. While observing by the human eye the yet higher image quality (compared to digital camera snapshots) was noted by most observers.
The use of the human eye pupil as the field aperture makes it possible to optimize the performance of the holographic display prototype, based on the commercially available digitally controlled matrix phase modulator.

References

[1] Slinger, C; Cameron, C; Stanley, M.; IEEE Computer, Volume 38, Issue 8, Aug. 2005, pp 46-53
[2] D. P. Kelly, B. M. Hennelly, N. Pandey, T. J. Naughton and W. T. Rhodes,. Opt. Eng. 48,095801 (Sep 04, 2009)
[3] H. Zhang, N. Codings, J. Chen, B. Crossland, D. Chu and J. Xie, , Opt. Eng. 50, 074003 (Jul 06, 2011)
[4] HOLOEYE Official Website: http://www.holoeye.com/spatial_light_modulatorstechnology. html
[5] D. P. Kelly, D. S. Monaghan et al., " International Journal of Digital Multimedia Broadcasting, vol. 2010, Article ID 759323, 14 pages, 2010. doi:10.1155/2010/759323

EMVPO2012_5749_042 STUDENT PRESENTATION

Waveform of the Pupil light reflex analysis taking into account intrinsically photosensitive retinal ganglion cells activity

W. Nowak[1], A. Hachoł[1], A. Sobaszek[1], M. Nakayama[2], H. Ishikawa[3]; [1]Wroclaw University of Technology, Group of Biomeasurements and Biomedical Signal Analysis, Wroclaw, Wybrzeze Wyspianskiego 27, Wroclaw, 50-370 (PL); [2]CRADLE, Tokyo Institute of Technology, 2-12-1 O-okayama, Meguro-ku, Tokyo, 152-8552 (JP); [3]School of Allied Health Sciences, Kitasato University, Sagamihara 228-8555 (JP).

Summary
The objective of this work was to analyze and qualitatively describe the human pupil light reflex to light stimuli with controlled waveform, wavelength and photopic level, taking into consideration the ipRGC activity mechanism.

Introduction
A new photoreception process based on intrinsically photosensitive retinal ganglion cells (ipRGC) which contain the photopigment melanopsin, contributes to the pupillary light reflex (PLR) in primates (Hattar et al. 2002, Peirson et al. 2006). It has been found that there are parallels between the electrophysiological response of ipRGC and the pupil response to chromatic stimuli (Dacey et al. 2005, Gamlin et al. 2007). Preliminary, qualitatively results have shown that the use of chromatic light stimuli to elicit pupil light reflexes may become a clinical pupil test which allows differentiation between disorders affecting photoreceptors and those affecting retinal ganglion cells (Kawasaki et al. 2007). PLR observations in clinical conditions are based mostly on the response to a single light pulse, so 1) the PLR waveform for different stimuli parameters should be analysed and 2) reliable and sensitive parameters describing PLR waveform in response to specific stimuli are required for clinical test.

Material and methods
In ten subjects we recorded PLR in response to light stimuli with different wavelengths, waveforms and photopic levels. Our pupillometer enables us to record pupil size with a resolution better than 0.02 mm, and at a high sampling rate, 100 Hz. The proposed, quantitative characteristic parameters of the PLR were assessed.

Results and discussion

Figure 1 show a typical shape of the PLR of a 10 *sec.* light pulse in normal subject. In the figure, red lines show PLRs for long wavelengths, and blue lines show PLRs for short wavelengths. Also, thick lines show PLRs for high intensity light, and thin lines show low intensity light.

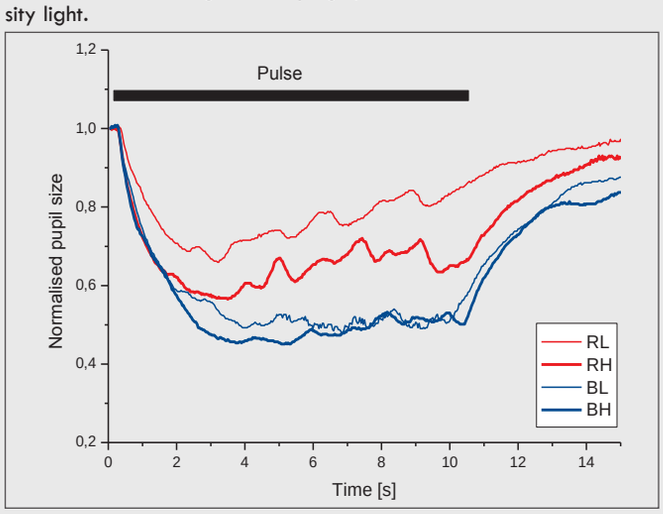

Fig.1. Example of Pupil Light Reflexes.

Statistical analysis confirmed a significant effect of all three light factors (wavelengths, photopic levels and waveform) on some PLR proposed parameters and allowed the determination of the contribution of each factor. Results indicate that markedly lower parameters values were obtained for long wavelength light at a low photopic level. The greatest value of the parameters is obtained for short wavelength light at a high photopic level. It confirms that the pupil light response reflects the activity of the melanopsin-expressing retinal ganglion cells in response to long-wavelength and short-wavelength light stimulus at low and high photopic levels.

This research has been supported by a research grant NN518 405338 from the Polish Ministry of Science and Higher Education

Reference

[1] S. Hattar, H. W. Liao, M. Takao, "Melanopsin-containing retinal ganglion cells: architecture, projections, and intrinisic photosensitivity", Science, **295**, pp. 1065-1070, 2002
[2] S. Peirson, R. G. Foster, "Melanopsin: another way of signaling light", Neuron, **49**, pp. 331-339, 2006
[3] P. D. Gamlin, D. H. McDougal, J. Pokorny, "Human and macaque pupil responses driven by melanopisn-containing retinal ganglion cells" Vision Research, **47**, pp. 946-954, 2007
[4] D. M. Dacey, H. W. Liao, B. B. Peterson, "Melanopsin-expressing ganglion cells in primate retina signal color and irradiance and project to the LGN", Nature, **433**, pp. 749-754, 2005
[5] A. Kawasaki, R. H. Kardon, "Intrinisically Photosensitive Retinal Ganglion Cells", J Neuro-Ophthalmol, **27**, pp. 195-204, 2007

EMVPO2012_5753_043 STUDENT PRESENTATION

Optical Quality and Intraocular Scattering in eyes treated of Amblyopia

J.C. Ondategui-Parra[1], J. Martínez-Roda[1], M. Vilaseca[2], A. Wert[3], J. Pujol[2]; [1]Technical University of Catalonia, University Vision Centre, Terrassa, 08222 (ES); [2]Technical University of Catalonia, Centre for Sensors, Instruments and Systems Development, Terrassa, 08222 (ES); 3Instituto de Microcirugía Ocular, Barcelona, 08035 (ES).
Email: ondategui@oo.upc.edu

Summary

We evaluated the values of optical quality (OQ) and intraocular scattering (IS) given by a double-pass (DP) system of treated and non-treated amblyopic eyes and compared them with a control group of healthy eyes.

Introduction

We evaluated and compared the retinal image quality of 30 treated amblyopic eyes (of 30 subjects) with 30 non-treated amblyopic eyes (of 30 subjects) and a control group of 43 healthy eyes (of 27 subjects). Mean ages (± SD) and corresponding ranges are given in Table 1. DP images with a pupil diameter of 4 mm were taken using a clinical instrument (OQAS, Visiometrics SL, Spain) [1] and several parameters related to the OQ and IS of the eye (Strehl ratio, OQAS values [OV] at contrasts 100%, 20% and 9%, and Objective Scatter Index [OSI]) [2][3], were computed. Moreover, we measured the best spectacle-corrected visual acuity (BSCVA) with a standard logMAR chart.

Groups	n (eyes)	Age (mean)	Age (SD)	Age (range)
Control	43	7,13	2,56	5,71-8,55
Treated Amblyopic	30	9,90	3,60	8,62-10,93
Non-treated Amblyopic	30	19,08	4,15	5,37-22,89

Table 1: Mean (±SD) and range of the age of the different groups considered: treated amblyopic, non-treated amblyopic and control.

Discussion

The visual acuity (VA) and OQ and IS parameters corresponding to all analysed groups are shown in Tables 2 and 3. When we compared both amblyopic groups (treated and non-treated) with the healthy eyes of the control group (statistic t test), the majority of the OQ parameters reported statistically significant differences between them ($p<0.05$), even they showed normal visual acuity values (see Tables 2 and 3).

Conclusions

We found lower OQ and IS values in treated and non-treated amblyopic eyes compared with those belonging to the control group. However conventional visual acuity tests did not show differences between treated and healthy groups. Future work will be focused on exploring the usefulness of retinal imaging analysis for the objective diagnosis and treatment of patients with amblyopia.

	OQAS values						
	Control			Treated amblyopic			p
Variable	Mean	SD	IC 95%	Mean	SD	IC 95%	
VA (logMAR)	-0.05	0.11	-0.08 -0.01	0.12	0.11	0.57 0.18	p>0.05
OV 100%	1.41	0.25	1.33 1.49	0.97	0.39	0.74 1.19	p<0.05
OV 20%	1.49	0.36	1.38 1.61	1.03	0.47	0.75 1.29	p<0.05
OV 9%	1.54	0.44	1.40 1.68	1.10	0.55	0.78 1.42	p<0.05
Strehl ratio	0.25	0.07	0.23 0.27	0.19	0.08	0,14 0.24	p<0.05
OSI	0.58	0.20	0.52 0.64	1.34	1.11	0.69 1.98	p<0.01

Table 2: Mean (±SD) and IC 95% of OQAS values for treated amblyopic and control groups.

	OQAS values						
	Control			Non-treated amblyopic			p
Variable	Mean	SD	IC 95%	Mean	SD	IC 95%	
VA (logMAR)	-0.05	0.11	-0.08 -0.01	0.23	0.09	0.57 0.18	p<0.01
OV 100%	1.41	0.25	1.33 1.49	0.89	0.47	0.74 1.19	p<0.01
OV 20%	1.49	0.36	1.38 1.61	0.88	0.48	0.75 1.29	p<0.01
OV 9%	1.54	0.44	1.40 1.68	0.89	0.47	0.78 1.42	p<0.01
Strehl ratio	0.25	0.07	0.23 0.27	0.16	0.07	0,14 0.24	p<0.01
OSI	0.58	0.20	0.52 0.64	1.80	1.58	0.69 1.98	p<0.01

Table 3: Mean (±SD) and IC 95% of OQAS values for non-treated amblyopic and control groups.

Acknowledgements

This study was supported by the Spanish Ministry of Education and Science under grants DPI2008-06455-C02-01, DPI2011-30090-C02-01 and the European Union.

References

[1] Güell et al., J Cataract Refr Surg., 30, 1598, 2004
[2] Martínez-Roda JA et al., Clin Exp Optom, 94, 223, 2011
[3] Artal et al., Plos, 6, e16823, 2011

EMVPO2012_5762_044 STUDENT PRESENTATION

A New Tool for Depth Perception Training for Autism and Other Conditions

E. Ansbro[1], C. Overhauser[2], Alova[2]; [1]Open University, PSSRI, Milton Keynes (GB); [2]RealView Innovations Ltd, Boyle (IE).
Email: eansbro@realview.ie

Summary
Many conditions, physiological and psychological, have been found to benefit from depth perception training, including autism. Recent research suggests that the original cause of autistic behaviour is perceptual. Recent developments in 3D technology address this problem.

Introduction
It is commonly recognised that vision is the dominant sense, as seventy-eighty percent of the information we receive enters the brain through the eyes. Any problems in how the brain processes visual information can cause difficulties in one's general ability to function and can result in various disabilities. When all the senses are integrated, a deficiency in one may lead to disturbances in the others. There are numerous conditions that benefit from depth perception training. The focus here will be on autism, but the discussion can easily be extended to ADD, ADHD, and other conditions.

Discussion
Children with autism are challenged by a sensory overload and by aversions to a variety of auditory, visual, and tactile stimuli. In addition, their ability to attenuate and/or ignore these stimuli differs from that of a "typical" child. Autistic people report unusual sensory experiences. Autism spectrum disorders are characterized by core deficits in social interaction, communication, and repetitive or stereotypic behaviour. It is crucial to develop intervention strategies to help individuals with autism. For this purpose, virtual reality (VR), a simulation of the real world, has been shown to be an effective training tool.[1] Technological advances including the VR have contributed enormously to improving the treatment, training, and quality of life of children with disabilities.
Virtual reality (VR) training has rehabilitative potential for people with intellectual disabilities, both as intervention and assessment. It can provide a safe setting in which to practice skills that might carry too many risks in the real world. Unlike human tutors, computers are infinitely patient and consistent. Virtual worlds can be manipulated in ways the real world cannot be and can convey concepts without the use of language or other symbol systems. The training can promote mental simulation of social events, potentially allowing a greater insight into minds. Practice of behaviours, both within and across contexts, encourages a more flexible approach to social problem solving. VR has been shown to help minimize the effects of the disability, enhance skills training, and improve the child's social participation and quality of life.[2]
Enhancing depth perception is a valuable addition to VR techniques. However, consumer 3D displays, like 3D TVs and games, force the viewer into an unnatural view of the world. This is directly opposed to what an autistic person needs.
This has been addressed by a new training tool called “Deep Screen” which provides a natural viewing experience with enhanced depth perception. In contrast to other technologies that require unnatural content rendering and/or unnatural eye-brain coordination, the Deep Screen utilizes only natural optical principles to enhance depth. The eyes and brain operate with their natural coordination.

Conclusion
Virtual reality technology requires the natural viewing attributes that are impossible with existing commercial 3D displays. It is important to provide a safe environment for learning without the side effects of existing 3D displays. This new tool can provide the necessary view of the world that could significantly improve the wellbeing of an autistic child. The long term use of the technology should address the symptoms of the reflections of the child’s mental construction of the world by creating normal set of sensory information over time.

References
[1] M. Wang, D. Reid, “Virtual reality in pediatric neurorehabilitation: attention deficit hyperactivity disorder, autism and cerebral palsy,” *Neuroepidemiology,* **36(1),** 2-18, 2011
[2] D. Gourlay, K.C. Lun, Y.N. Lee, J. Tay, Virtual reality for relearning daily living skills,” *Int J Med Inform.,* **60(3),** 255-61, 2000
[3] D.C. Strickland, D. McAllister, C.D. Coles, S. Osborne, “An Evolution of Virtual Reality Training Designs for Children With Autism and Fetal Alcohol Spectrum Disorders,” *J Intellect Disabil Res*, **46 (Pt 5),** 430-43, 2002
[many more references]

EMVPO2012_5768_046 STUDENT PRESENTATION

A Method to Evaluate Peripheral Visual Perception

I. Timrote, G. Krumina, T. Pladere, M. Skribe; University of Latvia, Department of Optometry and Vision Science, Riga, LV-1063 (LV).
Email: leva.Timrote@gmail.com

Summary
We are developing a method that should help evaluating peripheral visual perception. All the tests help looking at how different peripheral stimuli affect the performance of near vision task – whether the peripheral stimuli sidetracks attention hence worsening the time needed to accomplish the near vision task.

Introduction
In everyday life we do not differentiate central and peripheral visual field. It is known that P visual pathway is addressed to properties concentrated in central visual field and M visual pathway – in peripheral visual field [1]. And there are several disorders connected to M, P visual pathways that can be improved until certain age [2]. Because of this, it is essential to differentiate which pathway is responsible for the problem as soon as possible. Hence our goal is to make a test that would divide individuals in two different groups – with and without problem concerning peripheral visual properties.

Methods
We have made a method consisting from several tests. An individual has to count how many times one specific letter is repeated in a set of letters (ten letters in ten rows). This set of letters is demonstrated randomly in three different central conditions – on white background, in lines or in squares (overall three times per each central background). Three different days are used to perform this central task so that different peripheral noise could be used – white background, five times five or ten times ten black dots. To make the task more difficult, there can be peripheral stimulus appearing while counting the letters. Another kind of task is when an individual has to name all the letters appearing on the screen and changing every second. Meanwhile red, green or blue stimulus appears in the peripheral visual field.

Results
The results demonstrate that the time needed to accomplish the visual search task improves with adding the peripheral noise. All the individuals can be divided in two groups – there are ones whose performance is better when counting the specific letters in squares and worse on white central background. For the other group it takes less time to accomplish the task when they have to count letters in lines and more when counting on white central background. When adding a peripheral stimulus, there are cases when an individual can exclude their peripheral vision hence not seeing the peripheral stimulus of different size.

Discussion
Usually there are tests that consist of a single spot or a letter while there are several moving stimulus in the peripheral visual field [3]. We decided to improve the central stimuli so that an individual would be more occupied. Developmental Eye Movement Test is done naming all the letters from the blank and counting the score [4]. In this case they do not pay attention to the background that could affect the result. As far as there could be people whose peripheral vision sidetracks attention, these test results could be worsen with peripheral stimuli. For this reason we decided to add noise in the

periphery consisting from black dots either five times five or ten times ten across the screen. Hence an individual is asked to either name the letters while there are coloured peripheral stimuli side-tracking attention or count a specific letter from a grid of letters while the there are additional central and peripheral stimulus.

Conclusions
This test can be used to divide individuals in different groups hence looking for a problem in visual pathways. Still there have to be improvements made to adapt this test for children.

Acknowledgement
This work has been supported by the European Social Fund within the project «Support for Doctoral Studies at University of Latvia». Thanks to S. Fomins for the help with the program.

References
[1] E. Kaplan, The M, P, and K Pathways of the Primate Visual System, In: *The Visual Neurosciences*, ed., L.M. Chalupa, J.S. Werner (MIT Press, Hong Kong, 2004), pp. 481-493
[2] E.E. Parrish, D.E. Giaschi, C. Boden, R. Dougherty, The maturation of form and motion perception in school age children, *Vision Research*, **45**, 827-837 (2005)
[3] W.A. Monaco, J.T. Kalb, C.J. Johnson, Motion Detection in the Far Peripheral Visual Field, *Army Research Laboratory report* (ARL-MR-0684), December 2007
[4] J.M. Powell, K. Birk, E.H. Cummings, M.A. Ciol, The Need for Adult Norms on the Developmental Eye Movement Test (DEM), *Journal of Behavioural Optometry*, **16**, 38-41 (2005)

EMVPO2012_5770_047 STUDENT PRESENTATION

Vortex beams in Visual Optics

J.P. Trevino, J.E. Gomez-Correa, S. Chavez-Cerda; Instituto Nacional de Astrofisica, Optica y Electrónica (MX).
Email: trevinojp@inaoep.mx

Summary
We present an analysis of aberrations of Vortex Fields and suggest an application to increase resolution when imaging the photoreceptor mosaic of the retina.

Introduction
Many of the concepts and techniques currently employed in Visual Optics have their origin in astronomy. This is the case of Zernike Polynomials and Adaptive Optics systems for aberration correction. Recently, Optical Vortices have been implemented as coronagraphs [1] and to study the surroundings of bright stars to detect nearby planets, with this technique it is possible overcome Rayleigh's resolution limit [2]. We examine this novel technique presenting an aberration analysis of systems in the presence of Vortex Beams.

Discussion
An optical vortex is a wave field wich features an azimuthally varying phase factor of the form $e^{im\varphi}$. The azimuthal coordinate is φ and m is an integer known as the topological charge. The exponent in this factor represents a phase that varies linearly with respect to φ and thus generates a helicoidal wavefront. For a uniform field, as a consequence of the vortex, a dark core is created at the center of the point spread function (PSF). Vortices can be generated by Spatial Light Modulators or by refractive or reflective elements suitably shaped for this purpose. One of such devices, described in [3] is designed as an achromatic doublet having a helicoidal interface between the glasses. This device is designed for a specific wavelength and therefore has a limited bandwidth. The field at the focal plane, is obtained by means of the Frounhoffer integral:

$$U_f(\rho,\varphi) = PSF = \int_{-\pi}^{\pi}\int_{0}^{\infty} A(r)e^{ikW(\rho,\varphi)}\, e^{im\varphi} e^{i\frac{k}{2f}r\rho\cos(\varphi-\theta)} r dr d\varphi$$

where $W(\rho, \varphi)$ represents the wavefront aberration, k is the wave number for a specific wavelength and the focal distance. This integral is the PSF of the system and it gives information of its aberrations. An aberration free system with a vortex has a PSF that displays a central dark region and bright rings as depicted in figure 1B. Radial dependence of the PSF is shown in figure 1C for increasing values of the topological charge.

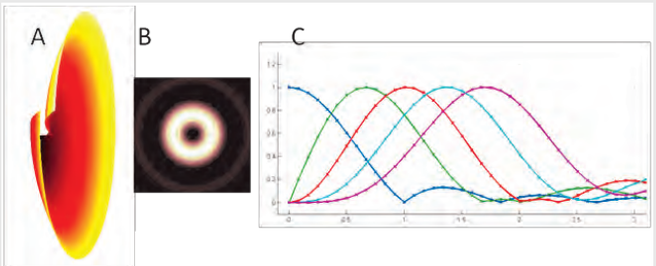

Fig. 1: A: Converging wavefront featuring a vortex phase factor. B: The psf of a system with = 2 C: Transversal cut of the psf for different values of .

Fig. 2: Effects of a vortex wavefronts on an aberrated field with comma. Left: Single source with no vortex. Center: Single source with = 2. Right: two sources with = 2. Notice that the dark regions are present and thus we can infer the presence of two close sources.

Two luminous sources cause the dark central dark zone to divide into dark zones. Given different coefficients of primary aberrations, the dark zones remain, as shown in figure 2. In this picture, a pair of barely resolved sources in a vortex field with comatic aberration are presented with no vortex = 0 (left) and with = 2.(right). We can distinguish the presence of two sources in the second case because of the pair of dark zones at the center of the PSF. Astigmatism shows fringe-like patterns even for single sources, so the system is sensitive to this aberration.

Conclusions
We apply the concepts first introduced by Swartzlander, to image the photoreceptor mosaic of the retina.. We explore the limit to which aberrated elements would still detect multiple sources and resolve them.

References
[1] G. A. Swartzlander. *Peering into Darkness*. Opt. Lett. **26**, 8. 2001.
[2] F. Tamburini, G. Anzolin, G. Umbriaco,, A. Bianchini, and C. Barbieri. *Overcoming the Rayieigh Criterion Limit with Optical Vortices.* Phys. Rev. Lett. **97**, 16. 63903 (2006).
[3] G. A. Swartzlander. *Achromatic Opyical Vortex Lens*. Opt. Lett. **31**, 13. 2006.

NOTES

EMVPO2012_5773_048 STUDENT PRESENTATION

Second-harmonic cornea microscopy enhancement with annular aperture filters

J.J. Li, B. Vohnsen; AOI Group, University College Dublin, School of Physics, Dublin (IE).
Email: jiajun.li@ucd.ie

Summary
Annular apertures have been used in confocal microscopy to enhance resolution by excluding low-angular components of imaging light and reducing the width of the effective PSF. Here, we report on the use of annular apertures to enhance image quality of cornea collagen fibril imaging.

Introduction
Annular apertures have previously been used to increase resolution in confocal microscopy by excluding low-angular components of scattered light creating a reduction of the effective PSF [1-3]. The approach has also been used with multiphoton imaging [4] and we have recently applied it to confocal retinal imaging and to match the PSF to the individual photoreceptors [5].
For linear imaging, the theoretical resolution improvement reaches nearly 60% when apodizing the incident beam with an annulus (although at the cost of signal) [5]. Likewise, apodizing the light scattered by the sample improves resolution although to a lesser degree. For nonlinear imaging the expected benefit is larger. Two-photon signals such as second-harmonic generation depends quadratically on the PSF and thus the potential resolution improvement with annular apertures is larger than for the linear case.

Discussion
We have implemented annular apertures on transparent foil to examine the usability of the annular-apodization approach for both the incoming pump beam and for the second-harmonic generated signal in forward-generated second-harmonic (SH) imaging of porcine corneas. Our previous studies found a strong directional component of SH radiation in the forward direction [6] which we here use for the alignment of the annular apertures by means of a CMOS camera with long integration time.
The aperture filters are used on an in-house build SH imaging microscope incorporating an ultrafast Ti:Sapphire fs laser and a range of high NA imaging objectives and motorized z-scan stage. We complement the experimental analysis with a numerical model for SH imaging of the collagen under the different illumination and detection situations. The experimental setup and image examples are shown in Fig. 1.

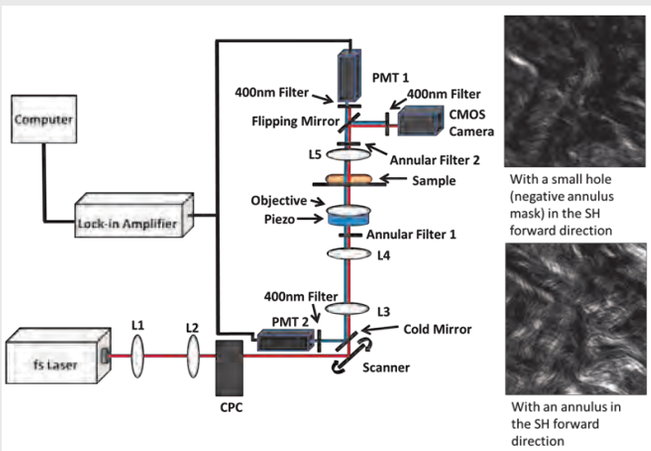

Fig 1. Microscope setup (left) and image examples (right) showing the impact of the annular filter in the forward direction when compared to a reduced aperture using only the central part of the SH signal (the negative mask of the annulus).

To confirm the higher level of detail in the images recorded with annular apertures these have also been Fourier analyzed confirming the enhancement of high-frequency components in the images.

Conclusions
Annular apertures can be used to improve resolution and enhance small details in SH imaging microscopy as demonstrated here for collagen fibrils in porcine corneas. A thin rim annulus has higher resolution potential but may also lead to unacceptable loss of signal.

References
[1] C. J. R. Sheppard and A. Choudhury, Image formation in the scanning microscope, Opt. Acta **24**, 1051–1073 (1977)
[2] G. J. Brakenhoff, P. Blom, and P. Barends, Confocal scanning light microscopy with high aperture immersion lenses, J. Micros. **117**, 19–232 (1979)
[3] T. Wilson and S. J. Hewlett, The use of annular pupil plane filters to tune the imaging properties in confocal microscopy, J. Mod. Opt. **37**, 2025–2046 (1990)
[4] S. W. Hell, P.E. Hänninen, A. Kuusisto, M. Schrader, and E. Soini, Annular aperture two-photon excitation microscopy, Opt.Commun. **117**, 20-24 (1995)
[5] B. Vohnsen and D. Rativa, Ultrasmall spot size scanning laser ophthalmoscopy, Biomed. Opt. Exp. **2**, 1597-1609 (2011)
[6] B. Vohnsen, J.J. Li and A. Jewel, Second-harmonic microscopy for cornea collagen fibril imaging: Theoretical and experimental optimization, FiO abstract (2011)

NOTES

EMVPO2012_5774_049 STUDENT PRESENTATION

Myopes visual acuity with positive and negative contrast stimuli

G. Ikaunieks, E. Caure, E. Kassaliete, Z. Meskovska; University of Latvia, Department of Optometry and Vision Science, LV-1063 (LV).
Email: gatis.ikaunieks@lu.lv

Summary
In this research influence of spectacle and contact lenses on positive and negative contrast visual acuity is evaluated for myopes. With each correction difference between positive and negative contrast visual acuity was not statistically different.

Introduction
Some researches showed that for corrected myopes visual acuity is better with positive Weber contrast (white symbols on black background) than with negative contrast (black symbols on white background) optotypes. One explanation of such phenomena is that myopes have neurological changes in ON and OFF pathways [1]. From another studies it is well known that in case of increased light scattering level in the eye symbols with positive contrast are resolved better than with negative contrast, because bright background increases retinal straylight more than dark background [2]. Additional source of retinal straylight for corrected myopes is spectacle [3] or contact lenses [4], so it cannot be excluded that corrected myopes have better visual acuity with positive contrast not only due to neurological but also optical factors. In our research we wanted to find out how optical correction influences myopes visual acuity with positive and negative contrast stimuli.

Discussion
17 persons (11 myopes and 6 emmetropes) at the age from 20 to 22 participated in this research. The spherical equivalent refractive error of the myopic subjects ranged from -2.5 to -6.75 D. Monocular visual acuity (VA) with positive (97%), reversed negative and low contrast (-10%) Landolt optotypes was determined using FrACT computer program. Measurements for myopes were done using spectacle or contact lenses correction. As was expected, the worst visual acuity was found with the low contrast optotypes. For myopes these values were lower than for emmetropes, but for myopes visual acuity obtained with high contrast stimuli also were lower, so we can't conclude that myopes have worse contrast sensitivity than emmetropes.

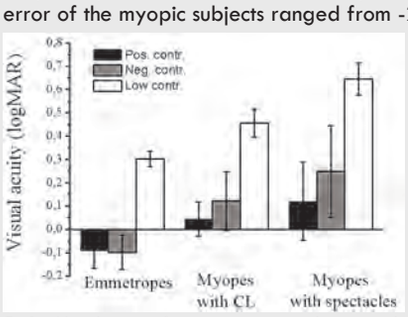

Fig1. Visual acuity for emmetropes and corrected myopes with different contrast stimuli. Standart deviations for each data serie are showed.

For emmetropes visual acuity with positive and negative contrast was not significantly different, while for myopes visual acuity was better with positive than with negative contrast stimuli. We tested myopes with their own spectacles which were used at least one year. Therefore we expected that difference between positive and negative contrast visual acuity will be greater with spectacles than with contact lenses. However differences in both cases were not statistically significant.

Conclusions
Better visual acuity for myopes with positive than negative contrast stimuli is related mainly with neurological not optical factors.

References
[1] B.D.Stoimenova, *Invest Ophthalmol Vis Sci*, 48, 2371-4, 2007
[2] G. Westheimer et al., *Optometry and Vision Science*, 80, 749-752, 2003
[3] G.C. De Wit and J.E. Coppens, *Optometry and Vision Science*, 80, 395-400, 2003
[4] A. Cervino, *Ophthal Physiol Opt*, 28, 151–156, 2008

EMVPO2012_5775_050 STUDENT PRESENTATION

Measurement of accomodative response curve based on brightness of the retinal reflex

V. Karitans[1,2], M. Ozolinsh[1,2], E. Skutele[2]; [1]Institute of Solid State Physics, Department of Ferroelectrics, Riga, LV-1063 (LV); [2]University of Latvia, Department of Optometry and Vision Science, Riga, LV-1063 (LV).
Email: variskaritans@gmail.com

Summary
We describe development of a device measuring the accomodative response based on brightness of the retinal reflex and the results obtained. A photodiode and light integrating circuit is used to measure the gathered light for various refractive states of an eye.

Introduction
It is known that brightness of the retinal reflex depends on the refractive state of an eye. It depends not only on the refractive error of an eye but also on accomodation. This phenomenon is observed when the patient's fundus is observed using ophthalmoscopy methods. Several devices measuring the refractive state and accomodation of an eye based on the retinal reflex have been designed [1,2]. In this study we describe an electronically optical system measuring dependence of brightness of the retinal reflex on accomodative state. It is known that the tonic accomodation is about 0.75 D. Below this value an eye accomodates lead while above this value the accomodative lag is observed [3]. We employ a light integrating circuit to collect the light reflected from the retina. The aim of the study is to create a device that allows to obtain the accomodative response curve.

Discussion
The optical setup used in the study is shown in Figure 1. An infrared laser emits radiation at the wavelength l = 850 nm. The light reflected from the retina gives rise to a photocurrent integrated by a capacitor. The photocurrent is generated by a photodiode S1337-66BR (*Hamamatsu*) [4]. Simultaneously with light integration the eye also views the stimulus. Accomodation response required to see the stimulus sharp is changed by varying the distance between the stimulus and the lens.

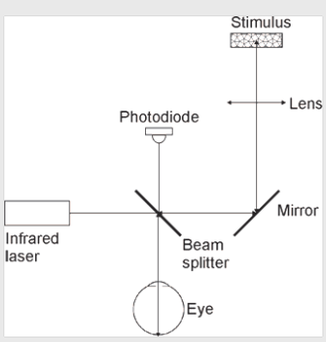

Fig 1. The optical setup used to measure accomodation response curve.

To obtain the accomodative response curve the calibration curve must first be obtained. This is done by placing trial lenses in front of the eye while the pupil is dilated and accomodation has been paralyzed. This was done by using 1 % cyclogyl solution. The calibration curve shows how the signal (voltage) across the capacitor varies with the power of the trial lenses. In the next stage the stimulus is placed at such the distance from the lens that it requires a certain accomodative response. It must be assured that the light gathered by the photodiode isn't altered as a consequence of pupil narrowing. For this purpose a phenylephrine solution was used. By measuring the real response, i.e., the voltage of the capacitor the real accomodative response can be read from the calibration curve. If the real accomodative response is measured and the required accomodative response is known then the response curve of accomodation can be obtained.

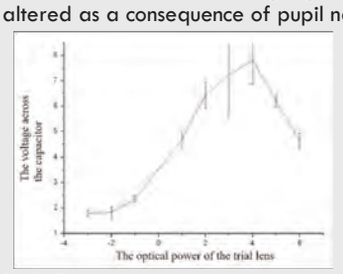

Fig 2. The calibration curve for one subject showing the relationship between the voltage across the capacitor and the optical power of the trial lens.

In Figure 2 the calibration curve for one subject is shown. On the x-axis the optical power of the trial lenses is given whereas on the y-axis the voltage across the capacitor is given. It can be seen that the relationship is an extreme

function. Obviously, the peak is reached when the photodiode is located in the near point where the vision becomes clear in the case of a myopic observer.

Conclusions

The device in progress may be usable as a convenient tool to measure the dynamic behaviour of accomodation.
The calibration and measurement procedure is complex because for calibration purposes accomodation must be paralyzed whereas for measurements accomodation must be possible. In both cases the effects of pupil diameter must be minimized.

References

[1] W.N. Charman, G. Heron, *British Journal of Physiological Optics*, **30**, 1 – 12, 1975
[2] A. Roorda, W.R. Bobier, M.C. Campbell, *Vision Research*, **38**, 1913 – 1924, 1998.
[3] B. Wang, K.J. Ciuffreda, *Survey of Ophthalmology*, **51**, 75 – 85, 2006
[4] Hamamatsu Photonics. *Application circuit examples of Si photodiode*, 4, 2008

EMVPO2012_5776_051 STUDENT PRESENTATION

Printed test plates for color discrimination threshold determination

K. Luse[1], S. Fomins[2], M. Ozolinsh[1,2]; [1]University of Latvia, department of Optometry and Vision Science, LV 1063 Riga (LV); [2]University of Latvia, Institute of solid State Physics, LV 1063 Riga (LV).
Email: kaiva.luse@gmail.com

Summary

The aim of the research is to study availability of different color print technologies (three layer photographic process, tint printing) for creation of color vision test plates, for an accurate diagnosis and grading of color vision anomaly.

Introduction

Color deficiency tests are widely used to diagnose the type and severity of color vision deficiencies. Among most frequently used are pseudoisochromatic test plates. For best efficiency of color vision deficiency diagnosis, correct color representation is essential. Previous studies have shown that the printing technology impacts the color display accuracy of the test plates, resulting in a wide distribution of color coordinates along the desired points on the confusion lines in CIE color space diagrams [1].

Discussion

The study incorporates (1) evaluating the adequacy of commercially available color vision deficiency test plates, (2) modeling the vision perception in terms of cone signals and thus predicting the outcome perception in case of deficiency and (3) evaluating the impact of non-standard illuminating conditions on the manifestation of color vision deficiency.

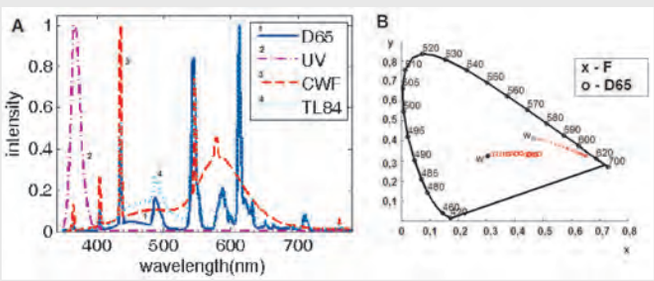

Fig.1 **A** – spectra of 4 light sources used in the experiment. **B** – an example of measured reflectances of 27 different saturation and lightness red samples in the CIE xy color space chromaticity diagram under two different illuminating sources F and D65 (w represents white sample).

There are different types of illumination sources nowadays, which have particular spectral characteristics and color rendering indexes. Fig.1A shows the spectra of four light sources used in the study (D65, UV, CWF, TL84). An additional source (F) was used in the experiment. Source UV was used to estimate the fluorescence of the colors in the samples.
Test plates were produced by photographic printing process (*Noritsu HD 3701* digital printer was used) and *Canon PIXMA mp550* inkjet photo printer on glossy photo paper. Spectral reflectance and colorimetric characteristic coordinates of two technologies are studied for the purposes of precise color reproduction (example is given in Fig.1.B). Measurements were made using QT-100W Lightbooth with D65 (CCT=6500K), F (CCT=2700K), CWF (CCT=4000K) and TL84 (4100K) standard illumination sources (Fig.1.A). Ultraviolet lamp (λpeak=365nm) was used to characterize ink fluorescence of mentioned printing technologies. Fluorescence was observed for red inks of inkjet technology.
For final assessment of printed tests both: color vision deficient an unaffected subjects to be tested using both: commercially available tests and sets of generated color plates, and their color discrimination thresholds to be acquired. The threshold increases with severity of color vision anomaly [2].
The results are to be used for the development of test plates for finer diagnosis of color vision deficiencies.

This work has been supported by the European Social Fund within the project «Support for Doctoral Studies at University of Latvia - 2» and project No. 2010/0259/2DP/2.1.1.1.0/10/APIA/VIAA/137.

References

[1] S.Fomins, M.Ozolinsh, Multispectral Analysis of Color Vision Deficiency Tests, *Materials science (Medžiagotyra)*, **Vol. 17(1)**, 2011
[2] E. Konstantakopoulou ,M. Rodriguez-Carmona, J. L. Barbur, Processing of color signals in female carriers of color vision deficiency, *Journal of Vision*, **Vol. 12(2)**, 2012

NOTES

EMVPO 2012 - 6th EOS Topical Meeting on
Visual and Physiological Optics
20 - 22 August 2012 | University College Dublin (UCD), Dublin, Ireland

www.myeos.org/events/emvpo2012

REGISTRATION CATEGORY

The registration fee includes full-time admission to the meeting, coffee breaks and lunches on all three meeting days, one copy of the extended programme (ISBN numbered) as well as the participation in the official welcome reception on Sunday, 19 August. The registration for the official conference dinner and social programme is closed.

Late/On-site registration (from 06 August 2012)	**Universities, private persons, German and non-EU companies and non-university research institutes**	**EU companies and EU non-university research institutes (except Germany)***
Late/On-site registration for members (conference only) **Member of:** ❑ EOS ❑ OSA	❑ 430.00 € (incl. 19% VAT)	❑ 361.34 €* (excl. VAT, VAT no. required)
Late/On-site registration for non-members (conference only)	❑ 490.00 € (incl. 19% VAT)	❑ 411.76 €* (excl. VAT, VAT no. required)
Late/On-site registration for student members (conference only) **Member of:** ❑ EOS ❑ OSA Copy of your current student ID required.	❑ 200.00 € (incl. 19% VAT)	❑ 168.07 €* (excl. VAT, VAT no. required)
Late/On-site registration for student non-members (conference only) Copy of your current student ID required.	❑ 220.00 € (incl. 19% VAT)	❑ 184.87 €* (excl. VAT, VAT no. required)

❑ **I have read and accept the General Terms and Conditions of the EOS - Events & Services GmbH at:**
http://www.myeos.org/aboutus/terms_and_conditions

***IMPORTANT:** Registrations from companies and non-university research institutes registered in EU countries (except Germany) are exempted from VAT. **Registrations without valid VAT no. will not be accepted. Please enter VAT no.:**

VAT no.: _____

PLEASE FILL IN YOUR NAME AND ADDRESS

❑ Ms. ❑ Mr. _____ _____ _____

Title First name Name

_____

Company

_____

Street

_____ _____ _____

City Zip/Postal code Country

_____ _____

Telephone Fax

_____ _____

Email address Homepage

PAYMENT OPTIONS

1) CREDIT CARD PAYMENT

Payment shall be made in € by credit card. If bank transfer is preferred see details below.

Charge to my: Mastercard[1] ❑ VISA[1] ❑ Eurocard[1] ❑ American Express[2] ❑

Card No.: ☐☐☐☐ ☐☐☐☐ ☐☐☐☐ ☐☐☐☐

Expiry Date: _____

Verification No.: _____

[1]**Mastercard, Visa, Eurocard:** The final 3-digit number located on the back of your credit card.]
[2]**American Express:** The four small numbers printed on the front of your card, above the last few embossed numbers.]

Name of credit card holder: _____

Signature: _____

Date: _____

2) PAYMENT BY BANK TRANSFER

❑ I wish to pay by bank transfer, please send me the invoice and banking details.

Please note: For payment via bank transfer we charge 15.00 € handling fee.
The full registration fee must arrive at the EOS bank account before the start of the meeting.
Please note that all bank fees must be paid by the attendee.

CANCELLATION POLICY

Requests for cancellation must be made in writing to the EOS Office (address see below).
Refunds are subject to a processing fee of 50 €.

Cancellations received **by 20 July 2012:** full refund minus processing fee (50 €).
Cancellations received **after 20 July 2012:** no refund.

EOS EVENTS IN 2013

3rd EOS Topical Meeting on "Blue" Photonics - Optics in the Sea

Royal Netherlands Institute for Sea Research (NIOZ), Texel, Netherlands | 18 - 20 March 2013

www.myeos.org/events/bluephotonics3 | bluephotonics3@myeos.org

3rd EOS Conference on Manufacturing of Optical Components (EOSMOC 2013)

International Congress Centre Munich (ICM), Germany | 13 - 15 May 2013

www.myeos.org/events/eosmoc2013 | munich@myeos.org

2nd EOS Conference on Optofluidics (EOSOF 2013)

International Congress Centre Munich (ICM), Germany | 13 - 15 May 2013

www.myeos.org/events/eosof2013 | munich@myeos.org

1st EOS Conference on Advanced Optomechanical Engineering (EOSOPE)

International Congress Centre Munich (ICM), Germany | 13 - 15 May 2013

munich@myeos.org

EOS EVENT CALENDER

For more information about EOS organised and EOS co-sponsored events, please go to **www.myeos.org/events.**

Should you wish to be kept informed about an EOS organised event, please send an email with your contact details to the above mentioned email address.

ISBN 978-3-9815022-3-7